'Breaking New Ground'; An investigation into coseismic ground cracking following the 2016 Mw 7.8 earthquake near Kaikoura, New Zealand

ROBERT STEPHEN DESSINGTON

'*Breaking New Ground*'; An investigation into coseismic ground cracking following the 2016 M_w 7.8 earthquake near Kaikoura, New Zealand

Robert S Dessington

Department of Geography and Institute of Hazard, Risk and Resilience

Durham University

November 2020

Thesis submitted for the degree of Master of Science

Declaration

I confirm that no part of the material presented in this thesis has previously been submitted for a degree in this or any other university. In all cases the work of others, where relevant, has been fully acknowledged.

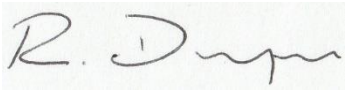

Robert S Dessington

Durham University

November 2020

ABSTRACT

Seismic shaking can cause landsliding throughout mountainous topography. Posing a direct hazard to the people and infrastructure that occupy these environments, landsliding receives considerable attention from the scientific community. However, few studies have detailed and analysed another form of earthquake-induced damage – ground cracks. Cracks could be a potential indicator of incipient landsliding and/or a surface expression of the retention of damage by hillslopes. Existing damage makes hillslopes more vulnerable to future failure. As such, ground cracking poses a lingering hazard presenting a need to better understand it – in particular its geomorphological characteristics and most influential controlling factors, and therefore how it can be detected/modelled. In 2016 the M_w 7.8 Kaikoura earthquake in New Zealand resulted in extensive ground cracking, providing an ideal case study. A ground crack inventory was digitally compiled using visual interpretation of post-event aerial photography. A detection attempt using a post-event digital terrain model (DTM) to semi-automatically extract cracks was unsuccessful. However, comparing this with an attempt using higher-resolution sample data emphasizes the necessity to consider the interdependence between feature scale and data resolution when attempting to detect/analyse. Feature analysis found that cracks are preferentially 7 m (~3-8 m) in length. Lack of small features may be due to minimum strain thresholds and strain accumulation. Larger cracks have likely developed into landsliding. Both offer new insight into internal hillslope forcing. Cracks preferentially form in a slope perpendicular direction, indicating a topographic control on propagation. Further potential controls were statistically analysed using Fuzzy Logic, which then informed a spatial prediction. The most influential control is proximity to landsliding, suggesting that in most cases cracking is an expression of incipient landsliding. Cracking preferentially occurs at ridgetop locations and on hillslopes facing the source of shaking. The latter is the inverse of behaviour exhibited by landsliding, highlighting the interdependence between directional shaking, local slope aspect and normal/shear stress. This conforms to and provides a new novel insight into the topographic site effects theory. Whilst quantitatively unsuccessful, the best performing spatial prediction model showed great promise in locating ground cracks in areas of high hazard, providing a solid foundation for improvement through further research so that eventually models like this can better inform ongoing hazard monitoring.

Keywords: ground cracking; incipient landsliding; fuzzy logic; hazard prediction; digital terrain model (DTM); hillslope; coseismic.

ACKNOWLEDGMENTS

Firstly, an immeasurable thank you to my three academic supervisors – Professor Nick Rosser, Dr Mark Kincey and Dr Tom Robinson. Since forging this idea with Nick at the end of my BSc, he has been a constant source of inspiration and wisdom. He has an open-door policy like no other and is always willing to talk through and make sense of difficult concepts. Mark has always been a valued source of honest, impartial advice as well as technical expertise, not just throughout this degree but also my BSc education. Tom's support has been pivotal – particularly regarding statistical techniques, and he has a knack of helping to make sense of complex scientific/mathematical problems. To all three of them, I would like to say a massive thank you.

Thanks also to Dr Matt Brain and Dr Chris Massey who were responsible for examining this thesis. Both provided critical insight and some valuable suggestions which have helped to improve this piece of work – I thank them both for their time and contribution. Chris, along with Dave Herron, Katie Jones and everyone else at GNS Science also helped to source and provide the excellent quality data used in this research, for which I am extremely grateful.

And finally, thank you to everyone who has contributed to an unforgettable four years at Durham. To the people at Team Durham, who played a major part in making this MSc possible; to the coaches and teammates past and present of the Rugby League Football Club, who've strove to take the club on a trip to the moon; to housemates and course mates, for being such good company throughout; and of course to my family who've been there every step of the way.

CONTENTS

LIST OF FIGURES

TITLE IMAGE – COSEISMIC GEOMORPHOLOGICAL DAMAGE INDUCED BY THE KAIKOURA EARTHQUAKE IN 2016.

LIST OF TABLES

LIST OF EQUATIONS

1. $$Fos = \frac{sum\ of\ resisting\ forces}{sum\ of\ driving\ forces}$$

2. $$Ph = \begin{cases} |(|Rb - As|) - 360|, & |Rb - As| > 180 \\ |Rb - As|, & |Rb - As| \leq 180 \end{cases}$$

3. $$\chi_A(x) = \begin{cases} 1, & x \in A \\ 0, & x \notin A \end{cases}$$

4. $$\{\mu_A(x) \in \mathbb{R}\ |0 \leq x \leq 1|\}$$

5. $$H_{GC} = \left[\prod_{F=1}^{j} f(I_{\text{norm}F})\right]^{1-\gamma} \cdot \left[1 - \prod_{F=1}^{j} (1 - f(I_{\text{norm}F}))\right]^{\gamma},$$

6. $$E_a = \begin{cases} |(|E_d - As|) - 360|, & |E_d - As| > 180 \\ |E_d - As|, & |E_d - As| \leq 180 \end{cases}$$

7. $$I_{x_{\text{norm}}} = \frac{I_x - \min(I)}{\max(I) - \min(I)}$$

LIST OF ABBREVIATIONS

ASTER – Advanced Spaceborne Thermal Emission and Reflection Radiometer

AUC – Area Under Curve

Cs – Standard Curvature

DFME – Difference from Mean Elevation

DEM – Digital Elevation Model

DSM – Digital Surface Model

DTM – Digital Terrain Model

Ea – Euclidean Aspect

FG – Fuzzy Gamma

FL – Fuzzy Logic

FoS – Factor of Safety

FP – False Positive

Fr – Fault Rupture

GIS – Geographic Information Systems

GTD – Ground Truth Data

Hr – Hillslope Relief

I – Influence

KDE – Kernel Density Estimate

L – Length

Lc – Landslide Crowns

LiDAR – Light Detection and Ranging

PGV – Peak Ground Velocity

Pl – Slope Parallel

Ps – Path Sinuosity

R - Roughness

ROC – Receiver Operating Characteristic

Rt – Ridgetops

RTP – Relative True Positive

Sa – Slope Angle

SD – Standard Deviation

SDE – Standard Deviation of Elevation

SDs – Standard Deviation Sinuosity

Sr – Sub-Hillslope Relief

Sv – Direction to Fault Rupture

SVF – Sky View Factor

t – Time

TP – True Positive

TSE – Topographic Site Effects

V – Valley Bottoms

vc – Velocity

1. INTRODUCTION

1.1. BACKGROUND & RATIONALE

Ground cracking (e.g. Jibson *et al.*, 2018), fissuring (e.g. Owen *et al.*, 2008) or lateral spreading (e.g. Cubrinovski *et al.*, 2017) is an often overlooked coseismic phenomenon. The lithosphere responds to coseismic accelerations and gravitational stresses by generating strain, manifest at the surface in the form of a rupture (e.g. Burbank & Anderson, 2012). This releases energy via surface waves, causing shaking (e.g. Hovius & Meunier, 2012) and consequently 'damage' to the landscape. Damage can be in the form of cracking, commonly resulting from direct surface rupture where the fault is exposed at the surface (e.g. Li *et al.*, 2010); liquefaction-induced ground movement (e.g. Green *et al.*, 2011); or coseismic gravitational (slope) displacements. There remains relatively little literature that has explored the nature, distribution and co- and post-seismic evolution of cracks that appear during earthquakes.

Ground cracking can therefore also be a potential indicator of incipient landsliding (e.g. Petley *et al.*, 2006), whereby coseismically triggered slope instability may have led to some deformation but not complete slope collapse. This phenomenon provides a clear link between ground cracking and one of the most fatal natural hazards affecting society (Petley *et al.*, 2005a). This link may be key as more recent research has suggested a retention of coseismic damage by hillslopes making sequences of widely spaced (> years) earthquakes a potentially important control on landscape response to shaking (e.g. Parker *et al.*, 2013; Brain *et al.*, 2017). The timescales on which damage is retained are debated but may last for much longer than first thought (Parker *et al.*, 2015) and almost-certainly make a hillslope more vulnerable to failure in the first few years after an earthquake (Marc *et al.*, 2015). As such, cracking may have the potential to precondition failure in subsequent seismic (e.g. Parker *et al.*, 2015) or pluvial (e.g. Lin *et al.*, 2008) events and the coseismic damage that it inflicts on the landscape should be an ongoing cause for concern (e.g. Massey *et al.*, 2014). For example, coseismic ground cracking induced by the Kashmir Earthquake in 2005 has been suggested to have enhanced landslide rates during the 2006 snowmelt/monsoon seasons (Saba *et al.*, 2010).

Coseismic landsliding has received considerable attention over the past ~40 years (Keefer, 1984; Harp & Jibson, 1996; Keefer, 2000; Dai *et al.*, 2011; Kritikos *et al.*, 2015; Roback *et al.*, 2018) as the advent and development of Geographical Information Systems (GIS) has made the curation and analysis of landslide inventories quicker, more accurate

and extensive (e.g. Guzzetti *et al.*, 2012). Understanding has been advanced and coseismic landslide inventories from different events have started to be amalgamated into global landslide databases (e.g. Petley *et al.*, 2005b; Tanyas *et al.*, 2017) to enhance theoretical understanding independent of event- and site-specific parameters. This can feed into predictive models which have important implications for hazard/risk perception and emergency response (e.g. Robinson *et al.*, 2018). These are extremely important given that both pluvial and coseismic landsliding is common in some of the poorest mountainous regions (e.g. Pakistan, Nepal, rural China) globally (Froude & Petley, 2018).

Coseismic ground cracking in comparison has received very little attention. As such, it is poorly understood from both a geomorphological and hazard/risk perspective. A key reason for this is that until recently, data has not been of the necessary resolution to detect and analyse small-scale features (e.g. Roback *et al.*, 2018). This is beginning to change with the increasing prominence of very high-resolution aerial photography, satellite imagery and Light Detection and Ranging (LiDAR) data. Given the link with incipient landsliding and post-earthquake legacy, discussion and investigation around coseismic ground cracking appears to be appropriate and timely.

The 2016 earthquake near Kaikoura, New Zealand, provides a suitable event to examine ground cracking in detail. The M_w 7.8 event caused widespread geomorphological damage, including surface fault rupture (e.g. Litchfield *et al.*, 2018), landsliding and ground cracking (e.g. Dellow *et al.*, 2017). Some ground cracking was indicative of incipient landsliding (Jibson *et al.*, 2018) and consequently highlighted as a cause for concern (e.g. Massey *et al.*, 2018), especially given the extensive history of seismicity in New Zealand (e.g. Hancox *et al.*, 2002). Given its recent occurrence, there is also a suite of very high-resolution (aerial photography and airborne LiDAR) data which has been made available by the Department of Geological and Nuclear Sciences (GNS Science) in New Zealand. This event provides a considerable opportunity to both enhance our understanding of coseismic ground cracking and its exposure within the scientific community; and to use this to see if coseismic ground cracks and incipient landsliding can be semi-automatically predicted by capitalising on the availability of high-resolution datasets and simultaneously assess the utility of these when working on the sub-meter scale.

1.2. AIMS AND RESEARCH QUESTIONS

The overall aim of this study is to improve our understanding of coseismic ground cracking – in the form of geomorphological characteristics, and the most influential controlling factors on their occurrence; and to then use this knowledge to inform an attempt at predicting ground crack locations to inform ongoing hazard/risk monitoring. This will be addressed by the following research questions:

1. Can high-resolution LiDAR data be used to semi-automatically and accurately detect and predict small-scale ground crack features?
2. What are the geomorphological characteristics of co-seismic ground cracking?
3. What are the spatial topographic controls on co-seismic ground cracking?

1.3. STUDY SITE – WAIAU, NORTH CANTERBURY

This study focuses specifically on a 54 km^2 area in Hurundi District, North Canterbury on New Zealand's South Island (***Fig. 1.01***). The site is ~4 km and ~8 km NE of Waiau and the epicentre respectively; and lies along the SW-NE path of rupture propagation from the earthquake epicentre (Kaiser *et al.*, 2017). As a result, this area contains multiple sites of fault rupture and so experienced strong ground motion. The proximal relationship between landslides triggered by the event and fault rupture locations (Massey *et al.*, 2018) means that there are numerous coseismic landslides present in this area. Ground cracking is also manifest and visually noticeable from both the ground and aerial photographs. Topography at the site is diverse, with extensive swathes of both flat ground and steep, fluvially incised slopes and convex rolling hills. Proximity to directional shaking from both the epicentre and fault rupture locations; the noticeable presence of coseismic ground cracking and landsliding; and the topographic diversity make the study site the ideal location to undertake research into the geomorphological characteristics of and controls on coseismic ground cracking. Extent was limited to 54 km^2 to allow a thorough and detailed focus, but with a statistically significant number of ground crack features.

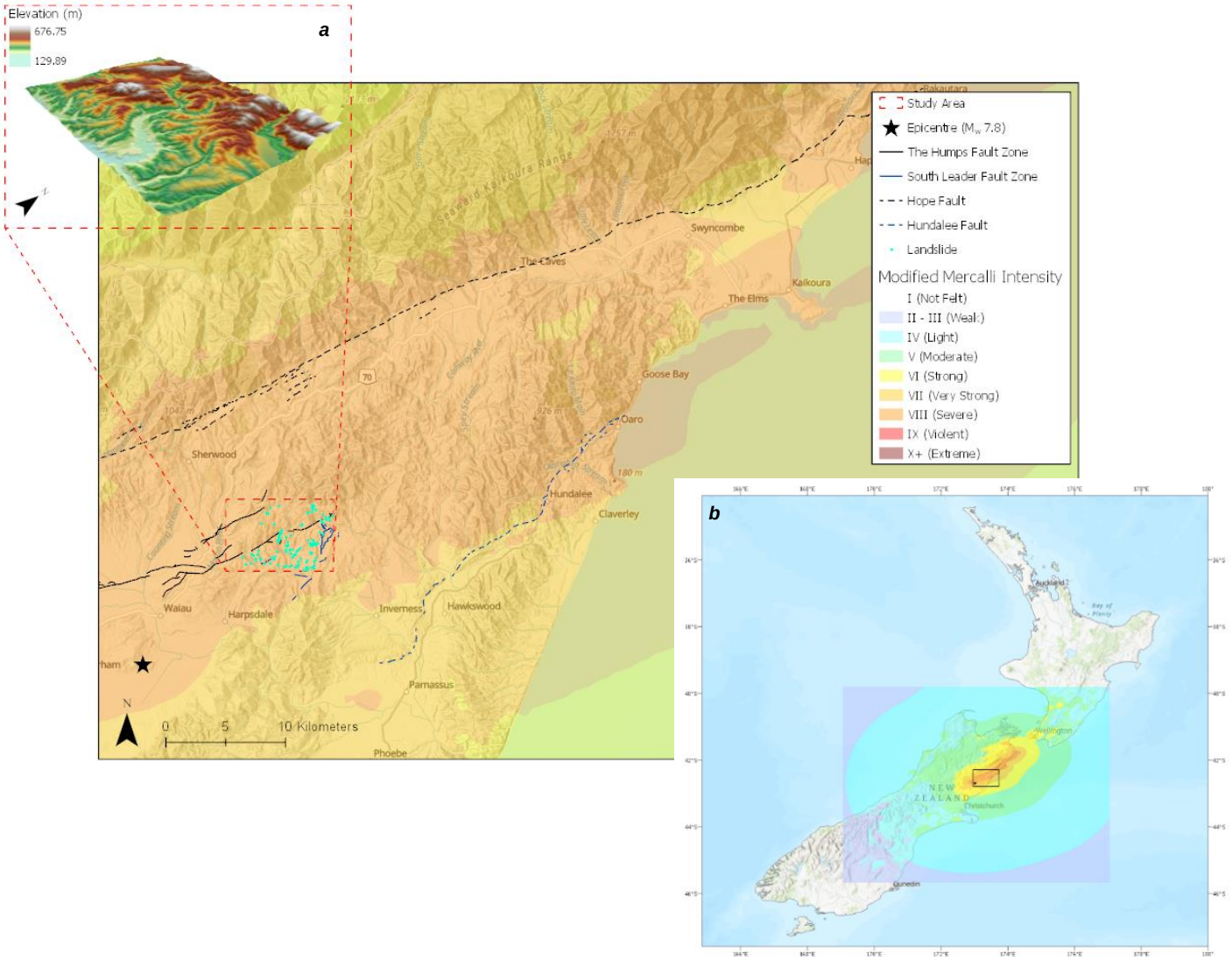

Fig. 1.01*: A map locating the study area ~4 km north-east of Waiau in Hurundi District, Canterbury, New Zealand. This has been expanded to display topographic variation (Inset: a). The study area experienced severe (MMI VIII) ground shaking due to its proximity to the epicentre and as both The Humps and South Leader Fault Zones ruptured directly through it, triggering numerous coseismic landslides. The Hope and Hundalee Faults have also been included for proximal indication, given the high slip rates along the Hope Fault in particular (e.g. Langridge & Berryman, 2005). Location, the epicentre and shaking intensity are contextualised on the national scale (Inset: b). Severe MMI VIII shaking propagated NE from the epicentre, up the east coast of the South Island.*

1.4. THESIS STRUCTURE

This thesis presents the results of a 12-month project, which has focussed on the use of high-resolution aerial photography and LiDAR to map coseismic ground cracks and consequently analyse their geomorphological characteristics and the controls upon their formation. This process can be visualised in ***Fig. 1.02***, which outlines the workflow linking the original study rationale/aims to methodologies through to the results, conclusions and future research suggestions. Following this introduction, the thesis comprises a further eight chapters.

Chapter 2 reviews coseismic ground cracking at all scales, and previous studies documenting evidence of this. As it is a secondary (seismic) hazard, a brief introduction to earthquakes is provided, before ground cracking is considered in the context of post-earthquake legacy; contextualising its pertinence as an ongoing geohazard.

Chapter 3 provides an in-depth contextual outline of the broader study area in the north-east South Island, New Zealand, providing site-specific context to the literature review in *Chapter 2*. Topographical influences and historical seismicity will be outlined, before a comprehensive review of the 2016 earthquake event is provided.

Chapter 4 documents the production of a coseismic ground cracking inventory. This chapter describes the methodological advances necessary to delineate cracking in the landscape, in the absence of existing methods and datasets. The data produced here is then considered in later chapters in the analysis of features (geomorphologically) and their topographic controls.

Chapter 5 presents an initial approach for an attempt at automatic feature detection applied to ground cracking, which was pre-informed using very high-resolution airborne LiDAR data from a section of the North Yorkshire coast where ground cracking is currently manifest.

Chapter 6 outlines the methodologies used to extract the geomorphological characteristics exhibited by coseismic ground cracks, and the results generated using these approaches.

Chapter 7 discusses statistical analysis of the data by presenting the Fuzzy Logic method used to determine the topographic controls on coseismic ground cracking and the relative importance of these. Results are presented and consequently used to inform a quantitative attempt at predicting potential ground crack locations.

Chapter 8 analyses results from ***Chapters 5***, ***6*** and ***7*** to address initial research questions. Detection and prediction attempts are discussed; potential geomorphological characteristics of ground cracks and the way that they propagate through the landscape are suggested; and, the respective importance of individual spatial topographic controls is presented and discussed with reference to pre-existing theory.

Chapter 9 provides concluding remarks in the form of a brief thesis overview; reporting of the main research findings and consequently, the implications of these within the context of seismic hazards and future research.

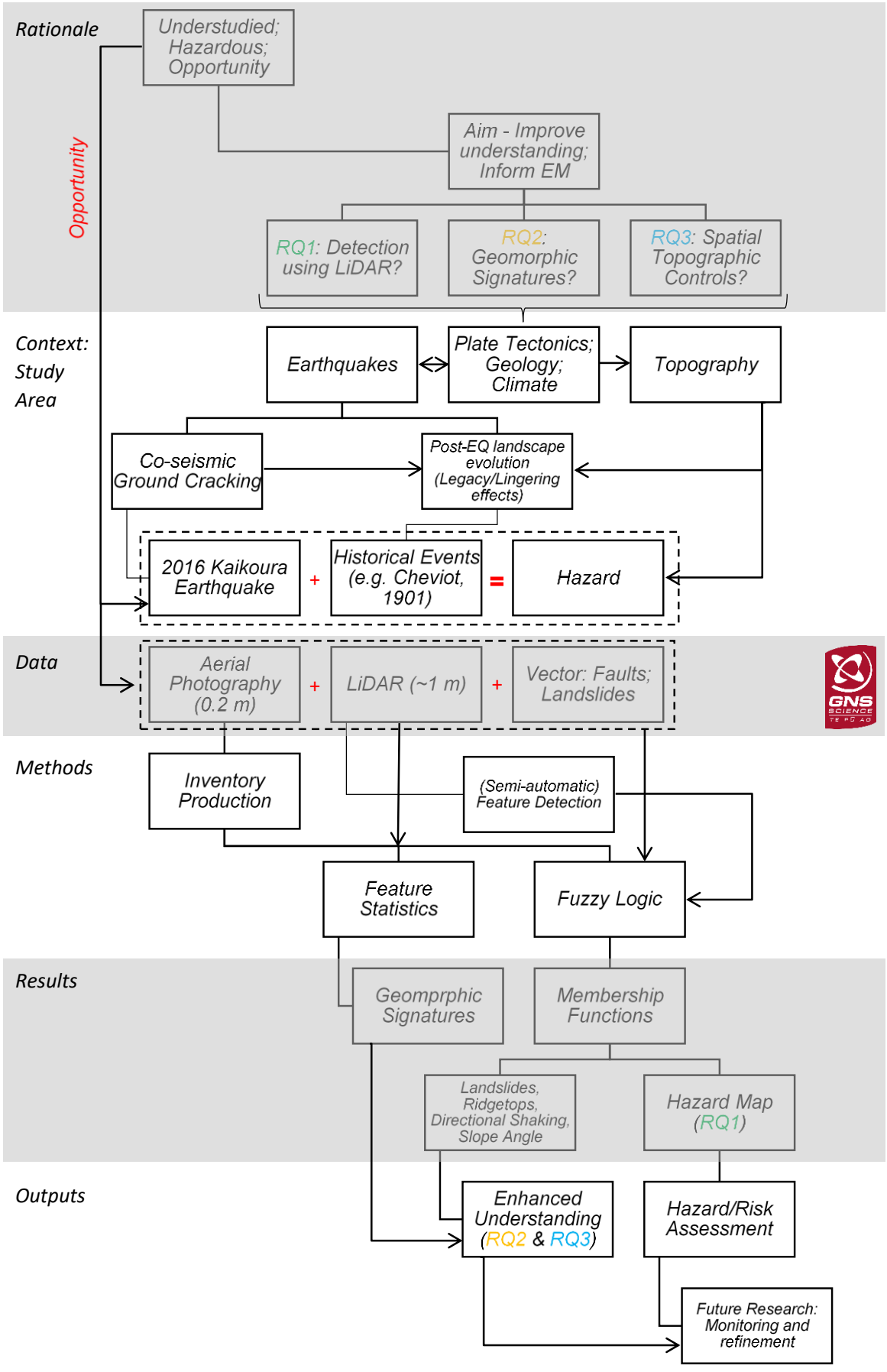

Fig. 1.02: *A visual outline of the entire thesis from start to finish, showing the workflow from original study rationale/aims right through to results and research outcomes/suggestions. Arrows have been added where appropriate to highlight important links and interconnections.*

2. COSEISMIC GROUND CRACKING

As the focal point of the study, the following chapter will explore previous research into coseismic ground cracking. Earthquakes, and their influence on stability, will be briefly outlined before the mechanics of coseismic ground cracking are explored and past occurrences summarized. As ground cracks have the potential to evolve into full hillslope failure and landslididng, post-earthquake landscape evolution will then be discussed.

2.1. FAULT RUPTURE

'Tectonic processes' is an umbrella term (Burbank & Anderson, 2012) encapsulating why the lithosphere behaves the way it does, and in turn how this can lead to deformation as a result of an earthquake. Three key pillars of this are: 1. The relative motion of lithospheric plates; 2. The slip that consequently occurs on individual faults; and 3. The resulting deformation of the lithosphere. Each will be discussed to outline the context underlying the occurrence of a seismic event and in turn, secondary seismic hazards such as ground cracking (Petley *et al.*, 2006).

Earthquakes occur due to variations in stress fields within the brittle crust (lithosphere) that stem from the (far-field) motion of plate tectonics and/or inhomogeneities in rocks or crustal strength (e.g. Burbank & Anderson, 2012). Plate tectonic motion is driven by 'dynamic topography' (Anderson & Anderson, 2010), which encompasses mantle flow and traction between this and the base of the lithosphere. Phase changes and the decay of radioisotopes transfer heat from the outer core to the mantle by conduction, fuelling convection and causing it to flow (***Fig. 2.01***). Friction between the fluid upper mantle (asthenosphere) and the lithosphere results in the horizontal motion of tectonic plate at rates of 5-15 cm/yr (Anderson & Anderson, 2010).

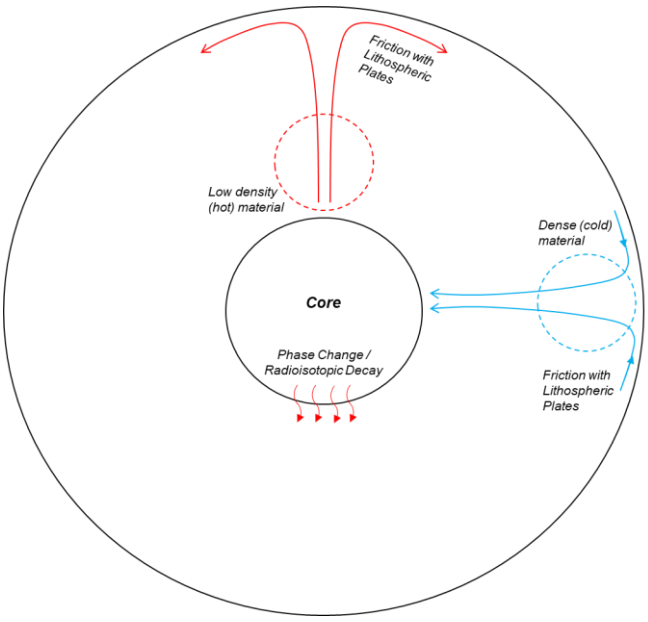

***Fig. 2.01**: A pictorial representation of the transfer of heat from the core to the mantle, and the resulting processes (convection and friction) involved in 'dynamic topography'.*

Due to its brittleness, the lithosphere can respond to the strain

imposed by far-field tectonic stresses by faulting (rupturing) or folding (e.g. Anderson & Anderson, 2010). A fold is a by-product of faulting should a fault rupture not daylight (e.g. Burbank & Anderson, 2012). Rupture occurs along 'faults' or 'fault planes', which are planes in the lithosphere across which shear can occur in response to stress/friction between two adjacent walls – the hanging wall and the footwall (Anderson & Anderson, 2010) (***Fig. 2.02***). Stresses from plate tectonic motion combine with gravitational forcing and surrounding matter. If a dominant deviatoric stress exists, frictional strength will be overcome and a strain (i.e. rupture) will occur along a fault plane (Burbank and Anderson, 2012). Strain will continue until stresses return to a state of equilibrium (Zielke & Arrowsmith, 2008). This is therefore proportional to levels of stress and frictional strength.

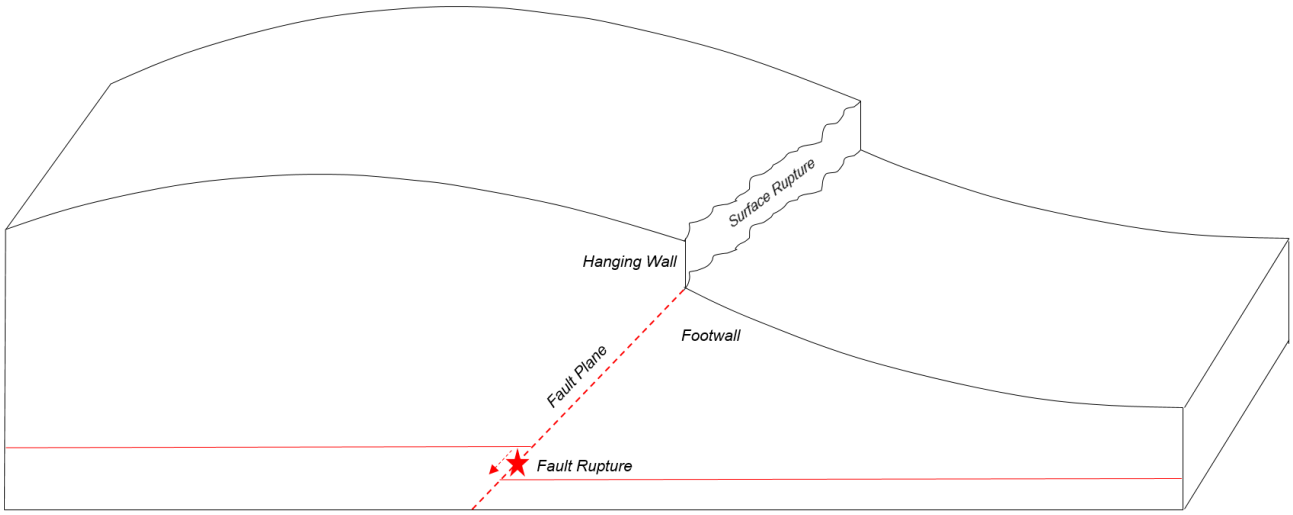

Fig. 2.02*: An illustration of the hanging wall and the footwall, showing their position in relation to the fault plane.*

Strain along a fault plane releases energy in the form of seismic waves (Duff, 1994) which propagate via body and surface waves (***Fig. 2.03***). Body waves (primary and secondary waves) travel through the Earth and tend to dissipate with distance due to a number of effects including anelasticity of rock mass and the scattering of waves on geological structures (Taylor *et al.*, 1986; Trifunac, 1994). When seismic energy reaches the surface, surface waves form. Two types of surface wave, Rayleigh and Love, are differentiated based upon their motion (orbital or horizontal respectively) (Duff, 1994). Surface waves have a lower velocity but a higher amplitude than body waves (Hovius & Meunier, 2012), resulting in strong ground motion/shaking with orbital or directional shear (Bindi *et al.*, 2010). These waves also dissipate with distance (Hovius & Meunier, 2012).

The size of a rupture and therefore the amount of seismic energy released is proportional to the relationship between the lithospheric strength, the amount of slip along a fault and the size of the area that slipped – known collectively as moment magnitude (M_w). A more extensive and complex rupture pattern can result in greater slip over a larger area and in multiple slip patches moving along a fault (Hovius & Meunier, 2012), releasing more seismic energy (Somerville *et al.*, 1999) in a much more complex rupture pattern (Wells & Coppersmith, 1994).

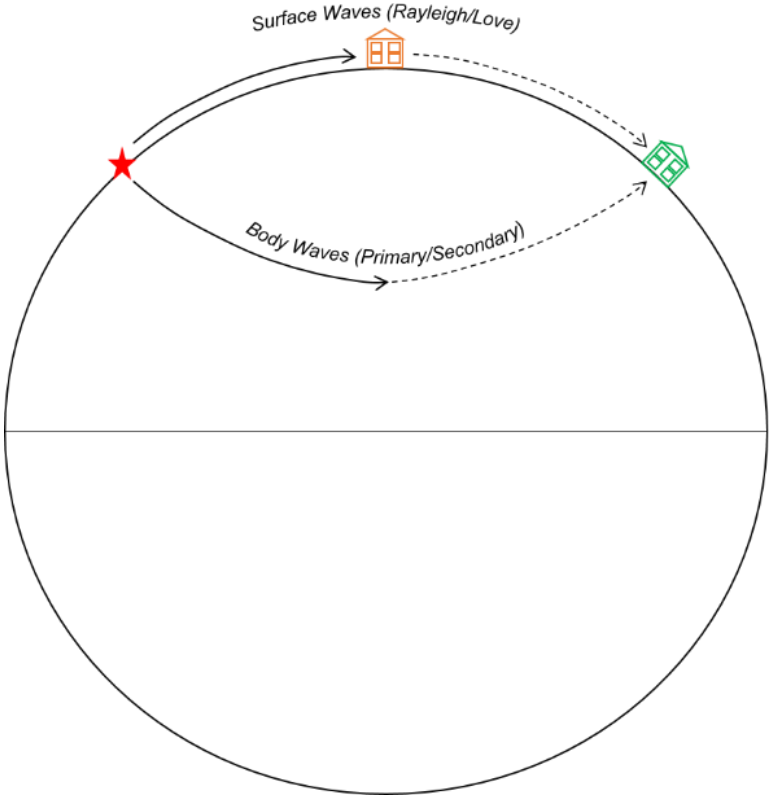

***Fig. 2.03**: A simplistic portrayal of the difference between the propagation of Body Waves and Surface Waves from the Focus. The solid and dashed lines represent the dissipation of energy and consequently shaking intensity. The orange house would therefore experience a higher shaking intensity than the green house. Adapted from Duff (1994).*

Complexity of fault networks can have an impact on both earthquake magnitude and occurrence. If interconnected, rupture to one fault can cause changes in stress in neighbouring faults (e.g. Harris *et al.*, 1995) as well as the surrounding crust (Stein, 2003). As a result, asperities (sticky patches) and barriers (unruptured patches) can propagate during a succession of earthquake events to induce 'stress roughening', where stress is not uniformly distributed (Burbank & Anderson, 2012) along a fault or fault system. They therefore impose a considerable control on fault rupture and are particularly pertinent to areas that experience high levels of seismic activity. Following an initial fault rupture, further ruptures can occur along asperities or barriers (Aki, 1984) - this is generally known as 'stress triggering' (e.g. Lin & Stein, 2004) or '*triggered slip*' (e.g. Pollitz & Sacks, 2002) and depending on spatial/temporal dimensions, could be termed an aftershock.

Topographic Site Effects (TSE) can also have a substantial impact on earthquake magnitude by controlling the amplification/dampening of seismic energy throughout a landscape, resulting in more or less concentrated impacts at specific locations (Bouchon *et al.*, 1996). TSE can cause local changes in ground acceleration throughout diverse topographic landscapes, whereby largest peak ground acceleration (PGA) values are recorded at ridge crests due to the internal reflection/diffraction of seismic waves within

mountains (e.g. Meunier *et al.*, 2007). Seismic energy is focused in an upwards direction leading to further constructive interference and reflection/diffraction and consequently increased energy towards ridge crests (Geli *et al.*, 1988). This phenomenon is strong in S waves, but not as pronounced in P waves (e.g. Hovius & Meunier, 2012). After reaching a ridge crest, seismic energy amplification can divert onto flanks facing away from the source due to oblique incidence as they move up through a mountain (Meunier *et al.*, 2008). Knickpoints and convexities can further amplify seismic waves – as such these features on source-opposing slopes can experience substantial shaking values. In comparison, other parts of the topographic landscape (e.g. source-facing slopes) tend to dampen seismic energy (Meunier *et al.*, 2007). TSE is thought to be dominant over topography itself in causing uneven ground acceleration across a landscape – seismic waves being asymmetrically amplified onto slopes facing away from the source provide evidence of this (Meunier *et al.*, 2008). Properties of topography (e.g. geology, lithology etc.) have also been found to have less of an impact on the propagation of seismic energy (ibid). For example, Parise & Jibson (2000) hypothesised that south-dipping strata may have primed certain hillslopes for failure during the Northridge earthquake in 1994. However, it has since been suggested that this may have been due to the abundance of regolith) due to the interrelationship between slope aspect and climate).

2.2. DEFINITION AND MECHANICS

Coseismic ground cracking (e.g. Petley *et al.*, 2006), fissuring (e.g. Owen *et al.*, 2008) or lateral spreading (e.g. Green *et al.*, 2011) can occur as a result of direct rupture to the surface following faulting (e.g. Li *et al.*, 2010); coseismic liquefaction-induced ground movement (e.g. Cubrinovski *et al.*, 2017); or be a potential indicator of incipient landsliding (e.g. Petley *et al.*, 2005b). ***Fig. 2.04*** shows all documented forms of ground cracking diagrammatically. After an earthquake, ground cracking inevitably raises concerns about future landsliding, but when, where and how ground cracks evolve into landsliding, or not, is poorly understood.

Direct Surface Rupture

Seismic energy from faulting can reach the surface and rupture it directly (e.g. Burbank & Anderson, 2009) as a form of strain/stress relief, resulting in ground cracking. This can take the form of a surface rupture which follows a fault (e.g. Li *et al.*, 2010; Saba *et al.*, 2010); or, a series of extensional cracks which can be an extension of a surface fault (e.g.

Rajendran *et al.*, 2001) or form on the crest of a fold or folded surface (e.g. Philip & Meghraoui, 1983). The latter is more widespread (e.g. Petley *et al.*, 2006) as faults tend to be vast but spatially confined to a single (or multiple) plane(s) (e.g. Anderson & Anderson, 2010).

Liquefaction

Ground cracking can also occur due to seismically induced liquefaction (e.g. Cubrinovski *et al.*, 2011), as earthquakes can trigger the process by applying a cyclic axial stress to a soil. If the soil is saturated this will increase the pore pressure and ultimately reduce shear strength, resulting in an axial strain and consequential deformation/ground movement (Ishihara, 1993). This can induce lateral spreading of the ground surface generating extensive fields of en echelon cracks (e.g. Chen *et al.*, 2010). Larger earthquake intensities and/or peak ground accelerations can apply a greater cyclic axial stress on a soil, increasing the risk of liquefaction (Huang & Jiang, 2010), lateral spreading and cracking. This relationship has not however been demonstrated and literature is lacking.

Incipient Landsliding

Finally, coseismic ground cracking can occur in the form of (micro) cracking within incipient landslides (e.g. Petley *et al.*, 2005b). Surface cracking is often identified as a precursor to incipient landslide activity (e.g. Owen *et al.*, 2008; Collins & Jibson, 2015; Jibson *et al.*, 2018), with more extensive fissuring generally indicating that a hillslope is closer to the point of failure than a hillslope without any such surface features. Therefore, in order to understand surface cracking as an expression of incipient landsliding, the mechanics of the latter need to be discussed. There are very few links between surface cracking and incipient microcracking and the localisation of shear onto a landslide rupture surface in terms of the mechanical propagation of the latter into the former throughout existing literature. Therefore, links will have to be inferred based on the mechanics/interrelations of/between stress, strain and ensuing deformation.

Despite incipient microcracking not always being visible on the surface, it may be the most common form of coseismic ground cracking and could offer fundamental insight into the relationship between the phenomenon, surface cracking and subsequent progressive hillslope failure both in the immediate aftermath of, and the months and years after an earthquake. In turn, incipient microcracking should therefore be considered an important ‘precursor’ which can make a hillslope more prone to reactivation. Reactivation may be encouraged following a future seismic or pluvial event but is not exclusively constrained to these events.

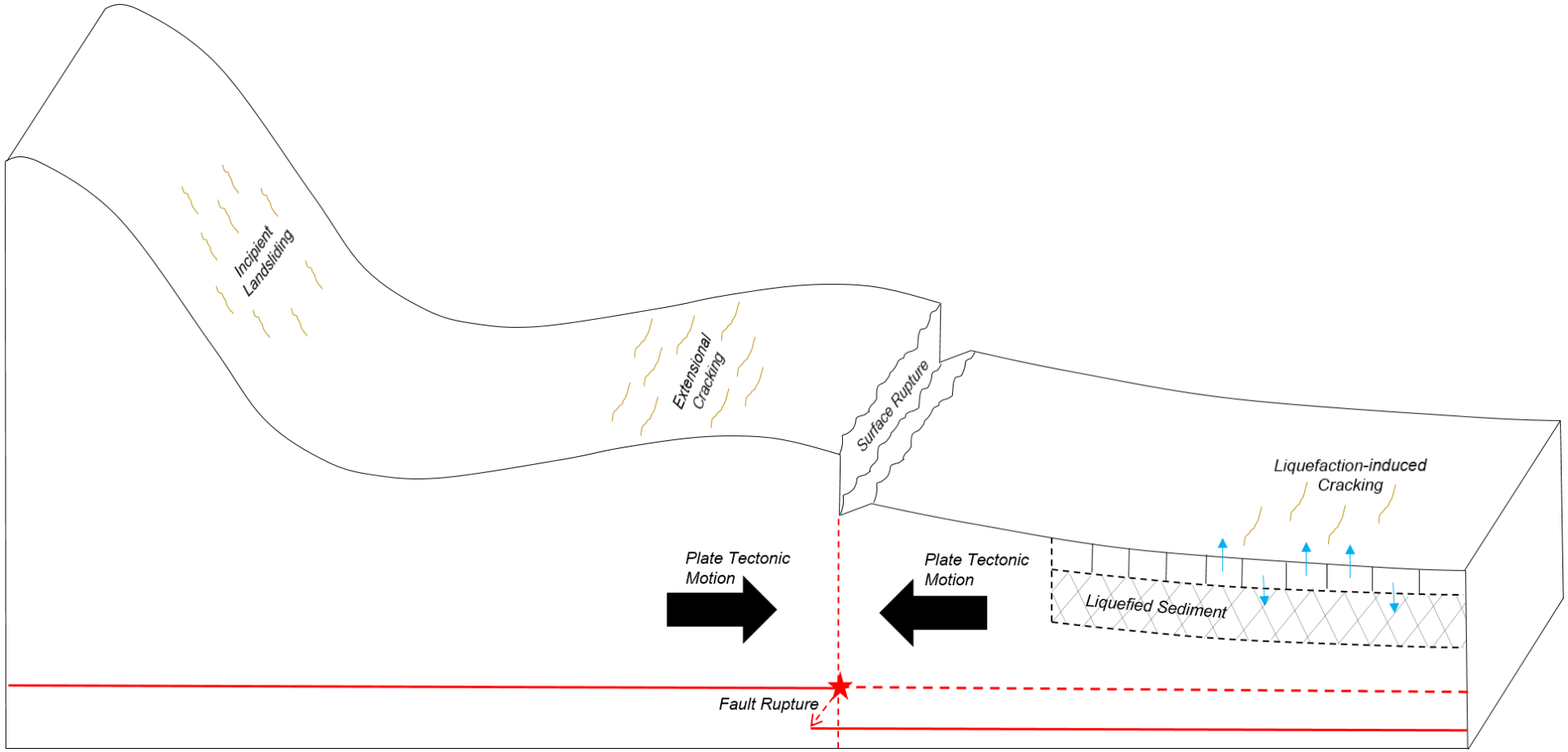

***Fig. 2.04**: An illustration of the different forms of coseismic ground cracking (gold). Coseismic ground cracking can manifest as direct surface rupture, extensional cracking or incipient landsliding as a direct result of strain induced by seismic shaking. Seismic shaking can also cause liquefaction in sediments, which unevenly displaces different parts of the ground (blue arrows), resulting in ground cracking. Adapted from Rajendran et al. (2001).*

Progressive (brittle-ductile) failure in slopes was first highlighted and discussed by Bjerrum (1967) however it was not until nearly thirty years later that Petley & Allison (1997) used laboratory experiments to ground this in contemporary mechanical theory and relate this to (micro) cracking. Progressive failure may help to explain the development of coseismic ground cracking (either incipient or on the surface) into post-earthquake hillslope failure. To precede this, it is suitable to briefly outline the differences between brittle and ductile deformation (Engelder, 1993) using standard stress-strain curves (***Fig. 2.05a-b***). When a load/stress is applied to a material, it deforms elastically (recoverable) to begin with (Phase 1) as bonds between particles are loaded and strained (hence the increase in gradient (strain)), but not broken. As load/stress increases, these bonds start to break, strain decreases (decrease in gradient – Phase 2) and the material transforms into an elastic/plastic phase of deformation. This will continue until a material reaches its peak strength. As load/stress increases further, the deformation of the material is heavily controlled by the confining pressure. If confining pressure is low, bonds will continue to break at an increasing rate and eventually lead to the development of a shear surface and failure. This causes the strength of a material to decrease (Phase 3), resulting in brittle

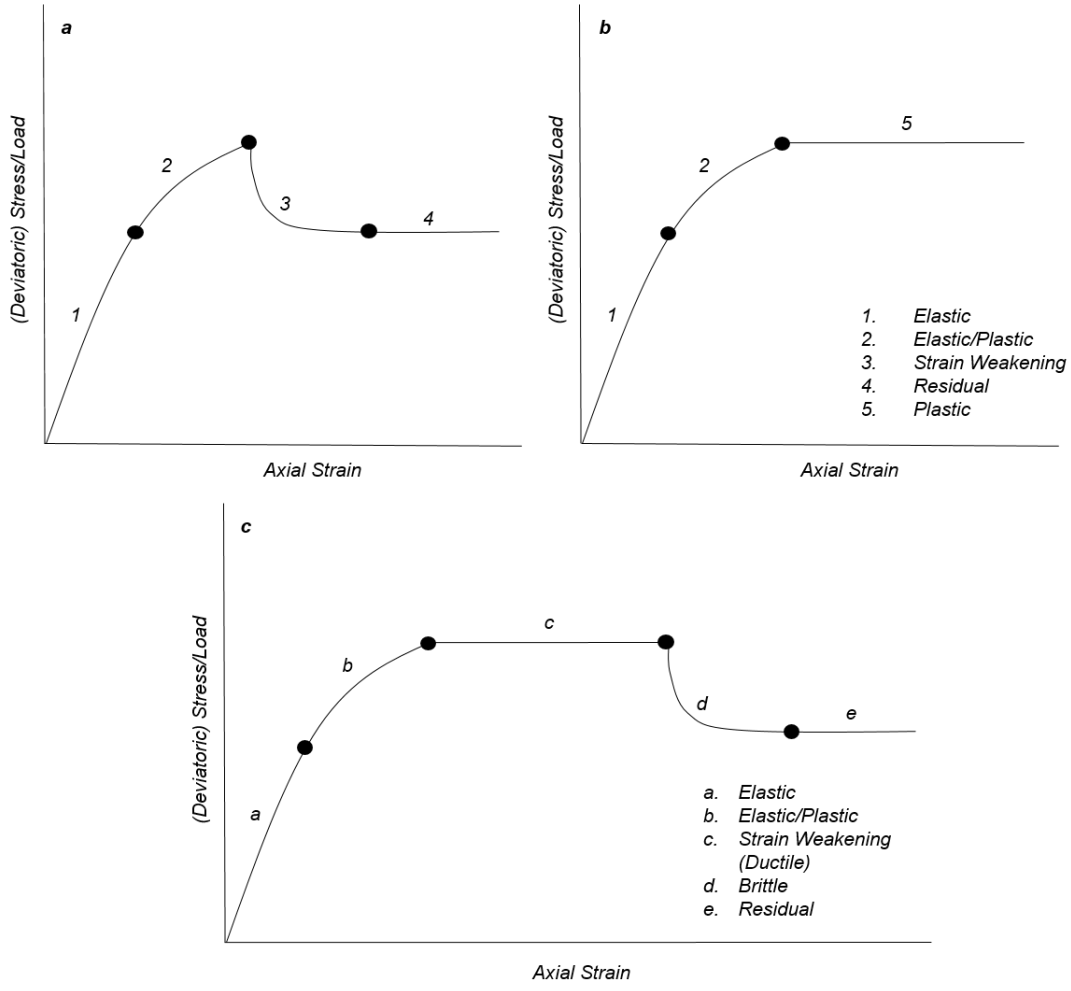

Figs. 2.05a-c*: Stress-strain curves, graphically illustrating brittle (a), ductile (b) and brittle-ductile (c) deformation in terms of stress/load and axial strain.*

deformation and a return to residual strength (Phase 4). If the confining pressure is high however, bonds will continue to break but no shear surface will develop. As such, the material will deform in a ductile manner at a constant stress (Phase 5) via the internal restructuring of particles.

Relating this to landslide mechanics, a very short phase of creep (Phase 1&2) preceding sudden failure (Phases 3&4) has been observed in landsliding along a shear zone in a brittle failure (e.g. Mudge, 1965). Long-term creep results in small but consistent movements (Phase 5), representing deformation within a shear zone, or ductile failure (e.g. Radbruch-Hall, 1978). This may translate to a failure 'creeping' down a hillslope over time. Catastrophic (seismic and/or pluvial) events can help to govern the rate at which this occurs by accelerating the process (e.g. Dadson *et al.*, 2004). Deformation within the shear zone may result in surface cracking as differential strains propagate to the surface of the landslide as the mass deforms (Petley *et al.*, 2005b). Consistent phases of creep followed by sudden hillslope failure (brittle-ductile) was less well understood, until Petley & Allison (1997) highlighted the role of incipient microcracking in this. At first, the growth and coalescence of microcracks accumulate strain, resulting in ductile deformation and reducing the strength of a hillslope (Main *et al.*, 1991). The coalescence of ground cracks can increase substrate permeability (Wang, 2004) in and around the surrounding area. As a result, pore water pressure may increase, increasing the shear stress and reducing the shear strength of the hillslope (e.g. Smith, 2004). These greater pore water pressures mean that the effect of buoyancy in a hillslope can become increasingly prominent and can counteract both the normal stress of the hillslope and the shear strength holding material on the hillslope together (Selby, 2005).

As discussed, ground cracking may become apparent on the surface at this point as an expression of both ductile and pre-failure deformation prior to levels of strain exceeding hillslope strength. Increasing coalescence of sub-surface microcracks results in a positive feedback and the formation of a shear surface (Voight, 1989), at which point strength is reduced and rapid (brittle) deformation ensues (***Fig. 2.05c***). Surface cracking could therefore indicate that brittle deformation and consequent failure is pending. However, to be certain that this is the case requires an understanding of basal mechanics within a hillslope and how this relates to deformation in real time (e.g. Terzaghi, 1950). This can be achieved through the following empirical theory.

Kilburn & Petley (2003) used the 'slow cracking' model to prove that brittle crack growth and coalescence was the physical explanation to validate the empirical (negative) linearity that was discovered between velocity^{-1} (*vc*) and time (*t*), termed *v-t space* (Saito,

1965; Voight, 1988; 89; Fukozono, 1990), in an accelerating hillslope failure. Ultimately, crack nucleation, coalescence and the consequential formation of a shear surface decrease the peak resistance threshold relatively. The role of circulating water can induce this (Atkinson *et al.*, 1984), by both increasing pore pressure (Hendron & Patton, 1985) and catalysing microcracking (Kilburn & Petley, 2003). As gravitational stress remains unchanged there will eventually be a force imbalance, leading to failure. In real terms, this correlates to slow creep (crack nucleation) preceding catastrophic failure with the shear surface providing the force imbalance needed for rapid acceleration (i.e. increasing velocity). This is unique to deeper-seated landsliding driven by gravitational failure that is otherwise unable to occur at shallow depths, as applied gravitational stresses are not large enough to overcome peak resistance strengths (Kilburn & Petley, 2003). As such, deformation in shallow and deep-seated failures can be quite different due to this association with overburden weight (and therefore stresses) (Petley & Allison, 1997).

Preceding this, linearity between *vc* and *t* was validated by Petley *et al.* (2002), who also proved that hillslopes deforming in a ductile manner show an asymptotic relationship in *v-t space*. In real terms, this relates to crack nucleation or failure along existing fractures (McGown *et al.*, 1997; Angeli *et al.*, 2000). Petley & Petley (2004) used both models to empirically highlight two periods of ductile deformation before the collapse of the Vaiont Landslide in Italy in 1963 (Muller, 1964). This corresponds to the ductile-brittle evolution in basal mechanics. As models only require simple velocity and time inputs, they can be driven by simple surface deformation measurements. This was proved in practice by Petley (2004), who used measurements from across a landslide to suggest that microcracks propagate from the centre of the landslide rupture surface. If considered in basic terms, this is where the greatest amounts of stress would accumulate (e.g. Selby, 2005). Petley *et al.* (2005c) advanced this further by using electronic distance measurement reflectors to obtain more accurate surface measurements. This could pave the way for the inclusion of more sophisticated technology to enhance model accuracy. The authors used this to suggest that a landslide propagates through four phases of movement (***Fig. 2.06***); and highlight the role of groundwater in this. Caution is aired as surface measurements may not always reflect internal mechanics (Petley *et al.* 2002), however all authors ultimately showed that these models can harness simple surface measurements to understand basal mechanics and as a predictive tool, using *v-t space* to predict the time until failure in a landslide deforming in a brittle manner. Voight (1989) suggests that this could have been done prior to the Vaiont Landslide, which killed ~2,400 people. In relation to the current study, there is now the potential to use ground cracks to

better understand subsurface landslide deformation, and to use them in combination with this theoretical insight to determine whether surface cracks highlight ductile deformation or impending sudden brittle failure.

Petley *et al.* (2005b) combined the aforementioned insight into basal defamatory mechanics with a reinflation model (simulating the hydrological conditions during hydrological triggering) to produce a new progressive hillslope failure model, also including the more conventional Factor of Safety (*FoS*) to show how a hillslope can progressively fail from a *FoS* > 1. Hillslope stability can be expressed in terms of *FoS* (Selby, 2005) whereby:

$$Fos = \frac{sum\ of\ resisting\ forces}{sum\ of\ driving\ forces} \quad [1]$$

If *FoS* > 1 then the sum of resisting forces is greater than the sum of driving forces, hence the hillslope is stable. If the reverse is true, *FoS* < 1 and a hillslope is conditioned for failure as shear stress increases or shear strength decreases (Smith, 2004).

The model involves four stages of development, which are ultimately characterised by linear decreases in *FoS* and v-t space. This is more suitably characterised in ***Fig. 2.06***. Petley *et al.* (2005b) conclude by grounding this in the context of seismic shaking, highlighting the different pathways that hillslope failure can take from this. The strength of ground accelerations may be such that a hillslope is taken through the four stages in ***Fig. 2.06*** instantaneously as, like gravity, seismic shaking can also induce huge force imbalances (Meunier *et al.*, 2008). Alternatively, shaking may take a hillslope to a critical *FoS* (Stage 3), which then remains short of full and final failure. This may be caused by, for example, a sudden decrease in pore pressure (Petley *et al.*, 2005b). In this instance, surface cracking may develop as an expression of deformation as a result of stress and stress relief within the failing mass. This deformation may be permanent and as such the hillslope will remain primed for future potentially catastrophic failure, which may be induced by a future trigger (e.g. seismic, anthropogenic or pluvial). Therefore, in basic terms, microcracking can propagate into landsliding by either failing instantaneously, or priming the landscape for future failure. Note that this does not necessarily mean that the next chronological event will induce this failure instantaneously – future events may instead contribute to taking a hillslope even closer to the point of catastrophic failure. This may translate to a defamatory mass ‘creeping’ down a hillslope over time as it is continuously reactivated, potentially by considerable events. Ultimately, what is crucial here is that ground cracking on the surface may be an indication of this incipient landslide activity (e.g.

Collins & Jibson, 2015; Jibson *et al.*, 2018) and thus an interim expression of strain that indicates that a hillslope is primed for failure at some point in the future.

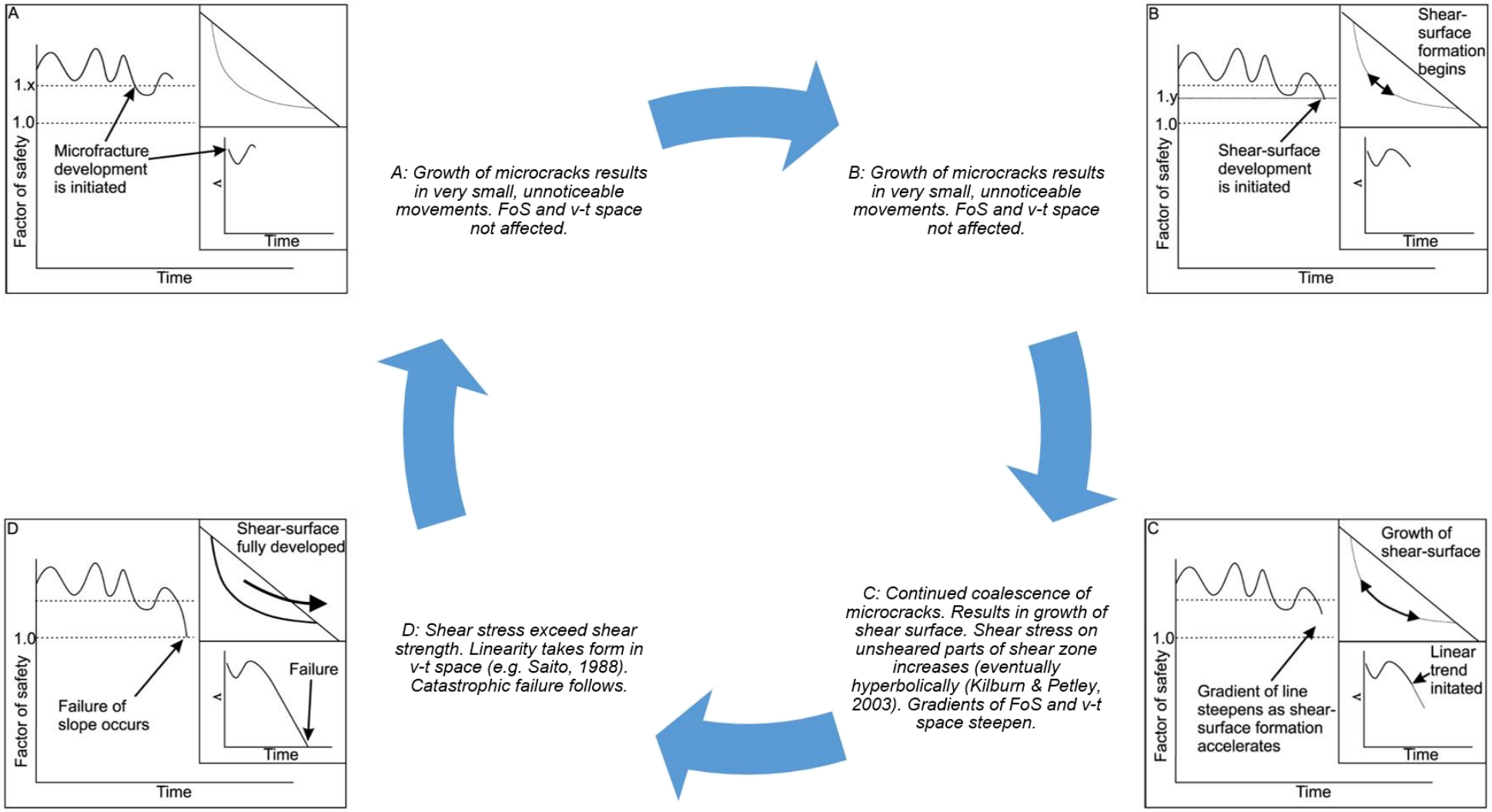

***Fig. 2.06**: Four stages of development of progressive hillslope failure. Full credit to Petley et al. (2005b) for the four inset diagrams – full reference in bibliography.*

Table 2.1: A summary of all (known) past studies which have, to at least some extent, focussed on coseismic ground cracking. The main focus of most of the papers is still co-seismic landsliding.

Citation	Location	Methodology	Observations	Conclusions
Rajendran et al. (2001)	Kutch (Bhuj), India	Field Reconnaissance	Liquefaction-induced lateral spreading throughout epicentral area - prominent in Budharmona; Extensional cracks in Manfara, Chobari, Bharodia.	More research needed on liquefaction-induced lateral spreading to feed into post-earthquake hazard assessment.
Petley et al. (2006)	Kashmir, Pakistan	Field Reconnaissance	Widespread ground cracking in bedrock and colluvium in the Jhelum Valley, most of it within 5km of the fault and confined to the handing wall.	Extensive cracking potentially due to drought conditions preceeding the earthquake; Warning of enhanced rates of landsliding in subsequent years.
Owen et al. (2008)	Kashmir, Pakistan	Field Reconnaissance and Digital Mapping	Widespread ground cracking across epicentral area including all of 174 landsliding sites studied.	Increased rate of landsliding potentially because of widespread ground cracking.
Chen et al. (2009)	Sichuan, China	Field Reconnaissance	Extensive liquefaction-induced fissuring over a 1000000 km^2 area surrounding the epicenter. Liquefaction-induced ground cracking also present in areas with lower shaking intensities.	Spatial non-uniformity of ground cracking due to a combination of factors including geological, hydrological and seismological.
Huang & Jiang (2010)	Sichuan, China	Field Reconnaissance	Liquefaction-induced lateral spreading at numerous sites throughout China. Particularly noticeable in Dujiangyang County.	Most important factors affecting liquefaction-induced ground cracking are seismic shaking, overlying earth pressure, groundwater levels, soil fabric.
Khattak et al. (2010)	Kashmir, Pakistan	Field Reconnaissance and Digital Mapping (multi-temporal)	No change in ~80% of the cracked slopes in the two years following the earthquake.	Cracked, unfailed slopes still posed a geohazard.
Li et al. (2010)	Sichuan, China	Field Reconnaissance	Surface rupture along northern segment of the fault between Beichuan and Qingchuan. Extensional cracks noticed in the hanging wall.	Surface fault rupture highlighted a number of different faulting mechanisms associated with the earthquake.
Saba et al. (2010)	Kashmir, Pakistan	Field Reconnaissance and Digital Mapping (multi-temporal)	Most cracks developed into full slope failures. Enhanced rates of landsliding for two years following the earthquake, followed by stability.	Cracking most likely contributed to the enhanced rate of landsliding in the years following the earthquake.
Green et al. (2011)	Haiti	Field Reconnaissance	Local-scale liquefaction-induced lateral spreading in Port Intl de Port-au-Prince.	N/A - observational paper.
Cubrinovski et al. (2011)	Christchurch, New Zealand	Field Reconnaissance	Local-scale liquefaction-induced lateral spreading in Christchurch CBD.	N/A - observational paper.
Massey et al. (2014)	Port Hills, New Zealand	Field Reconnaissance	Extensive cracking throughout the Port Hills area in response to earthquake shaking.	Slopes may continue to weaken over time due to physical/chemical weathering, wetting/drying and further ground movement. Failure of slopes is more likely than pre-earthquake.
Moss et al. (2015)	Gorkha, Nepal	Field Reconnaissance	Instance of liquefaction-induced lateral spreading along the Arniko Highway.	N/A - observational paper.
Collins & Jibson (2015)	Gorkha, Nepal	Field Reconnaissance	Ground cracking and incipient landsliding noticed throughout the Epicentral region.	N/A – observational paper
Cubrinovski et al. (2017)	Wellington, New Zealand	Field Reconnaissance	Local-scale liquefaction-induced lateral spreading in Wellington Centreport.	N/A - observational paper.
Dellow et al. (2017)	Kaikoura, New Zealand	Field Reconnaissance	Extensive ground cracking throughout Kaikoura region.	Risk of ground cracking developing into full hillslope failure.
Massey et al. (2018)	Kaikoura, New Zealand	Field Reconnaissance and Digital Mapping	Extensive ground cracking throughout Kaikoura region.	Risk of ground cracking developing into full hillslope failure
Jibson et al. (2018)	Kaikoura, New Zealand	Field Reconnaissance	Extensive ground cracking throughout Kaikoura region, particularly on ridgetops; Diversity in form and topographic position of cracks.	Extensive cracking at ridgetop locations may be due to topographic site effects; Cracking on steep slopes may be linked to incipient landsliding; and on flat areas may be linked to strong seismic shaking.

2.3. PAST EXAMPLES

Coseismic ground cracking is noticeably absent from existing post-earthquake literature aside from a handful of examples and as such, a summary of the most relevant research can be found in ***Table 2.1*** to accompany the forthcoming discussion. Lateral spreading was highlighted by Rajendran *et al.* (2001) as a secondary feature from the Kutch (Bhuji) Earthquake in India in 2001. Liquefaction-induced lateral spreading was noticed throughout the epicentral area (***Figs. 2.07a***). Extensional cracking was also recorded in a number of locations (***Figs. 2.07b***), however there was no direct surface fault rupture. Near Manfara, ground cracks were thought to have formed on the crest of the folded surface (Rajendran *et al.*, 2001). Although this paper only provides a summary through field reconnaissance, it does highlight and discuss ground crack features and in particular the need to better understand liquefaction-induced ground cracking and how the spatial distribution of this relates to earthquake hazard assessment.

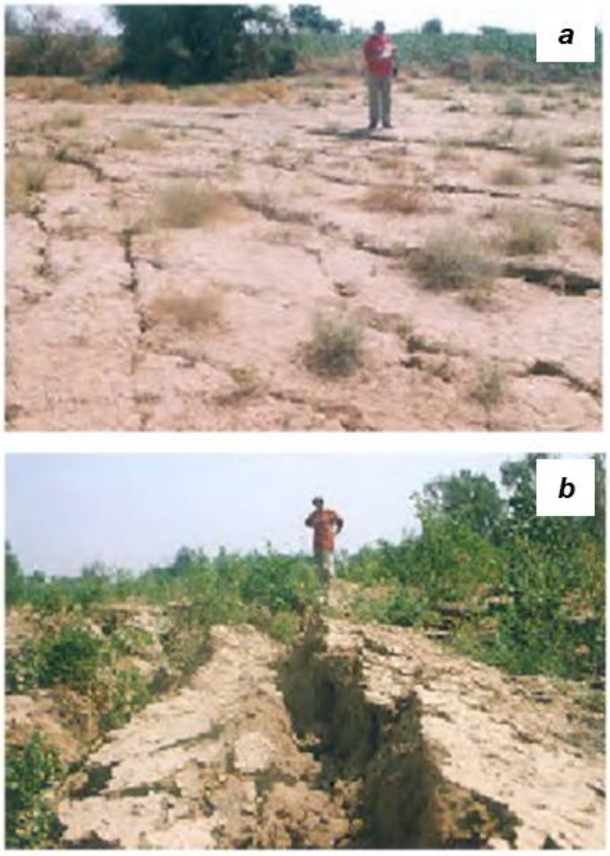

***Figs. 2.07a-b**: Extensional cracking and liquefaction-induced cracking from the Kutch Earthquake in India in 2001. Full credit to Rajendran et al. 2001 – reference in bibliography. Digital enhancement of the images has been tried, but to no avail as this is the quality at which they were initially published.*

Following this, the Kashmir Earthquake in 2005 brought coseismic ground cracking to the attention of the scientific community, albeit briefly. Cracking was widespread, and developed in a variety of forms including direct surface rupture and extensional cracking (e.g. Petley *et al.*, 2006); liquefaction-induced lateral spreading (e.g. Sahoo *et al.*, 2007) and most importantly, incipient landsliding (e.g. Dunning *et al.*, 2007; Owen *et al.*, 2008) There was considerable emphasis on the phenomenon following the event, with lots of speculation regarding the progression of ground cracks into full hillslope failure – which is ultimately the way in which cracks pose a continuing hazard. Given this link with post-earthquake landscape evolution, the Kashmir Earthquake will be covered in a following

sub-chapter to provide a novel applied example linking together all theoretical aspects covered in this chapter.

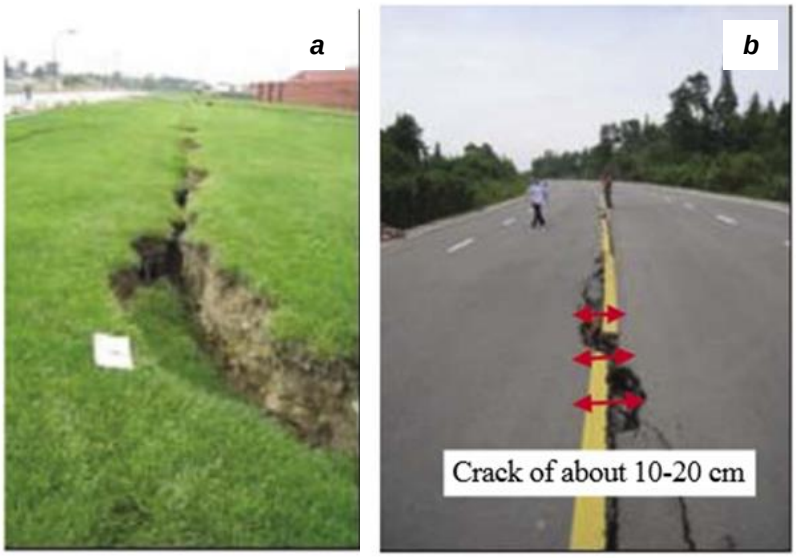

Fig. 2.08: *Examples of ground cracking documented following the Wenchuan Earthquake, China in 2008. Full credit to Chen et al. (2009) – reference in bibliography. Digital enhancement of the images has been tried, but to no avail as this is the quality at which they were initially published.*

The next major seismic event came in 2008 as the M_w 7.8 Wenchuan Earthquake struck Sichuan Province in south-west China (e.g. Cui *et al.*, 2011). Through field reconnaissance, Chen *et al.* (2009) highlighted extensive liquefaction-induced fissuring over a ~1,000,000 km^2 epicentral area (***Figs 2.08a-b***). The apparent spatial non-uniformity of this suggested that a combination of geological and hydrological conditions as well as seismic intensity can play a role in this. In general, there was more liquefaction-induced ground cracking in areas with greater shaking intensities, however Chen *et al.* (2009) also noticed the phenomenon at ~10 sites with lower shaking intensities, suggesting that seismic shaking may not always be the only factor controlling it. Huang & Jiang (2010) undertook a similar, much more localized study focusing on liquefaction-induced ground cracking in Dujiangyan County. They suggest that liquefaction was more widespread in areas with greater shaking intensities, but also dissect the generalized explanations from Chen *et al.* (2009) into a more comprehensive list of controlling factors including overlying earth pressure, density, groundwater levels and soil fabric. Soil fabric (namely compactness) can influence the passage of water through a soil and therefore the saturation levels within it (Ishihara, 1993), directly impacting the liquefaction process and therefore any resultant lateral spreading. Direct surface fault rupture and extensional cracking was also observed.

The event ruptured the ground surface for more than 200 km. Li *et al.* (2010) investigated this on a 75-95 km segment between Beichuan and Qingchuan. Extensive fieldwork highlighted surface rupture with scarps of between 1-6 m which followed the fault. From this, the authors infer a number of different faulting styles including pure thrusting, thrust and dextral slip, and pure dextral slip, perhaps indicating the complexity of the earthquake event. Tension cracks were also observed along the crest of the initial

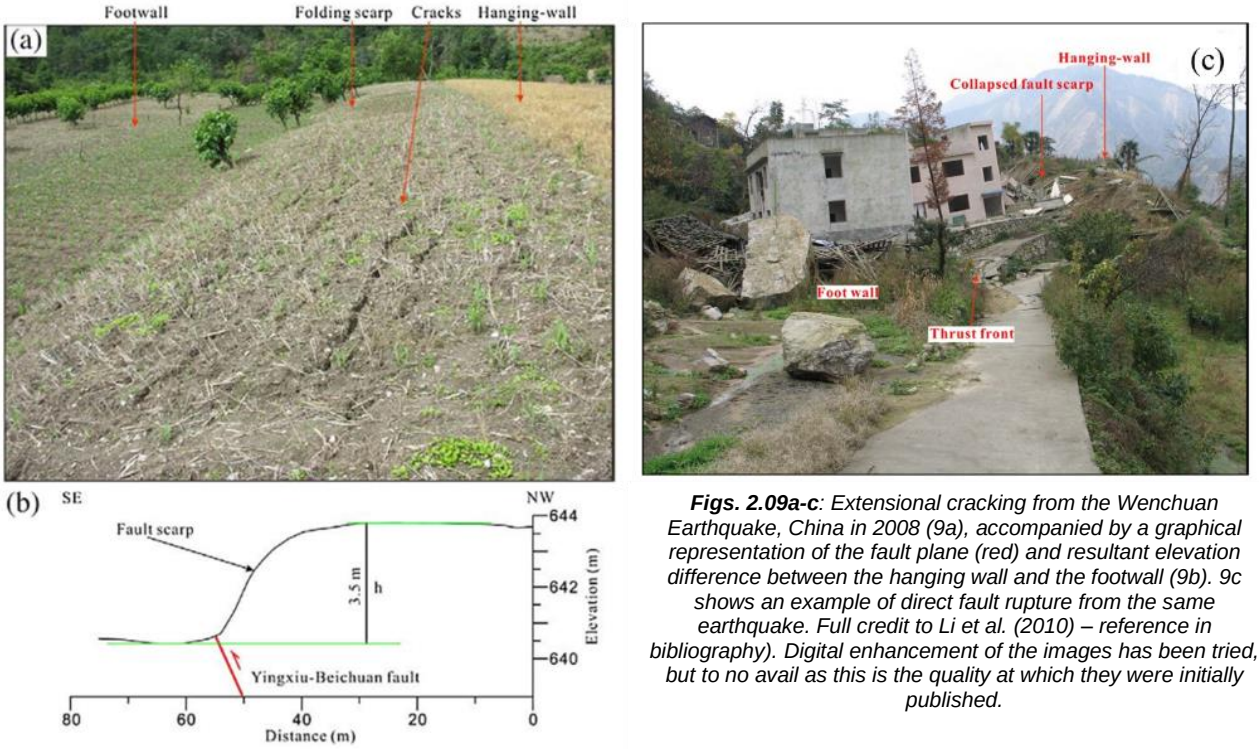

***Figs. 2.09a-c**: Extensional cracking from the Wenchuan Earthquake, China in 2008 (9a), accompanied by a graphical representation of the fault plane (red) and resultant elevation difference between the hanging wall and the footwall (9b). 9c shows an example of direct fault rupture from the same earthquake. Full credit to Li et al. (2010) – reference in bibliography). Digital enhancement of the images has been tried, but to no avail as this is the quality at which they were initially published.*

surface rupture (***Figs. 2.09a-c***). Ground cracking resulting from the Wenchuan earthquake appears to have been both directly seismically- and liquefaction-induced. This is similar to the Kutch Earthquake in 2001 but a contrast to the Kashmir Earthquake in 2005. Despite this being a catastrophic geomorphological event in terms of hillslope mobilisation (e.g. Yin *et al.*, 2011), little attention has been paid to coseismic ground cracking in the vast amount of literature on the earthquake (Petley, 2018). This knowledge gap is emphasized by Chen *et al.* (2009) who stress the need for further research into the relationship between liquefaction and ground fissuring if there is to be better understanding of post-earthquake landscape risk in some environments. This echoes the previous sentiments of Rajendran *et al.* (2001) following the Kutch Earthquake, and suggests that not much progress had been made on this matter in the interim.

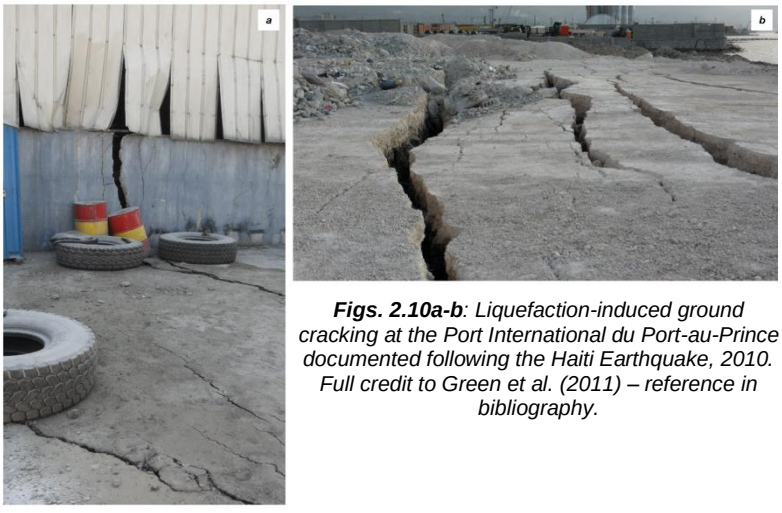

***Figs. 2.10a-b**: Liquefaction-induced ground cracking at the Port International du Port-au-Prince documented following the Haiti Earthquake, 2010. Full credit to Green et al. (2011) – reference in bibliography.*

Following Wenchuan in 2008, coseismic ground cracking literature has been scarce. Liquefaction-induced ground failure was observed following the 2010 Haiti Earthquake; however, the study was very spatially confined to the Port International de Port-au-Prince (Green *et al.*, 2011) (***Figs. 2.10a-b***).

The Gorkha earthquake in Nepal in 2015 also resulted in widespread liquefaction, however this only resulted in some local scale deformation along the Arniko Highway in lacustrine deposits of the Kathmandu valley (Moss *et al.*, 2015). Collins & Jibson (2015) briefly touched upon the presence of ground cracking in their post-earthquake reconnaissance report. They noted cracking throughout the epicentral region and attributed this to symbolise the presence of incipient landsliding. Surface cracks were present on some of their focussed study sites. On the Baisari Landslide Dam, cracks widened following the major aftershock ~2 weeks after the mainshock. No direct surface rupture was noted, although there is historical evidence of this in Nepal (e.g. Bollinger *et al.*, 2014).

Ground cracking has been documented in New Zealand following the earthquake events in 2011 and 2016 (e.g. Jibson *et al.*, 2018). For contextual purposes, this will therefore be outlined in a following chapter.

2.4. Post-Earthquake Landscape Evolution (Legacy)

The long-term impact of seismic shaking on a landscape is becoming an increasingly popular and contested narrative (e.g. Marc *et al.*, 2015; Parker *et al.*, 2015; Brain *et al.*, 2017). As has already been touched upon, weakened slopes due to seismic shaking (e.g. Mahmood *et al.*, 2015) can increase the susceptibility of a hillslope to failure during future rainfall or seismic events (e.g. Dadson *et al.*, 2003). This has been poorly understood until recently, partly due to data constraints (Brain *et al.*, 2017). However, it is becoming increasingly clear that earthquake legacy should be considered, at least qualitatively, when assessing the hazard of a landscape affected by seismicity on timescales ranging from the immediate to the historical (Parker *et al.*, 2015). Ground cracking, whether it be in the form of visible surface fissuring (e.g. Owen *et al.*, 2008) or incipient landsliding (e.g. Petley *et al.*, 2005), may be inherently linked to earthquake legacy and a key reason that a hillslope retains historical damage (Parker, 2013).

Dadson *et al.* (2004) was the first major study to quantitatively examine the legacy of seismic shaking using high-resolution (suspended sediment transport) data from the M_w 7.6 1999 Chi-Chi earthquake, Taiwan. They found that much of the debris displaced by the earthquake sequence remained on hillslopes until it was later reactivated, remobilised and evacuated from the mountains by typhoon storm events. Typhoon Toraji in 2001 also resulted in a pattern of landsliding which matched that of shaking intensity from the initial

earthquake. Dadson *et al.* (2004) therefore used this to suggest that strong ground motion from the earthquake had preconditioned these hillslopes for failure, which was then later caused by a subsequent catastrophic event, Typhoon Toraji in this case. Consequently, rates of mass wasting remained elevated at the time of writing, ~4 years after the event. Ultimately, the study hinted at the diverse range of impacts seismic shaking can have on the landscape, ranging from the immediate to the short- and long-term. Hovius *et al.* (2011) provided a follow-up in support of Dadson *et al.* (2004), using a time-series of landslide mapping and suspended sediment transport data to cite a ~6-year period of enhanced mass wasting following the earthquake. This suitably builds on the mechanical explanation provided in *Ch. 2.2.1*.

Marc *et al.* (2015) followed, suggesting (quantitatively) that landslide rates peak following an earthquake and then decay back to pre-earthquake levels after ~1-4 years – this decay timescale potentially being proportional to earthquake magnitude. By normalising for meteorological forcing, Marc *et al.* (2015) concluded that this initial failure and subsequent recovery of ground strength may be mechanically grounded primarily in a reversible recovery of rock mass strength following extensional cracking. This remains a speculative interpretation, but one which offers some insight into the impact of seismic shaking, independent of ensuing meteorological effects. Results from Owen *et al.* (2008), and others all support this through concluding that rates of mass wasting returned to background levels just two years after the Kashmir Earthquake in 2005.

Whilst agreeing on the decadal-scale decay of post-earthquake landslide rates (Uchida *et al.*, 2014), Parker *et al.* (2015) also suggest that a landscape can retain damage for much longer timescales – damage which can only be re-initiated to the point of failure by the stresses experienced in a further considerable seismic event. The authors compare the spatial pattern of landsliding resulting from two historical earthquakes in New Zealand in 1929 and 1968; concluding that similar spatial distributions could be attributed to progressive damage legacy from the 1929 event remaining persistent within the landscape, only being re-initiated by an event large enough to advance this progressive hillslope damage into full failure, i.e. the 1968 earthquake. Interestingly, no event (seismic or pluvial) in the interim appeared to cause this threshold to be exceeded.

Long timescales between strain accumulation and final failure adds weight to the suggestion that damage may accumulate progressively and incrementally through incipient microcracking. Cyclic loading and unloading over repeated earthquake cycles (Parker *et al.*, 2015) can accumulate to cause irreversible localised strain (Schijve, 2001), especially in rocks with pre-existing microcracks (Badge & Petros, 2005). Eventually, this will

culminate in hillslope failure (e.g. Leroueil *et al.*, 2012). As has already been discussed, this is only true for hillslope materials that behave in a brittle manner (Evans *et al.*, 2013). Materials that behave in a ductile manner tend to fail slowly (Petley & Allison, 1997) or strengthen a hillslope depending on the magnitude of the seismic event (Brain *et al.*, 2017). Brain *et al.* (2017) use geotechnical laboratory testing to suggest that low magnitude (i.e. does not cause catastrophic failure) ground shaking may actually increase bulk density and interparticle friction within ductile hillslope rheologies, strengthening and reducing susceptibility to mass wasting. This is particularly important for hillslopes displaying pre-failure strain in the form of ground cracking – which in real terms could be portrayed as a ductile response to seismic shaking that precedes the more brittle response of instantaneous failure. Lower magnitude events are much more common than higher ones (Gutenburg-Richter, 1954) and hence the findings are significant as they highlight the need to consider the effects of an earthquake sequence and not just the mainshock. Also, pre-failure strain proxies such as ground cracking (and incipient landsliding) could be an important parameter when considering the future susceptibility of a hillslope to landsliding.

Post-earthquake hillslope failure, whether instantaneous or not, can be thought of as a function of both current and historical seismic events (Parker *et al.*, 2015). Historical seismic activity needs to be considered, as does the sequence of shaking surrounding the mainshock of an event (Brain *et al.*, 2017). Ultimately, earthquake legacy must be considered whenever interpreting post-seismic hazards, particularly those with the potential to turn into something much more hazardous, i.e. coseismic ground cracking into post-seismic landsliding.

2.5. KASHMIR, 2005 – AN APPLIED EXAMPLE

The Kashmir Earthquake in 2005 is the only major event to have brought coseismic ground cracking to the attention of the scientific community. The M_w 7.6 earthquake took place on 8th October 2005 (e.g. Hussain *et al.*, 2006), with destructive effects being felt in both Pakistani- and Indian-administered Kashmir and beyond. Nearly 100,000 were killed, more than 75,000 injured and nearly three million displaced throughout Pakistan and India (Rossetto & Peiris, 2009). The earthquake triggered over 2,000 landslides (Sato *et al.*, 2007) and consequently, over 25,000 deaths were directly attributable to mass movements (Petley *et al.*, 2006). Landslides were concentrated according to seismological, geological and topographic controls (Sato *et al.*, 2007; Owen *et al.*, 2008; Kamp *et al.*, 2008; 2010)

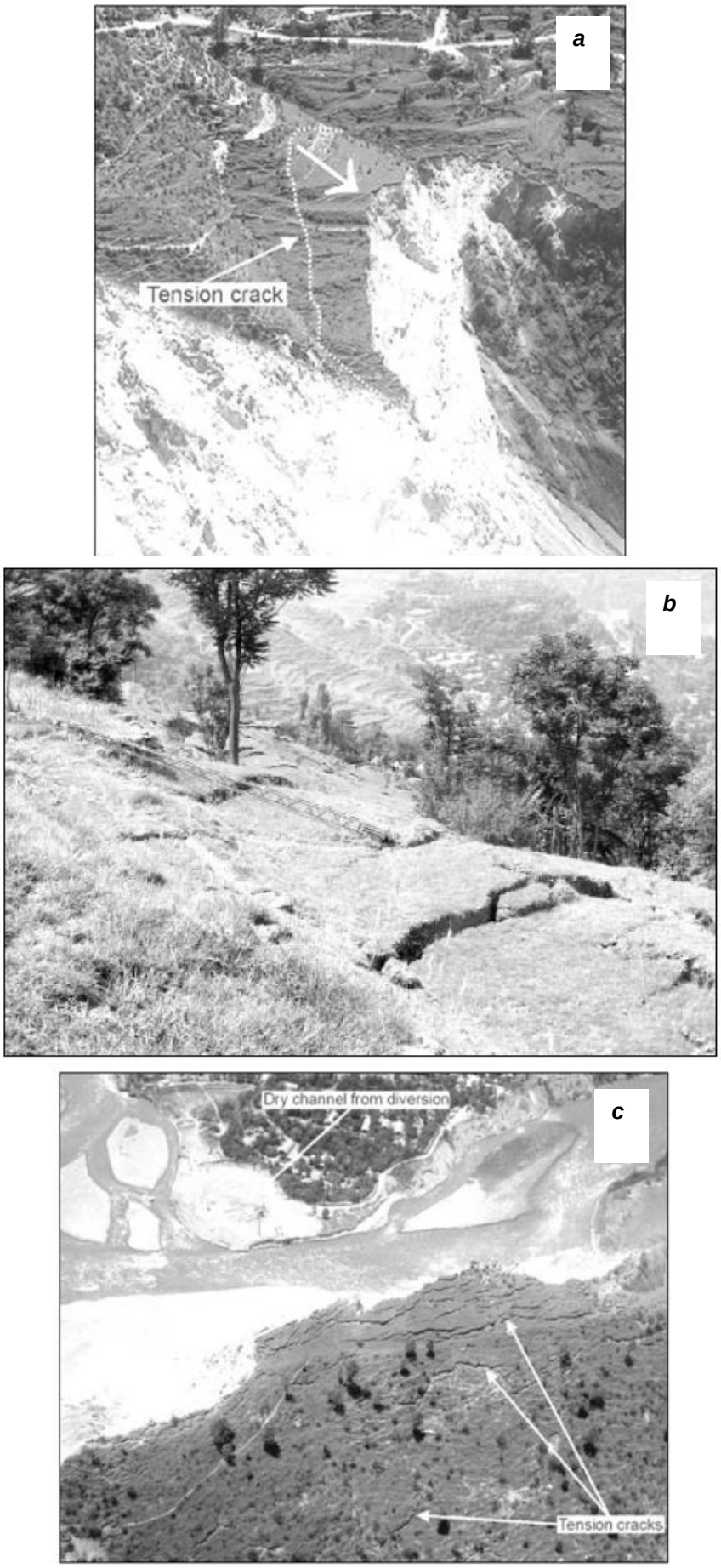

***Figs. 2.11a-c**: Extensional cracking documented on hillslopes in the epicentral area following the Kashmir Earthquake, Pakistan in 2005. Full credit to Petley et al. (2006) – reference in bibliography. Digital enhancement of the image has been tried, but to no avail as this is the quality at which they were initially published.*

The largest failure was the Hattian Bala rock avalanche, which killed ~1,000 and destroyed three villages (Harp & Crone, 2006; Dunning *et al.*, 2007).

Coseismic ground cracking was reported by many authors. Petley *et al.* (2006) provided an initial comprehensive overview of this in the Jhelum Valley. Cracking was evident in both bedrock and colluvium (***Figs. 2.11a-c***), most of it limited to the hanging wall within 5 km of the fault and resultant from direct surface fault rupture along the Balakot-Bagh Fault (Saba *et al.*, 2010), and extensional cracking. Ground fractures, some of which were liquefaction-induced, were reported by both Sahoo *et al.* (2007) and Jayangondaperumal & Thakur (2008) ~80 km and ~240 km south-east of the epicentre respectively. Sahoo *et al.* (2007) also documented a number of very thin (<0.5 m) but long (30-50 m) ground cracks, all of which were north-east/south-west oriented and parallel to the river channel (i.e. slope perpendicular) (***Fig. 2.12***). Both authors used the distance from the epicentre to highlight the importance of favourable ground conditions for the occurrence of liquefaction (and consequently lateral spreading). Owen *et al.* (2008) highlighted that fissuring throughout the epicentral area (***Fig. 2.13***) was more preferential on ridgetops and midslope areas and in areas associated with the Muzaffarabad Formation, suggesting the involvement of potential topographic and geological controls.

Both Petley *et al.* (2006) and Dunning *et al.* (2007) were the first to suggest that ground cracking indicated the presence of incipient landslides that had not yet developed to the full point of failure. Incipient landsliding may have been triggered by seismic shaking from the earthquake but low pre-earthquake ground water levels from a lack of seasonal precipitation may have prevented these from transitioning into full failure either during or following the earthquake (Petley *et al.*, 2006; Dunning *et al.*, 2007). Ground cracks may provide a pathway for water (from monsoonal precipitation) to enter a hillslope and consequently increase porosity and pore pressures (Schneider, 2009). This is speculative and direct evidence for the occurrence of this is uncommon.

bibliography. Digital enhancement of the image has been tried, but to no avail as this is the quality at which they were initially published.

However, increased pore pressure could progress incipient landslides over a critical threshold and induce full failure (Aydan *et al.*, 2009). Depending on the threshold required and in the case of the Asian subcontinent, this trigger could be seismic or pluvial (Dunning *et al.*, 2007).

Dunning *et al.* (2007) undertook an assessment of hillslope conditions before and after the earthquake, focussing on the Hattian Bala rock avalanche and consequent dam that this formed. The authors showed that there were incipient landslide clusters on the hillslope before the earthquake. This suggests that seismic shaking could have pushed damage accumulation over a threshold. The resultant formation of a shear surface may have accelerated the incipient landslide to full catastrophic failure (e.g. Petley *et al.*, 2005b). Remaining tension cracks and lateral shears provided evidence of further (coseismic) incipient landsliding, with the authors highlighting the need to monitor surrounding '*near critical*' slopes. Interaction of landslide toes with the reservoir was a particular concern and may have encouraged the formation of a shear surface. At the time a catastrophic failure behind the dam may have caused a landslide dam outburst flood, putting communities downstream at risk.

Subsequent studies provided an insight into whether this initial concern was justified using a combination of field reconnaissance and digital mapping. Owen *et al.* (2008) documented landsliding in 174 locations and confirmed that ground cracking was widespread throughout the 750km^2 study area. They hypothesised that this extensive fissuring had resulted in more landsliding during the 2006 snowmelt/monsoon seasons.

***Fig. 2.13**: Fissuring resulting from the 2005 Kashmir Earthquake, Pakistan. Full credit to Owen et al. (2008) – reference in bibliography. Digital enhancement of the image has been tried, but to no avail as this is the quality at which they were initially published.*

Results from a separate study by Saba *et al.* (2010) concurred, with the authors suggesting that elevated rates of monsoonal precipitation in 2006 had caused many co-seismic ground cracks to develop into landslides. An increase in landsliding from 2005-2006 reflected this, however after this, rates decayed despite higher-than-average monsoonal precipitation in 2008 and most fissures were no longer visible. This potentially suggests that the landscape became much more stable after a period of elevated mass wasting, and rates of hillslope failure had returned to pre-earthquake background levels after just two years. This provides a further example to concur with the findings of Marc *et al.* (2015).

Khattak *et al.* (2010) provided a direct follow-up to Owen *et al.* (2008) by revisiting 68 of their locations a further three times throughout 2006 and 2007. However, their results were contradictory to the initial speculative hypothesis of Owen *et al.* (2008) as they concluded that ~80% of the revisited locations showed little or no change, with only 11% of locations showing elevated rates of mass wasting. As per the initial suggestion from Petley *et al.* (2006), the authors cited insufficient levels of precipitation to trigger full hillslope failure. Consequently, Khattak *et al.* (2010) stressed that co-seismic ground cracking still posed a pertinent geohazard in the region.

Khan *et al.* (2013) provided further follow-up to Owen *et al.* (2008) and Khattak *et al.* (2010) by re-photographing 123 of the original 174 sites documented by Owen *et al.* (2008) in 2005. They concluded that landsliding had only increased negligibly between 2005-2010. 11% of locations showed an increase in scar area, whereas 45% showed little or no change and a further 44% showed considerable revegetation. This roughly concurs with Khattak *et al.* (2010) and as such the authors' interpretation follows suit. They also cite pre-earthquake dry (groundwater) conditions as preventing the threshold of pore water pressure being exceeded as a result of either the seismic shaking or monsoonal precipitation. In turn this stops progression from incipient to full hillslope failure. Khan *et al.* (2013) also discuss the role of vegetation, which may have a stabilising influence on a hillslope (e.g. Kamp *et al.*, 2010). However, root growth is unlikely to have had any influence on such short timescales, and instead the authors suggest that monsoonal precipitation may accelerate revegetation, which in turn further increases the pore water capacity of a hillslope, increasing the threshold required for failure. Khan *et al.* (2013) admit the tenacity of this, as revegetation may also apply a greater normal stress onto a hillslope (Popescu, 2002), however this is an alternative suggestion worth considering. Similar links between vegetation recovery and hillslope stabilisation have been noticed

following the Chi-Chi Earthquake in Taiwan in 1999 (Chou *et al.*, 2009; Hovius *et al.*, 2011).

The studies of Khattak *et al.* (2010) and Khan *et al.* (2013) appear to contradict that of Saba *et al.* (2010) and the initial speculative hazard concerns of Petley *et al.* (2006), Dunning *et al.* (2007), Owen *et al.* (2008) and others. There are advantages and disadvantages to all methods used, and some authors are quick to highlight the flaws in contradicting studies. For example, Saba *et al.* (2010) cite the methods of Khattak *et al.* (2010) as inferior as they were qualitatively grounded and have a lower temporal resolution. Conversely, Khan *et al.* (2013) attribute differences to the size of the respective areas. Saba *et al.* (2010) focussed on a 36km^2 epicentral area whereas all other studies focussed on the 750km^2 study area initially defined by Owen *et al.* (2008), which will have obviously skewed rates of failure progression respectively. As such, it may be unsuitable to compare these studies. This is interesting in itself, as it highlights that post-earthquake landsliding (progressing from co-seismic ground cracking) is more preferential near to the initial sources of shaking. Khan *et al.* (2013) also highlighted increased rates of landsliding in the immediate epicentral region. Further away from the epicentre, reduced shaking may have resulted in reduced hillslope damage (Hovius & Meunier, 2012) and therefore slopes which are less primed for future failure. This could be interpreted as seismic shaking being a key control on co-seismic ground cracking and subsequent hillslope failure.

The Kashmir Earthquake is a suitable case study through which to contextualise the aforementioned discussion on coseismic ground cracking and the lasting impact that this may, or may not, have on the landscape. An array of different forms of coseismic ground cracking were documented following the event, and their propagation into full hillslope failure is contested by a number of contrasting studies. Consequently, the ongoing hazard caused by these coseismic ground cracks is also unclear. The contradiction here highlights the current ambiguity surrounding coseismic ground cracking, its post-seismic influence on the landscape, and therefore the need to study it quantitatively and on the regional scale to provide further insight into it. Ultimately, this will only be feasible with a focused approach, which can be informed by automatic feature detection which first, needs to be trained by enhancing our theoretical understanding of coseismic ground crack features.

2.6. SUMMARY

This chapter has outlined the seismic causes of ground cracks, their different forms and their role in present and future hillslope stability. A detailed case study has been used to demonstrate the interrelationship between these components. Key points from *Ch. 2* are:

- Strong ground shaking can directly crack the surface; trigger liquefaction processes which in turn disturb the surface; or, trigger the growth and coalescence of microcracking deep within a hillslope.
- Failure can progress from microcracking, which may generate further cracking on the slope surface. Microcracking can permanently strain a hillslope, priming it for catastrophic failure which may be induced by a future trigger. Failure can be instantaneous or incremental over time.
- Despite some documentation, literature is still scarce on coseismic ground cracking
- Hillslopes may retain damage for considerable timescales following its infliction by seismic shaking
- Contradictions in literature from the Kashmir earthquake in 2005 highlight how the ongoing hazard posed by coseismic ground cracking is unclear, hence the need to further study this.

3. NEW ZEALAND

The following chapter will provide an in-depth, contextual outline of my broader study area in the north-east South Island, New Zealand, providing a site-specific application to the theoretical discussion in Chapter 2. Site-specific geological, seismological and climatic factors will be outlined for contextual purposes. Historical seismic events and the ensuing implications of these will be discussed, before a comprehensive review of the 2016 Kaikoura earthquake is presented.

3.1. REGIONAL SETTING

3.1.1. Plate Tectonics

New Zealand is tectonically active (e.g. Schulmeister, 2016) and therefore highly mountainous. Oblique convergence between the Australian and Pacific Plates at a rate of ~39-48 mm/yr (Beavan *et al.*, 2016) has driven both uplift and fault slip (Nicol *et al.*, 2012). In turn these compliment orogenesis from conventional uplift (Marc *et al.*, 2016) to create New Zealand's mountainous topography. Initial uplift of the inland Kaikoura ranges in the early Miocene was followed by the subsequent uplift of the seaward ranges during the late Pilocene (Kao, 2002). Rates of deformation (i.e. plate movement) are thought to have commenced during the Quaternary (Nicol *et al.*, 2012). Topography in the Kaikoura region has been formed by tectonically driven uplift and consequential fluvial incision (e.g. Massey *et al.*, 2018). Uplift is on-going (Bull, 2011) and erosion rates are high due to the tectonically induced fractured nature of rocks (e.g. Molnar *et al.*, 2007).

The present-day Australian-Pacific plate boundary has four main components (***Fig. 3.01a-b***). The North Island is dominated by subduction on the Hikurangi Subduction Thrust (Nicol & Beavan, 2003). Moving south, the Marlborough Fault System (MFS) (north South Island) is an area of transition linking the Hikurangi Subduction Thrust and the strike-slip dominated Alpine Fault (Nicol & van Dissen, 2002). The MFS (***Fig. 3.02***) includes four major southwest-northeast-trending strike-slip faults that accommodate the majority of relative plate motion (e.g. Wallace *et al.*, 2012). Slip rates along the system increase from north to south, with the northernmost faults (e.g. Awatere, Clarence, Wairau) slipping at 4-8 mm/yr (van Dissen & Nicol, 2009) and the southernmost faults (e.g. Hope and Kekerengu) slipping 18-24 mm/yr. The 220 km-long Hope Fault is the most active within the MFS (e.g. Cowan *et al.*, 1996). Slip rates are some of the largest in New Zealand

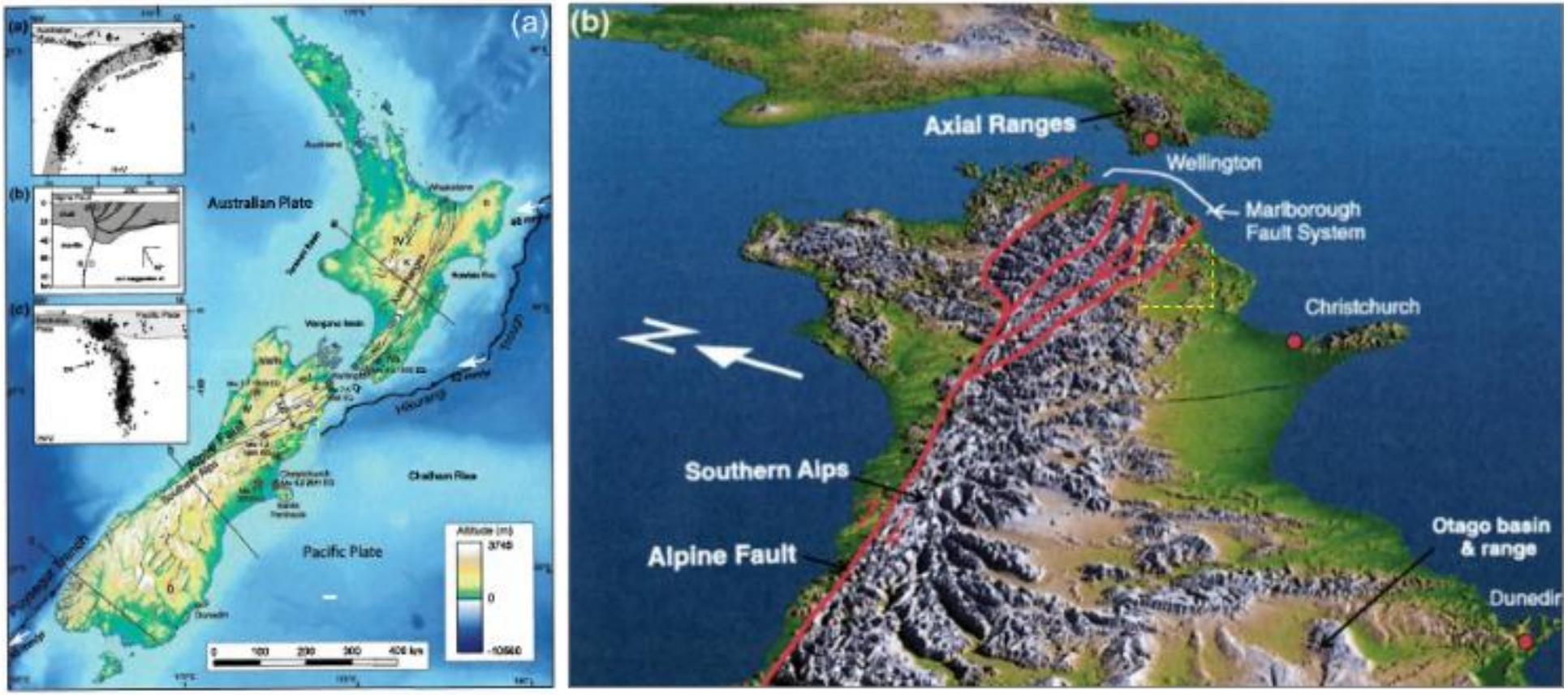

***Figs. 3.01**: **a**) A topographic map of New Zealand highlighting the Australian-Pacific Plate Boundary. From north-to-south this comprises of the Hikurangi Trough, Marlborough Fault System (MFS), Alpine Fault and Puysegur Trench. Graphs (Inset a, b, c) summarise past seismicity along the cross sections which coincide with these components. Notable seismic events are acknowledged (red stars). **b**) An oblique view of the north South Island from point 'o' is **Fig. 3.01a**, effectively highlighting the fault network and topography associated with the MFS. The study area has been highlighted (yellow) in both. Full credit to Nicol et al. (2012) – reference in bibliography. Digital enhancement of the images has been tried, but to no avail as this is the quality at which they were taken/received.*

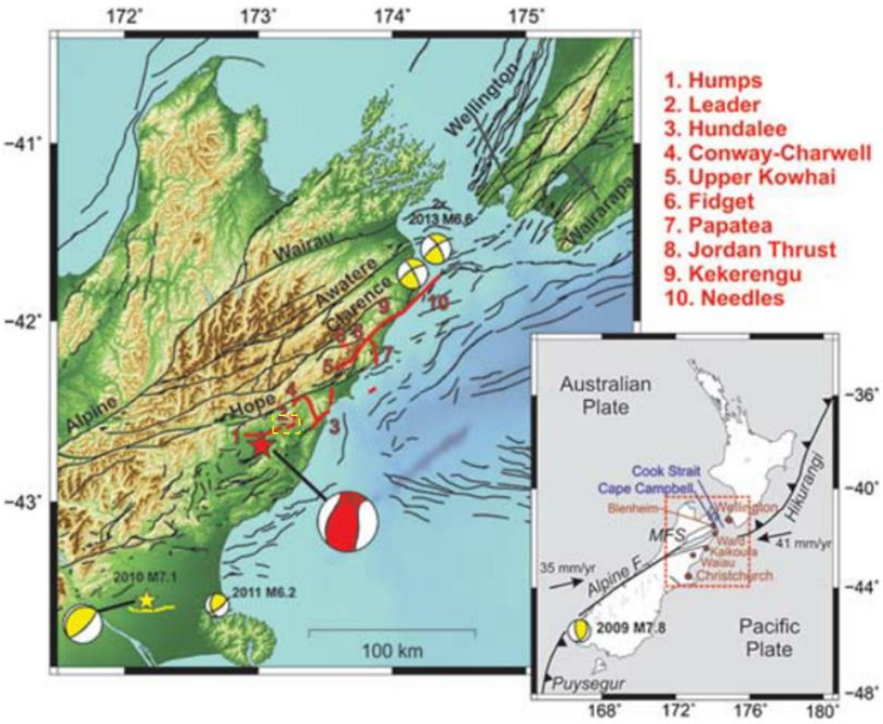

***Fig. 3.02**: A close-up of the MFS illustrating the most active faults, as well as those which do not usually appear on national-scale fault maps (red numbers). The study area (yellow) is ~8 km north-east of the epicentre (red star) and has been highlighted, through which the Humps and (South) Leader Fault Zones run. The close-up has been contextualised nationally along with some key locations (Inset). Waiau is ~4 km north-east of the epicentre, and the study area is ~4 km north-east of Waiau respectively. Full credit to Kaiser et al. (2017) – reference in bibliography.*

(Langridge & Berryman, 2005), making my study area along the Humps Fault (Fig. 3.03a-b) particularly interesting due to its proximity to the Hope Fault, as higher slip rates are likely to result in larger seismic events (e.g. Burbank & Anderson, 2012) and a greater geomorphic response.

South of the MFS, the Alpine Fault runs along the west side of the South Island. Both the MFS and Alpine Fault form a transpressional transform boundary between the Australian and Pacific Plates (Bull, 2009) and continental collision along the Alpine Fault has resulted in the uplift and formation of the Southern Alps (e.g. Norris & Cooper, 2001). Further south beyond the Alpine Fault, subduction dominates once more along the Puysegeur subduction zone beneath the Fjordland (Reyners *et al.*, 2002; Bull, 2011). The significance of the system as a whole is that over 70% of relative plate motion is accommodated for along the Hikurangi Subduction Thrust and the Alpine Fault (Nicol *et al.*, 2012). As a result, seismic activity may not be as severe as the collision boundary may warrant without this compensation.

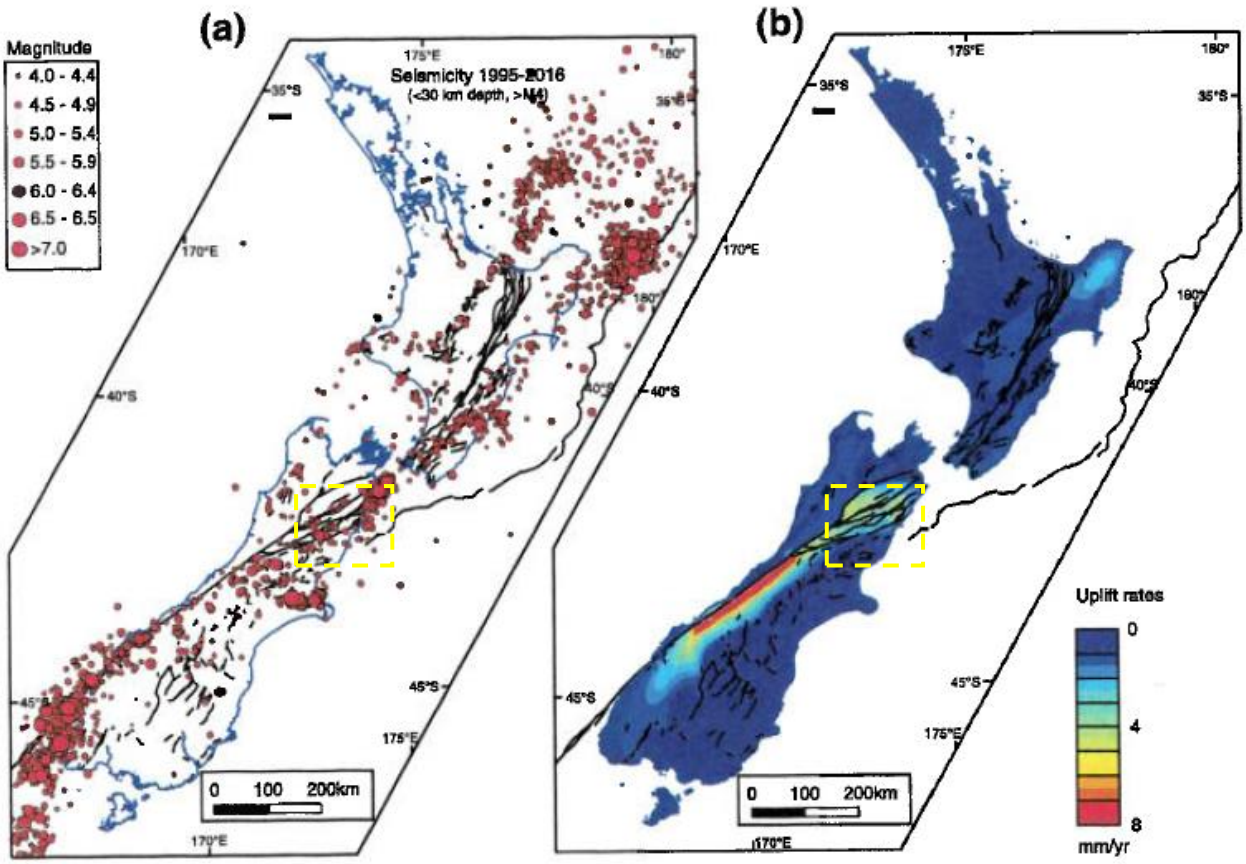

***Figs. 3.03a-b**: Fault maps of New Zealand highlighting past seismicity (a) and uplift rates (b). The area of interest (AOI) on the MFS has been highlighted (yellow), along which there has been a number of large past seismic events; and there is considerable present-day uplift. Also note the high levels of past seismicity to the south of the AOI around Christchurch. Full credit to Nicol et al. (2012) – reference in bibliography. Digital enhancement of the images has been tried, but to no avail as this is the quality at which they were taken/received.*

3.1.2. Geology

The north South Island is geologically separated into an eastern and western province by the Median Batholith. The eastern province is further geologically separated in the north-south direction by the Alpine Fault. The Kaikoura area to the south of the Alpine Fault is dominated by Paleozoic-Mesozoic rocks – Triassic-early Cretaceous Torlesse terranes (sedimentary Rakaia/Pahau terranes) (***Fig. 3.04***). The basement geology is composed of Mesozoic quartzofeldspathic sedimentary rocks (Bradshaw, 1989), which over time have amalgamated into Torlesse composite terrane. The four main geological units are (Rattenbury *et al.*, 2006):

- Lower Cretaceous Torlesse (Pahau terrane), primarily formed of greywacke
- Upper Cretaceous/Paleogene limestones, siltstones, conglomerates and minor volcanic rocks
- Neogene limestones, sandstones and siltstones
- Quaternary sands, silts and gravels

The inland Kaikoura ranges are formed predominantly of greywacke, which has a low rock mass strength. Combined with New Zealand's humid mesic climate, this results in high erosion rates (Bull, 2011). The seaward ranges are composed of faulted slivers of the latter two geological units (Massey *et al.*, 2018).

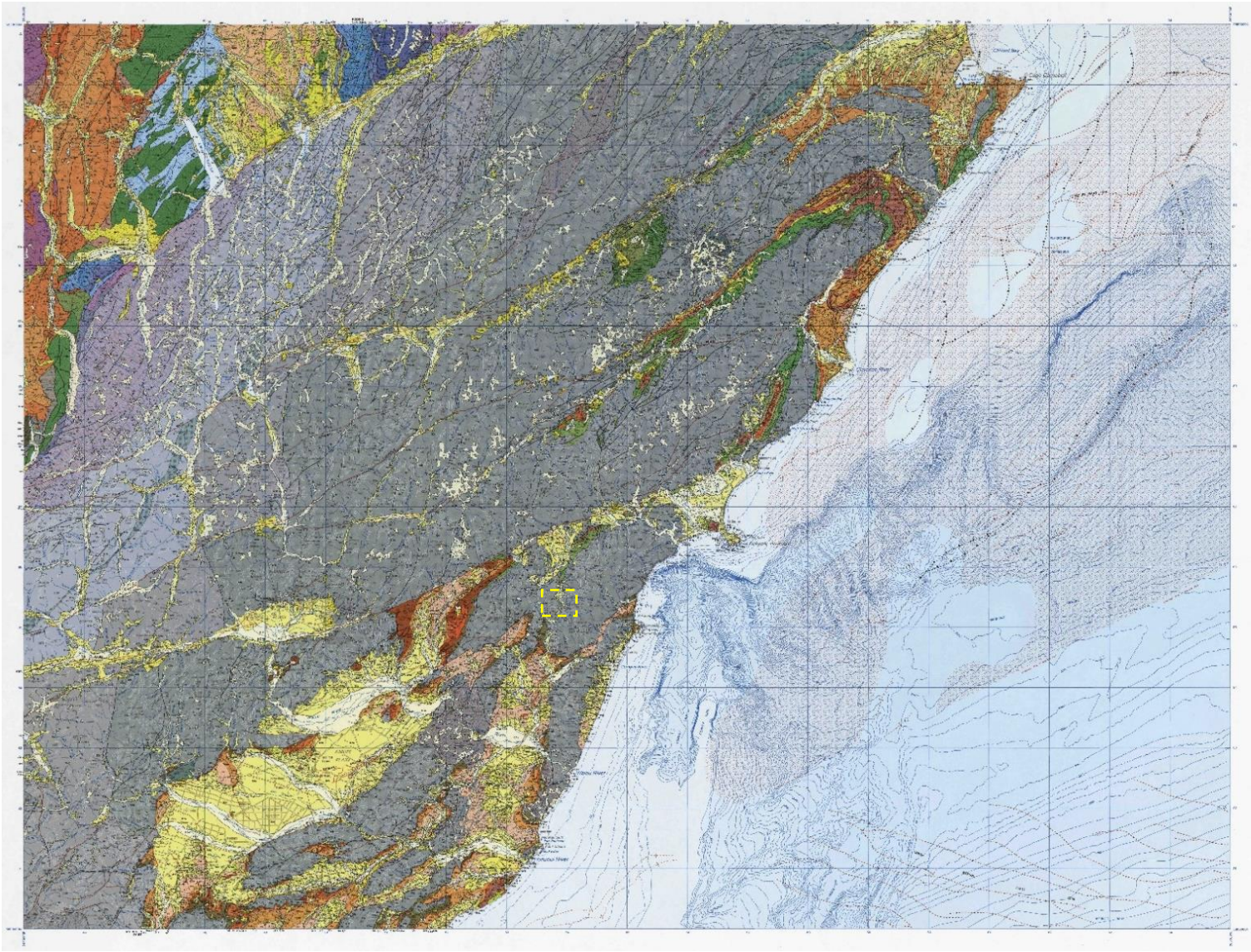

Fig. 3.04*: The most detailed (1:250,000) geological map of the Kaikoura area from Rattenbury et al (2012). The study area (yellow) is dominated by basement rocks (Torlesse Greywacke – grey). Digital enhancement of the image has been attempted but to no avail as this is the quality at which it was published– however, the figure's sole purpose is to provide visual clarity of geological units. Full credit to Rattenbury et al. (2012) – reference in bibliography.*

3.1.3. Climate

New Zealand is at an oceanographic boundary between the warm subtropical waters of the South Pacific and the cold, fresh waters of the Southern Ocean (Lorrey & Bostock, 2012). The complex ocean bathymetry around New Zealand adds to the already-complex circulation of these waters and their associated currents (e.g. Smith *et al.*, 2013) (***Fig. 3.05***). As such, the climate is extremely complex and spatially diverse (e.g. Sturman & Tapper, 2006). The north-east South Island is affected by the Southland Current, which is dominated by subantarctic waters (Sutton, 2003).

Nationwide, New Zealand is subject to a typical maritime climate as a result of the landmass being surrounded by water and therefore moisture-laden maritime air masses (e.g. Brenstrum, 1998). The area is humid (Bull, 2011) and mean annual precipitation in the Kaikoura region can range from 1.5-4 m (Chiswell *et al.*, 2015) (***Fig. 3.05***). Prevailing eastward-migrating cells/fronts have considerable control over the progression of weather (Fowler, 1999). These combine with the Southern Alps to exert a noticeable orographic control on precipitation on the South Island (Salinger, 1980), with eastern regions tending to be drier than western regions (Chiswell *et al.*, 2015) (***Fig. 3.06***). Teleconnections, particularly the El Nino Southern Oscillation (ENSO) and the Southern Annular Mode (SAM), can further complicate and impact weather and climate across New Zealand. Both can cause seasonal and spatial variations in precipitation and temperature (Jiang *et al.*, 2004) as both affect meridional and zonal flow across the country (Lorrey & Bostock, 2012).

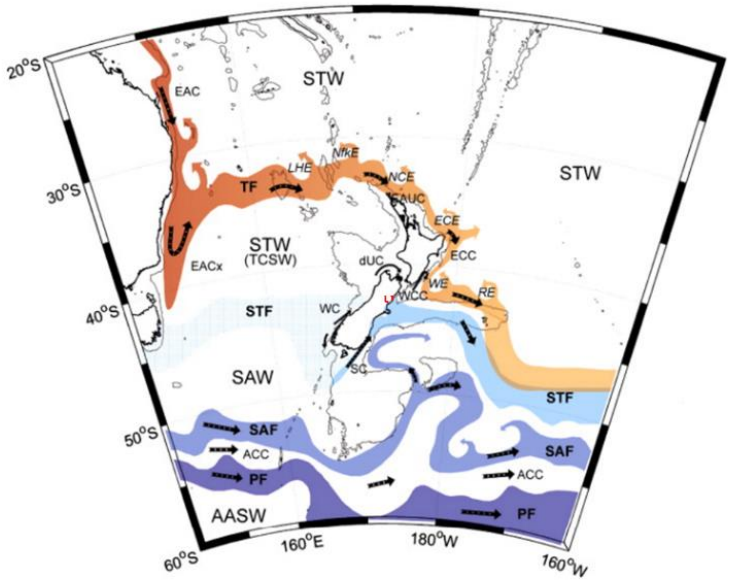

Fig. 3.05*: A map of the ocean currents affecting the New Zealand landmass. Full credit to Chiswell et al. (2015) – reference in bibliography.*

3.2. HISTORICAL EVENTS

The north-east South Island is a region of high seismicity (***Figs. 3.06***) with an extensive history of earthquakes and associated secondary hazards. As of 2006, there had been eight seismic events in the north-east South Island with a M_w > 6.0 since records began (Rattenbury *et al.*, 2006). Since the publication of Rattenbury *et al.* (2006) there have been a further four (NZ Parliament, 2019), including the Canterbury Earthquake Sequence in 2010-11. The largest historical earthquakes were in 1848 and 1888, with very few casualties recorded. In 1848, the M_w 7.5 Marlborough earthquake ruptured for ~105 km along the Awatere Fault (Grapes *et al.*, 1998). In 1888, the M_w 7.0-7.3 North Canterbury earthquake ruptured a ~30 km segment of the Hope Fault (Cowan, 1991). The Kaikoura region has also been subject to seismic shaking from large earthquakes with epicentres elsewhere – for example the 1855 M_w 8.1 earthquake in Wairarapa (North Island) resulted in widespread shaking across the Kaikoura region (Rattenbury *et al.*, 2006). As already discussed, owing to the fact that lower magnitude events are more common than higher magnitude events (Gutenburg-Richter, 1954), it has to be assumed that lower magnitude earthquakes are also abundant throughout the north South Island. This needs to be considered due to the strengthening influence of these on hillslope materials (Brain *et al.*, 2017) as discussed in *Ch. 2.4*. In the context of this

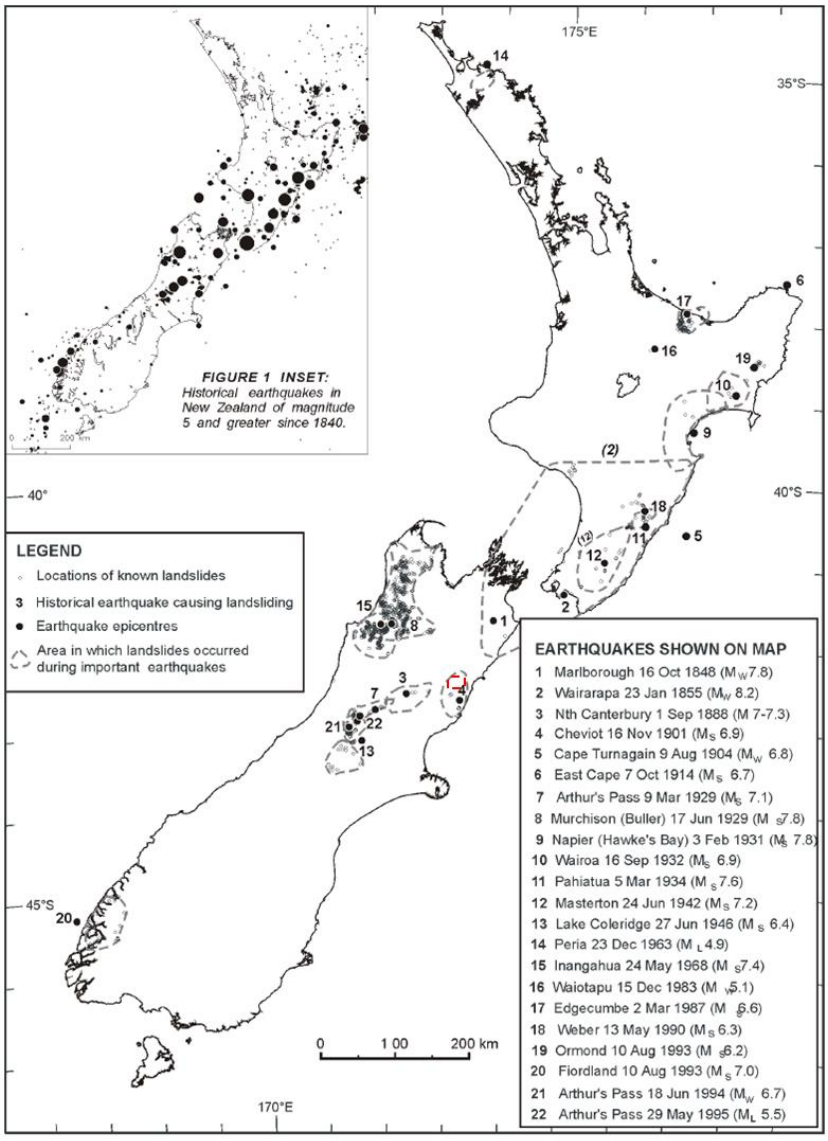

Fig. 3.06*: A map of significant historical earthquake epicentres across New Zealand which are known to have triggered extensive hillslope failure. Notice the proximity of EQ no.'s 3 and 4 (North Canterbury and Cheviot) to the study area (red) and the ensuing landslide activity. Full credit to Hancox et al. (2002) – reference in bibliography.*

case study, this may increase the threshold of shaking required to initiate hillslope damage.

Hancox *et al.* (2002) summarised at least 22 historical seismic events that have resulted in landsliding/ground damage, despite this having been poorly documented in the past (***Fig. 3.06***). In the north South Island, the 1929 Murchison (Buller) M_w 7.8 earthquake (Pearce & O'Loughlin, 1985) appears to have been the largest historical earthquake-induced mass wasting event on record, resulting in over 7000 km^2 of landsliding and 16 direct deaths (Hancox *et al.*, 2002). This may have preconditioned hillslopes for failure following the 1968 M_w 7.1. Inangahua earthquake (Anderson *et al.*, 1994). Parker *et al.* (2015) highlight a spatial correlation between the landsliding triggered during the two earthquake sequences and use this to highlight the lasting impact seismic shaking can have on progressive damage accumulation within a hillslope. No historical co- or post-seismic mass wasting has been reported for the Kaikoura region to date.

Owing to the potential legacy effects of past earthquakes (e.g. Lin *et al.*, 2008) the Canterbury Earthquake Sequence of 2010-11 is of relevance to the forthcoming study. The sequence consisted of four earthquakes, all of which had a M_w > 6.0 and three of which were particularly damaging (***Fig. 3.07***). The 4th September 2010 M_w 7.1 Darfield earthquake ruptured the surface (Gledhill *et al.*, 2011) along the Greendale Fault, causing widespread damage to infrastructure and to older buildings in Christchurch. No fatalities ensued due to the rural location of the epicentre. A large M_w 6.2 aftershock resulting from reverse-slip towards the eastern edge of the aftershock zone (Kaiser *et al.*, 2011) followed on 22nd February 2011. The epicentral location in the outer suburbs of Christchurch resulted in 181 fatalities in the city. Widespread ground cracking and landsliding in the Port Hills also ensued (Massey *et al.*,

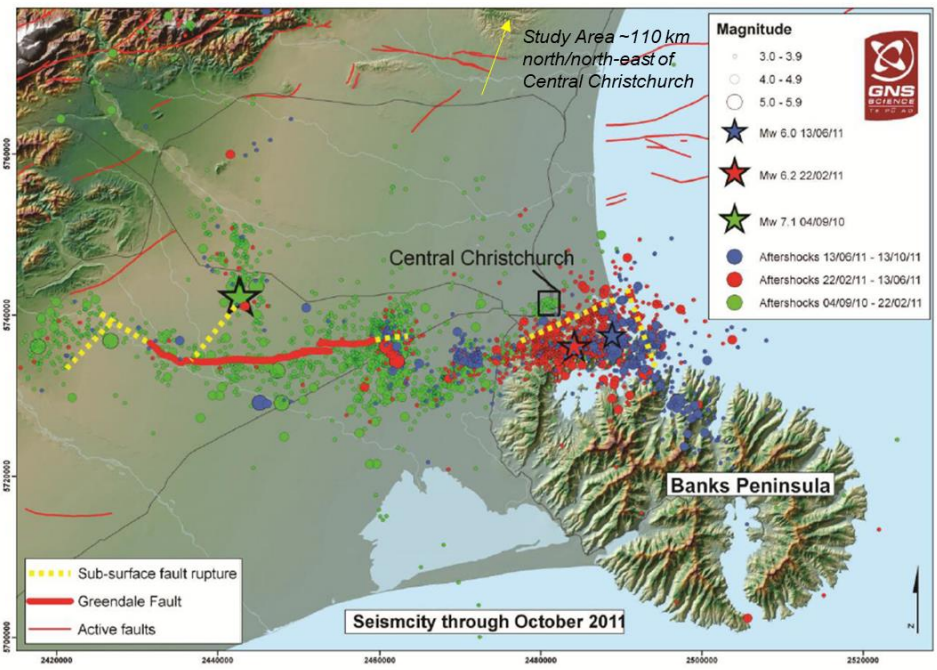

Fig. 3.07: A map illustrating the key ruptures (mainshocks and aftershocks) and their associated properties of the Canterbury Earthquake Sequence in 2010-11. Although on a different fault system, geographically this is not too far (yellow arrow) from the study area near Waiau in the north of the region. Full credit to Dellow *et al.* (2011) – reference in bibliography.

2014a). Landsliding caused further extensive damage, directly resulting in a further four fatalities and damage to hundreds of buildings (Dellow *et al.*, 2011). Two more large aftershocks then followed on 13/06/2011 and 23/12/2011 respectively, both measuring M_w 6.0.

Dellow *et al.* (2011) observed co-seismic ground cracking throughout Christchurch and the surrounding area (***Fig. 3.08***). Cubrinovski *et al.* (2011) documented liquefaction-induced lateral spreading in Christchurch's CBD following the 22nd February 2011 event. The authors cited the importance of ground material, as differential levels of ground cracking were experienced throughout the CBD. This supports other papers that have also highlighted the importance of material type in liquefaction-induced lateral spreading (e.g. Huang & Jiang, 2010). Extensive ground cracking in some areas of the Port Hills (Redcliffs and Richmond Hill) was also documented, representing both localised shallow ground deformation and evidence of larger mass movement (Massey *et al.*, 2014). Hillslopes and rock masses were consequently weakened due to the ingress of runoff water and much of the debris that was removed from the area by mass wasting was deemed resultant of earthquake-induced cracking. Massey *et al.* (2014) stressed that earthquake-induced fractures had reduced the strength of rock masses/hillslopes and that these would continue to weaken over time, increasing the susceptibility of the masses/slopes to future failure, particularly in the event of another earthquake. This happened to be the case, as elevated rates of mass wasting following the latter two earthquakes in the sequence were attributed to this co-seismic ground cracking (Parker *et al.*, 2015). Whilst an interesting insight, this is extremely spatially confined. Aside from that which resulted from the Christchurch Earthquake Sequence, the only other form of earthquake-induced ground cracking was documented following the 2013 M_w 6.6 Lake Grassmere earthquake (Massey *et al.*, 2018). This was said to be extensive, but no further research was conducted.

The 2010-11 Canterbury Earthquake Sequence is a significant event that, along with other historical seismic events (both large and small), must be considered when contextualising the 2016 Kaikoura earthquake. Damage from earthquake sequences may have persisted within the surrounding hillslopes (e.g. Marc *et al.*, 2015; Parker *et al.*, 2015), triggering more widespread damage during and following the 2016 earthquake than would have been the case had the event not occurred. Alternatively, the abundance of smaller seismic events and the accumulation of the strengthening effect of these may have enhanced the resistance of hillslopes (Brain *et al.*, 2017), resulting in lower-than-expected damage rates.

Figs. 3.08a-f*:* Examples of ground cracking in Christchurch which manifested during the Canterbury Earthquake Sequence in 2010-11. Documented by Dellow *et al.* (2011). Full credit to Dellow *et al.* (2011) – reference in bibliography.

3.3. 2016 KAIKOURA EARTHQUAKE

At 12:03am, the M_w 7.8 earthquake (USGS, 2016) struck with an epicentre ~4 km from Waiau, North Canterbury (Kaiser *et al.*, 2017) (***Fig. 1.01***). This resulted in extensive surface fault rupture (e.g. Litchfield *et al.*, 2018) and ground cracking (e.g. Dellow *et al.*, 2017); triggered tens of thousands of landslides (Jibson *et al.*, 2018), some of which formed landslide dams (e.g. Robinson *et al.*, 2018); caused two fatalities, tsunami and damage to a number of older buildings in the rural areas surrounding Kaikoura (Kaiser *et al.*, 2017); and damaged infrastructure (NZTA, 2016). The cost to the New Zealand Government was ~NZ$3-8bn (e.g. Kaiser *et al.*, 2017) and effects were felt, and continued to be felt, as far away as the capital city, Wellington (Deloitte, 2017).

Source back-projection suggests that rupture initiated ~4 km from Waiau at a shallow depth of ~15 km and propagated NE/SW for ~170 km to the coast where it continued offshore (Kaiser *et al.*, 2017). Global and regional moment tensor solutions revealed that the rupture was dominated by reverse and strike-slip (Hamling *et al.*, 2017). The mainshock was oblique thrust (Kaiser *et al.*, 2017) and the largest surface ruptures were dextral strike-slip of an oblique/transpressional nature (Litchfield *et al.*, 2018). Aftershocks ensued, four of which M_w > 6.0 - most resulting from reverse and strike-slip (Hamling *et al.*, 2017). Field measurements and GPS data confirmed considerable but variable vertical and horizontal displacement (Hamling *et al.*, 2017) (***Fig. 3.09***). This is not surprising given that peak ground acceleration (PGA) reached 1.0g and 2.7g in the vertical and horizontal respectively (Bradley *et al.*, 2017), and that spectral accelerations exceeded a 500-year return period (Kaiser *et al.*,

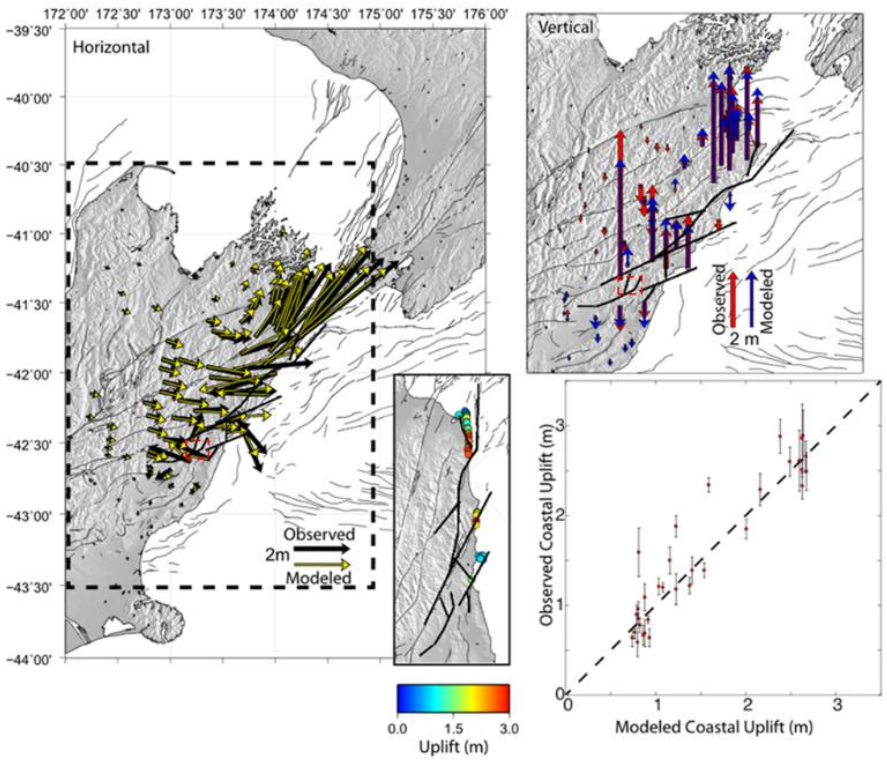

Fig. 3.09*: Maps of the observed and modelled horizontal/vertical ground displacement accompanied by the resulting rates of coastal uplift caused by the 2016 Kaikoura Earthquake, New Zealand. Horizontal and vertical displacement roughly follows the north-east direction of rupture propagation from the epicentre. Displacement and resultant uplift is highest in the north-east corner of the South Island. Both horizontal and vertical displacement are significant in and around the study area (red). Full credit to Hamling et al. (2017) – reference in bibliography.*

2017). Post-earthquake synthetic aperture radar (SAR) analysis and high-rate GPS/motion data confirmed an extremely complex fault rupture involving four stages of rupture; three distinct phases of north-eastward energy propagation (***Fig. 3.10***); and at least 13 different faults (Hamling *et al.*, 2017). This meant that ground shaking was more similar to a M_w 7.1 event than a M_w 7.8 event (Hamling *et al.*, 2017).

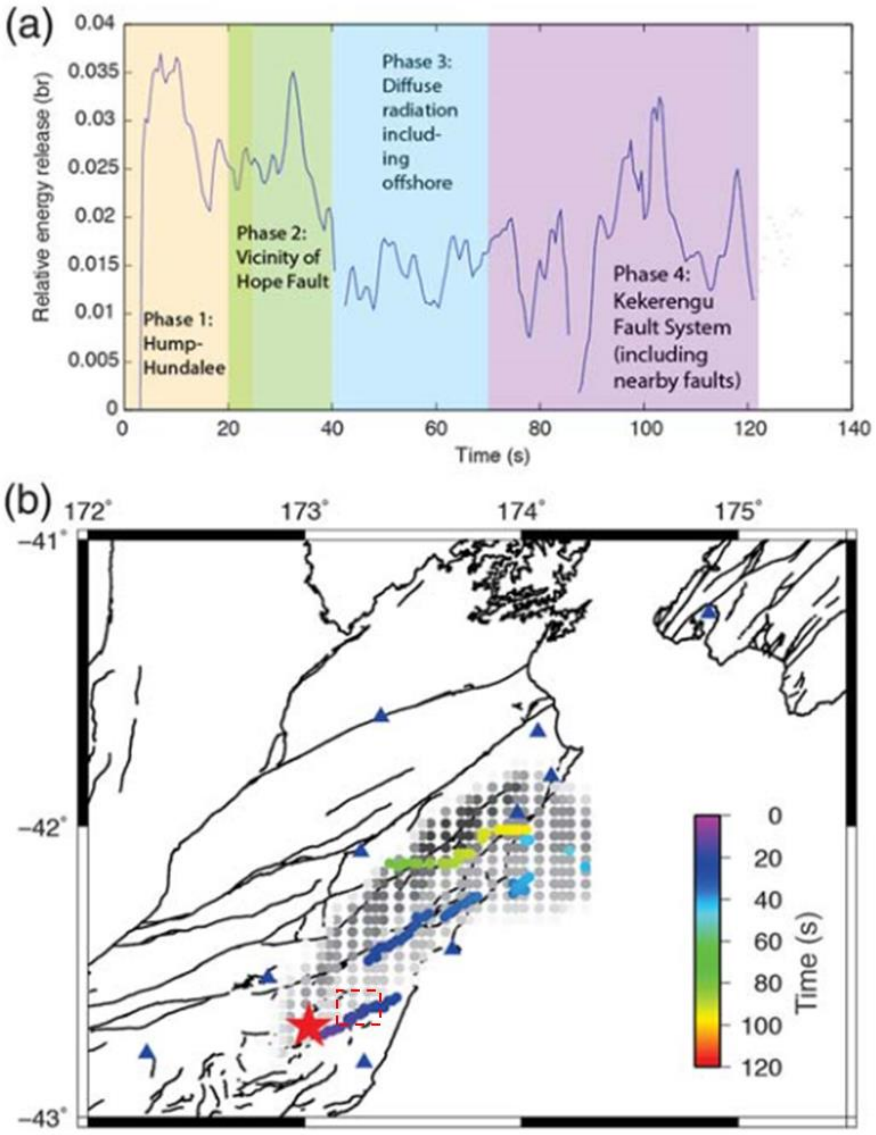

Figs. 3.10a-b: ***a****) A graphical temporal representation of the four stages of rupture. The three distinct phases of energy propagation are clearly represented by the three spikes in relative energy release, br.* ***b****) A cartographic temporal representation of the three distinct phases of north-east energy propagation. The first phases propagates north-east from the epicentre along the Humps Fault Zone, directly impacting the study area (red). Full credit to Kaiser et al. (2017) – reference in bibliography.*

The rupture may have been complex because it involved a number of different faults and fault types. A 15 km '*fault jump'* between the Humps and Hundalee Faults was of particular interest as it was unexpected and is not accounted for in rupture propagation models. This may be explained by the '*keystone hypothesis*' which supports the spontaneous propagation of a rupture across a range of different faults (and fault types)

with different orientations (Beavan *et al.*, 2011). Ultimately, Hamling *et al.* (2017) use this example to conclude that whilst a variety of different modelling types/techniques are available to explain such an event, the reliability of such modelling remains an issue especially when working with complex ruptures.

Extensive landsliding was triggered throughout the region (e.g. Jibson *et al.*, 2018). No direct fatalities resulted from these and associated building damage was kept to a minimum (Stevenson, 2017). However, landslides caused major disruption to vital infrastructure, particularly road and rail networks throughout the region (Davies, 2017). Kaikoura was completely cut off following the event (Bradley *et al.*, 2017). Tens of thousands of landslides were triggered over a 10000 km^2 area, the majority of which were densely concentrated within a 3500 km^2 area surrounding surface fault rupture (***Fig. 3.11a***). The largest failures were located on or adjacent to surface fault rupture suggesting a strong structural geological control (in the structural form of the rupture as opposed to the compositional form of the landscape) on the distribution of landsliding (Dellow *et al.*, 2017) (***Fig. 3.11b***).

Massey *et al.* (2018) compiled a detailed coseismic landslide inventory (***Fig. 3.11a***) and used this to quantitatively investigate any spatial relationships evident from landsliding. Firstly, the number of landslides triggered by the earthquake was relatively small compared to events of a similar magnitude. This confirmed initial estimates from Jibson *et al.* (2018), who qualitatively compared landslide numbers with predictions from established magnitude-frequency analyses (Keefer, 2002; Malamud *et al.*, 2004).

Rupture complexity and the consequential reduced actual ground shaking could explain this (Hamling *et al.*, 2017). Secondly, the clustering of landslides around surface fault ruptures suggested a spatial correlation with ground shaking intensity (***Fig. 3.11a***). This supports a wealth of recent literature advocating links between peak ground acceleration and landslide density (e.g. Meunier *et al.*, 2007; Hovius & Meunier, 2012). Finally, coastal slopes had greater landslide densities than inland areas. The authors highlighted that this could be due to differences in source area topography (***Fig. 3.11c***) and therefore the amplification of shaking intensity (Meunier *et al.*, 2008). The types of landslides triggered also differed between coastal slopes and inland areas. Large, deep, coherent slides were much more prevalent inland due to less rugged topography and a weaker geological composition of Upper Cretaceous/Neogene sedimentary rock (Jibson *et al.*, 2018) (***Fig. 3.11b***). Conversely, rockfall and shallow debris slides were more common on coastal slopes (*ibid*).

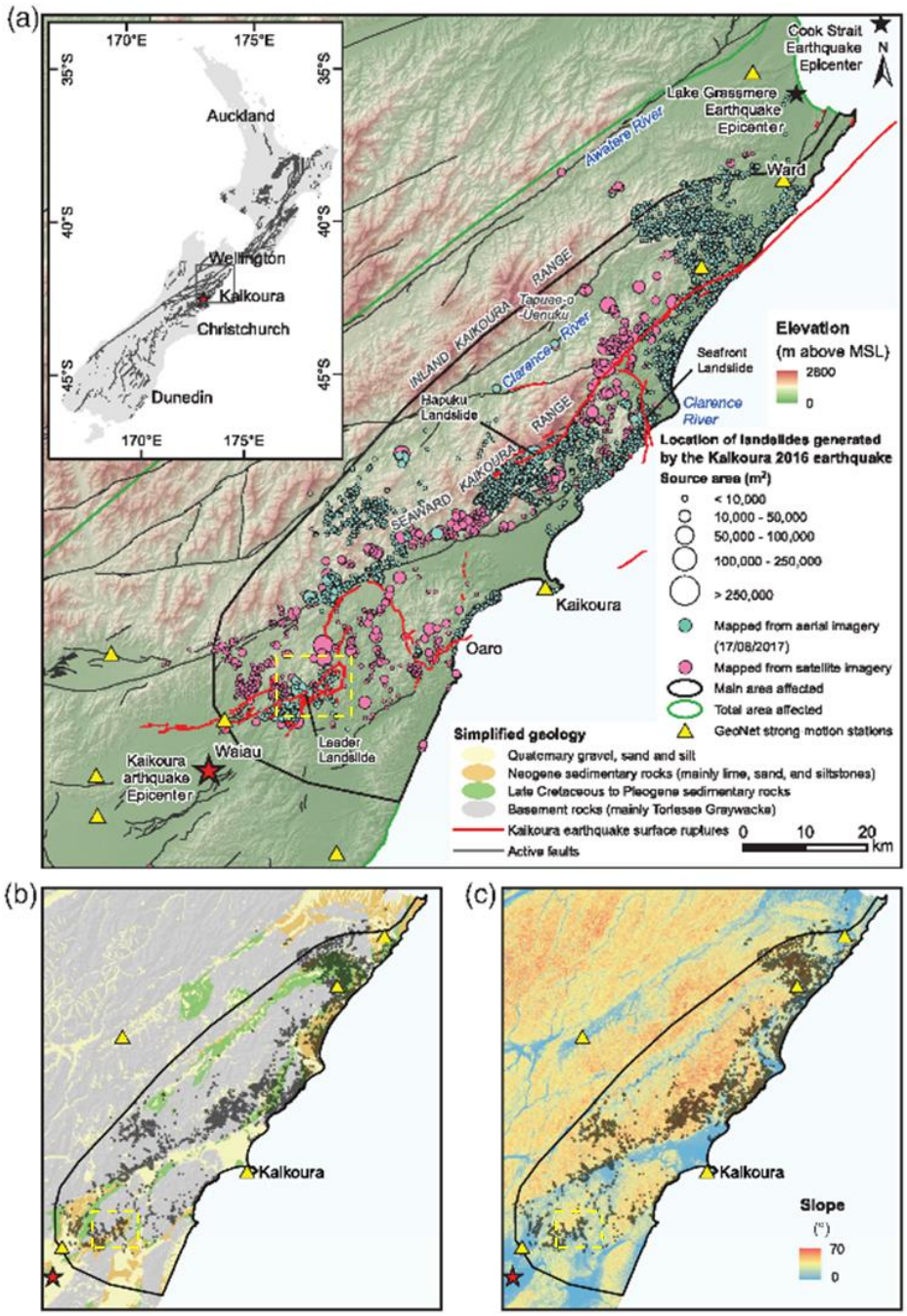

***Figs. 3.11a-c**: **a**) Mapped co-seismic landslides triggered by the Mw 7.8 Kaikoura Earthquake, New Zealand in 2016. Mapping involved the use of aerial photography and satellite imagery. Landslides are contextualised in terms of simplified geology (**b**) and slope angle (**c**), both of which exert a notable influence on spatial distribution. Note that the pattern of landsliding follows the north-east path of rupture propagation from the epicentre. The study area is shown for contextual purposes (yellow). Full credit to Massey et al. (2018) – reference in bibliography.*

The earthquake also triggered extensive ground cracking on hillslopes throughout the region (e.g. Dellow *et al.*, 2017) (***Figs. 3.12a-e***). Jibson *et al.* (2018) highlight the potential link between widespread ground cracking on steep slopes and incipient landsliding as well as cracks unrelated to topography which may have been caused by strong seismic shaking. They also claim that ground cracking was extensive at ridge ends, possibly due to topographic site effects (Meunier *et al.*, 2008). Both Dellow *et al.* (2017) and Massey *et al.* (2018) highlight ground crack activity as an ongoing cause for concern

as cracks may develop into full hillslope failure following a future trigger. Coseismic ground cracking following the M_w 6.6 Lake Grassmere Earthquake in 2013 may have preconditioned slope failure during the 2016 event (Massey *et al.*, 2018). As discussed in *Ch. 2.2.1.*, catastrophic failure or the development of incipient landsliding into full failure may not be instantaneous. Hillslope deformation can 'conveyor' down a hillslope over time, with substantial events contributing to a 'creeping' mass movement. Ground cracking may be a surface manifestation of this – and the earthquake in 2016 may have either been the sole cause or may have just accelerated a pre-existing area of hillslope deformation (from a past event) down a hillslope. As there has been little documentation of coseismic ground cracking in the past, this is not a question that we'll be able to answer at the present but certainly something that will need to be considered going forwards. Aside from this, field observations confirmed meter-scale surface fault rupture on at least 12 faults (Litchfield *et al.*, 2016) and liquefaction-induced lateral spreading at Wellington's CentrePort (Cubrinovski *et al.*, 2017) and along river channels throughout the affected region (Jibson *et al.*, 2018).

This coseismic ground cracking will be investigated in this study. Characteristics of ground cracking will be extracted, and topographic controls will be deduced to see if there is an explanation for the extensive occurrence of co-seismic ground cracking. Consequently, I will assess whether ground cracking can be modelled in a similar manner to that now used for coseismic landsliding in future predictive purposes.

***Fig. 3.12a-e**: Sightings of ground cracking throughout the Kaikoura region documented by Jibson et al. (2018) during immediate post-earthquake field reconnaissance. Full credit to Jibson et al. (2018) – reference in bibliography.*

3.4. SUMMARY

This chapter has provided contextual, site-specific grounding to the theory outlined in *Ch. 2*. Key points from *Ch. 3* are:

- Sitting on a plate boundary, New Zealand as a whole and the north-west South Island in particular is very tectonically active. Geologically, the study area is formed of greywacke which has a low rock mass strength, and the island has a typical maritime climate.
- The study area is no stranger to seismically induced geomorphological events. Historical events, and in particular the 2011 and 2013 events event and may have preconditioned hillslopes for failure during the 2016 event.
- Unlike landsliding, ground cracking from the 2016 Kaikoura earthquake has been documented but not analysed in detail. As such, this is a timely piece of research with the potential to begin to quantify the impact that that ground cracks have on the landscape.

4. INVENTORY PRODUCTION

Due to the lack of previous work focused on the documentation of coseismic ground cracking and the wealth of literature that exists on coseismic landslide inventories, the production of a ground cracking inventory will be informed by the methods used in the study of coseismic landsliding. The aims and objectives of this study are therefore similar to those that have used inventory maps to analyse coseismic landsliding, and so these methods are anticipated to be transferable.

4.1. INVENTORY MAPS

Inventory maps record the geographical location of given features under investigation, in this case coseismic ground cracks, that have a noticeable presence on the landscape (e.g. Roback *et al.*, 2018). They can be produced for a number of reasons, including but not limited to:

- Documenting the extent of features (e.g. Triglia *et al.*, 2010)
- Investigating the distribution and pattern of features (e.g. Massey *et al.*, 2018)
- Informing hazard and risk assessment (e.g. Guzzetti *et al.*, 2006)
- Assessing the evolution of features and their wider influence on landscape evolution (e.g. Parker *et al.*, 2011)

Inventory maps can be classified according to their type and scale and a full review of this and landslide inventories in general can be found in Guzzetti *et al.* (2012). This study has involved the compilation of a medium-scale geomorphological event inventory, documenting ground cracks that are resultant of a single trigger (an earthquake in this case (e.g. Harp & Jibson, 1996; Dai *et al.*, 2010)) through the systematic interpretation of aerial photography (e.g. Ardizzone *et al.*, 2007). The inventory will be used to address all of the above, which in turn can inform event-specific responses and discussions including:

- Information on the extent and magnitude (e.g. Malamud *et al.*, 2004)
- Monitoring ongoing risk levels
- Emergency response and post-event recovery efforts (e.g. Robinson *et al.*, 2017; 2018)
- Model verification (Robinson *et al.*, 2017)

Inventory maps are now much easier to produce thanks to the increasing prominence and development of Geographical Information Systems (GIS) with the ability to quickly and easily produce, update, visualize and analyse inventories (Guzzetti *et al.*, 2012). GIS has therefore been employed in the production of this inventory.

4.2. METHODOLOGY

Geospatial data such as inventories are increasingly being used to inform real-life situations (Tralli *et al.*, 2005) such as hazard monitoring and post-event recovery efforts. As such, the choice of resources and techniques used to produce these is paramount and needs to be considered carefully, as resources and techniques are highly interdependent.

4.2.1. Imagery Acquisition

Sources of imagery were considered within the context of this study to reach an informed selection (Morgan *et al.*, 2010). Previous studies have highlighted coseismic ground cracking using satellite imagery. Owen *et al.* (2008) used 15 m-resolution ASTER and ~2.5 m-resolution Quickbird imagery. Saba *et al.* (2010) used 0.5 m WorldView-1, 1 m Quickbird/IKONOS and 2.5 m SPOT imagery. Although these studies highlighted some cracking, they were predominantly focused on landsliding and the authors would have chosen their remote sensing sources for this purpose. The use of satellite imagery has its benefits (***Table 4.1***) and some current high-resolution sensors may have been sufficient for this study. However, it is important to consider the trade-off between spatial, spectral and radiometric resolution within the context of the scale of ground crack features and the chosen methodology.

Table 4.1*: For comparative purposes, a brief summary of the advantages and disadvantages of aerial photography and satellite imagery respectively as a means of a remote sensing image source. Adapted from Morgan et al. (2010).*

Image Source	Advantages	Disadvantages
Aerial Photography	High spatial resolution (can be sub-m); Can be tailored for specific needs (scale, resolution etc.); Conditions can be optimized (both flying and capture)	Characteristics tend to be project-specific; Expensive (especially to introduce a multi-temporal element – i.e. repeat surveys)
Satellite Imagery	Multi-temporal (revisits automatically); Systematic; Large spatial coverage; Extensive spectral range	Coarser spatial resolution; Atmospheric influence

High-resolution aerial photography is ideal for mapping small-scale features (e.g. Fensham & Fox, 2002). As such, 0.2 m true-colour (RGB) 8-bit orthorectified aerial photographs were used for this study. These were captured by AAM NZ on behalf of GNS Science within two months of the earthquake (Dec 2016/Jan 2017) using medium format camera imagery, which was orthorectified using a pre-processed Digital Elevation Model (DEM) (AAM NZ Limited, 2017). The proliferation of high-resolution satellite imagery has perhaps negatively influenced the perceived utility of aerial photography (Sader & Vermillion, 2000) however it was decided that spatial resolution should be the most important consideration. The aerial photographs had better spatial resolution than any satellite imagery currently available on the market (***Table 4.2***). Harvey and Hill (2001) used aerial photography in favour of satellite imagery in their study of Australian wetlands as steep ecological gradients may have had narrower units than a single pixel – this has been the case with ground cracks in the past, many of which tend to be sub-meter in scale (see Sahoo *et al.*, (2007), Ch. 2.3). Spectral and radiometric resolution were therefore considered secondary and not worth a compromise in spatial resolution. For example, harnessing the use of false colour composites offered by multi-spectral capabilities may have been useful, however the WorldView-3's 1.24 m multi-spectral sensor does not offer a suitable compromise for the spatial resolution of the 0.2 m- aerial photography.

Table 4.2*: A summary of the spatial, temporal and digital capabilities of the most readily available optical satellite remote sensors on the market today. Only true-colour (RGB/NIR) resolution has been included. Some sensors have panchromatic capabilities which o offer a better spatial resolution than what is listed above, but this would not be of use for the study in question and is therefore irrelevant. The characteristics of the aerial photography used in this study has been added to the table (highlighted in red) for a means of comparison. Adapted from Zhu et al. (2017).*

Satellite	Spatial Resolution (m)	Image Dynamics (Bits)	Revisit Times (Days)	Reference
Landsat-7/8	30	16	16	USGS/NASA
Sentinel-2	10	12	5	ESA
SPOT-6/7	6	8	~1	SIC/ESA
Pleiades-1A/1B	2	12	~1	SIC/ESA
GeoEye-1	1.65	11	<3	WVDOC
WorldView-3/4	1.24	11	~1	WVDOC
Aerial Photo.	0.2	8	N/A	AAM NZ

As a means of comparison and to justify the use of aerial photography, ground cracks have been mapped in ArcGIS Pro (v. 2.3.3) using 3 m-resolution multi-spectral satellite imagery provided by PlanetLabs from December 2016. This imagery was used as it is a suitable compromise between the spatial resolutions offered by WorldView, GeoEye, Pleiades and SPOT (***Table 4.2***). As ***Figs. 4.01a-b*** highlight, a reduction in spatial resolution results in a considerable difference in mapping accuracy such that the ability to

use multi-spectral capabilities is rendered irrelevant. The visibility of cracks was also assessed using layers derived from the 1 m DEM (***Figs. 4.02a-c***). Only the largest cracks were visible in this, suggesting that a spatial resolution of 1 m is inadequate to detect smaller-scale features. Whilst tenable, this could suggest that even the 1.24 m-resolution multi-spectral imagery offered by WorldView would be inadequate for detecting ground cracks.

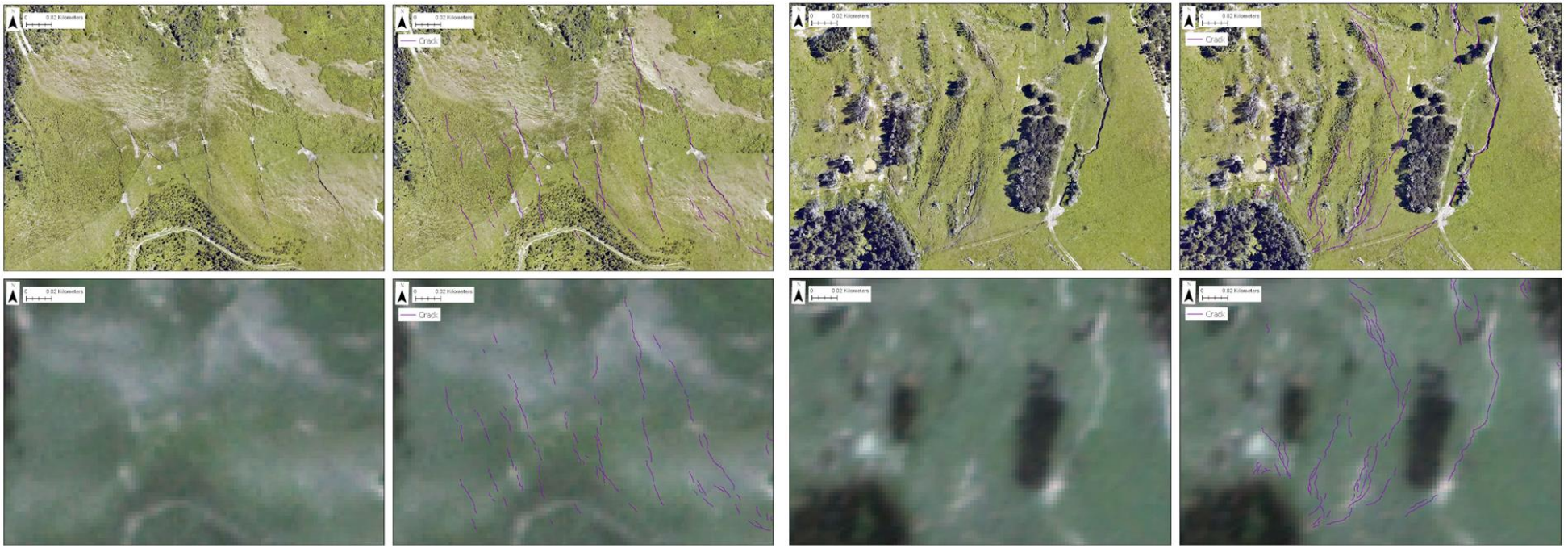

***Figs. 4.01a-b**: Comparison of spatial resolution between aerial photography (0.2 m) (top images) and PlanetLabs imagery (3 m) (bottom images), and the impact that this reduction has for the purpose of mapping small scale features such as ground cracks. The left and right images are identical, but without (left) and with (right) ground crack polygons.*

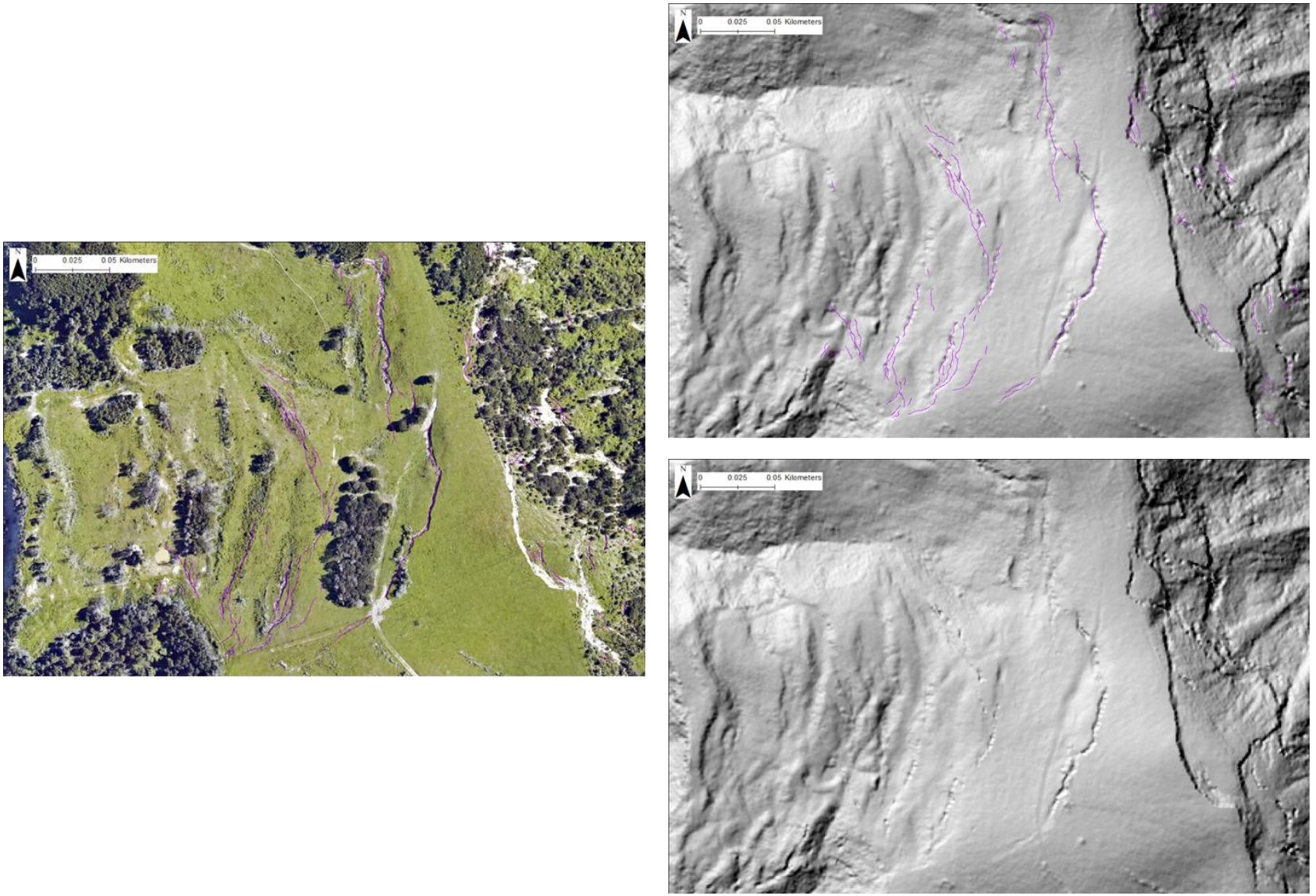

***Fig. 4.02a-c**: Maps showing the visibility of ground cracks from the hillshaded DTM (spatial resolution 1 m). Only the most pronounced features are visible, whilst smaller scale features are much less discernible.*

4.2.2. Visual Interpretation

When selecting the most appropriate methodology for inventory compilation, the following must be considered (e.g. van Westen *et al.*, 2006):

- Purpose of the inventory (*Ch. 4.1*)
- Available imagery (characteristics, scale, resolution etc.) (*Ch. 4.2.1*)
- Resource availability (financial, human, logistical) (*Chs. 4.2.2 & 4.2.4.1*)

In light of these, manual mapping informed by visual interpretation of aerial photography has been chosen as the most suitable method for this study. The novelty of this study means that undertaking statistical analysis to inform any controls/characteristics on/of coseismic ground cracking must be a priority. Inventory accuracy is therefore paramount, and maps prepared through visual interpretation are most suitable for this purpose (Galli *et al.*, 2008; Guzzetti *et al.*, 2012). Resource constraints have also influenced technique selection. Whilst the use of aerial photography has been discussed and justified above, the acquisition of very high-resolution (i.e. WorldView/GeoEye) satellite imagery was cost prohibitive.

4.2.3. Manual Mapping

The creation of accurate and complete geomorphological event inventory maps through visual interpretation requires both of the following criterion to be met (Guzzetti *et al.*, 2008):

- That the features under investigation show a distinct morphological signature (Pike, 1988) which can be accurately mapped through visual interpretation (e.g. Guzzetti *et al.*, 2000)
- That the features under investigation are not randomly distributed (i.e. there is a relative clustering of features as a result of an event)

Ground cracks are clearly visible on the aerial photography and all features in the inventory were resultant of the 2016 Kaikoura earthquake. GIS has improved and simplified inventory mapping through visual interpretation (Wolf & Dewitt, 2000) such that it can now be done by digitally delineating polygon/polyline boundaries (Morgan *et al.*, 2010) and saving these within a GIS. It is important to stick to a single method of delineation (Williams *et al.*, 2018) and scale of mapping. Ground cracks have been digitally mapped in

ArcGIS Pro as 2D polylines, tracing their alignment as closel7 to as possible (e.g. ***Fig. 4.01a***) using polylines according to the visual criteria outlined in ***Fig. 4.03*** and ***Table 4.3***. Initially, ground cracks were mapped liberally to produce Version 1.0 which was then subject to quality checking.

Table 4.3*: Contextual outline of the visual criteria used to manually map co-seismic ground cracks via visual interpretation. To complement the feature-specific application of this in illustrative form in* ***Fig. 4.03****.*

Characteristic	Contextual Description
Shape/Size - form	Recognizing the distinctive form and knowing the physical dimensions and extent of a ground crack in contrast with the surrounding environment – meter-/sub-meter-scale linear features.
Colour/tone - brightness	Variation in the intensity of light reflected by the surface – often lower in ground cracks, which appear darker.
Mottling/texture - roughness	Variation in the roughness of the surface – ground cracks tend to produce rougher surfaces.
Pattern - arrangement	Spatial arrangement of features – ground cracks tend to be random and non-systematic.
Site/Context - position	Setting in terms of the wider landscape – ground cracks are commonly found around areas of hillslope failure and will not be visible underneath vegetation/obscured areas.

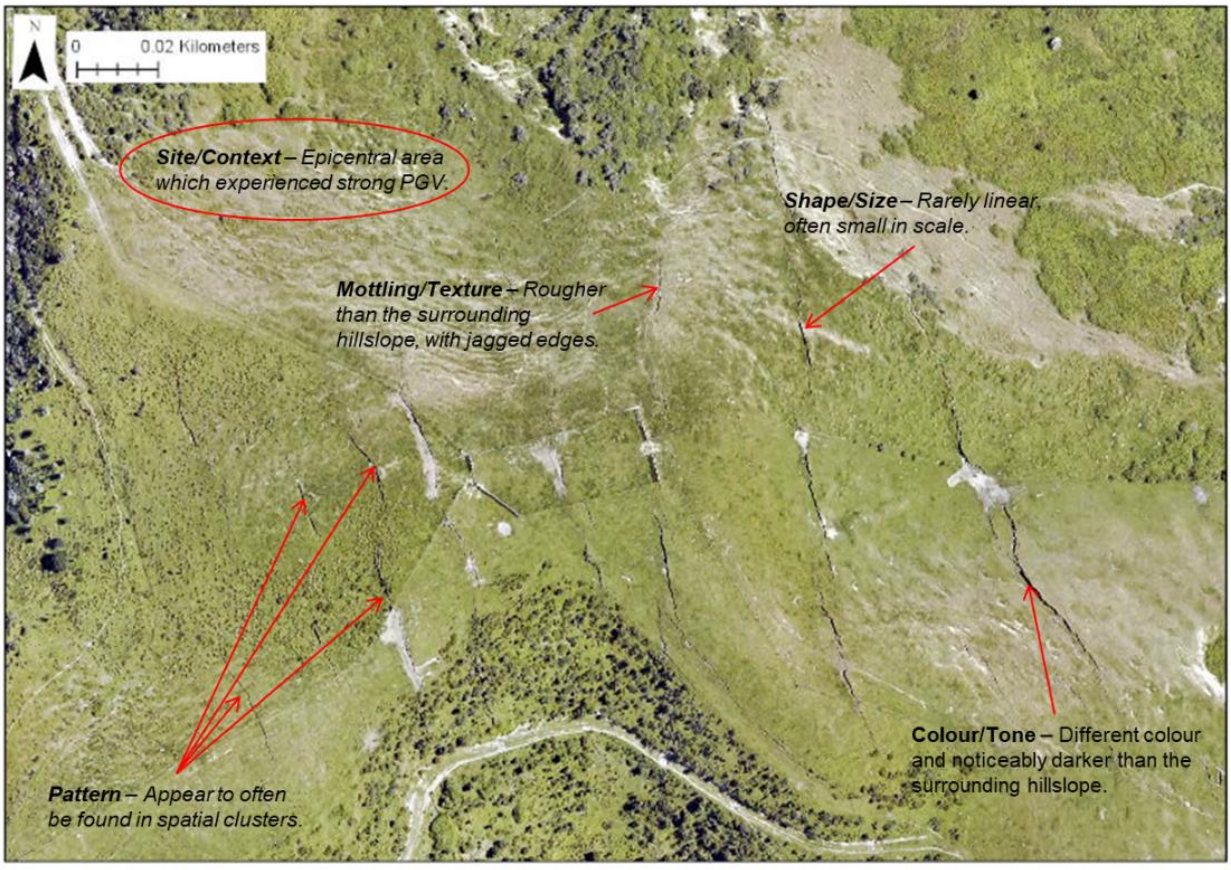

Fig. 4.03*: An illustration of the characteristics of co-seismic ground cracks which make them discernible for the purposes of manual mapping via visual interpretation. To accompany contextual description in* ***Table 4.3****.*

A scale of 1:600 was used throughout the mapping process (***Fig. 4.04***). Through trial and error (Harvey & Hill, 2001), this was found to be the best compromise between visibility, accuracy and time to map. Where possible, individual ground cracks were mapped as opposed to ‘areas of cracking’ (Guzzetti *et al.*, 2012) (***Fig. 4.04***) to provide a larger sample size and inform a more representative statistical analysis.

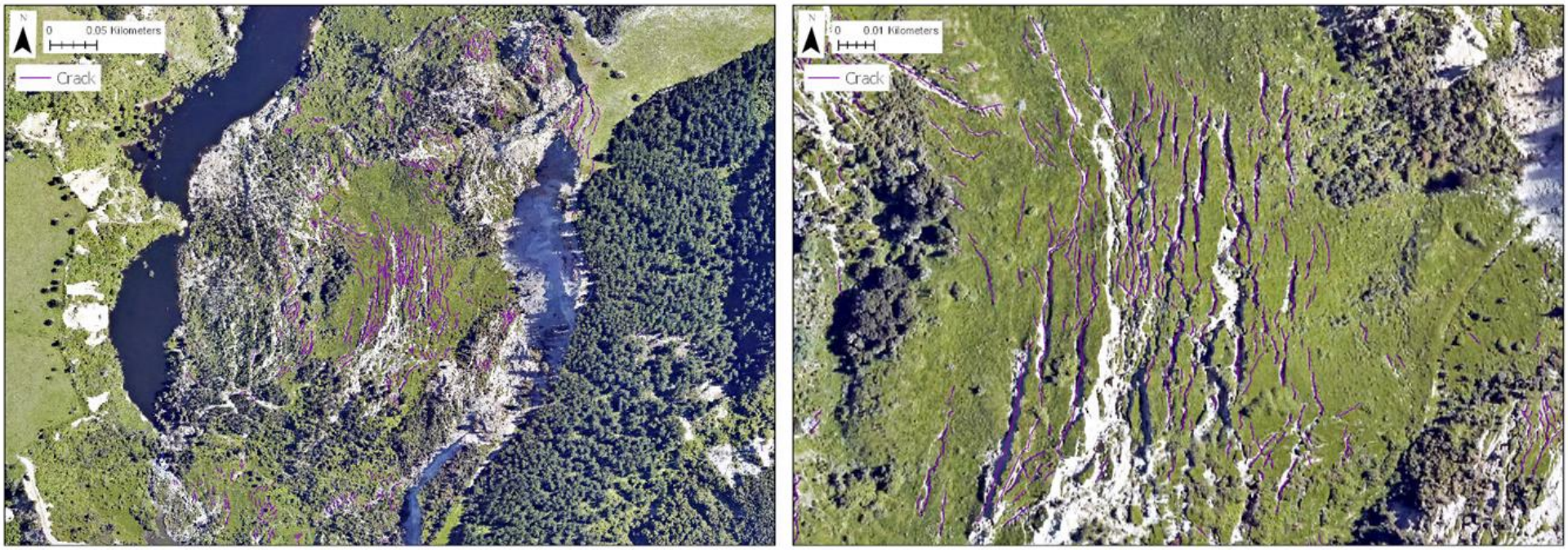

***Fig. 4.04a-b**: **a**) An example of an area of dense ground cracking at a scale of 1:600, which is what was systematically used to initially map ground crack features (purple). **b**) A zoomed in version of **Fig.4.04a** with a scale of 1:50, showing the dense area of cracking in much more detail. When a dense area of cracking was tackled, zooming in was required to ensure that all features were accurately mapped. Note that this was a source of error.*

4.2.4. Quality Checking

For quality control purposes, all ground cracks in Version 1.0 were scrutinised. The creation of a clear, semi-quantitative decision tree reduced the need for field validation and instances of subjective mapping error.

4.2.4.1. *Field Validation*

To assess their accuracy, inventory maps are typically validated by field surveys even if these only cover a fraction of the entire study area (Guzzetti *et al.*, 2012). Through extensive comparison of landslide inventories and the methods used to produce them, Galli *et al.* (2008) conclude that the most accurate framework for inventory production by visual interpretation should include extensive field validation. However, the authors also stress that the accuracy of a study should be considered within its context. This in itself is a function of the resources (including time) available to conduct it. Field validation was not possible in this study. The lack of field validation may slightly affect the accuracy of this study and must remain under consideration throughout. However, the resources, both temporal and financial, were not available to conduct such fieldwork. Finally, the quality of the imagery (spatial resolution and capture conditions) used to compile the inventory along with the strict quality checking stage goes some way to reducing the need for field validation, especially given the context of this research. Supplementary field data supplied by GNS Science also alleviated this influence to some extent.

4.2.4.2. *Sources of Error*

Despite the visual criteria in ***Fig. 4.03*** being followed, it must be assumed that not all ground cracks were clearly visible (Guzzetti *et al.*, 2012). Issues with visual interpretation in landslide studies coexist and are perhaps even exaggerated when looking for smaller-scale features such as ground cracks. Two sources of error are highlighted in ***Fig. 4.05***.

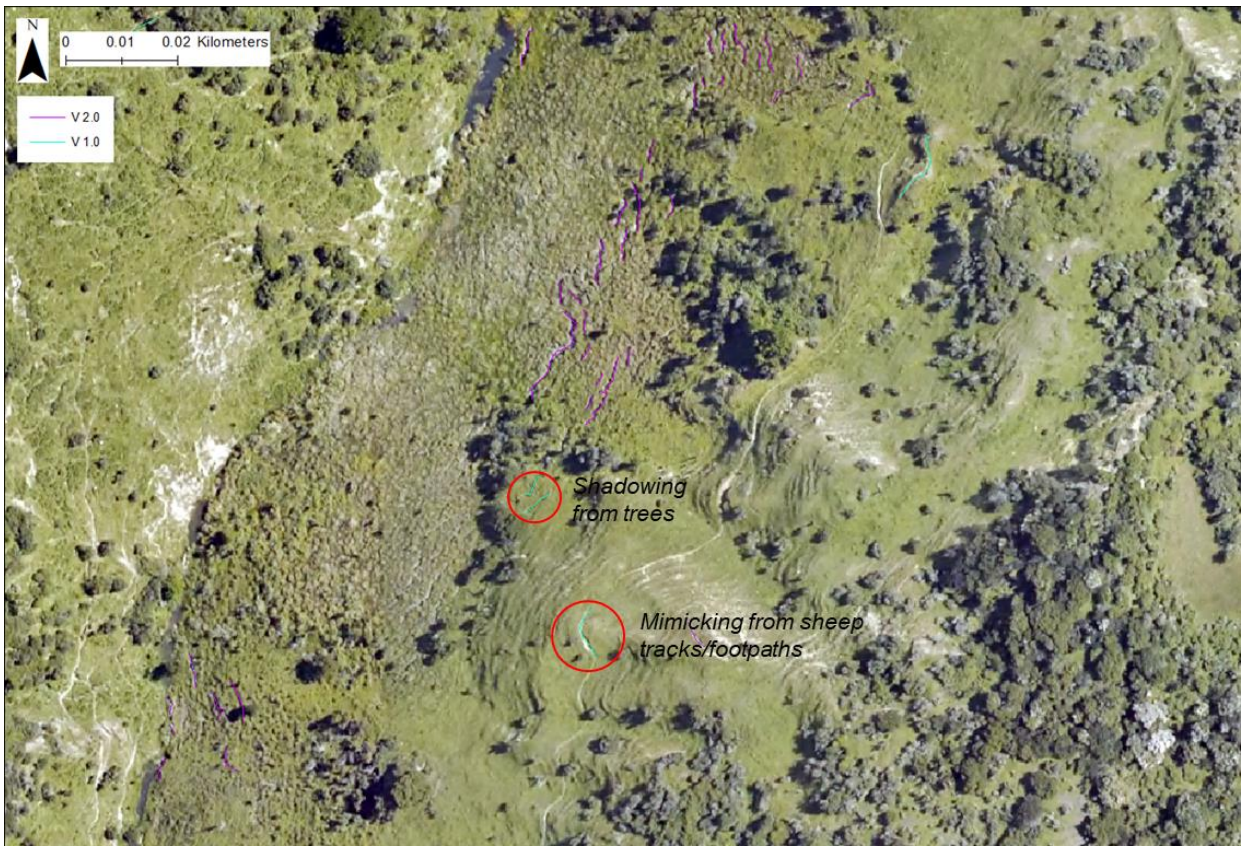

***Fig. 4.05**: Examples of error sources (highlighted) faced with when mapping co-seismic ground cracks by visual interpretation. Erroneous ground cracks were removed during quality checking, and as such some cracks from V 1.0 have been removed (highlighted in light blue, as have not been overlaid by V 2.0, the quality checked dataset). Note that density (**Figs. 4.04a-b**) was also a considerable source of error.*

4.2.4.3. Vegetation

The presence of vegetation is a major issue when visually interpreting aerial photography (e.g. Rib & Liang, 1978). Dense woodland can render small scale features invisible to detection (e.g. Korup, 2005) and therefore mapping. This is the case for landslides (e.g. Guzzetti *et al.*, 2012) and therefore most certainly the case for smaller scale ground cracks. A major advantage of Light Detection and Ranging (LiDAR) data is its ability to (objectively) penetrate the tree canopy and detect features underneath (e.g. Evans, 2016). The 1m Digital Terrain Model (DTM) was visually examined in areas of dense woodland, however like the rest of the study area, no discernible traces of ground cracking could be detected. It was therefore decided to mask out all areas obscured by vegetation, so that any ensuing statistical analysis will not be skewed. This was done using Digital Surface Model (DSM) and DTM surfaces derived from the LiDAR data to produce a canopy height model (***Figs. 4.06a***). A canopy height of 2 m was chosen using a trial and error approach and relating outputs to the high-resolution aerial photography and land-use maps from Land Information New Zealand. Overall, 17km^2 of the study area was masked out (***Fig.***

4.06b). This may sound substantial, but the number of ground cracks detected and mapped in this area was negligible and removing them made no real difference to the overall sample size. Instead, this would only have served to skew any statistical analysis.

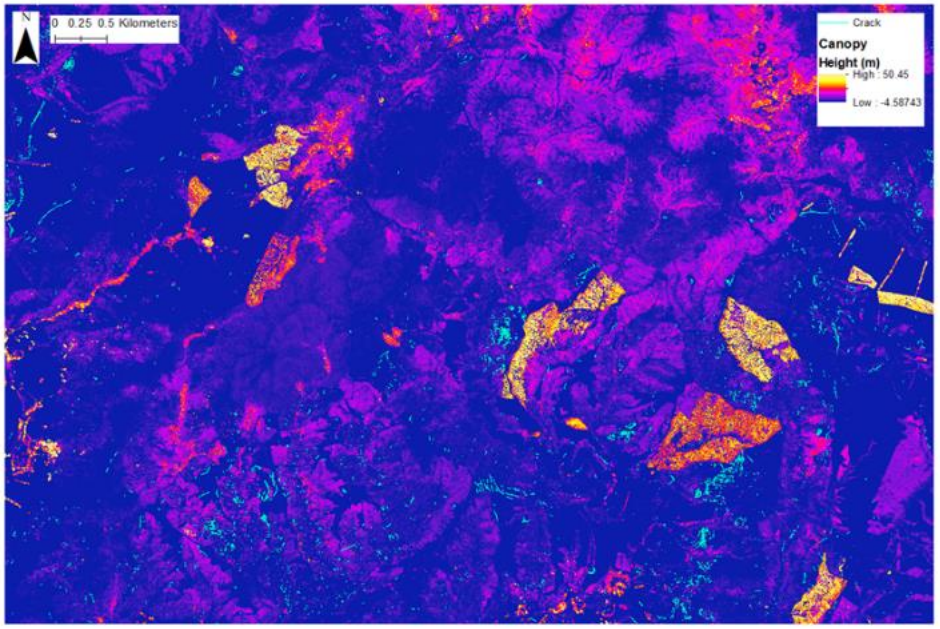

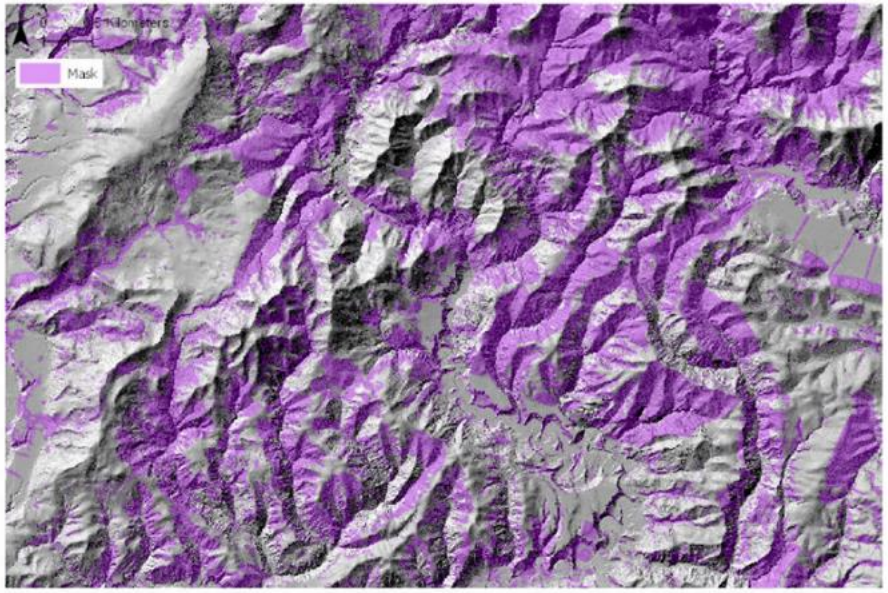

Figs. 4.06a-b: ***a***) *Canopy Height Model (CHM) produced by differencing the digital terrain model from the digital surface model. This resulted in the highlighting of trees and other ground obscuring features (positive elevations). Individual trees and collective forests can clearly be seen (yellow). The CHM was then used alongside aerial photography and land-use maps to qualitatively define a threshold of 2 m, which was consequently used to produce the study area mask (**b**).*

4.2.4.4. *Decision Tree*

To minimize the misclassification error outlined in the previous section, a decision tree has been created similar to that developed in Williams *et al.* (2018) (***Fig 4.07***) in an attempt to make a semi-quantitative inventory by reducing subjective error through following a given set of criteria. Williams *et al.* (2018) used their decision tree to inform image selection and mapping decisions. Whilst image selection has been handled independently, a similar model is followed here to semi-quantitatively determine if a feature is a ground crack and therefore determine whether or not it should be mapped.

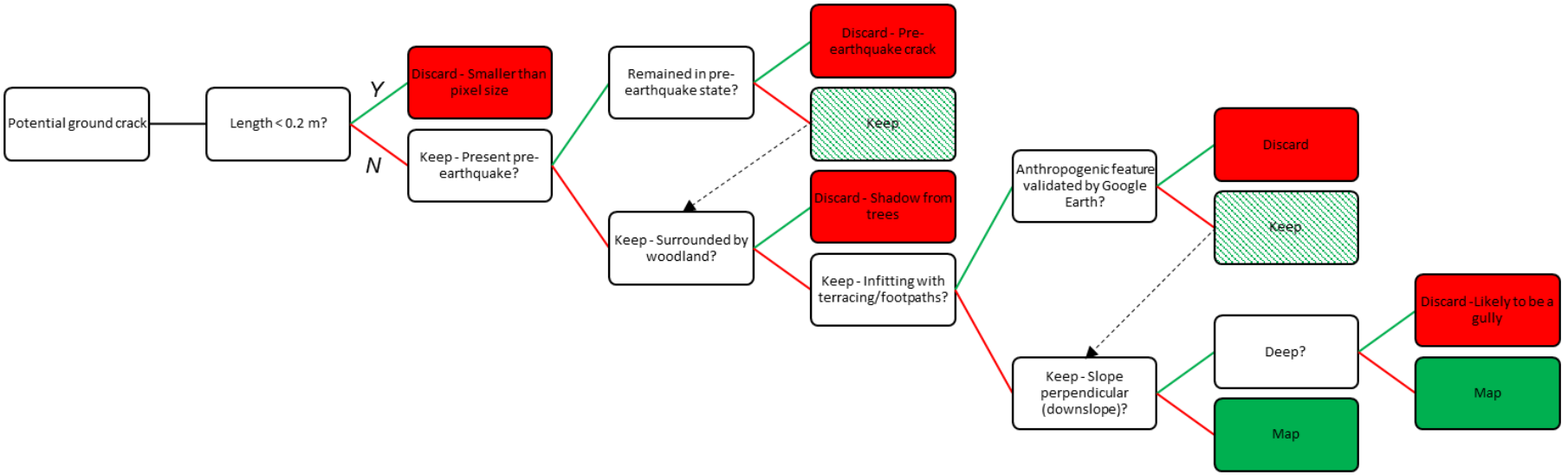

Fig. 4.07: Decision tree created for the quality checking of V 1.0 of the ground cracking inventory. This outlines the decision process which was followed when mapping and quality checking each ground crack feature to ensure the accuracy and validity of the final inventory.

4.3. FINAL INVENTORY

Version 1.0 of the inventory contained 9995 ground cracks. After the Quality Checking process, the sample reduced in size to 9102. Ground cracks were both added and removed during quality checking. Upon visual inspection, the spatial distribution of ground cracking appears to be uneven. Cracking is concentrated in the southern half, and even more so in the south eastern corner, of the study area (***Fig. 4.08***). Cracks appear to be clustered, which potentially has some correlation with areas of slope failure. These observations are explored further below.

4.4. SUMMARY

Key points from *Ch. 4* are:

- Due to a lack of pre-existing literature, the coseismic ground cracking inventory has been informed by studies involving the creation of a coseismic landslide inventory.
- Imagery and methodology have been logically informed according to its required purpose, potential application and resource availability/constraints.
- Aerial photography and manual visual interpretation were used to create the inventory due to the combination of the high spatial resolution of the aerial photography and the geomorphological signatures expressed by ground cracks.
- The inventory has been quality checked and validated – sources of error have been highlighted, decisions regarding these suitably justified and all areas of vegetation masked out.
- The distribution of ground cracks in the final inventory appears to be spatially uneven.

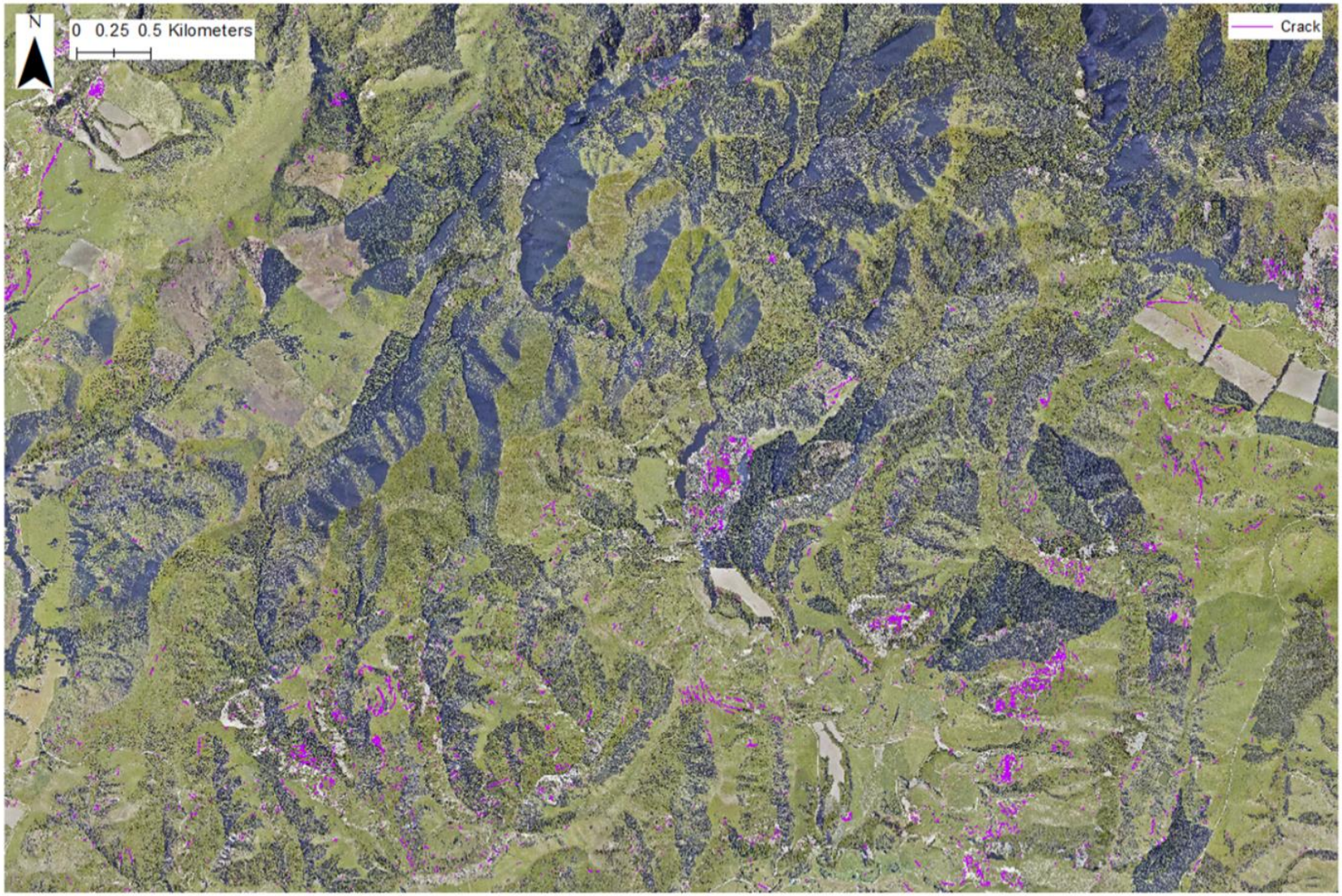

Fig. 4.08: *A map illustrating the final, quality checked, ground crack inventory produced from manual mapping via the visual interpretation of aerial imagery.*

5. AUTOMATIC FEATURE DETECTION – FROM NORTH YORKSHIRE TO NEW ZEALAND

With the increasing supply and application of high-resolution Light Detection and Ranging (LiDAR) data, attempts at automated small-scale feature detection are becoming increasingly common. If its resolution will allow, LiDAR has the ability to objectively (e.g. Baltsavias, 1999) detect small-scale features whilst offering some opportunities to overcome the impacts of vegetation and spectral/atmospheric interference which hamper the use of optical data for such a purpose. Whilst automatic feature detection appears to have never been attempted for ground cracks, it has been applied to internal deformation features within landslide scars (e.g. Glenn *et al.*, 2006), gullying (e.g. Evans & Lindsay, 2010) and small-scale archaeological features (e.g. Challis *et al.*, 2011). The chapter will investigate whether or not ground cracks can be accurately detected using high-resolution LiDAR data. If successful, this will enable the topographic signatures of ground cracks to be quickly and easily extracted and then analysed to provide information on their geomorphological characteristics.

5.1. DATA PROCESSING

Two datasets will be used for this purpose due to the inability to visually see any but the largest ground cracks in the New Zealand airborne LiDAR dataset provided (see *Ch. 4.2.1*). As well as this, a higher resolution airborne LiDAR dataset from North Yorkshire, UK will be used to assess that if given sufficient data density, cracks become detectable. Widespread, pronounced ground cracking has been reported along the Cleveland Way in North Yorkshire due to its location on top of an unstable section of clifftop (e.g. Rosser *et al.*, 2005). This, along with the higher resolution of the LiDAR data provided the opportunity to undertake preliminary analysis on this dataset, with a view to using any findings to inform an attempt at automatic ground crack detection in the much larger 54km^2 study area in New Zealand, as the topographic signatures exhibited by ground cracks are anticipated to be comparable.

The processing for both datasets was very similar. Raw point cloud data was uploaded into ArcGIS (v. 2.3.3) and converted into ESRI's '.lasd' format. The study areas

were clipped before the pulse counts were extracted. This extracted only the number and density of last return (i.e. ground) hits. From this, the point count per m^2 could be calculated to inform Digital Terrain Model (DTM) resolutions of 1 m for New Zealand, and 0.1 m for North Yorkshire, UK (***Fig. 5.01***). This was the highest-possible resolution that could be achieved whilst maintaining an average point count of >4 per m^2 (Baruch & Filin, 2011). Using these, derivatives of the DTM (e.g. slope) potentially relevant to the detection of ground cracks were processed.

Local slope angle describes abrupt changes in topography. Given the high-resolution of the LiDAR data, a sharp increase in local slope angle relative to background levels could be indicative of local hillslope disturbance and/or the internal walls of a ground crack. In the field of archaeology where detecting small scale features is of great value, Challis *et al.* (2011), Stular *et al.* (2012) and others have highlighted the value of using local slope angle for such a purpose, if the LiDAR data is of suitable resolution to do so. This can be assumed so in this case.

Local relief models, for example difference from mean elevation (DFME), attempt to provide a representation of the landscape containing only the relevant features under investigation (e.g. Evans & Lindsay, 2010; Hesse, 2010; Challis *et al.*, 2011) - ground cracks in this case. DFME is the difference in elevation between centre points and the surrounding area within a moving filter window to detect local topographic change relative to the neighbourhood average (i.e. the moving filter window) (Gallant & Wilson, 2000). For flat areas this should tend to zero but increasing discrepancies in topography should have greater departing values. DFME could detect both the tips (areas of lowest difference) and edges (areas of sudden difference) of cracks. Evans & Lindsay (2010) highlight the importance of edge detection when attempting to automatically extract gully networks, features which can be of a similar scale to ground cracks. They also emphasise the importance of the window size and threshold values when undertaking the process. If window size is too small, too much noise will be detected whereas if it is too large, smaller features will be ignored. Circular windows were found to be the most suitable, as all points are within a set maximum radius of the point of interest. The window type/size therefore needs to be chosen in line with the scale and morphology of the features so that it is suitable and slightly exceeds the average size so that the majority of feature is captured by the window. As such, a circular window with a diameter of 5 m was chosen for both datasets, as few ground cracks will be wider than this based on previous studies (Sahoo *et al.*, 2007). Focal Statistics was used to apply the mean 5 m circular filter to the DTM. This was then subtracted from the original DTM.

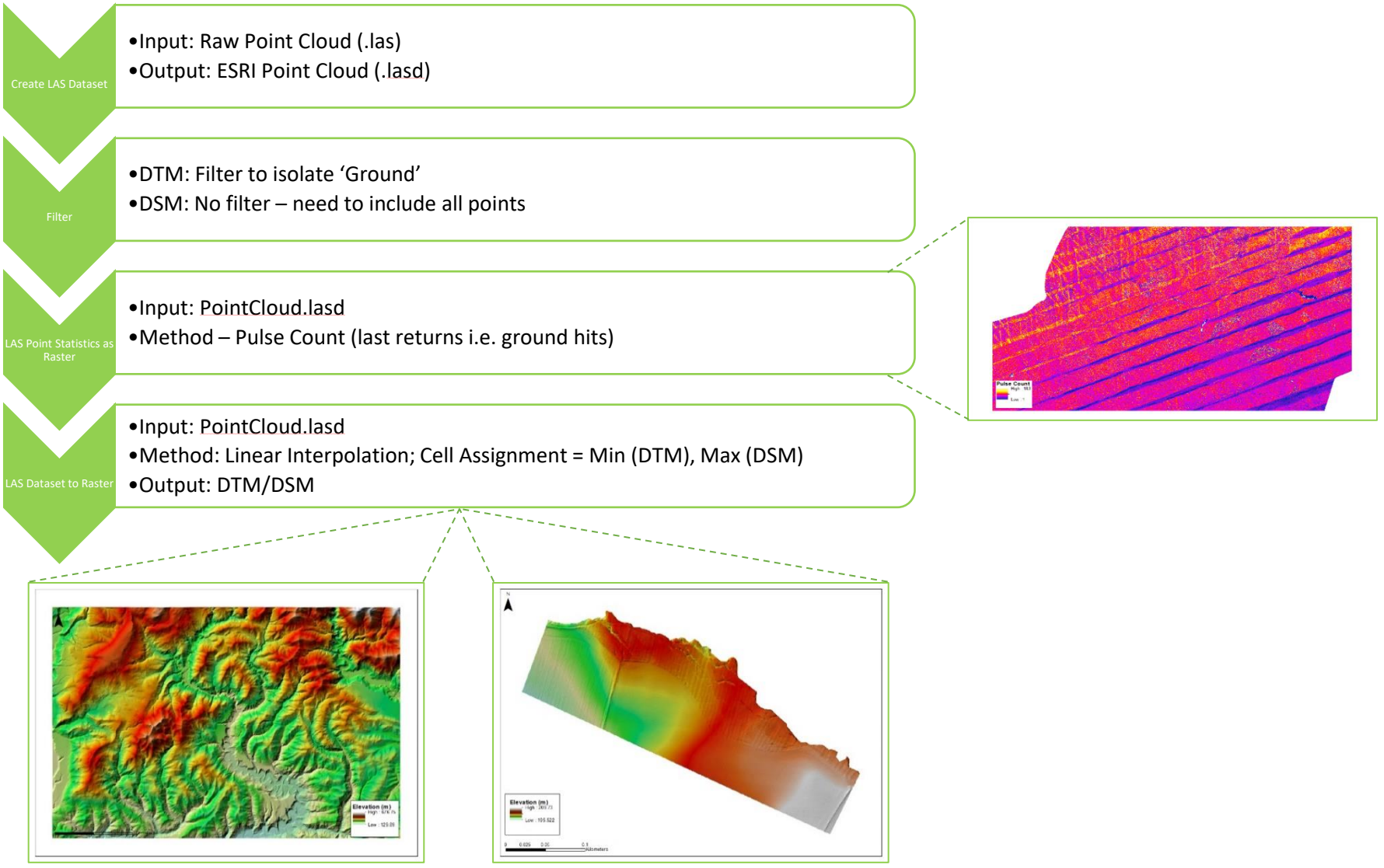

***Fig. 5.01**: Flow diagram outlining the processing of raw point cloud data into an ESRI compatible DTM's for New Zealand (left) and North Yorkshire (right).*

Thresholding should be straightforward in this case, with values < 0 representing the presence of a ground crack or other locally steep features.

Standard deviation of elevation values (SD) can be used as a measure of surface roughness and to detect deformation features such as cracks and scarps (Ventura *et al.* 2011). Fractured surfaces have greater levels of surface roughness than smoother surfaces (Glenn *et al.*, 2006) and would be represented by higher SD values. Like DFME, SD values were obtained using Focal Statistics. 1 m and 3 m circular windows were chosen for North Yorkshire and New Zealand respectively based both the size of the features and resolution of the LiDAR datasets.

Local convexities and concavities can be summarised by curvature values (e.g. McKean & Roering, 2003). In previous studies, extremes have been used to represent ridges, scarps, slope shoulders (Robinson *et al.*, 2018) and gullies (Baruch & Filin, 2011). In this case, LiDAR resolution allowed abnormal convexity/concavity values to potentially highlight ground crack scraps/tips respectively. Profile (slope parallel), planform (slope perpendicular) and standard curvature (combination of profile/planform) values were all processed from the DTM.

Solar insolation modelling determines how much solar insolation is received by a single DTM cell (e.g. Challis *et al.*, 2011). In theory, most cracks (particularly internal walls and the tips) should receive considerably less solar insolation than the surrounding open hillslope due to the heavy shadowing created by the feature. To represent this, Sky-View Factor (SVF) (Zaksek *et al.*, 2011), a tool based on the inverse of occlusion, was used. Sky-View factor calculates the amount of sky visible from each cell location.

5.2. NORTH YORKSHIRE

Individual topographic derivatives, as described above, were processed and visually analysed to determine the (range of) values which were indicative of the topographic signatures of the ground cracks. This was possible to do qualitatively due to the resolution of the data, and the knowledge that a number of well-defined cracks were present at this location. This, along with the study area extent and the fact that there are only ~11 ground cracks present meant that the creation of an inventory was not necessary.

Upon inspection, it was discovered that crack tips had noticeably different topographic signatures to crack walls (***Figs. 5.02a-b***). Therefore, detection was attempted on these independently first, before adding them together to produce a final attempt. There was an issue with layers created using the original 0.1 m resolution of the data

(Slope/Curvature layers) as they contained far too much noise. To combat this, the DTM was smoothed to a resolution of 1 m using a mean filter in. Layers were re-created to provide a more useful product to work with (***Figs. 5.03a-b***) due to reduced noise levels and therefore potential for false detection. Because of the original resolution of the data, the 1 m smoothed layer still had a higher resolution than the New Zealand dataset.

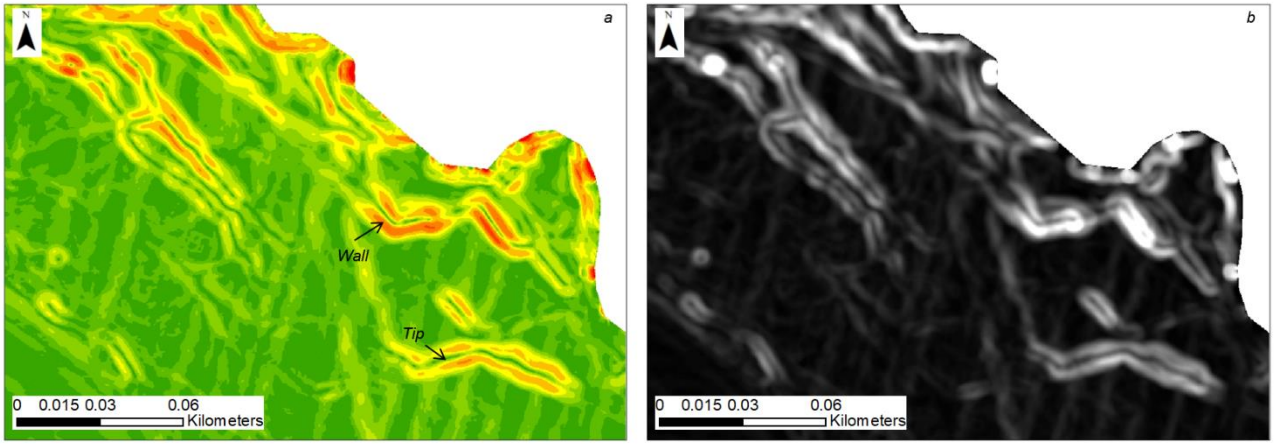

Figs. 5.03a-b*: Slope (**a**) and roughness (**b**) layers from North Yorkshire, highlighting the difference between the geomorphic signatures expressed by crack walls and crack tips. In Fig. 5.02a, crack walls show steeper slopes (yellow/red) whereas crack tips exhibit more shallow surfaces (green). In Fig. 5.02b, crack walls are 'rougher' (grey/white) than crack tips (black) likely due to a rockier surface as the earth has 'opened up'. When envisaging the shape of a crack, steep, rough sides and a smooth, shallow tip conforms to this.*

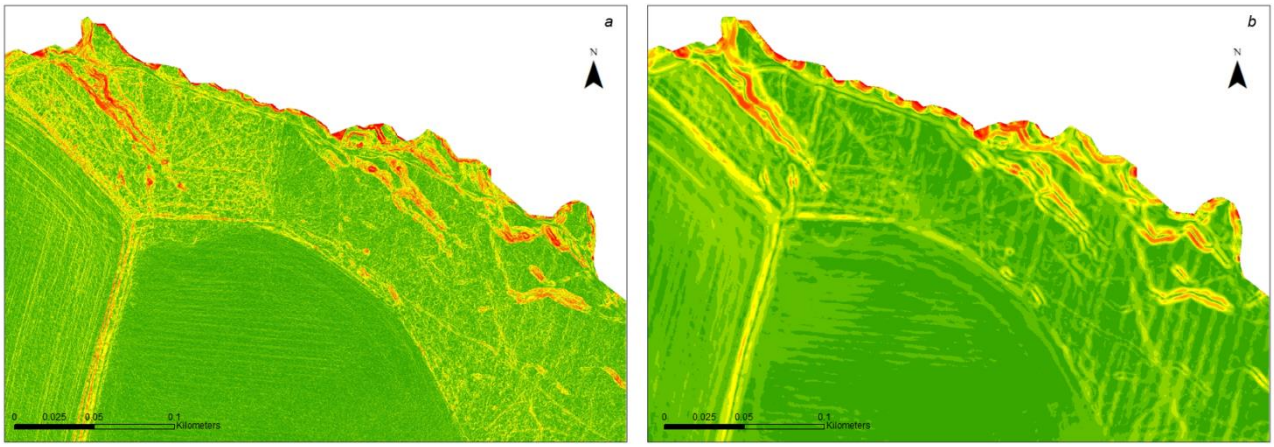

Figs. 5.02*: Difference between spatial resolutions of 0.1 m (**a**) and 1 m (**b**), exhibited by the greater amount of noise (i.e. noticeable intermixing between green and yellow pixels) in **Fig. 5.03a**. **Fig. 5.03b** has been smoothened over and exhibits a much smoother surface. The 0.1 m data may be more accurate, however the amount of noise that comes with this extreme precision is detrimental to using it on the small scale. The 1 m data has been created by smoothing the 0.1 m dataset, meaning that although smoothened to 1 m, it is more accurate than the 1 m DTM that has been curated from raw point cloud data for New Zealand.*

Different layer combinations (explained below) specific to the detection of walls and tips respectively were calculated to produce a series of binary rasters, whereby the presence of a wall/tip, or not, was signified using a value of either 1 (presence) or 0 (absence) respectively. This was to find the layer combination that most accurately portrayed the presence of the walls/apexes which was decided qualitatively. The most

accurate tip and wall detection attempts were summed together to produce a final ground crack raster.

Evans and Lindsay (2010) found the use of DFME and planform curvature particularly useful when attempting to detect gullies, particularly the base. Therefore, the same approach was used as a starting point to detect crack tips and was relatively successful. A threshold of –0.5 was used for DFME. Adding in the slope and SD layers respectively decreased the success of the detection. Although qualitatively both exhibited topographic signatures of the tip, upon closer inspection there were several anomalies (***Fig. 5.04***). SVF strengthened the detection by marginally reducing noise, particularly on the clifftop edge (***Figs. 5.05a-b***). Standard curvature and planform curvature were discarded as they offered no improvement to the model performance. A combination of DFME, planform curvature and SVF most accurately detected ground crack tips according to qualitative comparison with cracks that were visible in the original DTM. This was appropriate due to the high resolution and discernible morphological signature of cracks in the data.

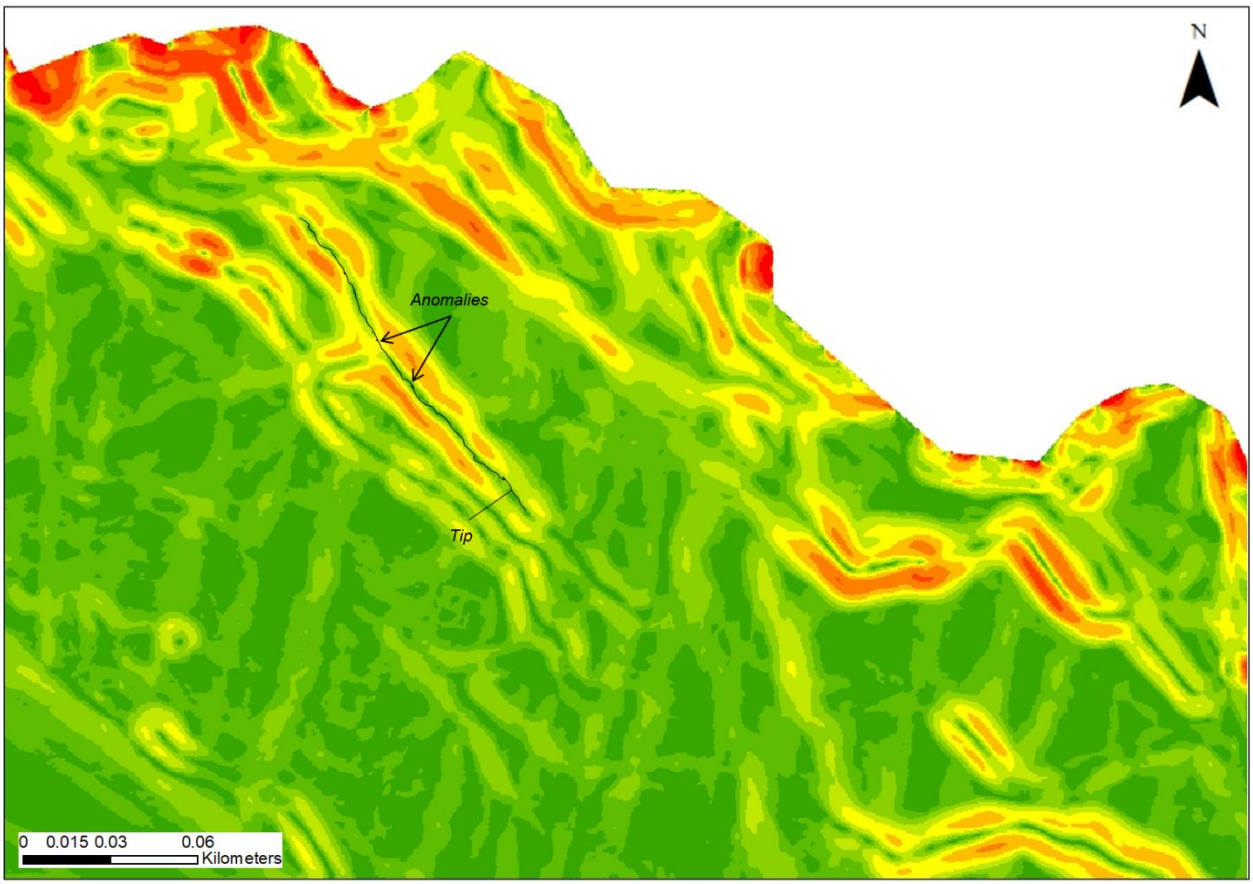

Fig. 5.04*: Measurement anomalies in crack tips, North Yorkshire, UK. Notice how parts of the same tip (as shown by the arrows) exhibit different slope angle signatures – yellow (top) and green (bottom) respectively.*

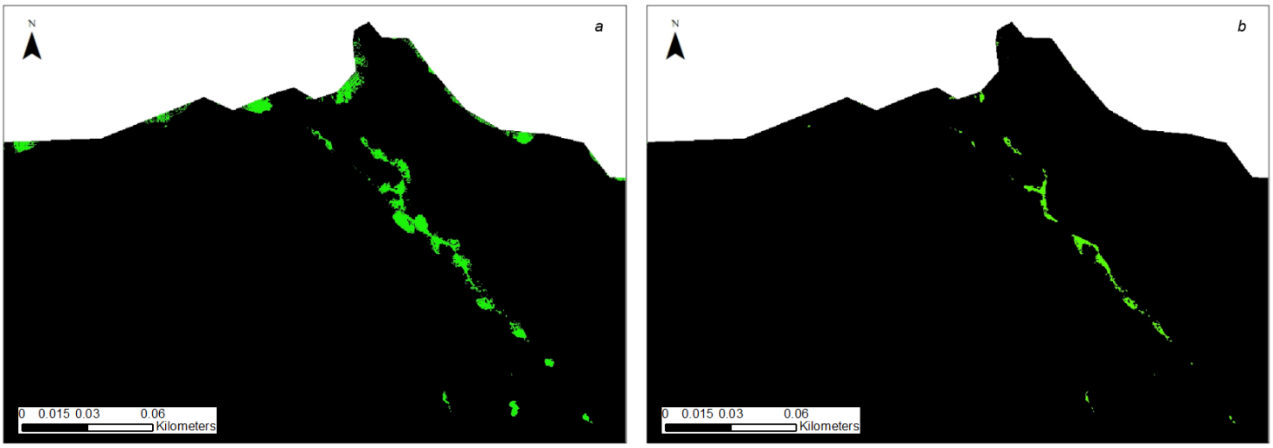

***Fig. 5.05a-b**: Detection attempts before (**a**) and after (**b**) the application of SkyView Factor (Kokalj et al., 2011). Notice the reduction in false detections in b compared to a, particularly the green around the cliff edge.*

Cracks naturally showed an increased slope angle in relation to the surroundings, and SD was useful in filtering out smoother, particularly anthropogenic features (likely fences/hedges) in ***Fig. 5.06a***. A combination of DFME, slope angle and SD most accurately detected ground crack walls when again qualitatively comparing the output to crack walls that were visible in the original DTM.

Tip and wall binary rasters were summed and reclassified to produce a final binary raster output (***Fig. 5.07***).

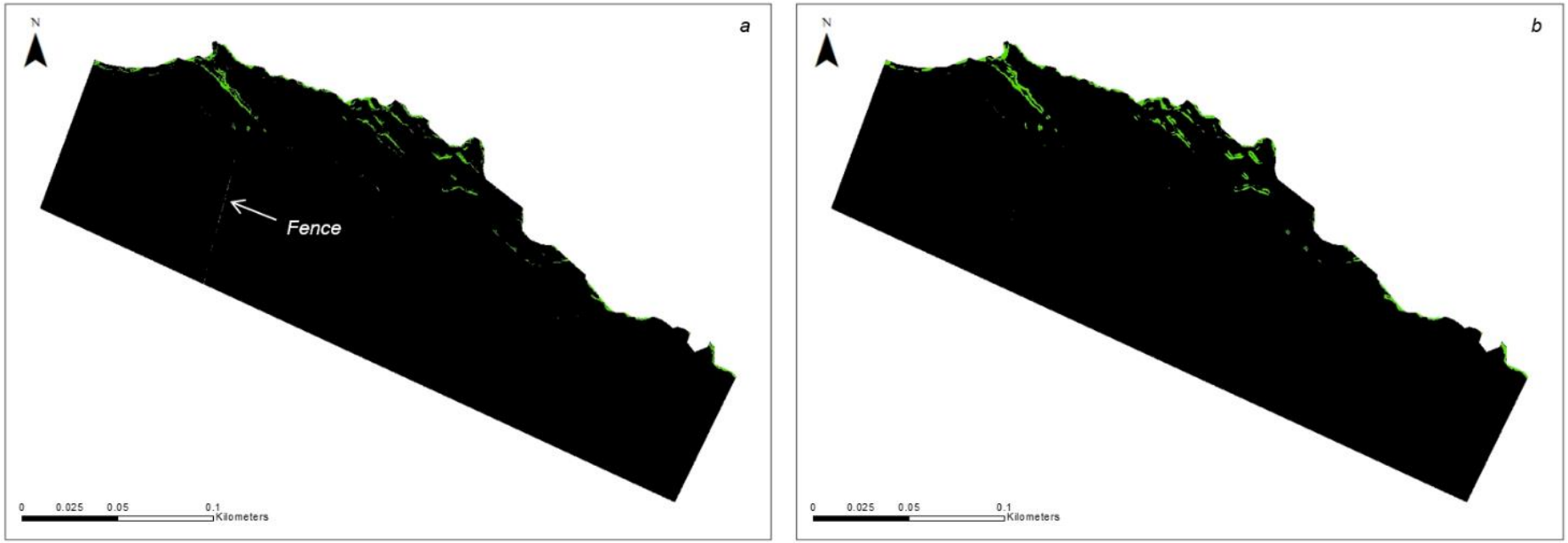

***Figs. 5.06a-b**: Detection attempts before (a) and after (b) the application of roughness. Notice the omission of fences/hedges and other anthropogenic factors, which have smoother surfaces and therefore smaller roughness indices than ground cracks.*

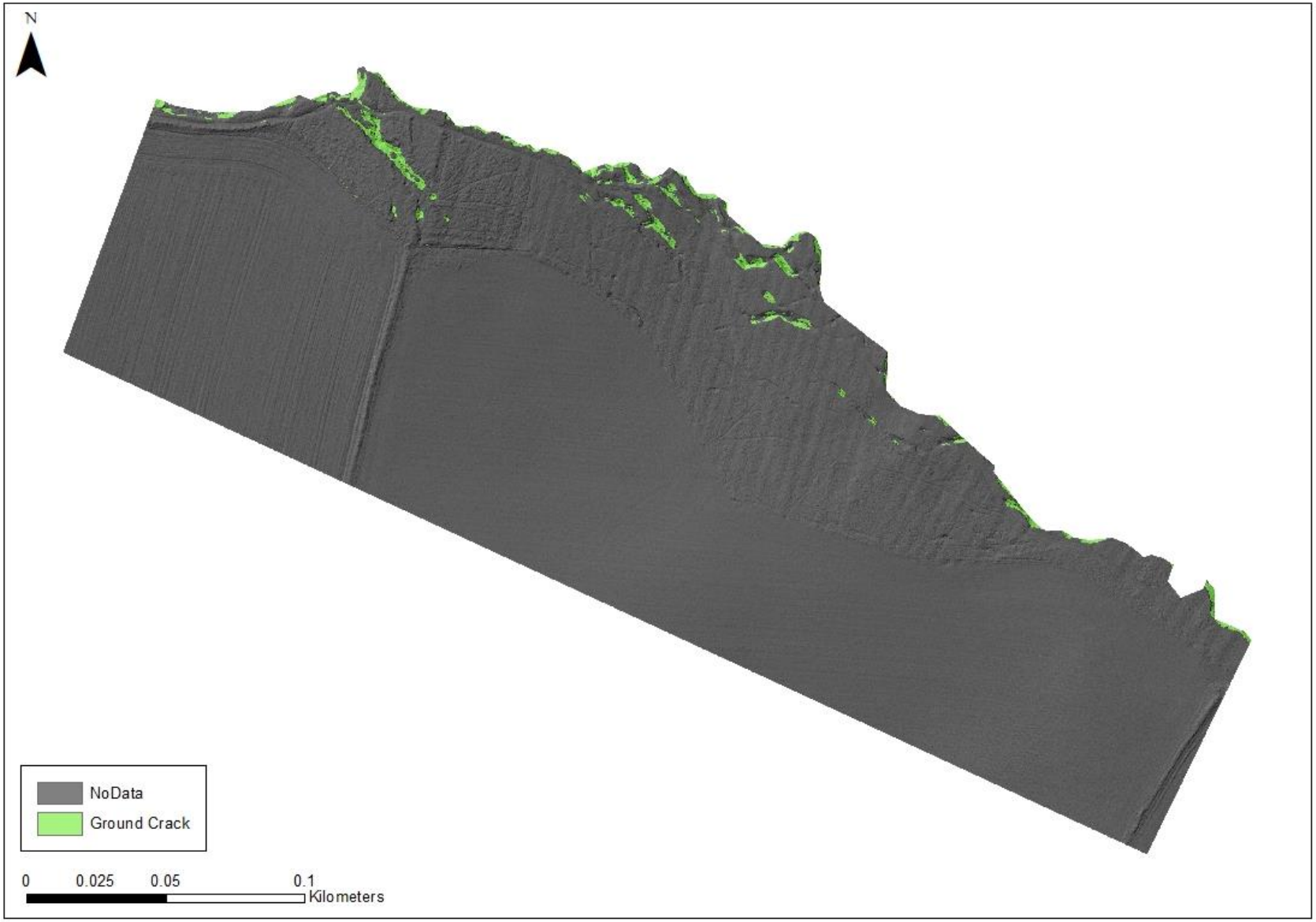

***Fig. 5.07**: Hillshade (0.1 m) overlaid by the final detection attempt using DFME, planform curvature, slope angle and roughness parameters. As can be seen qualitatively, there is a good match between 'ground crack detections' (green) and depressions in the hillshade.*

5.3. NEW ZEALAND

The findings from the North Yorkshire dataset were applied to the study area in New Zealand. Upon further inspection and unlike the North Yorkshire dataset, the resolution of the DTM was not sufficient to display the different topographic signatures shown by ground crack walls and tips, and upon qualitative inspection, signatures did not seem to favour either form of detection (***Figs. 5.08a-b***). Therefore, signatures shown by both ground crack walls and tips in North Yorkshire were carried forward and used independently once more, to see if one performed better than the other and to see if they could combine to produce a satisfactory classification. Standard curvature (combination of Profile and Plan) was used in place of planform curvature as it highlighted ground cracks with more consistent values. Planform curvature values showed a signature but fluctuated between maximum and minimum on a cell-by-cell basis within the ground cracks. This along with profile curvature were therefore discarded as too noisy. Layer values were optimized based on qualitative inspection in order to improve model performance in a different environment.

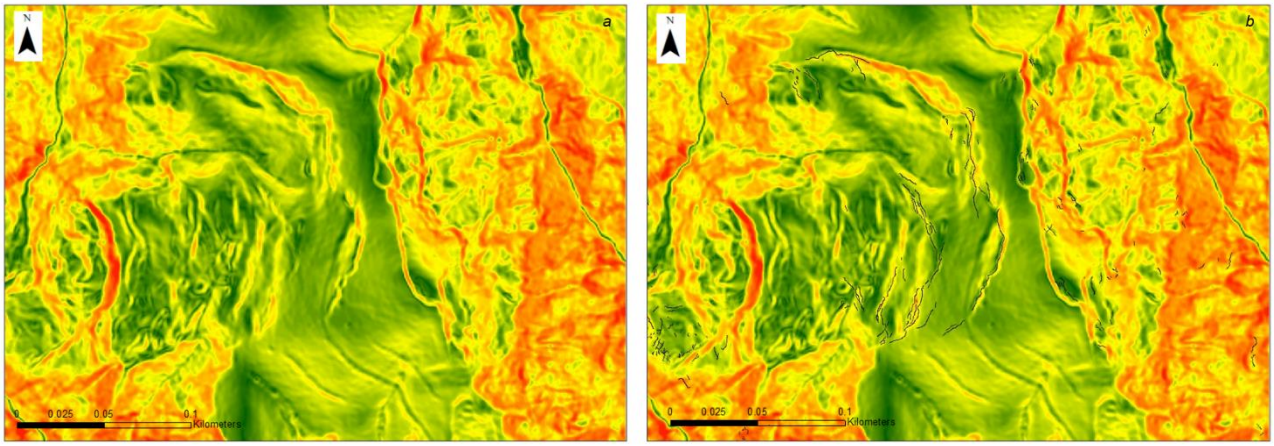

Fig. 5.08a-b*:* Unlike the North Yorkshire dataset, the New Zealand dataset is not precise enough to be able to distinguish between ground crack apexes and walls. ***a***) This is the slope layer applied to the New Zealand dataset, where ground cracks only show one signature as opposed to two in the North Yorkshire dataset for crack walls and tips respectively. ***b***) Same as ***Fig. 5.08a***, but with the addition of ground crack polygons for context.

Similar to the processing of the North Yorkshire dataset, a number of layer combinations for each respective part of the feature were calculated to produce a series of binary rasters. Qualitative accuracy assessment was carried out through comparison against a binary raster created from the ground crack inventory. As can be seen from Figs. 5.09a and 5.09b, a number of detections are located in valley bottoms. On a regional scale this is perhaps unsurprising as ultimately similar topographic signatures will be exhibited by small-scale ground crack features and large-scale valley bottoms, their scale being the only difference. This suggests that the method of detection may not be flawed, as

ultimately topographic lows/depressions have been detected, just not on the local scale of co-seismic ground cracks. This could indicate that the resolution of the data is too coarse for automatic feature detection at this scale. To prevent this from skewing results, valley bottoms with a buffer of 5 m are masked out of all classification outputs, as these areas were also unlikely to be the location of slope-related ground cracking.

Upon initial observation, levels of successful detection appear to be poor. However, upon closer inspection of areas of dense ground cracking, classification using crack wall signatures was considerably more successful than tip signatures (***Figs. 5.09a-b***). Detection by wall signatures appears to have detected some of the ground truth inventory, however it has done so by extreme over-classification. Classification using tip signatures has done the opposite, through misclassification by under-classification. Results were extremely poor, such that the addition of tip signatures to wall signatures made little difference to the overall classification result (***Fig. 5,09c***). Although a semi-promising initial attempt, results were ultimately too unsatisfactory to be of any use, due to severe over-classification. Statistical analysis will hopefully refine these results and offer further filtering suggestions.

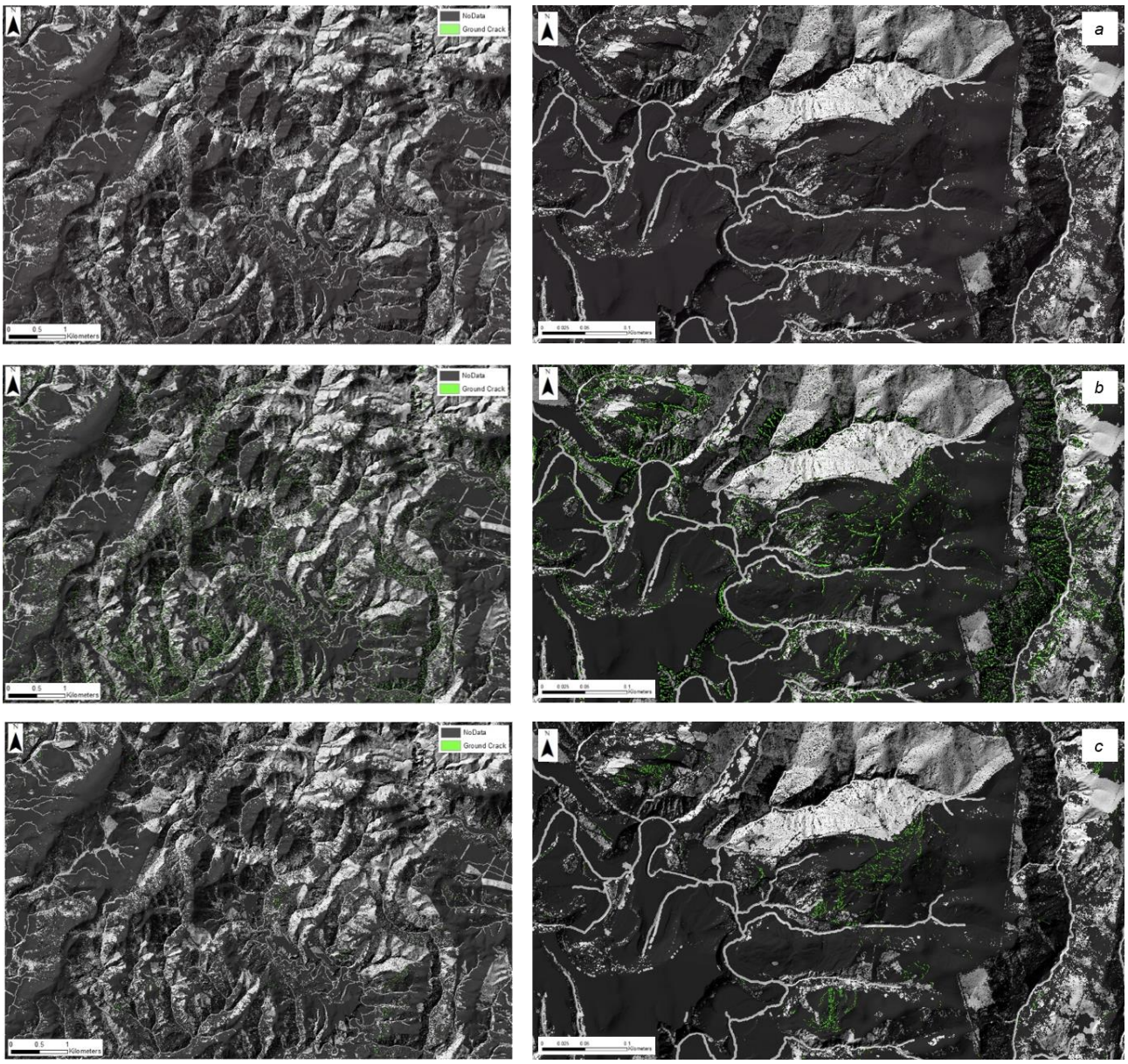

Figs. 5.09a-c*: Detection attempts using apex signatures (**a**), wall signatures (**b**) and a combination of the two (**c**). Notice the under- and over-prediction in the close-up images of **Figs. 5.09a** and **5.09b** respectively.*

5.4. SUMMARY

This chapter has outlined an initial qualitatively driven attempt at automatically extracting small-scale ground crack features, using high-resolution LiDAR data from North Yorkshire to inform the attempt on the LiDAR data from New Zealand. Key points from *Ch. 5* are:

- Methods were informed by literature from similar previous studies such as gulley and small-scale archaeological feature detection.
- DTM's were created, enabling topographic derivatives to be calculated. These showed qualitative differences in the signatures shown by crack tips and walls in the North Yorkshire dataset.
- Different layer combinations were used to extract walls and tips respectively, which were combined to extract whole ground cracks. This was relatively successful for North Yorkshire.
- When applied to NZ, results were poor with low and high levels of detection and misclassification for tips and walls respectively (qualitatively). Crack wall detection performed better but was still poor.
- The impact of resolution on the success of feature detection appears to be considerable.
- It is necessary to find another way to attempt to extract ground crack features for ensuing analysis. A more manual approach will be required, and this will be explored in the following chapters.

6. GEOMORPHOLOGICAL CHARACTERISTICS – FEATURE STATISTICS

Before undertaking detailed statistical analysis, it is useful to explore and outline the intrinsic form of geomorphological features (e.g. Xu *et al.*, 2015). Factors such as frequency, area, volume (e.g. Marc *et al.*, 2016), location (e.g. Dai *et al.*, 2011) and shape/form can provide useful insight into how features can pose a hazard (Roback *et al.*, 2018).

Most recent coseismic landslide studies have tended to focus on automatic feature detection for the wider purpose of hazard prediction/mitigation, however many still provide a basic overview of features in an inventory and how these are distributed spatially across the landscape (e.g. Martha *et al.*, 2017). In this instance, automatic feature detection has proved unsuccessful at extracting/analysing ground crack features, and therefore a more manual approach must be taken to investigate these. As a comprehensive landslide classification system already exists (Varnes, 1978; updated by Hungr *et al.*, 2014), it can be relatively straightforward to classify landslides in an inventory based on specified criteria (including shape and form). This is not the case for coseismic ground cracking as no such classification system exists as of yet, which provides even more of an impetus to investigate the form and spatial distribution of these features with a view to providing suggestions to potentially inform a preliminary classification system.

6.1. METHODOLOGIES

The following section will outline the methodologies used to summarise all features in the ground crack inventory. This includes the use of probability densities to investigate the relationship between crack length and frequency; and the analysis of shape, form and position to investigate any feature characteristics, which can potentially indicate whether or not coseismic ground cracking is random or is to some degree predictable in form and location.

6.1.1. Probability Density

Probability density can be used to portray the relationship between frequency and another hazard-specific variable, for example magnitude (e.g. Harp & Jibson, 1995) or area (e.g. Roback *et al.*, 2018) (***Fig 6.01***). Further relationships can be established from this, as is the case with landslide area and volume (Larsen *et al.*, 2010), which can consequently be used to derive an indication of volume-frequency. Probability density graphs typically include a rollover and a power-law scaling relationship (e.g. Hovius *et al.*, 1997) (***Fig. 6.01***). The rollover is suggested to be due to the under-sampling of features which are below the resolution of the data source (Stark & Hovius, 2001), or may reflect a lower than expected frequency of features at a particular scale in reality (Tanyas *et al.*, 2018). Power-law scaling relationships can be useful for purposes of comparison between feature frequency and extent when triggered by different events (Xu *et al.*, 2015). Xu *et al.* (2015) and Roback *et al.* (2018) use their power-law values to compare the extent of landsliding from the Gorkha and Lushan earthquakes respectively to past events. Probability densities from different events can also be combined to explore wider scaling relationships. Malamud *et al.* (2004) undertook this for earthquake magnitude and coseismic landslide frequency. More generic scaling relationships such as these can be harnessed to predict the number and extent of features following an event of a given magnitude as they are less influenced by location-specific factors.

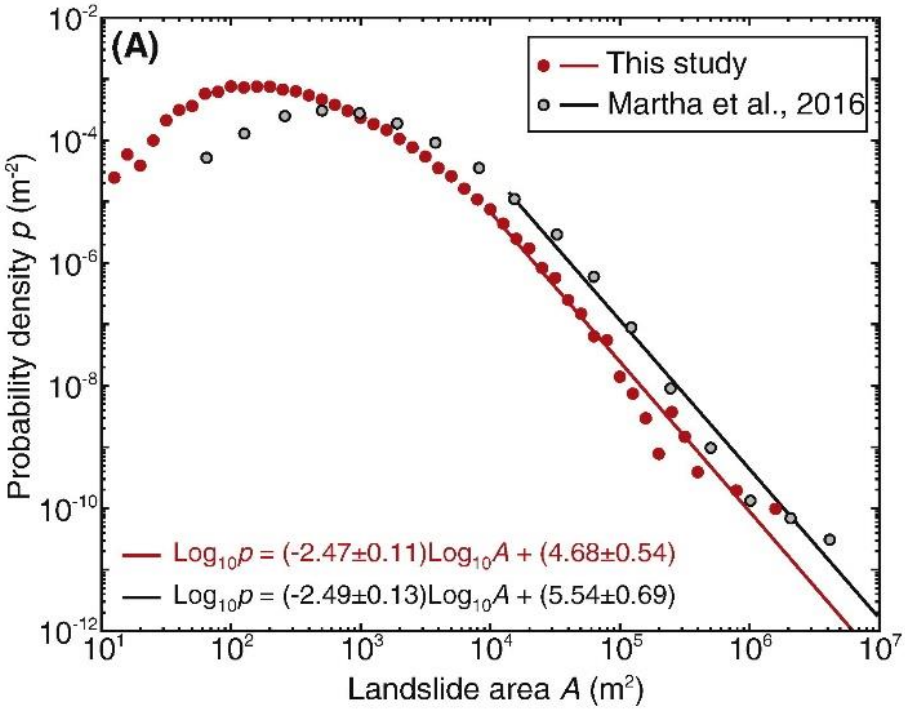

Fig. 6.01*: Frequency-area relationships for coseismic landslides from Roback et al. (2018) (red) and Martha et al. (2017) (grey). This is to prove that shape can be used to establish probability density relationships with features. Full credit to Roback et al. (2018) – reference in bibliography.*

In the case of this study, area cannot be used. Length will therefore be used instead. The novelty of this research also means that any resulting probability density cannot be directly compared as is frequently the case with coseismic landslide studies. However, it will be interesting to see if coseismic ground cracking exhibits similar rollover/power-law scaling properties to those shown by landslides. The length of each feature was calculated in and extracted from ArcGIS Pro (v. 2.3.3) and plotted in Stata (v. 15) using Kernel Density Estimate (KDE) on a logarithmic scale for the purposes of clearer visualisation. A power-law was then statistically fitted to the curve using SigmaPlot's (v. 14) Regression Wizard, which performs a number of iterations on the curve to find the most suitably fitting function.

6.1.2. Shape, Form and Position

Landslides tend to have distinct forms and characteristics, enabling them to be classified based on pre-existing criteria (Varnes, 1978; updated by Hungr *et al.*, 2014). However, all landslides possess the coherent trait of propagating in a downslope direction with a source area that is always above the toe, due to the influence of shear stress and gravity (Selby, 2005). Due to a lack of research, it is unclear whether or not ground cracks display any such similarities – something which investigating shape, form and position will hopefully identity. If they do, this has the potential to form the basis of suggestions towards the classification of ground cracks into distinct categories based on these. As such, the profile (long- and cross slope-), plan, orientation and hillslope position of ground cracks have been investigated and summarised. ***Fig. 6.02*** provides a visual aid.

6.1.2.1. *Long Profile*

Long profile can indicate the position of ground cracks (topographically) in the landscape, as well as their shape/form on a hillslope. Points were generated along the ground cracks at 1 m intervals and elevation values were extracted. These were imported into Stata, where raw elevation values were plotted to indicate the topographic distribution of the ground cracks. The KDE of this distribution was then plotted, alongside that of ridgetops, landslide crown and landslide toe elevations to see if ground crack distribution could be explained by any of these features. Start elevations were then normalised to a constant source elevation (labelled 0 m) and replotted to counteract topographic smoothing and enhance the shape of the ground cracks. This could also be manipulated to provide further information on their position on a hillslope (***Fig. 6.03***). Point density for both plots was then

calculated by smoothing over the graphs using KDE, to create a contour plot providing a more definitive indication to the most common elevation and shape of ground cracks, to counteract any clustering caused by line density. The above was then repeated with the same dataset which had outliers excluded using a threshold of > three standard deviations in width. This was done for visualisation purposes. ***Fig. 6.04*** provides a more detailed workflow.

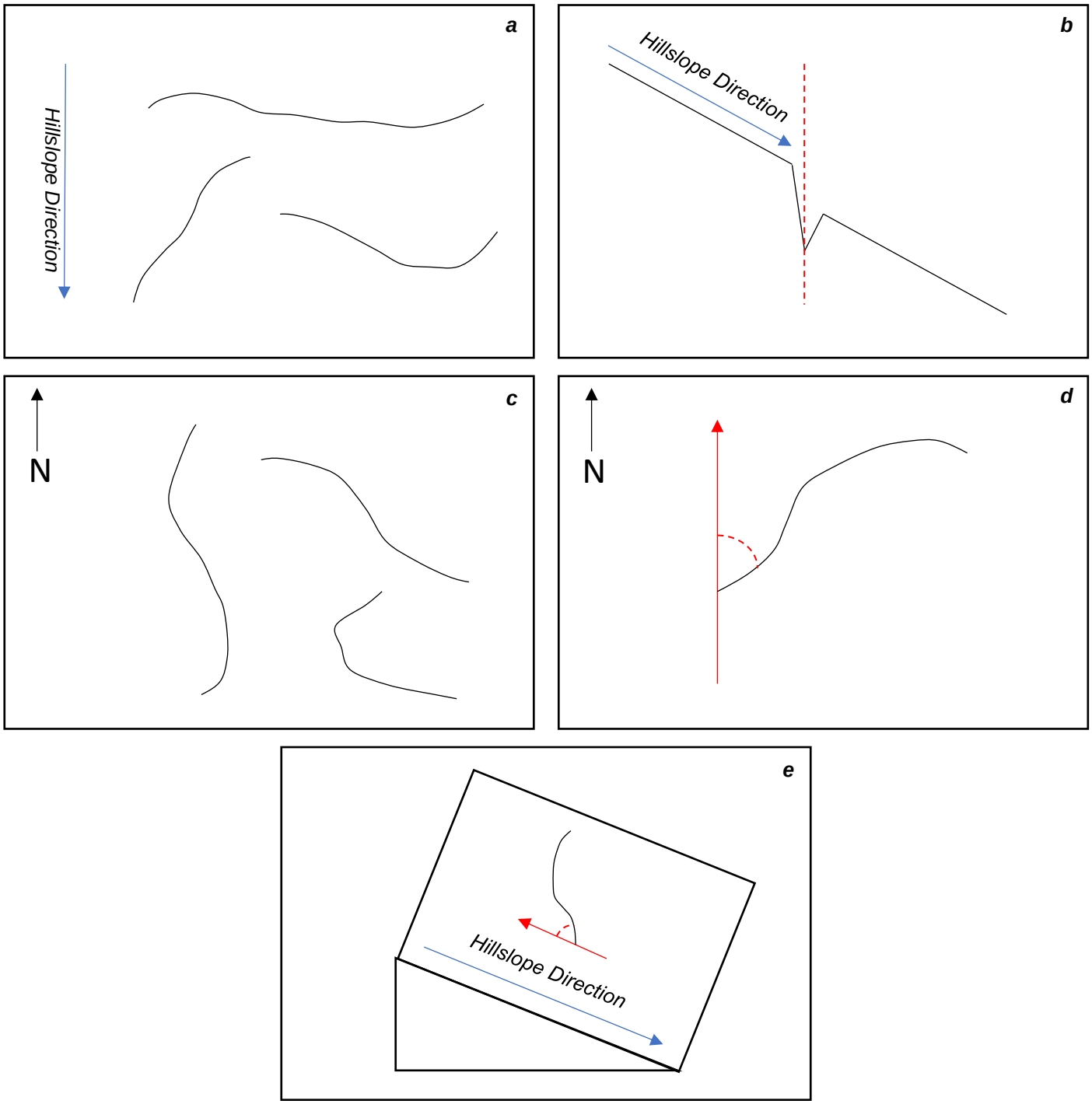

Figs. 6.02a-e*: Visual aide depicting the different measurements of, and geomorphic signatures that may be shown by, ground cracks under investigation in this study. Hillslope Direction and North Arrows are included for clarity.* ***a****) Long Profile: The view of a ground crack if looking at it on a hillslope face-on;* ***b****) Cross Profile: The view of a ground crack if looking at it side-on 'through' a hillslope;* ***c****) Plan (Sinuosity): The view of a ground crack if looking at it from above;* ***d****) Orientation: The true bearing of a ground crack in raw space, relative to north;* ***e****) Position on Hillslope: The position (orientation) of a ground crack on a hillslope.*

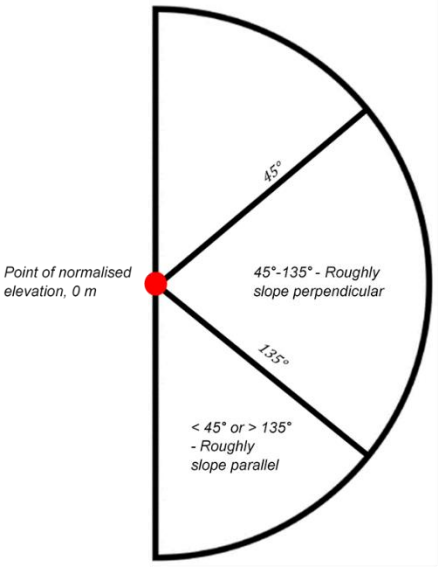

***Fig. 6.03**: Basic diagram to illustrate how long profile shape can be used to indicate the position of ground cracks on a hillslope, through their direction of manifestation from a normalised elevation.*

6.1.2.2. Cross Slope Profile

Cross Slope Profile was investigated to assess the extension mechanism of ground cracks, and whether or not there were any consistencies between this and the position of ground cracks in the landscape. ***Figs. 6.05a-b*** show hypothetically how cracks positioned on a hillslope may show more of a 'step', whereas those situated on flatter ground may show more of a clean 'constructive-like' extension. 20 m transects were drawn perpendicular to ground cracks at 1 m intervals. Elevation values were then extracted at 1 m intervals along these transects. The following workflow (***Fig. 6.06***) outlines how this was achieved

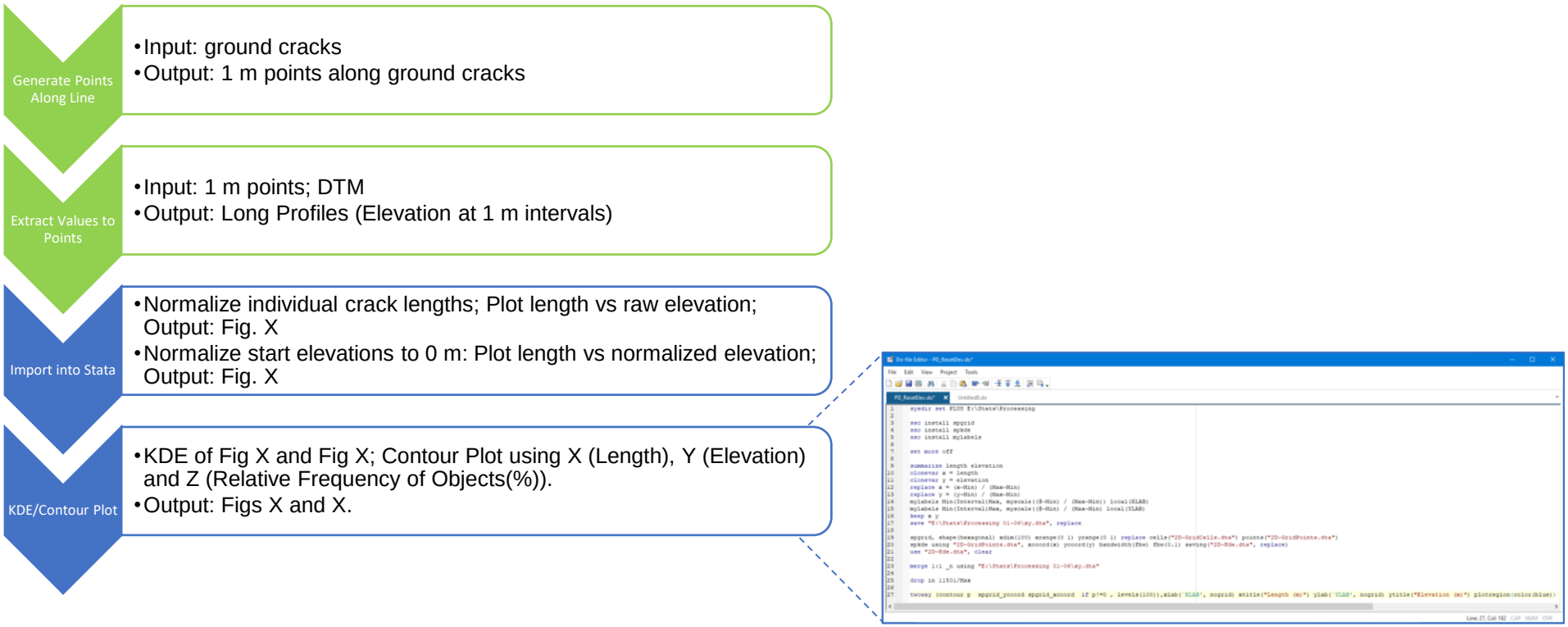

***Fig. 6.04**: Flow diagram illustrating the step-by-step calculation of Long Profile, involving processing in ArcGIS (green) and Stata (blue). The Stata 'Do' file used for the creation of contour plots has been included.*

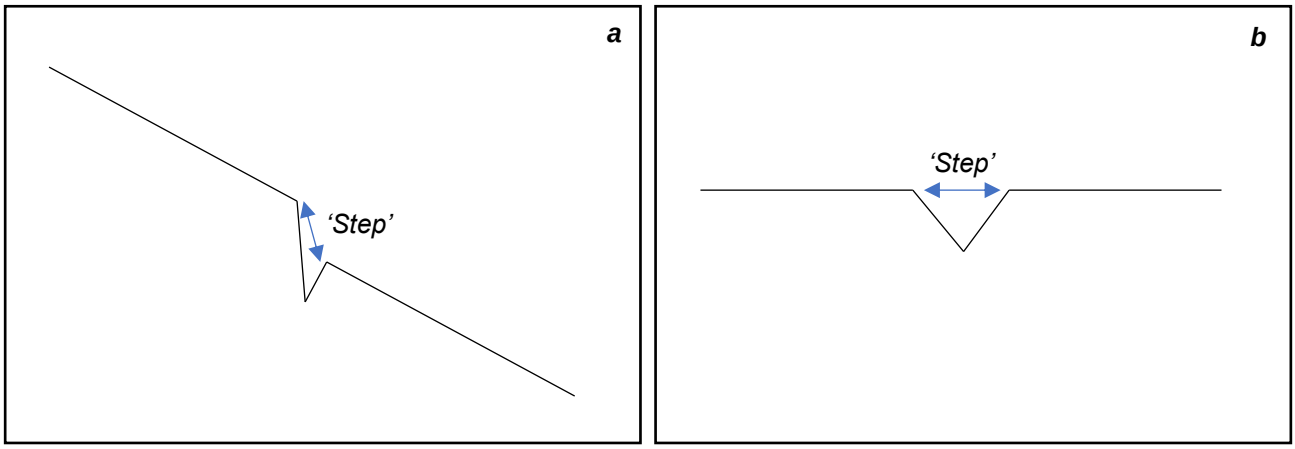

***Figs. 6.05a-b**: Diagram depicting how the extension mechanism of ground cracks may differ depending on whether they occur on: a) A hillslope, where steeper gradients may result in more of a 'step-like' extension mechanism, or b) Flat ground, where the gradient may lead to a 'cleaner' extension.*

ArcGIS. Once the data was imported into Stata, all elevation values along a single transect on one side of a ground crack were linearly regressed. This was then repeated for all points along the transect on the other side of the ground crack. Constants from these regressions were then differenced to ascertain whether or not a 'step' existed along the transect. This was repeated for every transect using a 'Do' file (***Fig. 6.06***) and summarised for every ground crack. ***Fig. 6.07*** explains the concept in graphical form. Resulting 'step' values were then plotted against mean slope angles for each ground crack, which indicate whether or not a ground crack is situated on a hillslope (steep slope angle) or flat ground (low slope angle). Step values were also plotted against distance to nearest landslide crown.

6.1.2.3. *Orientation and Position on Hillslope*

The orientation/bearing of ground cracks in raw space is calculated to investigate any directional similarities or influences (e.g. the direction of shaking) on the propagation of cracking, and to determine the position of cracks on hillslopes. Calculations are grounded in trigonometry and the detailed workflow can be found in ***Fig. 6.08***. Using the 1 m points previously generated, cracks were densified, and the bearing of each 1 m segment was calculated using the cosine of the dimensions ascertained from the segment length and start/end coordinates (***Fig. 6.08: Inset a***). Based on the direction of calculation, angles were either added to or subtracted from 90° to provide raw bearings on a scale of 0-180°. This prevented ground cracks from having two different bearings for a single orientation, which was plausible (***Fig. 6.09***).

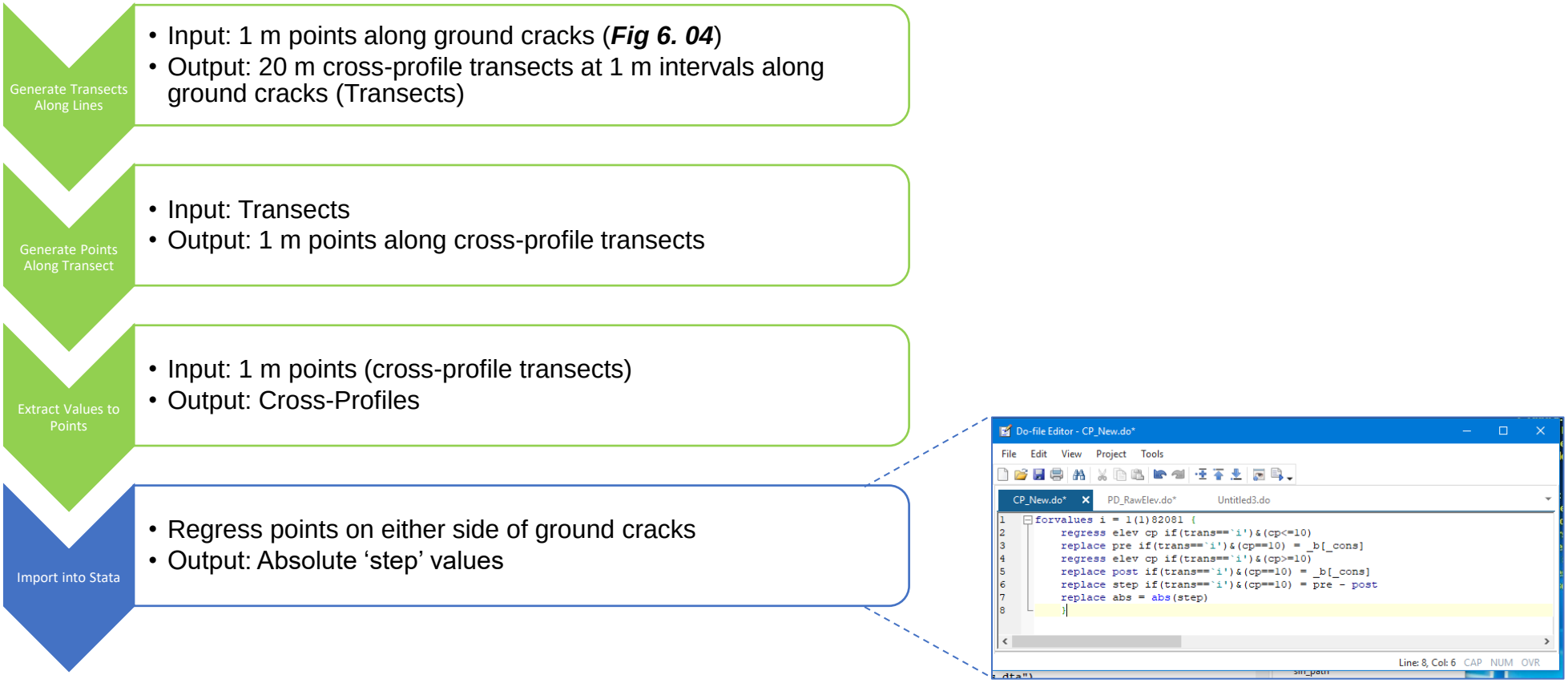

***Fig. 6.06**: Flow diagram showing the step-by-step workflow for the calculation of Cross profile. ArcGIS (green) and Stata (blue) processing were used to calculate individual cross profiles. The Stata 'Do' file has been included for extra clarity.*

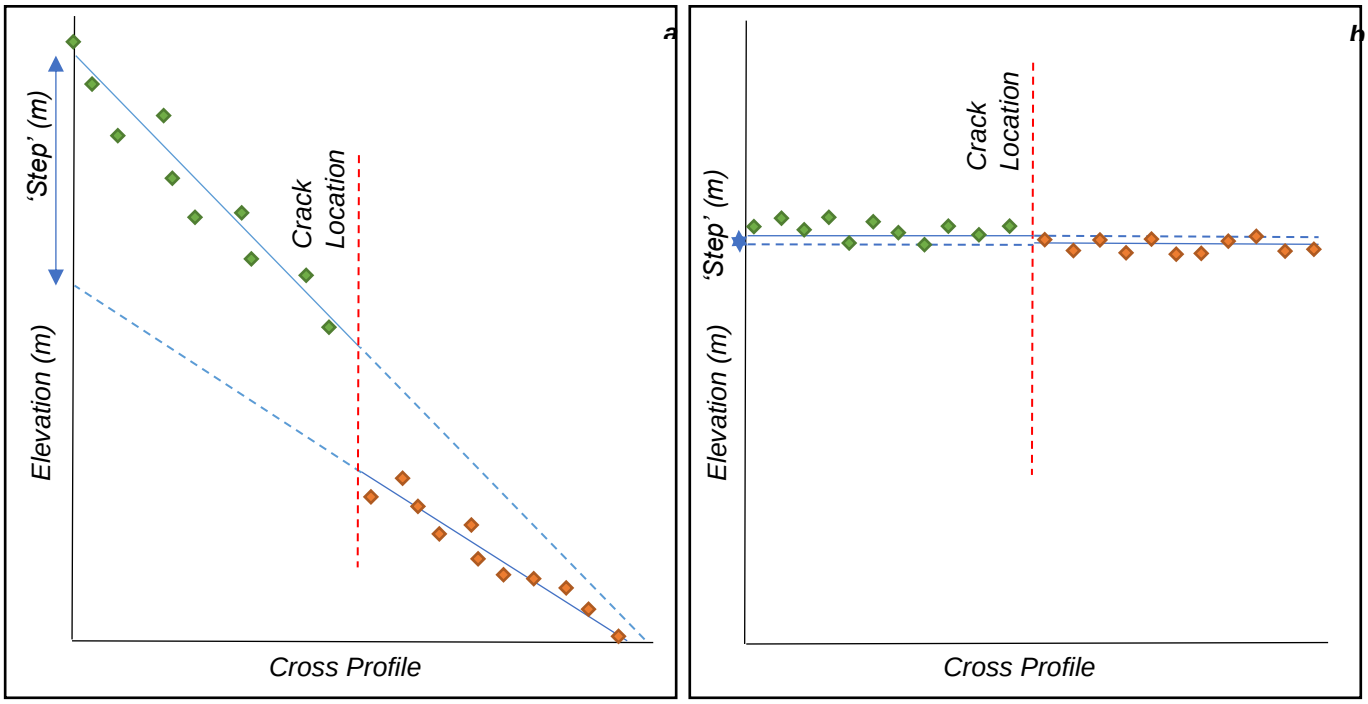

***Fig. 6.07a-b**: Graphical depiction of the concept of differing extension mechanisms according to hillslope gradient. **a**) 'Step-like' extension mechanism; **b**) Clean Extension.*

The position of ground cracks on their respective hillslopes was calculated using their raw bearing and the local slope aspect. This is based on a method presented in Robinson *et al.* (2017) to explore Euclidean Aspect – the relationship between local slope aspect and euclidean direction to seismic shaking, which in this case is replaced by the direction of ground cracks. Local slope aspect was calculated from the DTM. Beforehand, this was smoothed by a 50 m window to exclude any noise. The 50 m window size was qualitatively selected as it provided the most coherent hillslope-scale aspect whilst avoiding any detrimental reduction in detail (***Fig. 6.10***). Local slope aspect values were extracted for each 1 m segment and respective raw ground crack orientations were subtracted. Resulting values were then normalised to a 0-180° scale using the following formula (Robinson *et al.*, 2017):

$$Ph = \begin{cases} |(|Rb - As|) - 360|, & |Rb - As| > 180 \\ |Rb - As|, & |Rb - As| \leq 180 \end{cases} \quad [2]$$

As such, a value of 0/180° would indicate a slope perpendicular crack and a value of 90° would label a crack as slope parallel (***Fig. 6.08: Inset b***).

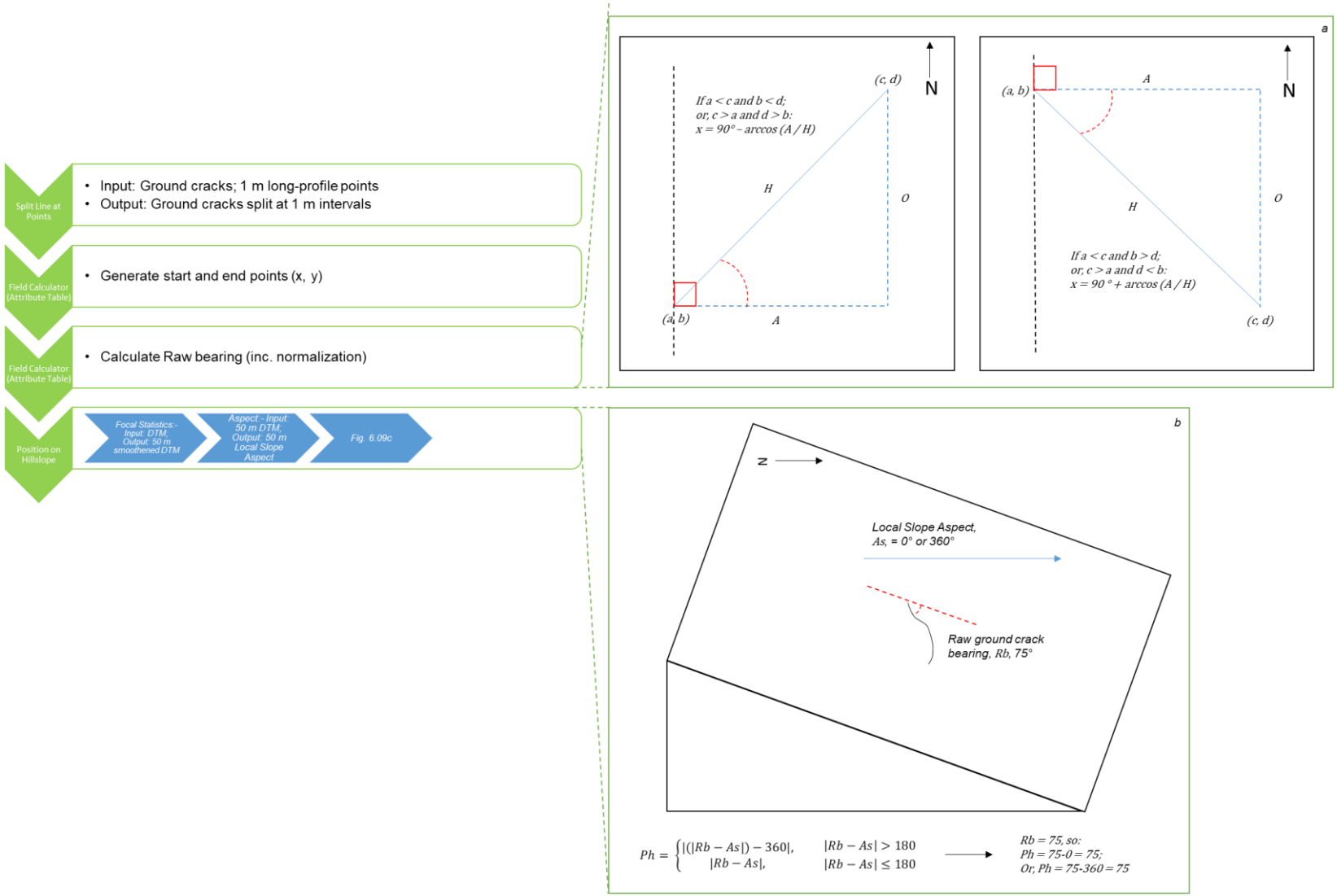

***Fig. 6.08**: Flow diagram to illustrate the calculation of raw ground crack bearings (**Inset a**) and their position on the hillslope (**Inset b**). Inset a shows mathematically how the relationship between the start and end coordinates is used to determine whether the inverse cosine of the raw bearing is either added to or subtracted from 90deg in order to normalise it on a 0-180° scale. Inset b shows how raw bearing is then used alongside local slope aspect to calculate the position of a ground crack on a hillslope. The equation used is included, along with a worked example. Equation adapted from Robinson et al. (2017).*

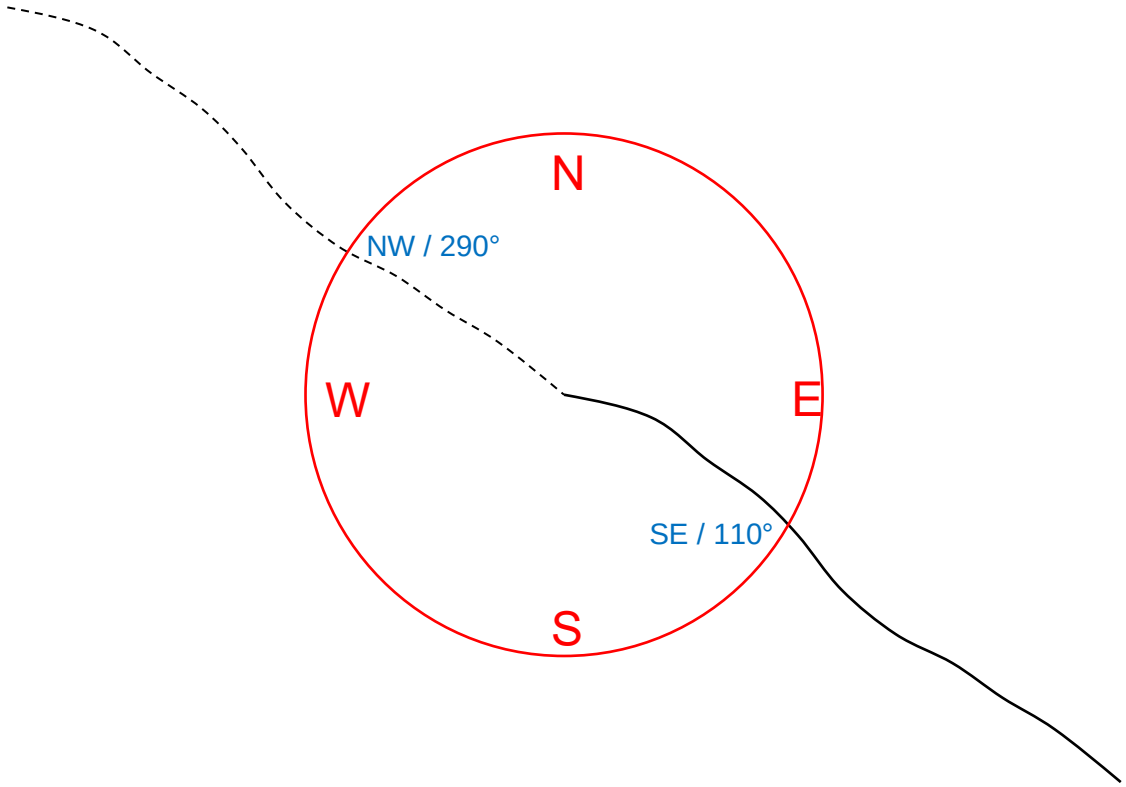

***Fig. 6.09**: Diagram showing how a single ground crack can have two different orientations; henceforth all bearing and hillslope position measurements have been normalised to a 0-180° scale.*

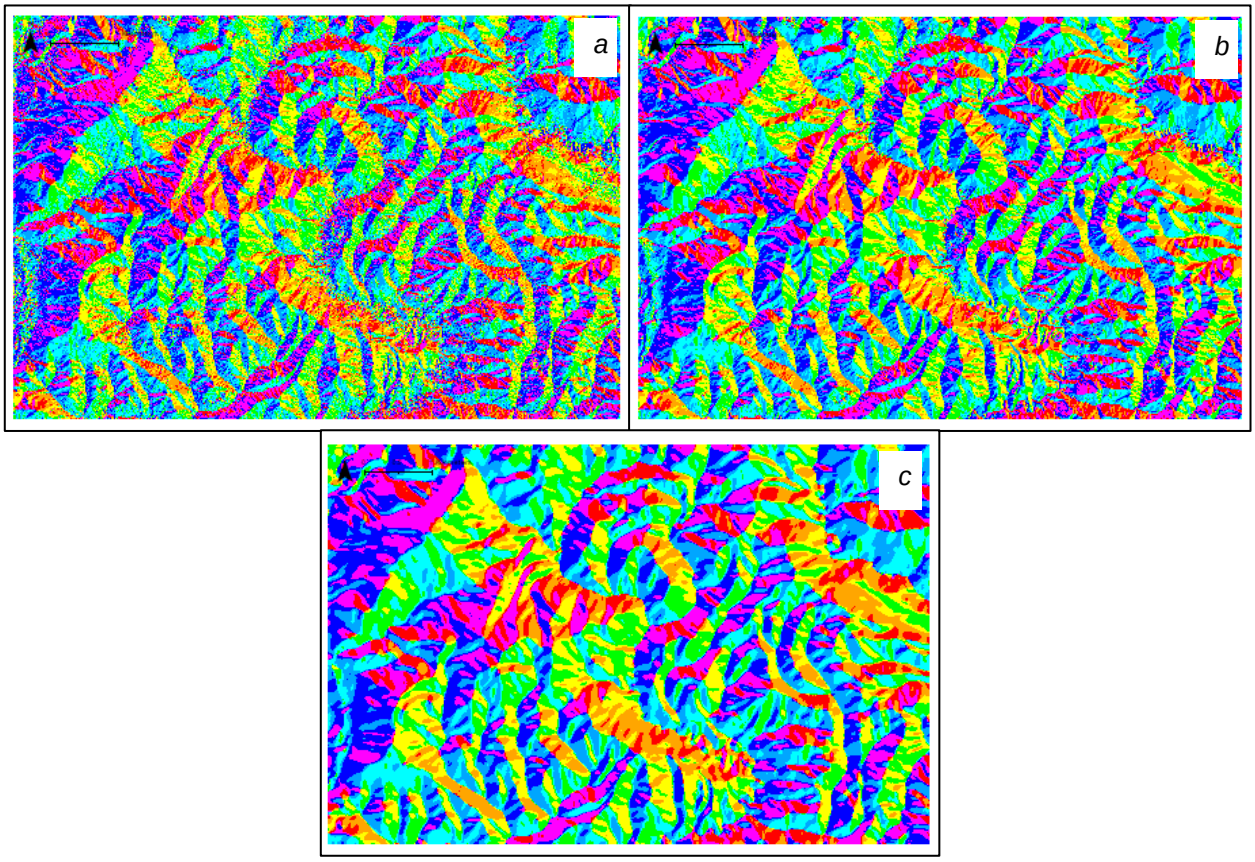

***Figs. 6.10a-c**: Illustrations of the difference between hillslope-scale local slope aspect measurements when calculated on a 1 m (**a**), 10 m (**b**) and 50 m (**c**) scale. A 50 m scale was chosen in this instance as, although smoothened, it provides the best representation of local slope aspect on a hillslope-scale. The 1 m layer contains too much noise and discrepancies at the level of the individual pixel.*

6.1.2.4. *Plan (Sinuosity)*

Viewing ground cracks from a planar perspective can provide further insight into their shape. Sinuosity was used as the quantitative measurement to investigate this. Cracks can either be linear or sinuous to varying degrees (***Fig. 6.11***) and as such, two measurements of sinuosity were calculated. The first will be referred to as 'Path Sinuosity' (*Ps*) and is based on a conventional method primarily used to calculate the sinuosity of river channels (Snow, 1989). This is based on the ratio of feature length to straight line length between the start and end points of the feature. Crack length has already been ascertained (*Ch. 6.1.1*) and straight-line length was calculated using the start/end coordinates and Pythagoras' Theorem (***Fig. 6.12***). Crack length was then divided by straight line length. *Ps* was plotted against crack length.

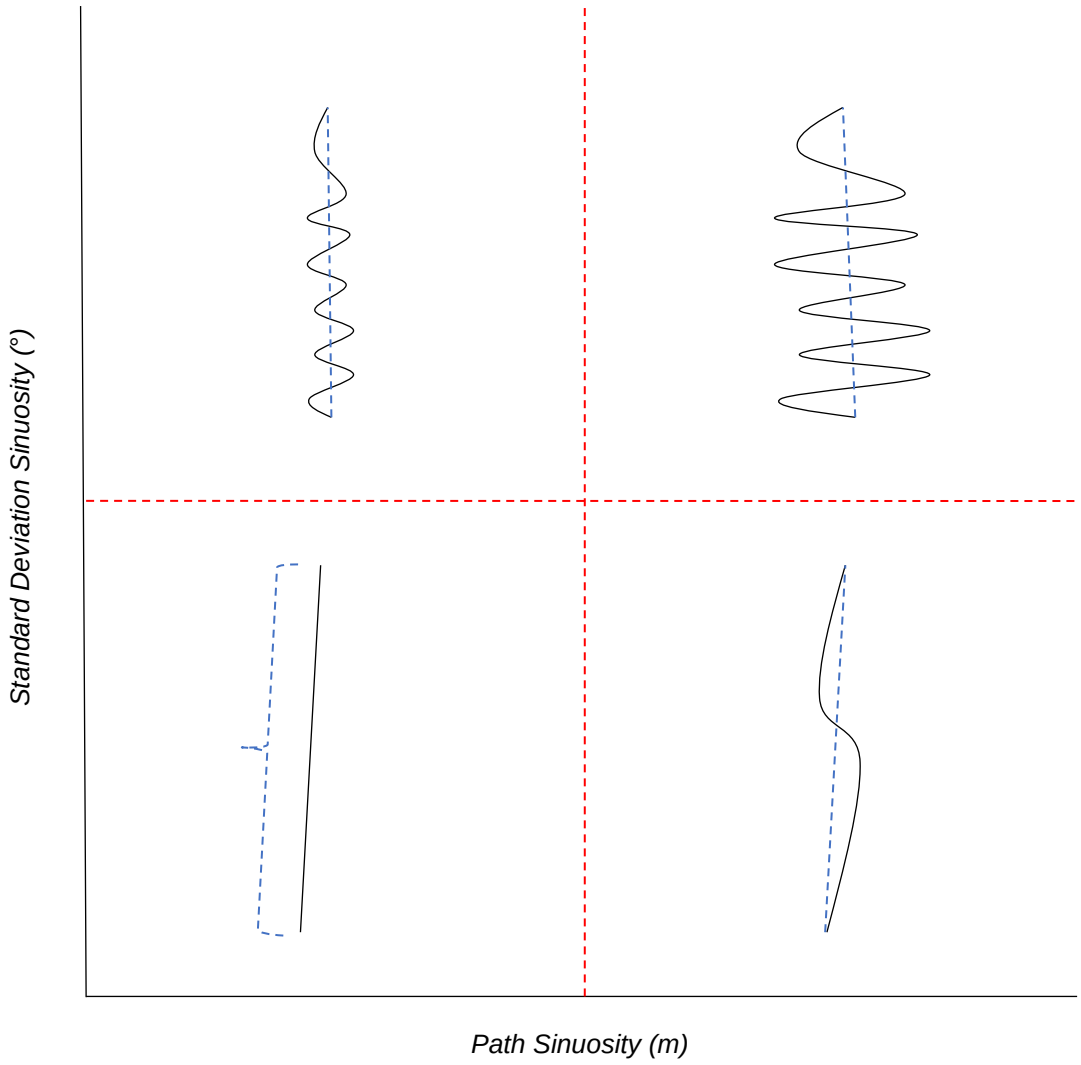

Fig. 6.11*: Graphical representation of the difference in ground crack form, and how this may be represented through the relationship between path sinuosity and standard deviation sinuosity. Straight lines (blue) are added to aid the visualisation of path sinuosity.*

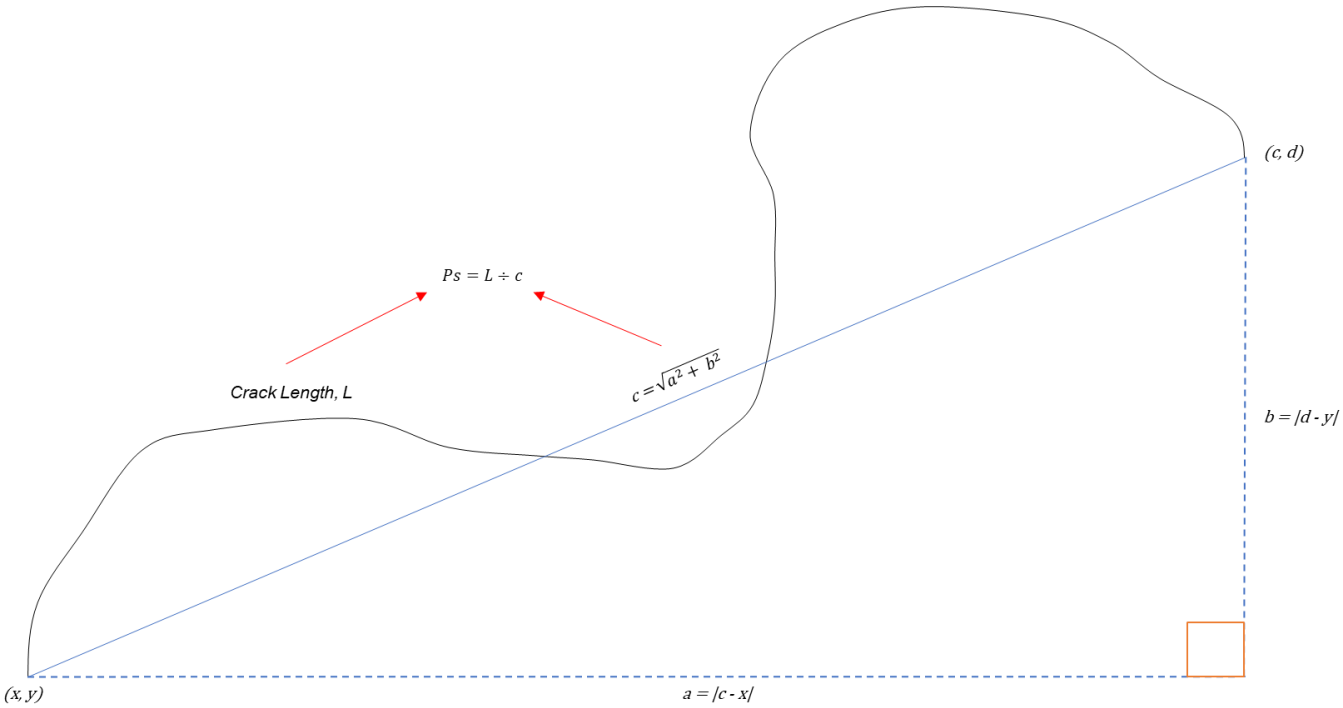

***Fig. 6.12**: Diagram of path sinuosity (Ps), showing the difference between crack length (black) and straight line length (blue) and how the latter is calculated using start/end coordinates, and then Pythagoras' Theorem. Crack Length, L, is supplied in the polygon Attribute Table.*

The second measurement of sinuosity will be referred to as 'Standard Deviation Sinuosity' (*SDs*). For this, the standard deviation of raw orientation measurements (Ch. 6.1.2.3) was calculated per crack. In theory, a perfectly linear crack should have a standard deviation of 0/180, which will then tend towards 90 (the maximum) as sinuosity increases.

Ps and *SDs* were plotted against each other, with ***Fig. 6.11*** hypothesising what the position of points on the graph may refer to in real terms. Both values were scaled using a logarithm (base-10) for alternative visualisation.

6.2. RESULTS

Results from the aforementioned methodologies will be presented forthcoming. The following results table (***Table 6.1***) provides summary statistics for all metrics that are being investigated. It will be included here because it will be referenced throughout the chapter.

Table 6.1 *– Results table summarising the key statistics for all ground crack parameters under investigation in this chapter. Mean, mode, median, standard deviation and range have all been calculated for each ground crack parameter.*

Feature Statistic	Mean	Mode	Median	STD	Range
Length (m)	7.0	3.0	5.0	8.3	275.0
Elevation (m)	280.2	296.4	281.3	63.9	523.2
Cross Profile Step (m)	1.9	0.5	1.4	1.7	25.5
Orientation (°)	108.2	150.0	117.0	46.1	177.0
Position on Hillslope (°)	97.0	103.0	99.0	38.7	179.0
Path Sinuosity (m)	2.4	4.0	2.2	1.0	16.6
Standard Deviation Sinuosity (m)	33.3	0.0	18.9	29.0	124.1

6.2.1. Probability Density and Crack Length

Coseismic ground cracking shows evidence of a typical magnitude-frequency relationship between feature length and frequency (***Fig. 6.13***). Both a rollover and power-law scaling are expressed as per other studies (e.g. Stark & Hovius, 2001). Rollover occurs at a length of ~6.3 m, suggesting that features are more commonly small (~3-8 m) in scale and that there are fewer very small- (<~2 m) and large- (>~10 m) scale features. Feature Statistics (***Table 6.1***) support this through a mean length of 7 m, a median of 5 m and a mode of 3 m. However, due to the variation in crack length (as exhibited by a range of 275 m) and the accuracy at which it is calculated the modal value is unlikely to be of much significance here. Power-law scaling is present after the rollover. As such, the decay of crack frequency as length increases can be fitted to a function ($f(L)$ - ***Fig. 6.13***) and therefore potentially harnessed for predictive purposes.

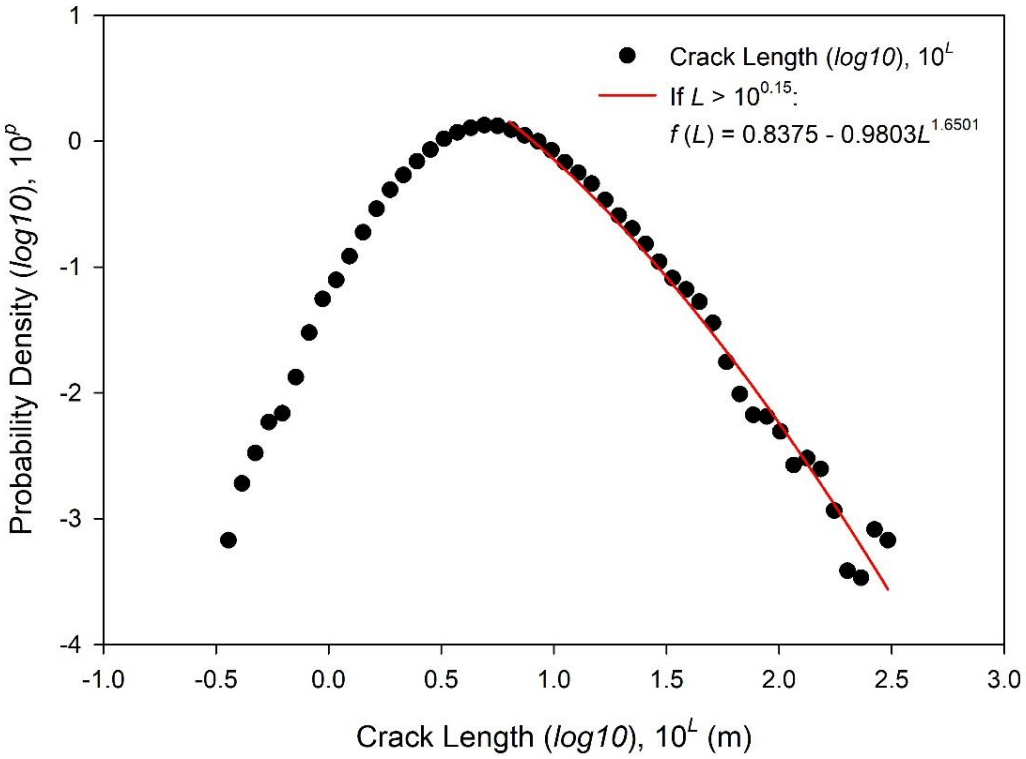

***Fig. 6.13**: Probability Density, P, graph for Crack Length, L, showing how P changes with L. Rollover is present, as is power-law scaling, which has been summarised using the function f (L). Both axes have been scaled logarithmically to aid interpretation and comparison with other studies.*

6.2.2. Long Profile

Long profile supports what has been outlined in *Ch. 6.2.1.* in that crack frequency of a given length appears to decay quickly after ~10 m. There are fewer features and a lower density of features as length surpasses ~10 m. This is qualitatively clear in ***Figs. 6.14a-b*** & ***6.15a-b***. No clear linear correlation is evident between crack length or frequency and elevation. Although it may qualitatively appear that crack frequency is highest at mid- and lower-slope locations, the KDE curve of ridgetop elevations (which peaks at ~325 m) suggests that this may not be the case (***Figs. 6.14a-b*** & ***6.15a-b***). Crack KDE has two distinct peaks ~325 m and ~250 m and as such closely aligns with the KDE of ridgetop elevation. Landslide crown and toe KDE's peak at ~250 m and ~200 m.

Ground cracks appear to (qualitatively) be preferentially oriented between ~45-135° from the point of origin, particularly as they increase in length ***(Figs. 6.16a-b*** & ***6.17a-b***). This is quantitatively confirmed with a mean position on hillslope of 97°, a mode of 103° and a median of 99° in ***Table 6.1***. Very small-scale (<~2 m) features appear to occur in most directions (***Figs. 6.16a-b***) apart from true slope parallel, however when data skewness is removed (***Figs. 6.17a-b***) even these are predominantly slope perpendicular in form.

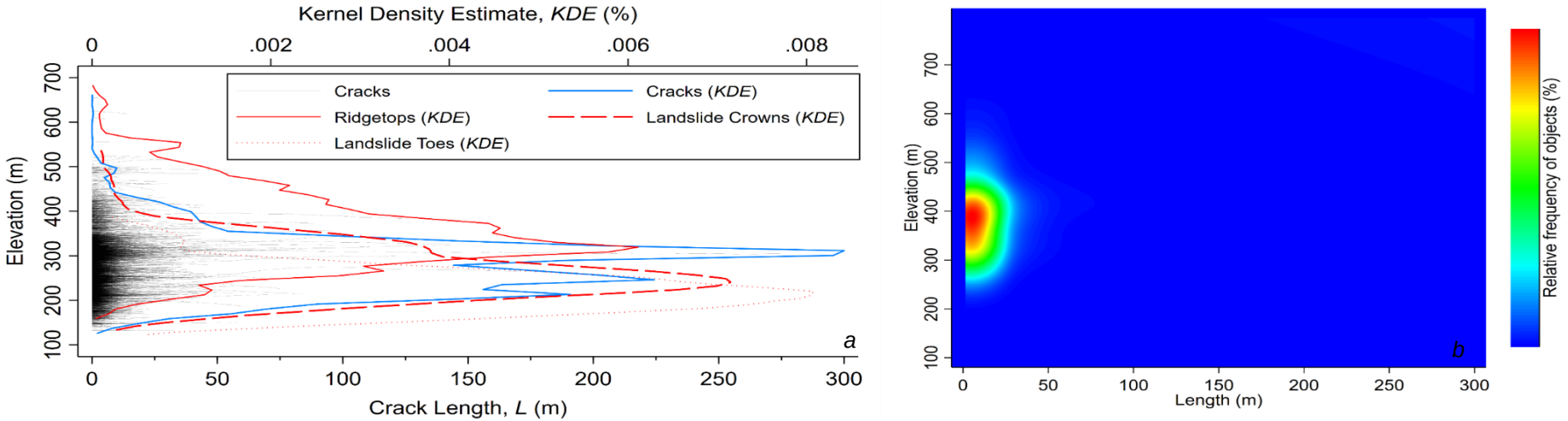

***Figs. 6.14a-b**: **a**) Long Profile graphs showing the raw elevation of ground cracks (black) and the kernel density estimate (KDE) of this distribution (blue). KDE's of landslide crown, toe and ridgetop elevations have also been plotted for interpretive purposes. **b**) Crack density in **Fig. 6.13a** has been converted into a contour plot heatmap*

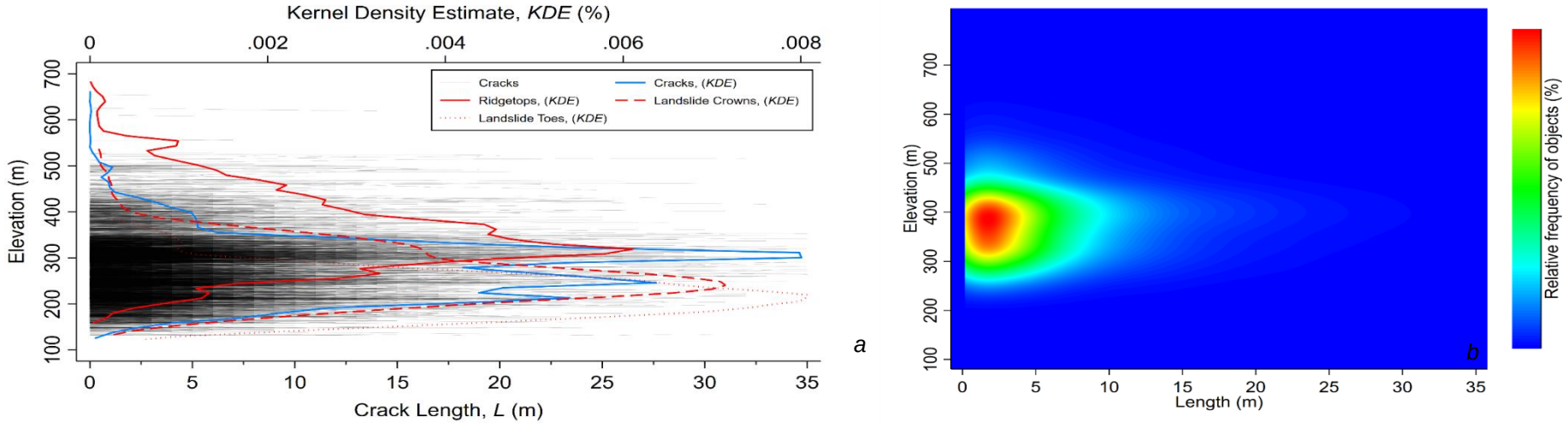

***Figs. 6.15a-b**: **a**) Long Profile graphs showing the raw elevation of ~99.9% of ground cracks (black) and the kernel density estimate (KDE) of this distribution (blue). KDE's of landslide crown, toe and ridgetop elevations have also been plotted for interpretive purposes. **b**) Crack density in **Fig. 6.14a** has been converted into a contour plot heatmap. Outliers were discarded prior to plotting using a threshold > than three standard deviations in width, to ensure that only the most extreme outliers were discarded.*

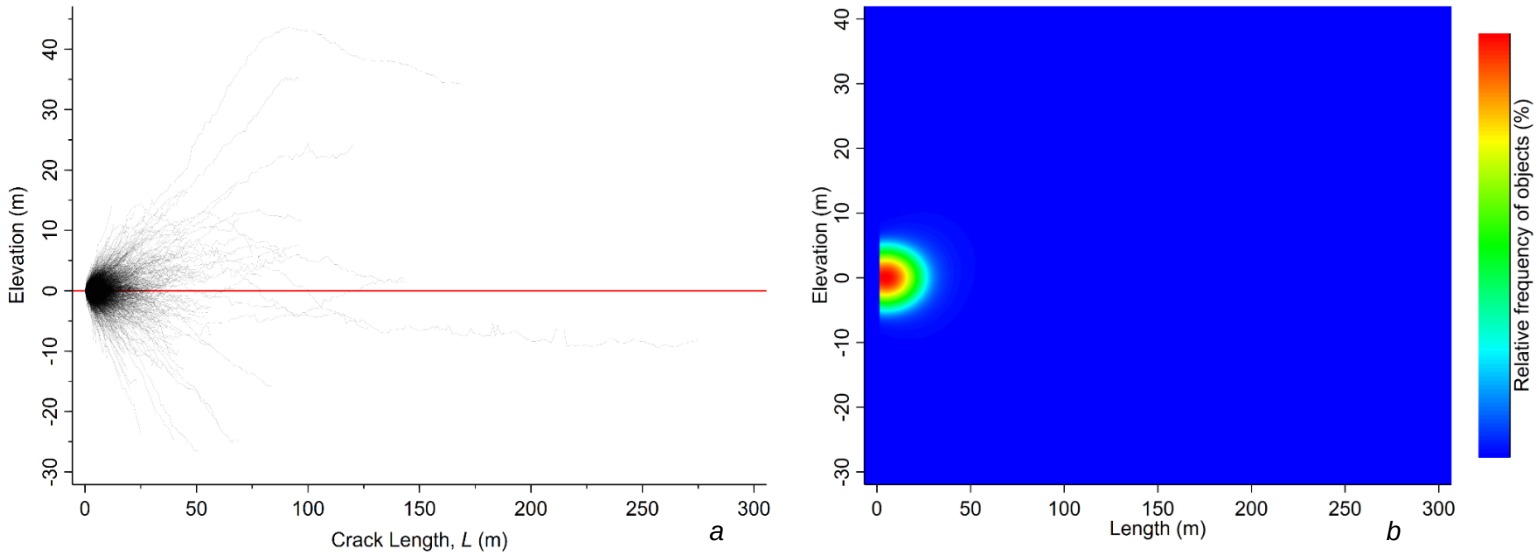

***Figs. 6.17a-b*:*a*)** *Long Profile graphs of ground cracks which have been reset to manifest outwards from a normalised elevation, enhancing the shape of cracks across a hillslope.* ***b*)** *Crack density has been converted into contour plot heatmaps.*

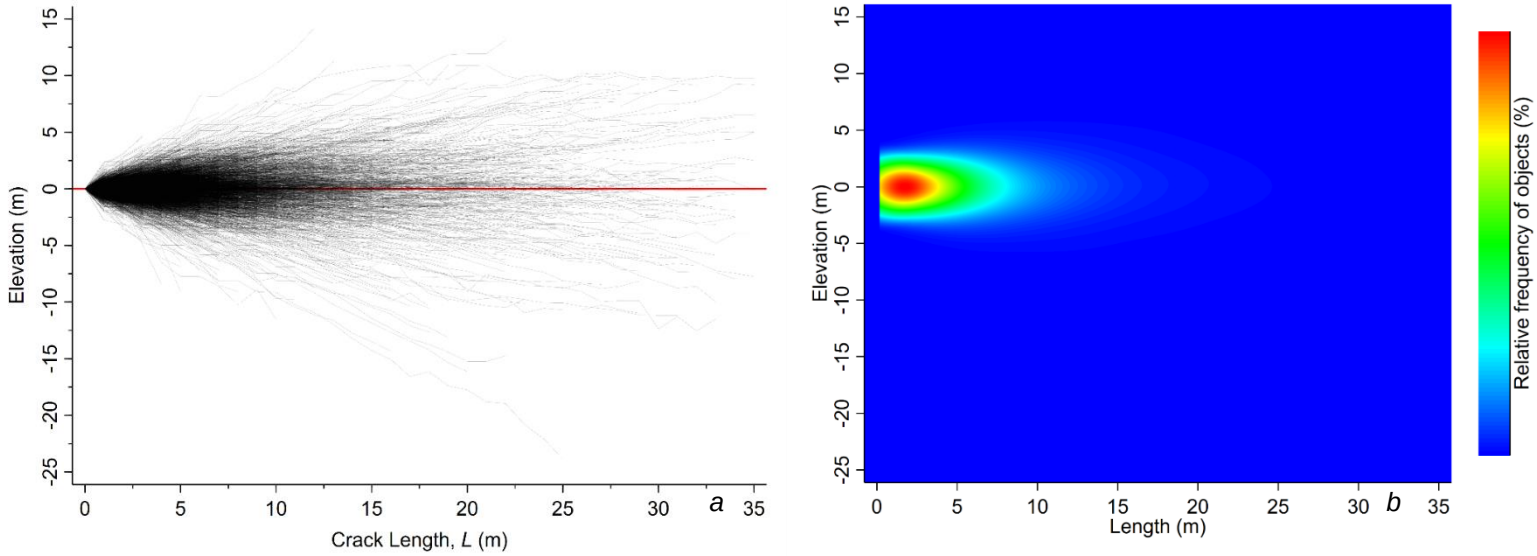

***Figs. 6.16a-b*: *a*)** *Long Profile graphs of > 99.9% of ground cracks which have been reset to manifest outwards from a normalised elevation, enhancing the shape of cracks across a hillslope.* ***b*)** *Crack density has been converted into contour plot heatmaps.*

6.2.3. Cross Slope Profile

The majority of crack-defined steps appear to be small in size and consistent in form across all slope angles, clustering <~3 m (***Fig. 6.18a***) and between ~0.3-3 m in (***Fig. 6.18b***) up to a slope angle of ~45°. A mean of 1.9 m, median of 1.4 m and standard deviation of 1.7 m (***Table 6.1***) confirm this quantitatively. A mode of 0.5 m may suggest that step size is preferentially smaller than this, but as mentioned above too much emphasis cannot be placed on modal values here. ***Fig. 6.18b*** particularly highlights the diversity of step values across all slope angles. That said, there is a very weak positive correlation in step values up to a slope angle of ~10° (***Figs. 6.18a-b***), highlighted by a clear lack of higher step values which in turn is supported by a low standard deviation value of 1.7 m in comparison to the range of 25.5 m (***Table 6.1***).

In terms of crack distance from landslide crowns, clustering <~3 m on (***Fig. 6.19a***) and ~1 m (***Fig. 6.19b***) indicates that smaller (<~3 m) step values occur at all locations. However, larger step values are more preferentially located closer to landslide crowns, highlighted by the weak negative correlation <~1700 m from the nearest landslide crown (***Fig. 6.19a***).

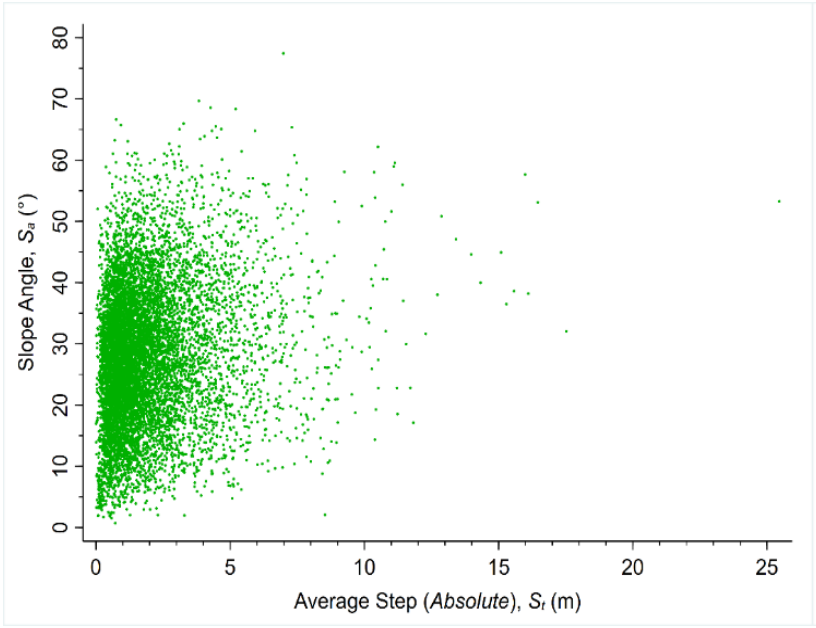

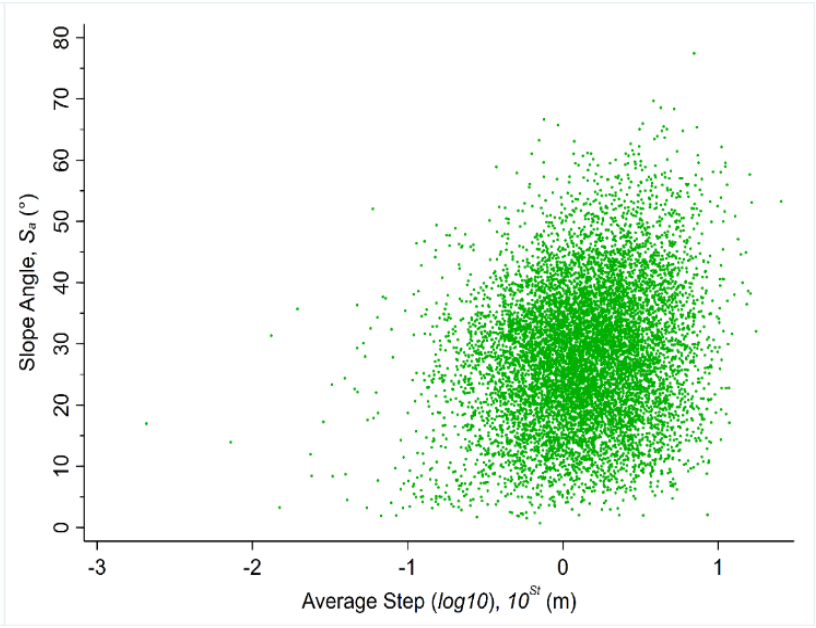

***Figs. 6.18a-b**: Cross Slope Profile graphs of the average (absolute (**a**)) and logarithmic (**b**) step values, plotted against slope angle at step locations.*

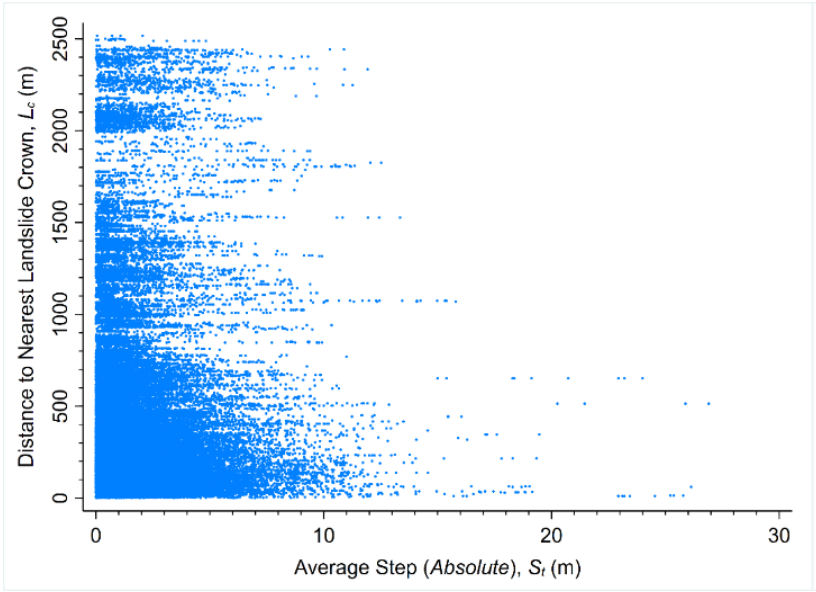

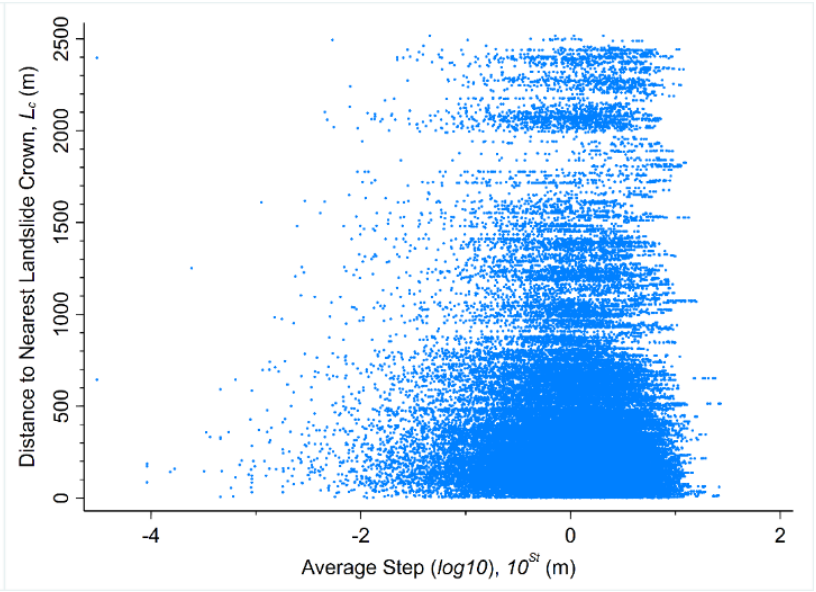

***Figs. 6.19a-b**: Cross Slope Profile graphs of the average (absolute (**a**)) and logarithmic (**b**) step values, plotted against distance to the nearest landslide crown at step locations.*

6.2.4. Orientation and Position on Hillslope

Ground crack orientation has been plotted using average normalised bearing (see 5.2.4.) to see if the presence of coseismic ground cracking is randomly oriented in the landscape. Cracks are preferentially oriented between 90-180° in a SE/NW direction (***Fig. 6.20***) with a mode of 150°,a mean of 108° and a median of 117° (***Table 6.1***). A standard deviation value of 46.1° also supports the preferential SE-NW orientation. There is another mode at ~45° (***Fig. 20***) which may have skewed this value slightly. A vector mean strength of 71% indicates that results are significant (***Fig. 6.20***).

Ground crack position (on hillslope) was calculated using average raw bearing and local slope aspect, and then normalised to determine the most common direction in which a ground crack propagates across a hillslope. Cracks are preferentially slope perpendicular with a mean of 97° also appearing to represent the mode in the data distribution of 99° (***Table 6.1*** and ***Fig. 6.21***). Along with a median of 103° and a low standard deviation of 38.7° this suggests a strong average. Frequency continuously increases as direction tends towards slope parallel (*Pl*). Results are significant, as per a vector mean strength of 79% (***Fig. 6.21***).

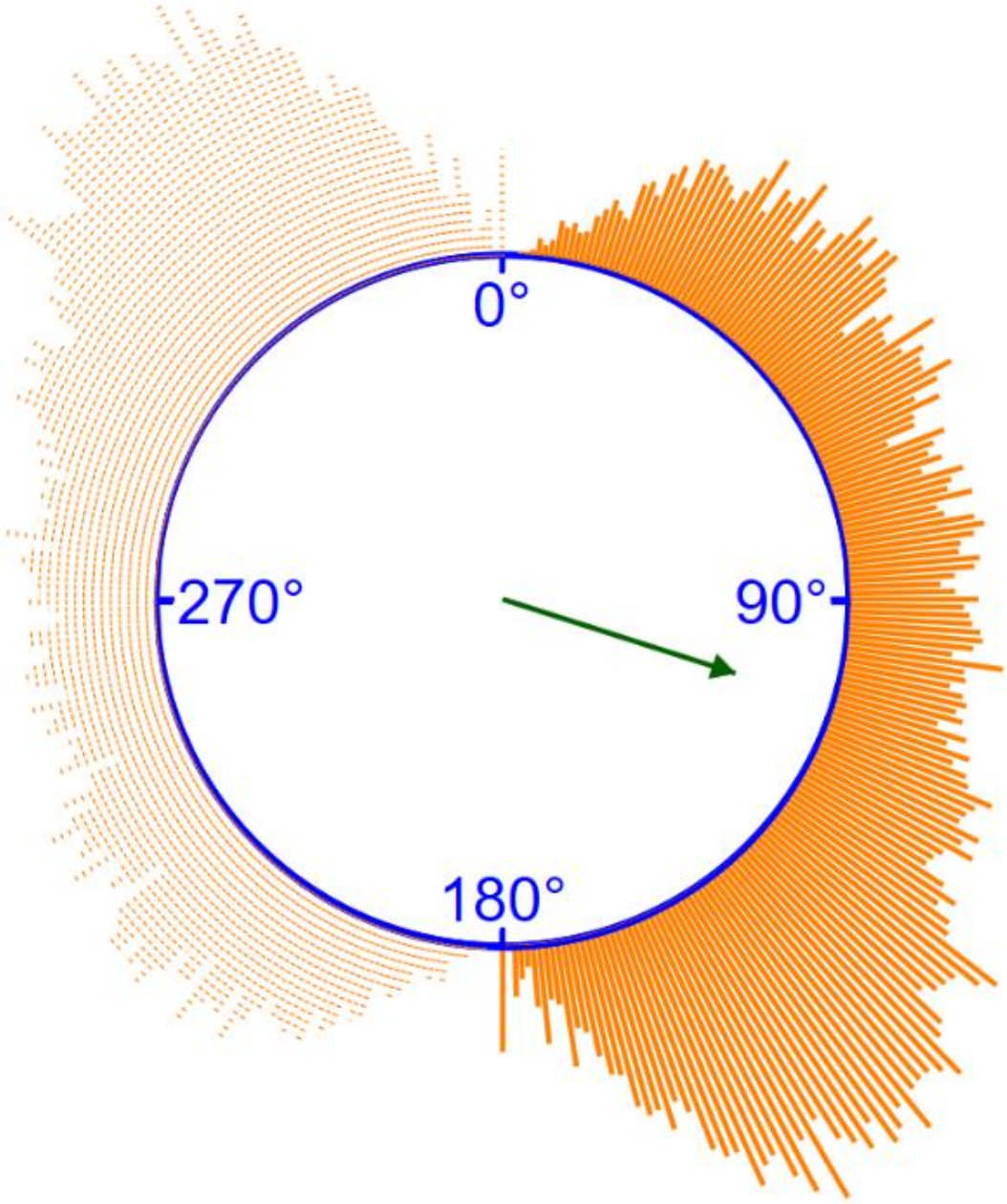

Mean = 108°; Strength = 71%

***Fig. 6.20**: Circle Plot showing the raw bearing of ground cracks, in degrees*

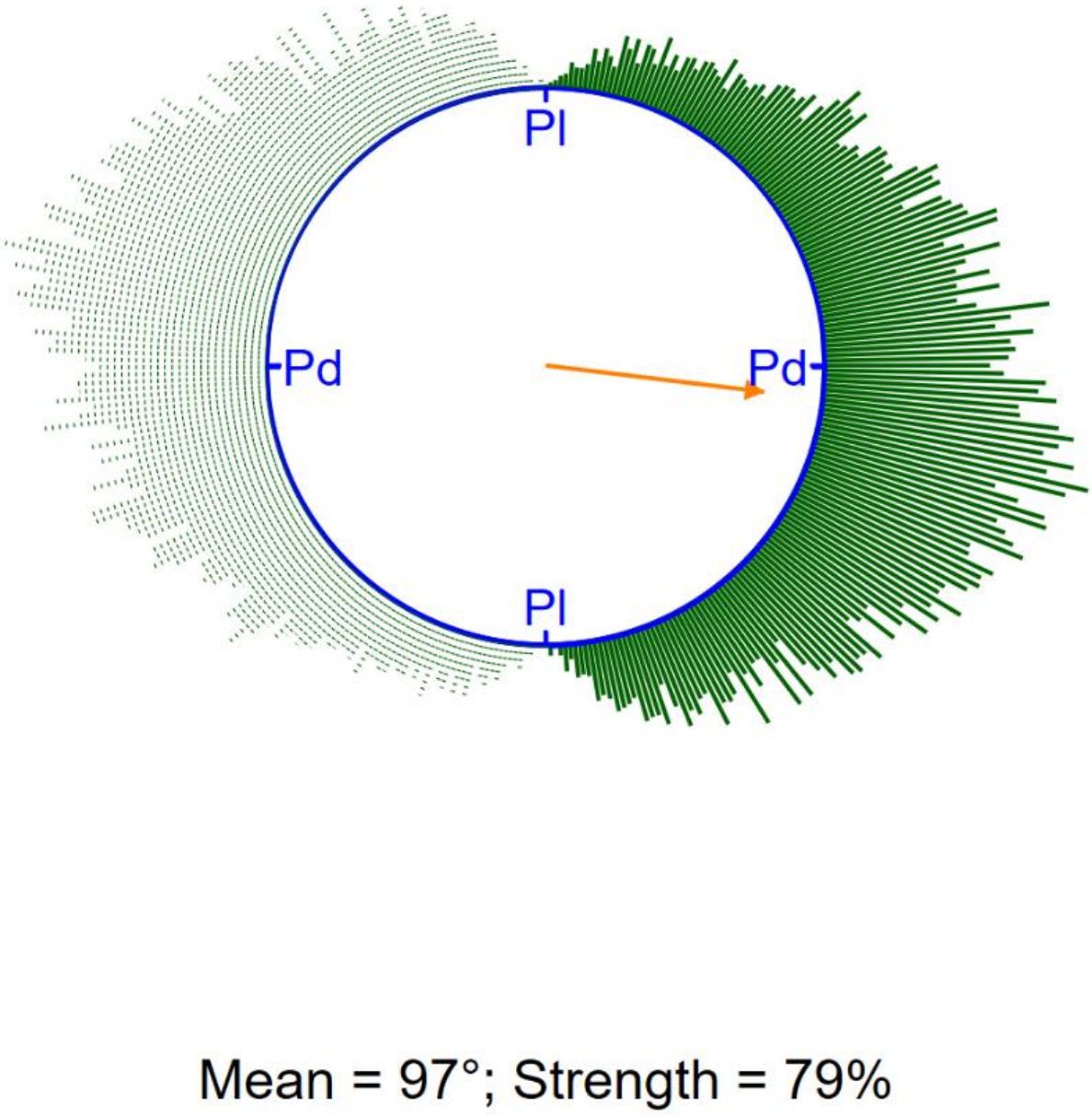

Fig. 6.21*: Circle Plot showing the position of ground cracks on a hillslope, with 0/180° indicating slope parallel (Pl) and 90° indicating slope perpendicular (Pd). These have been used instead of numerical measurements to aid contextual interpretation.*

6.2.5. Plan Sinuosity

Path Sinuosity (*Ps*) does not appear to correlate linearly with Standard Deviation Sinuosity (*SDs*) and instead appears to have a strong positive but non-linear correlation with crack length (*L*) (***Fig. 6.22***). *Ps* has a mean of 2.4 m, a mode of 4.0 m, a median of 2.2 m and a standard deviation of 1 m – reflecting the concentration of data < 5 m (*Ps*) in ***Fig. 6.22*** and suggesting that cracks are preferentially sinuous (i.e. *Ps* does not have a value of (or close to) 0 m). ***Figs 6.23a-b*** show two distinct clusters, separable by lower and higher *SDs* measurements. This is reflected in the mean and mode for SDs, which are very different at 33.3 m and 0 m respectively (***Table 6.1***). A standard deviation of 29 m and a range of 124 m support this further by highlighting the vast spread of values. In the lower cluster, ***Fig. 6.23b*** effectively highlights a sub-cluster of almost linear features, which have both low *SDs* and *Ps* measurements, and which are limited to cracks <5 m in length. The SDs mode of 0 m appears to quantitatively confirm the presence of this sub-cluster (***Table 6.1***). *SDs* has no correlation with either *Ps* or *L* in the lower cluster. The higher cluster reveals that the smallest features have the highest *SDs* measurements (>~75°), and that *SDs* then decreases as *Ps* and *L* increase. Ultimately, the shortest cracks appear to be the least sinuous but the most variable.

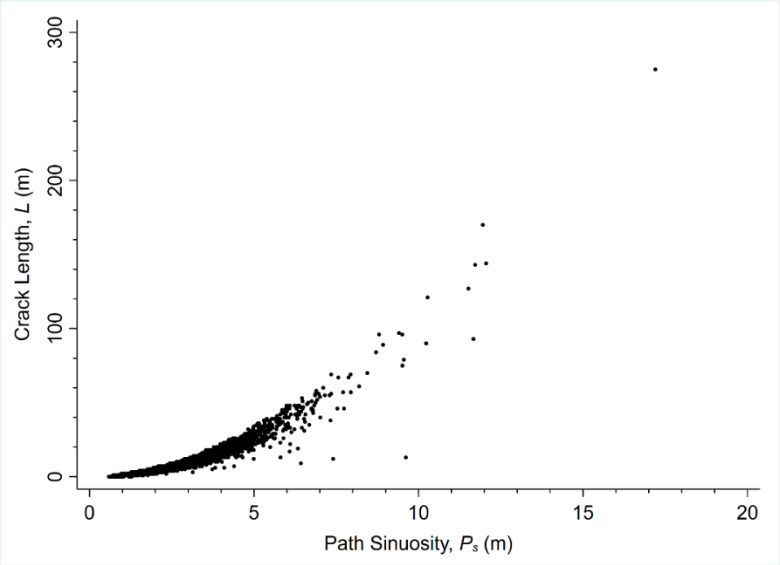

***Fig. 6.22**: Graph of Path Sinuosity, Ps, plotted against Crack Length, L.*

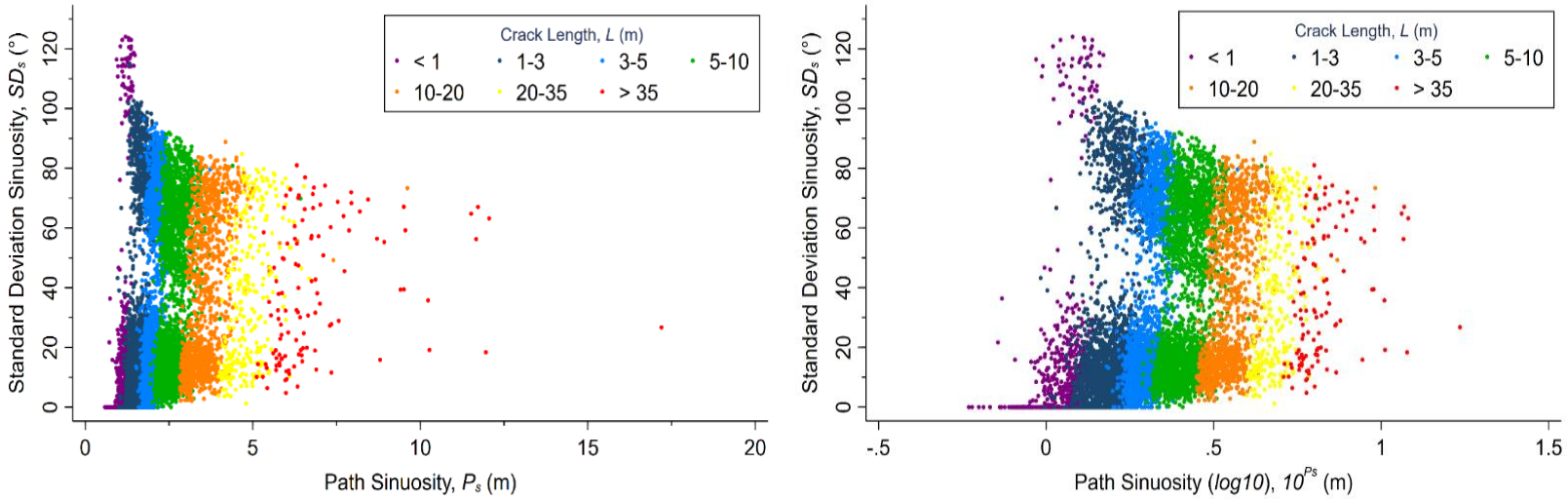

***Figs. 6.22a-b**: Graph of Path Sinuosity, Ps, plotted against Standard Deviation Sinuosity (SDs), with Crack Length, L, incorporated* through the colour scale. Raw *Ps measurements (**a**) and logarithmic measurements (**b**) were used to* provide alternative visualisation of potential trends.

6.3. SUMMARY

Using the coseismic ground cracks identified during inventory production, a range of methods have been used to analyse their form in the landscape, namely to see if there are any emergent characteristics which could be used to enhance our understanding of these features and their propagation across the landscape. Before interpreting results further in *Ch. 8*, key points to draw from *Ch. 6* are:

- Cracks are preferentially small in scale (7 m on average and ~3-8 m according to Probability Density) and they express similar distributional characteristics (rollover and power-law scaling) to magnitude-frequency relationships exhibited by coseismic landsliding.
- Crack elevations appear to concentrate at both ridgetop and landslide crown elevations; and are preferentially slope perpendicular with a mean of 97° and a mode of 99°.
- The smallest step values across the width of a crack are present across all slope angles and occur irrespective of proximity to landslides. A weak positive and weak negative correlation exists between step size and slope angle/proximity to landslide crowns respectively. As such, higher step values preferentially occur on steeper slopes and closer to landslide crowns.
- Cracks are preferentially oriented ~150° in a SE/NW direction, with another mode ~45°. Path Sinuosity (*Ps)* shows a strong positive correlation with Length (*L)*. Standard Deviation Sinuosity (*SDs)* shows no correlation with either *Ps* or *L*.

7. SPATIAL TOPOGRAPHIC CONTROLS – STATISTICAL ANALYSIS

To understand the hazard and the role in wider-scale landscape evolution caused by coseismically generated features such as ground cracks, the fundamental controls on their occurrence must be understood. This requires identifying and evaluating the potential controlling factors that influence ground cracking (e.g. Garcia-Rodriguez *et al.*, 2008). The recurrence of these conditions may also promote future failure of cracked hillslopes as they transition to full landslides (Dai & Lee, 2002). Therefore, identifying their spatial and temporal distribution is key to determining the likelihood of future ground cracking events (Godt *et al.*, 2009). Empirically based models can objectively and quantitatively define relationships between causative factors and the locations in which features are more likely to occur (Remondo *et al.*, 2003; van Westen *et al.*, 2006; Parker, 2010), offering some indication as to the relative influence of such causative factors on feature occurrence.

In past studies on coseismic landsliding, a range of statistical techniques have been used for this purpose including discriminant analysis (e.g. Carrera, 1983), susceptibility indexing (e.g. Parise & Jibson, 2000), principal component analysis (e.g. Hervas & Bobrowsky, 2009), multi-criteria evaluation (e.g. Kamp *et al.*, 2008; 2010), bivariate/multivariate regression (e.g. Keefer, 2000; Parker, 2010; Parker *et al.*, 2015; Massey *et al.*, 2018) and fuzzy logic (FL) (e.g. Kritikos *et al.*, 2015; Robinson *et al.*, 2017; 2018). Recently, multivariate regression (e.g. logistic regression) has become a popular method when analysing the controls on coseismic landslides as it can consider multiple variables without the need for any prior assumptions regarding the relationships between these variables and landsliding (e.g. Keefer, 2000). This is crucial when analysing features where multiple factors are thought to affect their spatial distribution (Parker, 2013). For example, in the case of New Zealand, Massey *et al.* (2018) used logistic regression to determine that slope, peak ground acceleration (PGA) and distance from fault were the most influential factors controlling coseismic landsliding during the 2016 Kaikoura earthquake. However, multivariate regression tends to be much more site specific (and therefore less widely applicable) and resource (temporally and computationally) intensive than, for example, fuzzy-based approaches; which carry a similar, but more widely applicable, statistical function indicating where in the landscape a feature may or may not occur (Robinson *et al.*, 2017). Therefore, to address research questions whilst enhancing

the future applicability of results, FL will be used to attempt to identify the controlling factors on coseismic ground cracking.

7.1. FUZZY LOGIC

FL can be used within and alongside Geographical Information Systems (GIS) to establish empirical relationships between causative factors and feature occurrence based on detailed inventories. If successful, relationships can then be used to estimate the probability of feature occurrence in areas without detailed inventories (Kritikos *et al.*, 2015). FL is fast and simple to apply (Ross, 2004) and has shown good performance in previous studies (e.g. Bui *et al.*, 2011; Robinson *et al.*, 2018). Most importantly, like multivariate regression, FL has the ability to model complex phenomena whilst incorporating uncertainties including but not limited to knowledge deficiency and data limitations/imprecision (Ross, 2004). As little is currently known about coseismic ground cracking, either mechanically or spatially, this approach may therefore be appropriate. A number of data limitations have also previously been highlighted and discussed (e.g. *Ch. 4*), therefore using a method that is relatively robust against these issues is beneficial. The model is sensitive to the quality of the inventory (Robinson *et al.*, 2017) which if substandard can lead to under/over prediction. However, the inventory used in this study has been quality checked to attempt to account for this (see *Ch. 4.2.4*). The spatial distribution of features within inventories should also be as large and diverse as possible, incorporating as many different feature settings as is feasible, and clustering should be avoided (*ibid*). The former has been ensured by mapping all visible ground cracks across the 54 km^2 study area to avoid any spatial bias. In addition, invisible areas were masked out of all ensuing analysis at the onset to prevent statistical skewing which may have occurred from including data which has not been suitable to map from and in which features may therefore be underrepresented.

FL derives from Fuzzy Set Theory and in turn, Classical Set Theory (Ross, 2004). Classical Set Theory is based on the concept of membership whereby a parameter (x) either belongs (= 1), or does not belong (= 0), to a set.

$$\chi_A(x) = \begin{cases} 1, & x \in A \\ 0, & x \notin A \end{cases} \quad [3]$$

FL is based on partial memberships on a continuous scale (Zadeh, 1965), whereby:

$$\{\mu_A(x) \in \mathbb{R} \mid 0 \leq x \leq 1 \mid\} \quad [4]$$

In the context of this research, membership values for each parameter (*x*) (in this case a particular value of a causative factor – e.g. a slope angle of 20°) portrays how it influences feature occurrence (Robinson *et al.*, 2017). Raw membership values of each parameter are then fitted to membership functions, which describe the overall 'influence' (i.e. whether a value encourages or discourages) each parameter has on ground cracking. Membership functions can be data- or semi-data-driven (Kritikos & Davies, 2014) depending on the amount of subjective input required and can be compared between inventories (Kritikos *et al.*, 2015) and altered based on this comparison to attempt to ascertain more generalised, location independent functions that are physically meaningful. The addition of new membership functions from new inventories therefore increases the accuracy and robustness of these more generic functions, whilst also providing a measure of uncertainty. For example, Robinson *et al.* (2016) further validated the membership functions calculated by Kritikos *et al.* (2015) by showing that they performed adequately when modelling other inventories. Despite having no existing functions to compare my results to, I hope to provide initial templates and suggestions, which can then be built upon going forward. Membership functions for each individual parameter are aggregated into a susceptibility map using Fuzzy Gamma (FG), (Robinson *et al.*, 2017), displaying the cumulative probability of feature occurrence over an entire area:

$$H_{GC} = \left[\prod_{F=1}^{j} f(I_{\text{norm}F})\right]^{1-\gamma} \cdot \left[1 - \prod_{F=1}^{j} (1 - f(I_{\text{norm}F}))\right]^{\gamma}, \quad [5]$$

Gamma is used (as opposed to Sum, Or, And, and Product (Bonham-Carter, 1994)) as it has the ability to incorporate two fuzzy operators (Sum and Product) to evaluate inputs and weight areas of high and low susceptibility appropriately (Kritikos & Davies, 2014).

FL is particularly useful as effective susceptibility maps should draw on a combination of influential factors. FL can be harnessed to suggest why cracking occurs where it does and therefore for hazard perception purposes (using controlling factor influence values) to predict where the ground may be susceptible to cracking in the future.

7.2. DATA EXTRACTION

The entire FL workflow can be visualised in ***Fig. 7.01***, which can be referred back to throughout. Using the previously processed Digital Terrain Model (DTM), proximal (i.e. proximity to a given feature e.g. landslides, sites of fault rupture etc.) and topographic layers potentially relevant to the occurrence of coseismic ground cracks (see below) were processed and extracted for ground crack locations and the wider study area respectively using ArcGIS Pro (v. 2.3.3). ***Fig. 7.02*** shows the general workflow for this procedure. The 1 m DTM could be used for this, as ground cracks showed virtually no topographic signatures in this layer (see *Ch. 4.2.1*) and therefore the DTM is representative of the conditions prior to cracks forming.

Layer selection was based on similar previous studies (e.g. Martha *et al.*, 2011; Kritikos *et al.*, 2015; Robinson *et al.*, 2017) and physically reasonable influences on the occurrence of coseismic ground cracking. The lack of a precedent on coseismic ground cracking means that in many cases, this directly relates to theory underpinning coseismic landsliding which may be a consequence of cracking either on the surface (Saba *et al.*, 2010) or internally (Petley & Alison, 1997) as previous studies (e.g. Parker *et al.*, 2015) have shown that this type of damage can influence hillslope failure over time. This will enable the study to address whether or not coseismic ground cracking exhibits controls that can be deemed to precondition hillslope mass wasting.

7.2.1. Extraction of Proximal Layers

Using vector shapefiles provided by GNS Science, the proximity of all ground cracks and study area cells to several other feature types was calculated to determine if these had any relationship with the spatial distribution of coseismic ground cracks. Features included: landslides, geological units and fault rupture shapefiles (supplied) and ridgetops/valleys which had to be curated directly from the DTM.

Firstly, distance to landslide crowns was calculated. Landslide crowns were chosen (as opposed to source areas or debris runout) as upon qualitative inspection, proximity to the crown is more closely associated with remnant cracking, possibly due to the lateral expansion or retrogressing of landsliding. This could evolve into a future hazard through progressive or fresh hillslope failure or remobilisation (Petley *et al.*, 2005; Samia *et al.*, 2017).

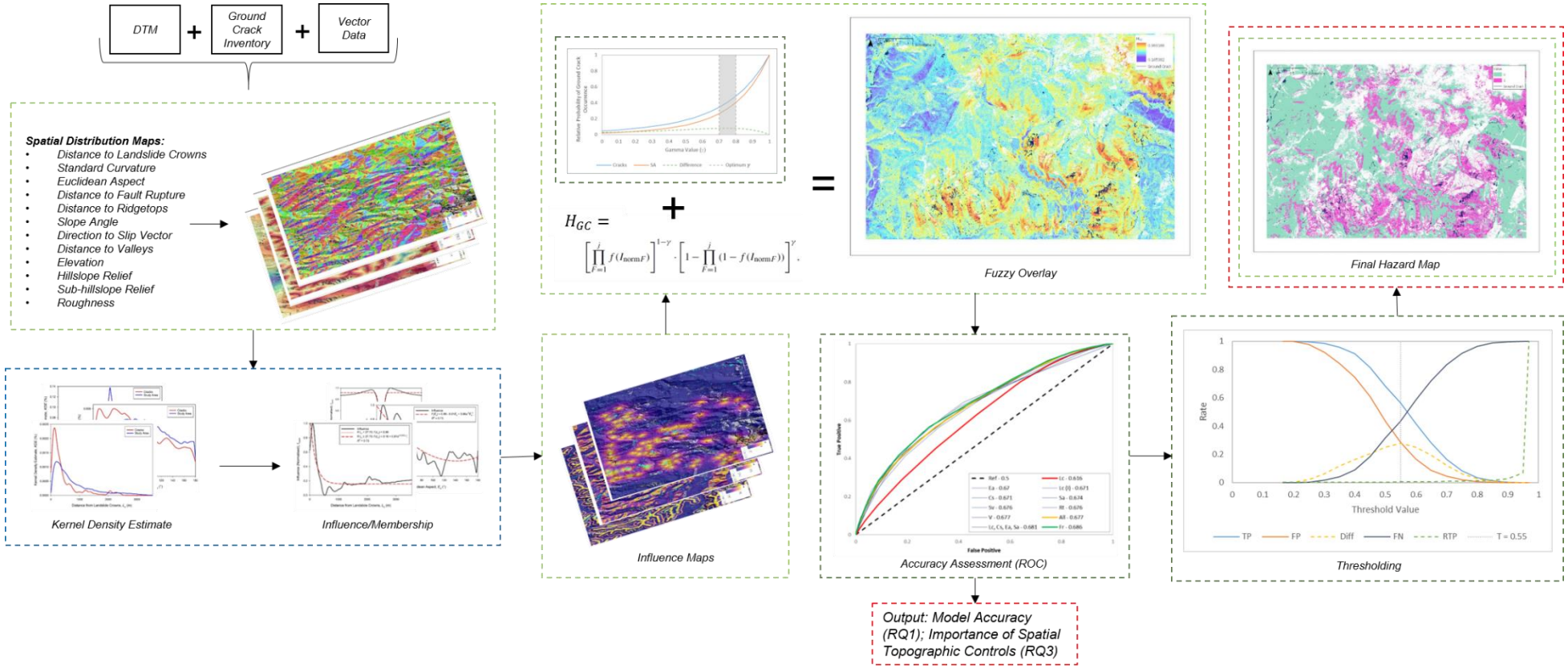

***Fig. 7.01**: Illustration of the entire Fuzzy Logic workflow to accompany the forthcoming methodological discussion, including inputs, step by step outputs and final outputs (red) which inform original research questions. Box colour varies depending on the program used for that stage of the process. ArcGIS (light green), Stata (blue) and Microsoft Excel (dark green) were all used.*

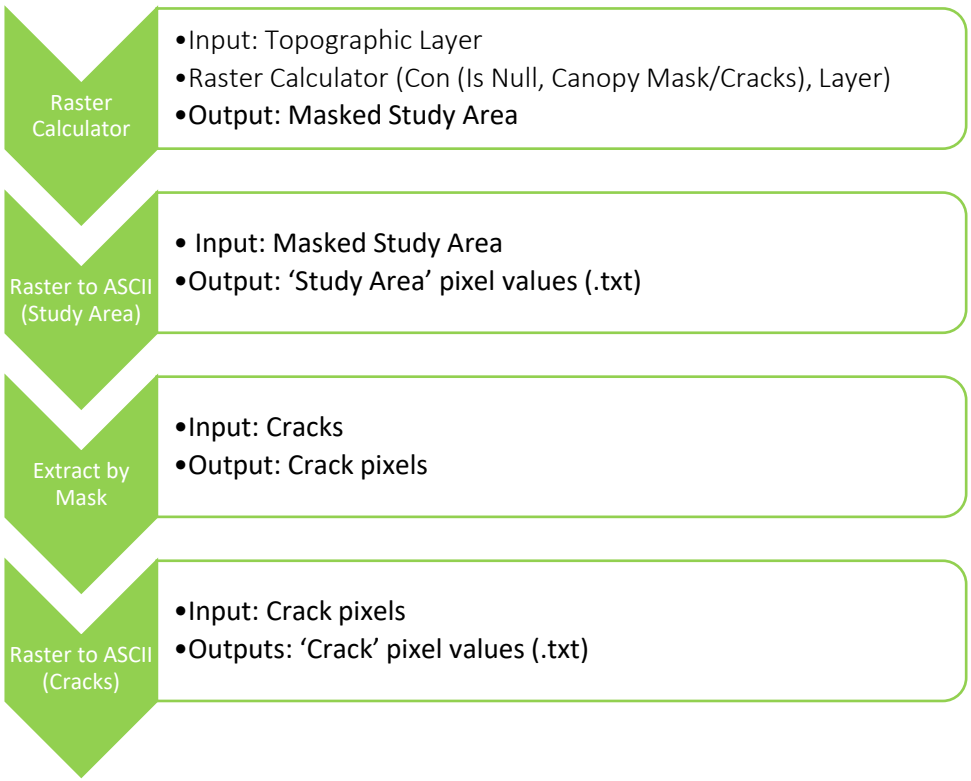

***Fig. 7.02**: Workflow illustrating extraction of study area and ground crack pixels respectively from a topographic/proximal layer. Note that these could be done in tandem.*

The prominence of ground cracking in different geological units has not been investigated, as the 54 km^2 (masked) study area does not provide enough variety in bedrock lithology to harness any meaningful or more widely representative results (***Fig. 7.03***). A regional-scale inventory and study would be needed to determine this (e.g. Massey *et al.*, 2018). Even if this was possible, geology/lithology tends to be site-specific and would thus reduce the wider applicability of any findings (Robinson *et al.*, 2018).

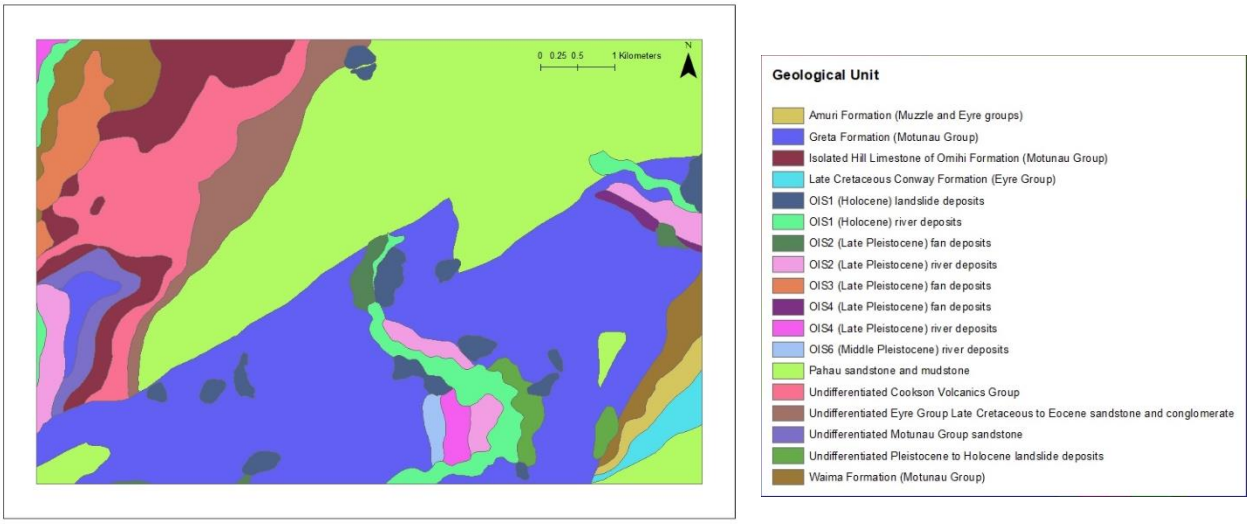

Fig. 7.03*: Geological map of the study area, showing the lack of substantial geological variability. This can thus only be included when the area of interest included a variety of geological/lithological units.*

Coseismically generated features have tended to follow a spatial pattern consistent with fault rupture (e.g. Roback *et al.*, 2018; Massey *et al.*, 2018) which may be due to a reduction in rock mass strength caused by damage from active faults (Kellogg, 2001). Following the 2016 Kaikoura earthquake, Massey *et al.* (2018) highlighted this qualitatively through the mapping of coseismic landslides (see ***Fig. 3.12***) before supporting this quantitatively, using logistic regression to determine that distance to fault rupture was a key control on landsliding in this instance. A key question therefore is whether coseismic ground cracking has a similar spatial pattern. ***Fig. 7.04*** shows two substantial paths of fault rupture throughout the study area along the Humps and South Leader Fault Zones.

Proximity to fault rupture will remain the only triggering variable under investigation in this study. Similar to the above, the study area does not provide enough variety in shaking values (peak ground velocity (PGV)) to deem the study of this appropriate (***Fig. 7.05***). As such, if done on the regional scale, it would be expected that the entire study area would return a relatively homogeneous membership value.

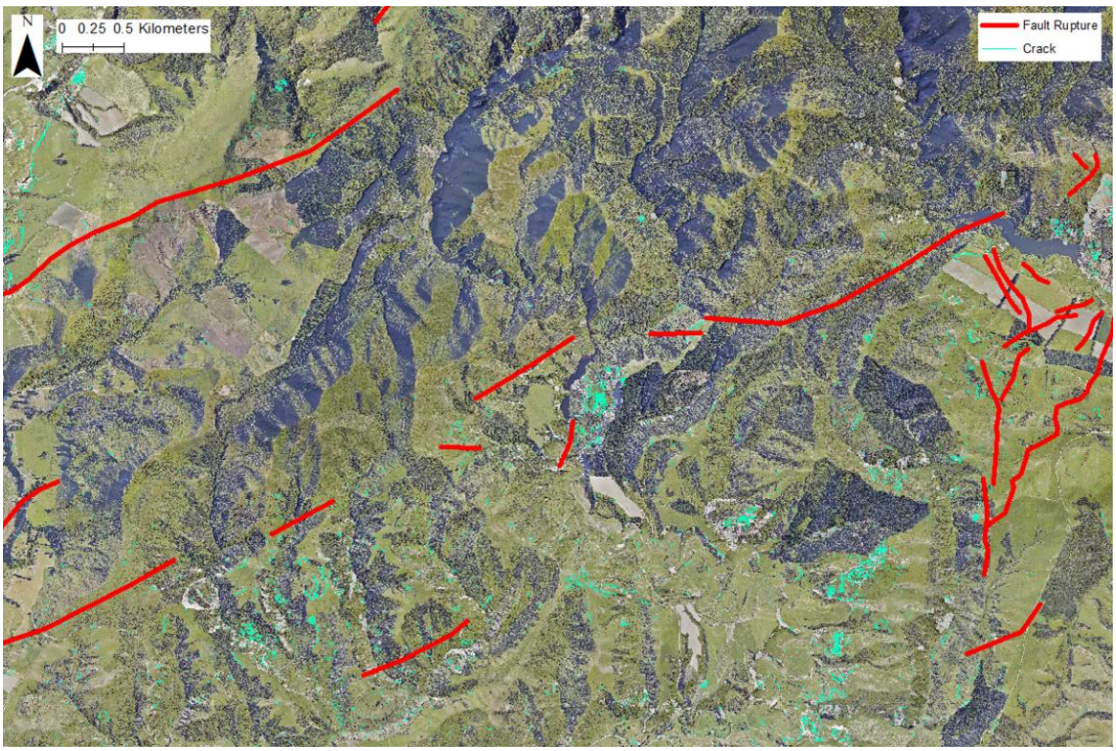

***Fig. 7.04**: Fault rupture propagation through the study area following the Mw 7.8 2016 Kaikoura Earthquake. Data courtesy of GNS Science.*

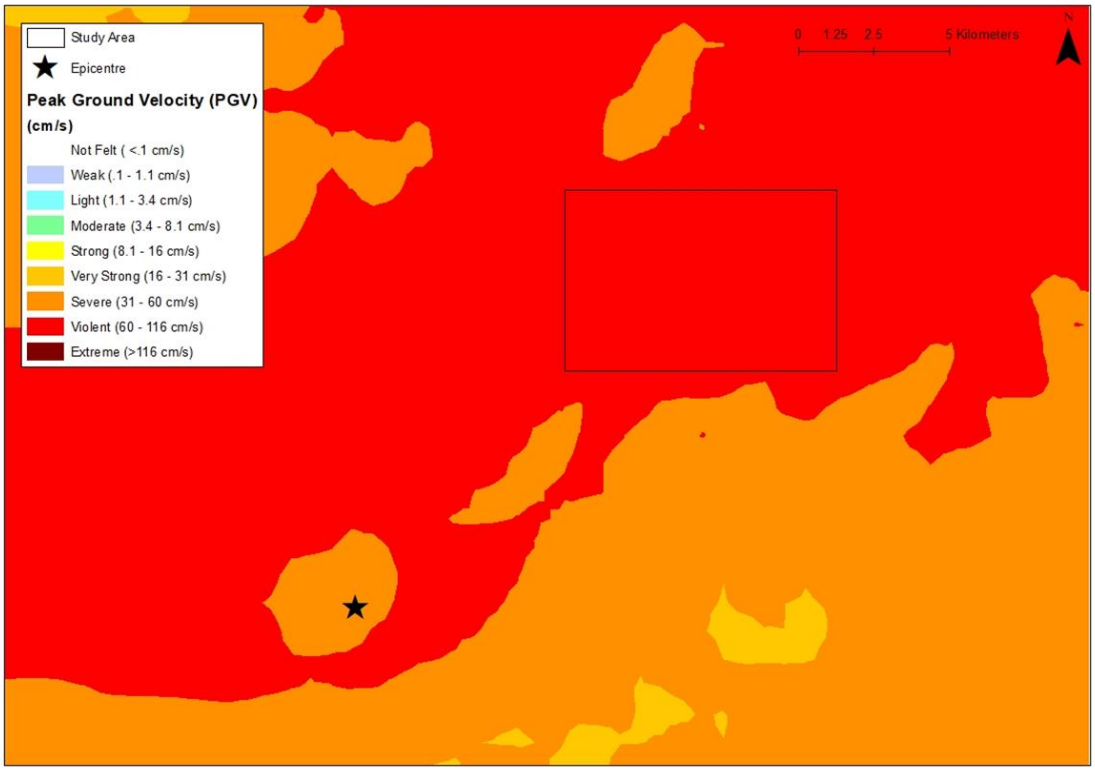

***Fig. 7.05**: PGV measurements in and around the epicentre and study area. The study area experienced violent peak ground velocities, however the lack of variety in PGV evident here means that this cannot be considered in the coming investigation. Like geology, the investigation of the impact of PGV requires a variety of measurements which consequently involves a large study area. Data courtesy of USGS.*

7.2.1.1. Creation of Ridgetop and Valley Bottom Datasets

Coseismic landslides are commonly found at ridge crests (Densmore & Hovius, 2000) or other localised concavities due to the topographic amplification of seismic waves (Meunier *et al.*, 2008). This occurs as vertically incident seismic waves (usually S waves (*ibid*)) enter the base of a topographic ridge and are reflected by and diffracted within the rock mass. This can focus seismic waves upwards towards the ridge crest, leading to enhanced ground acceleration at topographic peaks (e.g. Bouchon & Baker, 1996). In turn, shaking may also be 'dampened' in some areas due to the interaction between topography and seismic shaking (e.g. Bouchon *et al.*, 1996). As is the case with landsliding, exclusively of coseismic origin, it is plausible that ground cracking will also show a correlation with proximity to ridges and in turn, topographic site effects.

Proximity to valley floors has also been investigated. Earthquakes can progressively damage a hillslope, which can have a prolonged legacy on the landscape (e.g. Parker *et al.*, 2015). Post-seismic rainfall triggered landsliding may be more likely to occur on earthquake-damaged hillslopes (e.g. Dadson *et al.*, 2004; Hovius *et al.*, 2011) – for example, coseismic ground cracking during the Kashmir earthquake in 2005 resulted in an increase in rainfall triggered hillslope failure throughout the epicentral area during the following monsoonal/snowmelt seasons (Owen *et al.*, 2008; Saba *et al.*, 2010). As rainfall triggered landslides tend to cluster near hillslope toes (Densmore & Hovius, 2000), it is therefore important to determine whether coseismic ground cracking holds a proximal relationship with valley bottoms. If so, these have the potential to develop into total hillslope failure.

Ridgetop and valley floor shapefiles were created using Flow Accumulation. This summarises where water will be most likely to collect in a landscape on a cell-by-cell basis, based on the elevation of a raster cell in relation to neighbouring cells (***Fig. 7.06***). The output raster layer was displayed using standard deviations, enabling extreme values to be easily extracted and converted to polygon shapefiles. These represented valley bottoms. Not all of these may have sufficient upstream catchment areas for a flowing stream, but they still represent local topographic low points. This process was then repeated on an inverted DTM, to use the same principal to detect ridgetops (***Fig. 7.07***).

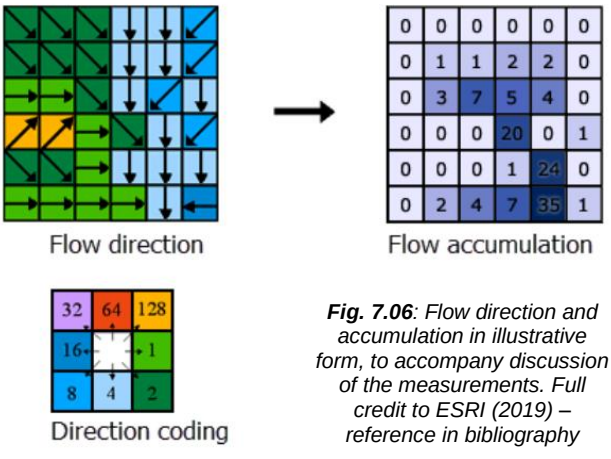

***Fig. 7.06**: Flow direction and accumulation in illustrative form, to accompany discussion of the measurements. Full credit to ESRI (2019) – reference in bibliography*

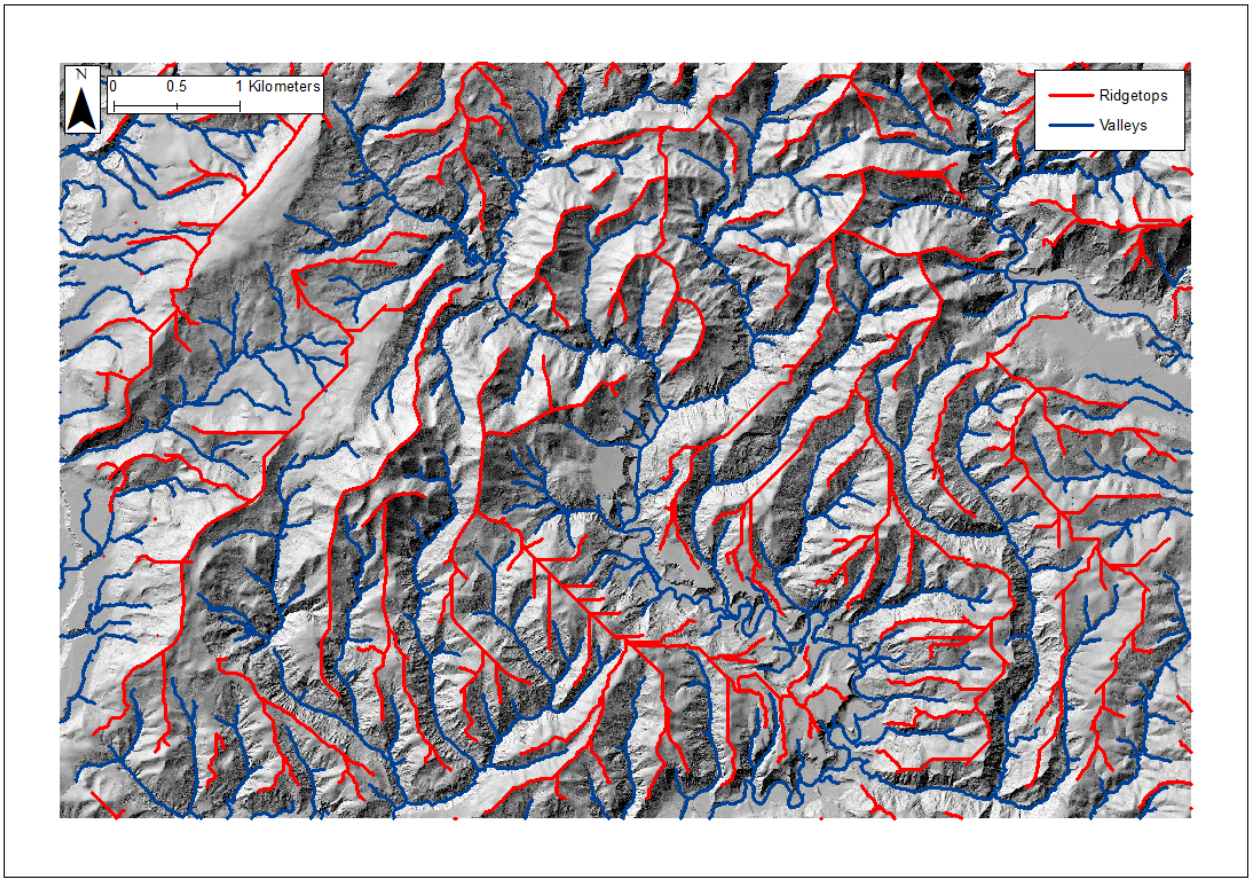

***Fig. 7.07**: Final ridgetop and valley proximal shapefiles, curated using a flow accumulation.*

7.2.2. Extraction of Topographic Layers

Generally, there is a strong positive non-linear relationship between slope gradient and coseismic landslide density (e.g. Keefer, 2000; Dai *et al.*, 2011) until a certain threshold value is reached (i.e. there are few slopes beyond this as most have already failed (Khazai & Sitar, 2004)). Some authors suggest that it is the most important predisposing factor affecting mass wasting (e.g. Jibson *et al.*, 2000). Steeper slopes increase levels of gravity-induced shear stress (Kritikos *et al.*, 2015) due to an increase in downslope force (Selby, 2005). Consequently, the intensity threshold of seismic shaking required to induce failure is lower on steeper slopes (Hovius & Meunier, 2012). As ground cracking may precede hillslope failure (e.g Petley *et al.*, 2005), this too may exhibit a relationship with slope gradient which was therefore extracted.

As discussed (*Ch. 5.1*), standard deviation of elevation values (SDE) can be used as a measure of topographic roughness (e.g. Glenn *et al.*, 2006). Hillslopes that have already failed and that are therefore already occupied by landslide scars and surface cracks will be rougher than surrounding areas. A positive relationship between ground

cracking and SDE could indicate that ground cracks preferentially occupy slopes that have already (partially) failed. SDE was calculated using Focal Statistics and a circular filter with a 3 m radius as cracks will rarely be wider than this according to previous studies (e.g. Sahoo *et al.*, 2007).

Local slope aspect has no direct impact on shear stress or strength on aseismic instability. Aspect influences sunlight and pluvial exposure and in turn vegetation cover, erosion/weathering and groundwater levels. This may have some impact on coseismic landslide distribution (Chen *et al.*, 2012) however is less likely to influence coseismic ground cracking, which is potentially less dependent on the aforementioned factors. That said, aspect can be normalised in relation to the direction to a source of shaking (i.e. the epicentre and sites of fault rupture) (Parker *et al.*, 2015; Robinson *et al.*, 2017). Landsliding is preferential on hillslopes facing away from the seismic source due to the patterns of topographic amplification and the dominant direction of coseismic stresses relative to slope and aspect (Meunier *et al.*, 2008). Coseismic ground cracking may therefore exhibit a similar relationship. Euclidean aspect and direction to fault rupture are calculated using local slope aspect and euclidean direction (to the epicentre/fault rupture). Values are normalised to a 0-180° scale so that values of 0/180° indicate a facing/opposing slopes to the epicentre respectively. This was calculated using the following formula (Parker *et al.*, 2015; Robinson *et al.*, 2017):

$$E_a = \begin{cases} |(|E_d - As|) - 360|, & |E_d - As| > 180 \\ |E_d - As|, & |E_d - As| \leq 180 \end{cases} \quad [6]$$

Standard, profile and planform curvature layers were extracted to explore the effect of different measures of curvature.

Finally, raw elevation and relief values were extracted. The spatial distribution of ground cracks in relation to elevation has already been touched upon in the previous chapter, however it has also been incorporated into statistical analysis to further quantify its influence. Ground cracks can be expected to be more prevalent at higher elevations due to the influence of topographic site effects (Meunier *et al.*, 2008). However, the link between ground cracking and incipient landsliding (e.g. Petley *et al.*, 2005b) means that the location of cracks may predominantly be governed by hillslope failure. Regional and local relief, justified by average hillslope length, was calculated using the standard deviation of elevation values within a 1 km and 100m window respectively. The prevalence of ground cracks is expected to increase as relief increases as this could indicate sharper

increases in elevation, and therefore slope angle. It has already been outlined (*Ch. 5*) how both of these factors may control the occurrence of ground cracking.

7.3. STATISTICAL ANALYSIS

7.3.1. Kernel Density Estimation

Layer values for ground cracks and the rest of the study area respectively were imported into Stata (StataCorp, v. 15) for statistical analysis.

Kernel Density Estimation (KDE) was used to measure the influence of unique values of each factor by comparing the prevalence of these at ground crack locations and throughout the rest of the study area (Robinson *et al.*, 2017). KDE approximates the frequency density of values in a dataset, similar to a histogram (StataCorp, 2017) but provides a smoothened probability density distribution (Cox, 2007). It is superior to histograms due to its ability to use overlapping intervals to obtain frequency density (StataCorp, 2017), thus reducing the need for arbitrary binning and issues that may arise from this such as data omission and obscuring (Cox, 2007). Smoothing can also reduce any sampling variation/irregularities, typical of geomorphological datasets (ibid).

Despite its advantages, one challenge with KDE comes when resulting curves need to be differenced to calculate the overall influence of a given factor. When generating resulting curves, KDE selects x-values systematically in consultation with the dataset, which it then uses to draw the curve. As such, different x-values will be created and used to draw the curves for the ground cracks and study area datasets respectively, meaning that they cannot be (accurately) differenced. To overcome this, an approach was developed to ensure that both curves were drawn using the same respective x-value intervals. These were parameter-specific and decided based on the data range. If the interval chosen was too small, the KDE curve would be too noisy; too large and it would be too generalised. All ranges used can be found in ***Table 7.1.***

***Table 7.1**: Parameter ranges used in Stata to normalise both ground crack and study area influence curves.*

Parameter	Minimum	Maximum	Range/Grid
Lc	0 m	3550 m	710 (5 m)
Cs	-25 m^{-1}	25 m^{-1}	1000 (0.1 m^{-1})
E	128 m	678 m	1110 (0.5 m)
Ea	0°	180°	360 (0.5°)
Fr	0 m	2550 m	510 (5 m)
Hr	0 m	95 m	190 (0.5 m)
Sr	0 m	45 m	90 (0.5 m)
Rt	0 m	660 m	660 (1 m)
Sa	0°	88°	350 (0.25°)
Sv	0°	180°	360 (0.5°)
V	0 m	410 m	410 (1 m)
R	0 m	17 m	170 (0.1 m)

Once all curves were created, study area curves were differenced from ground crack curves for each parameter to determine the influence (positive or negative – ***Fig. 7.08***) of a certain parameter on ground cracking (Robinson *et al.*, 2017). These were then normalised to enable aggregation:

$$I_{x_{\text{norm}}} = \frac{I_x - \min(I)}{\max(I) - \min(I)} \quad [7]$$

After initial attempts, it was decided to pre-process the curvature layer for the sake of attaining a more meaningful membership function. Due to the high-resolution of the airborne Light Detection and Ranging Data (LiDAR), extreme outliers were skewing results and making statistical analysis much more complicated and computationally taxing. In reality, these outliers represented < 0.01% of the data. After inspecting the raster layer and isolating outliers, it was decided that they were unlikely to be real. As such, they were discarded. A semi-data-driven approach was used to isolate outliers as opposed to using a purely data-driven (e.g. using standard deviation) as the latter would have resulted in discarding larger amounts of data. Given the smoothing capabilities of KDE this would have been unnecessary.

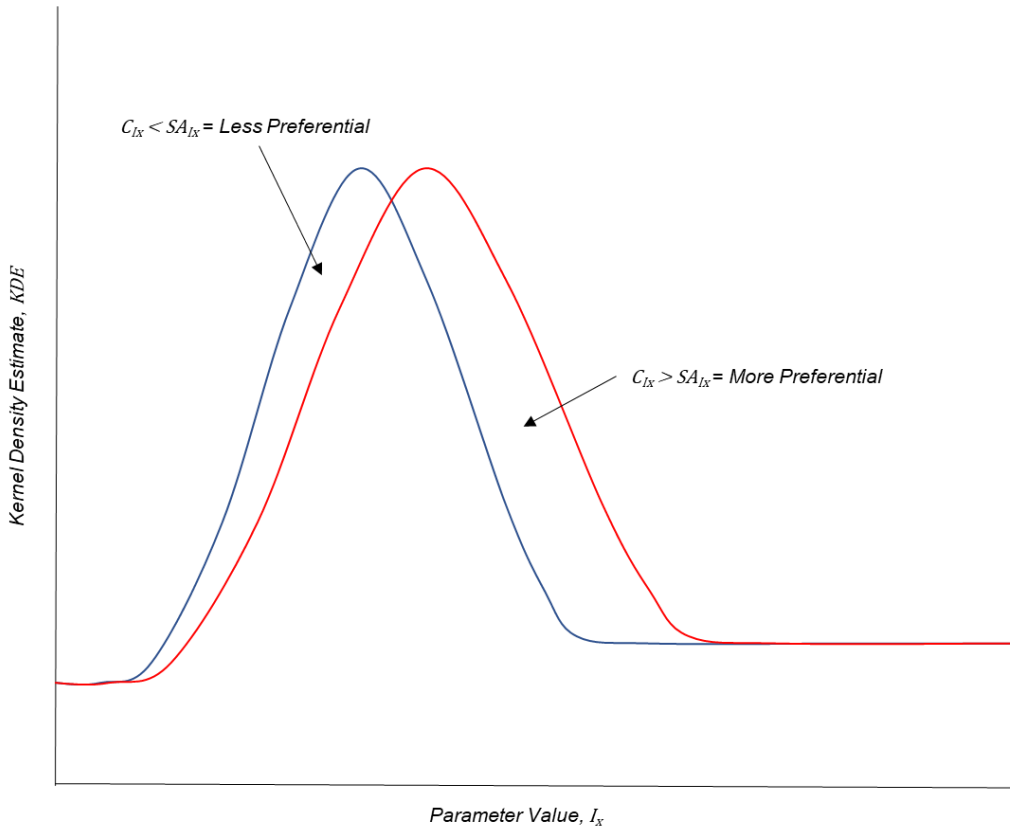

***Fig. 7.08**: Simplistic graphical explanation to describe the relationship between the ground crack (Cix) and study area (SAIx) curves, and what this means in real terms.*

7.3.2. Membership Functions

SigmaPlot (Systat Systems Inc., v 14) was used to semi-quantitatively assign (multiple in some cases) membership functions to raw influence curves. The purpose of this is to smoothen out the data and make findings more widely applicable by identifying generalised relationships. This was a semi-data-driven process, as membership functions had to be fitted whilst considering real-life mechanical processes (Robinson *et al.*, 2017). Data-driven approaches on the other hand focus more on the statistical accuracy of a function. This may render a function less realistic and more site-specific, and therefore less widely applicable, and so using expert elicitation along with the statistical data is a sensible compromise (Kritikos & Davies, 2014).

Functions had to be both realistic and statistically significant, in that R^2 values had to be acceptable, and p values < 0.05. However, fitting a realistic function took precedence over statistical significance, so long as the aforementioned criteria were met. Robinson *et al.* (2017) considered each influence curve and membership function in line with pre-existing knowledge on coseismic landslide mechanics. This enabled them to discard some parameters based on their lack of influence and alter the membership functions of those

carried forward to most suitably reflect expected processes. This cannot be done to the same extent in this study as little is currently known about coseismic ground cracking, however; sampling errors can be accounted for, expected relationships taken into consideration and parameters can still be dropped based on their lack of influence.

Influence curves were examined, to determine whether or not they should be carried forward to the regression stage. Regression Wizard in SigmaPlot was then used for this. A number of curves of polynomial, gaussian, exponential and power origin were fitted to each influence curve before the most realistic, representative and statistically significant was selected and carried forward for each factor.

7.3.3. Fuzzy Gamma

Spatial distribution layers were transformed into influence layers for each topographic/proximal control using their requisite membership functions. All influence layers were then aggregated via Fuzzy Overlay with gamma used as the overlay function. A gamma value has to be manually input. A value of between 0.8-0.9 has been used in similar previous studies (***Fig. 7.09***). However, as this was specific to coseismic landslide hazard, it was decided to undertake independent investigation into the optimum gamma output for coseismic ground cracking, as this influences the balance between influential/non-influential factors in the calculation of overall susceptibility (Kritikos & Davies, 2014) which may differ according to the hazard in question and result in severe inaccuracies if not addressed. An appropriate gamma value should assign high/low susceptibility values to areas covered by cracking/normal conditions respectively (*ibid*). The workflow for this will be elaborated on in the Results (*Ch. 7.4.2.2*).

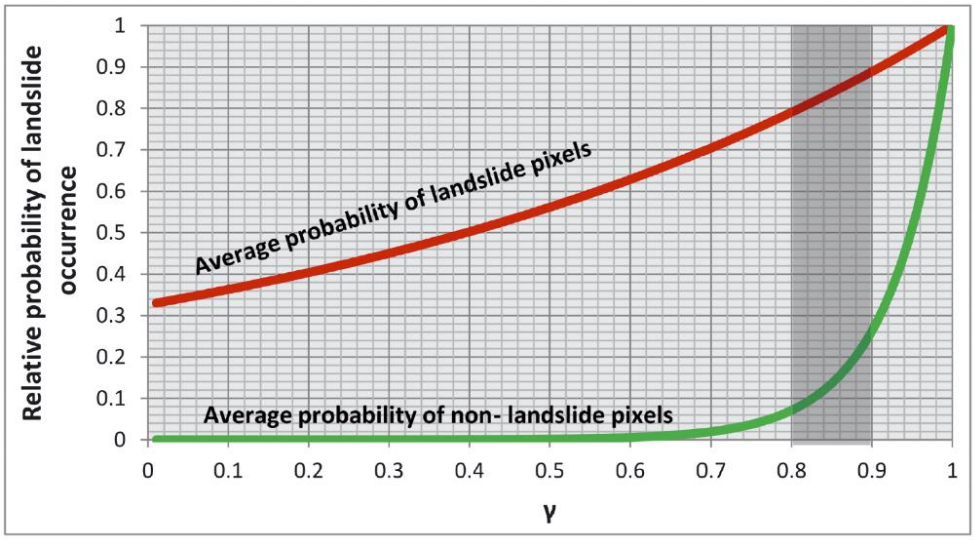

***Fig. 7.09**: Optimum gamma values, as used by Kritikos et al. (2015).*

7.3.4. Accuracy Assessment and Sensitivity Analysis

The final step in the process is a detailed accuracy assessment and sensitivity analysis. Accuracy assessment will quantify to what extent the model has predicted the spatial distribution of coseismic ground cracking. Sensitivity analysis will determine the best performing classification output, and in turn the most influential controls on the occurrence of coseismic ground cracking; as well as the optimum value for converting this into a binary product indicating 'cracked' and 'non-cracked' areas respectively. This knowledge can be harnessed and potentially used to predict where these conditions may be present, as recurrence may indicate future failure (Dai & Lee, 2002).

Success rate curves (e.g. van Westen *et al.*, 2003; Remondo, 2003) have been used for this purpose. Receiver Operating Characteristic (ROC) curves can quantify accuracy (in this case the number of cracked locations which are correctly assigned high FG values) by comparing true and false positive (TP/FP - both defined below) rates at threshold values (e.g. Metz, 1978). Area under curve (AUC) values can be used to inform sensitivity analysis by indicating the level of influence certain controls have on ground cracking through the comparison of the performance of model outputs with different combinations of input controls. All controls which had been continued (see *Ch. 7.3.3*) were used in a first attempt. Each layer was then in turn removed from the overlay attempt to see if the omission of a particular control improved the accuracy of the attempt, potentially indicating their importance on the occurrence of coseismic ground cracking.

Accuracy was measured by comparing each classification against ground truth data from the ground crack inventory. The ground crack inventory was converted into a binary raster, whereby pixels occupied by ground cracks equalled 1 and all other cells were 0. A threshold was then applied to each classification and converted into a binary raster at 0.01 intervals, where values above the threshold indicated locations where the occurrence of ground cracking was likely. These were assigned a value of 1. Values below the threshold were assigned a value of 0, indicating that the occurrence of cracking was unlikely.

Tabulate Area was used to compare classifications against ground truth data. TP, FP and relative true positive (RTP) rates were consequently extracted (Robinson *et al.*, 2018). TP is a measure of the number of cells predicting ground crack occurrence, where a ground crack is actually present according to the ground truth data (GTD), as a percentage of the total number of ground crack pixels in the GTD. FP outputs the number of pixels predicating ground crack occurrence, where no cracking exists in reality, as a percentage of the total number of pixels where cracking is not present according to the GTD. The RTP rate measures the number of TP's as a percentage of all pixels predicting

ground crack occurrence, providing a measure of success independent of other parameters (the study area in this instance) (Robinson *et al.*, 2018). RTP also provides overprediction rates. TP and FP rates at each threshold were used to create ROC curves and consequently calculate the AUC for each modelled iteration to assess accuracy by quantifying how well it fits the data; and therefore, predicts the spatial distribution of coseismic ground cracking. In turn, this will indicate the relative importance of certain factors on the occurrence of ground cracking (sensitivity). If a model/iteration has an area under curve (AUC) value > 0.7 it can be considered successful/accurate.

7.4. RESULTS

7.4.1. Spatial Distribution and Influence

The difference in spatial distribution between ground crack locations and the rest of the study area, and the consequential influence of each tested parameter on the probability of coseismic ground cracking will be presented. Parameters displaying relationships which can be mechanically explained were carried forward and will be discussed in the forthcoming individual sub-chapters (*Ch's. 7.4.1.1-8*). Those which were discontinued will also be discussed (*Ch. 7.4.1.9*). Overall results can then both provide insight into the respective importance of each test parameter and inform an attempt at automatic feature prediction.

7.4.1.1. *Distance from Landslide Crowns, Lc*

Fig. 7.10a shows the spatial distribution of the proximity of all cells to coseismic landslide crowns. Most ground cracks appear to lie in close proximity to landslide crowns, apart from those in the north-west corner of the study area. Both ground crack and study area locations show a general decrease in KDE as *Lc* increases (***Fig. 7.10b***). The prevalence of ground crack locations peaks at ~200 m before decreasing rapidly to return to near background levels at ~1000 m. Study area locations follow a similar but more dampened pattern, with a less extreme peak at ~200 m and smoother tail off in KDE. These differences result in an influence curve which can be summarised using an exponential (decay) function (***Fig. 7.10c***), suggesting that coseismic ground cracking is heavily preferential nearer to coseismic landslide crown locations (***Fig. 7.10d***). By affiliation, it could be suggested that a landslide inventory may therefore be able to infer ground crack locations.

7.4.1.2. Standard Curvature, Cs

The Spatial distribution of *Cs* is shown in ***Fig. 7.11a***. Because of outliers, ***Fig. 7.11a*** does not provide any qualitative speculation as to the location of ground cracks in relation to *Cs* values. Both KDE curves (***Fig. 7.11b***) follow a normal distribution peaking at congruent *Cs* values (*Cs* = 0), but with differences in magnitude. Study area and ground crack locations peak at 0.14 and 0.06 respectively. As such, while ground cracks are observed most frequently on flat slopes (*Cs* = 0), the relative proportion of these slopes that are cracked is significantly smaller than for curved slopes. Conversely, convex and concave slopes (*Cs* < -3 or *Cs* > 3) have a significantly higher proportion of locations with cracks and therefore cracking is considered more preferential on these curved surfaces. The influence curve can be suitably modelled using an inverted normal (gaussian) distribution (***Fig. 7.11c***). Qualitatively, ground cracks are less preferential on flat surfaces, highlighted by the purple colour scheme in the Influence map (***Fig. 7.11d***).

7.4.1.3. Euclidean Aspect, Ea

Fig. 7.12a shows a clear delineation between slopes facing the epicentre (grey/red) and slopes facing away from the epicentre (blue/purple). Qualitatively, cracks appear to propagate on slopes facing the epicentre. Ground crack KDE generally decreases as angle increases, whereas study area KDE remains relatively constant. As such ground crack locations are more preferential than study area locations between ~0-60° (slopes facing the epicentre). They then become less between ~60° and 180° (tending towards perpendicular slopes and slopes facing away from the epicentre) (***Fig. 7.12b***). A quadratic polynomial function can be applied to this influence (***Fig. 7.12c***), which highlights that cracks are more preferential on hillslopes facing towards the epicentre (yellow) than on hillslopes perpendicular to or facing away from the epicentre (purple) (***Fig. 7.12d***).

7.4.1.4. Distance to Fault Rupture, Fr

The path of fault rupture is evident from ***Fig. 7.13a***. Qualitatively, there appears to be no relationship between ground cracks and proximity to fault rupture. Ground crack and study area KDE's follow the similar pattern of peaking ~200 m *Fr* and then decreasing (***Fig. 7.13b***). However, like *Lc*, there are differences in curve behaviour. At fault rupture locations (*Fr* = 0), ground crack locations are more preferential than the remainder of the study area. The initial peak in ground crack KDE is lower than that for the study area, suggesting that cracking is less preferential close to but not at fault rupture locations. Both ground crack and study area KDE's then decrease, until after ~1000 m *Fr*, ground crack

KDE spikes whilst study area KDE continues to decrease. Ground cracking is more preferential at these locations.

This spike dominates the influence curve (***Fig. 7.13c***) which has been fitted using a normal (gaussian) distribution. Ground crack influence peaks at fault rupture locations. The influence curve has not been fitted to this, as the rate at which influence decreases suggests that this may be due to sampling errors. Both the peak and trough have therefore been ignored when fitting the function. The translation of the membership function into an influence map (***Fig. 7.13d***) is interesting, with ground cracks clearly evident in both areas of high and low influence. To attempt to understand the normal distribution, the respective KDE for landslide locations has been added (***Fig. 7.13c***). The initial decrease in ground crack prevalence concurs with an increase in landslide incidence. This is to such an extent that the trough of ground crack prevalence and the peak of landslide incidence occur at the same *Fr*. Ground cracking then becomes more preferential as landslide incidence decreases, peaking and then decreasing ~1000 m *Fr*.

7.4.1.5. *Distance from Ridgetops, Rt*

Fig. 7.14a clearly shows the extent of ridgetops and scarps throughout the study area. Ground cracks show no initial qualitative affiliation to ridgetops throughout the study area. KDE decreases with increasing *Rt* for both ground crack and study area locations (***Fig. 7.14b***). However, there are two distinct spikes in the KDE of ground crack locations. As such, ground crack locations are more preferential at ~25 m (ridgetop shoulders) and ~175 m *Rt*. This is expressed in the influence curve (***Fig. 7.14c***), which is modelled using a number of functions including exponential (decay) and normal (gaussian). Both spikes are represented by the two waves of high incidence (yellow) (***Fig. 714d***). To aid interpretation, a KDE of landslide locations has also been plotted (***Fig. 7.14c***). Ground cracks are more prevalent close to ridgetop locations. The rapidly decreasing prevalence after ~25 m coincides with an increase and then peak in landslide incidence. Ground crack influence culminates in a second peak ~175 m. Landslide incidence is decreasing back to background levels at this point. This could infer that cracks are located both above the crests and below the toes of landslides.

7.4.1.6. *Slope Angle, Sa*

Ground cracks appear to occur on steep slopes ~40° (yellow). Ground crack KDE is less than study area KDE until ~20°, after which it peaks and remains greater than it (***Fig. 7.15b***). Ground cracking is therefore less preferential and more preferential on slopes <

and > ~20° respectively. The influence curve reflects this and has been fitted with a quadratic polynomial (***Fig. 7.15d***). The function has been manually altered to tend to 1 at ~40° as a decrease in influence does not make mechanical sense and is more likely to be due to a sampling limitation. As such, much of the study area is deemed to have a high influence on coseismic ground cracking (***Fig. 7.15d***). Flat areas are also clearly delineated.

7.4.1.7. *Direction to Fault Rupture, Sv*

Slopes facing towards (grey/red) and away from (blue/purple) fault rupture locations are clearly delineated in ***Fig. 7.16a***. Ground crack KDE generally decreases as *Sv* increases, whilst study area KDE remains relatively constant (***Fig. 16b***). Therefore, ground crack locations are more preferential at lower *Sv* values (slopes facing the nearest fault rupture location) and less preferential at higher *Sv* values (slopes facing away from the nearest fault rupture location). Influence can thus be reflected using a cubic polynomial (***Fig. 16c***). Influence values fall within a short range and differ across hillslopes (***Fig. 7.16d***).

7.4.1.8. *Distance from Valleys Bottoms, V*

Like ridgetops, valley bottoms are also clearly defined in ***Fig. 7.17a***. KDE decreases as *V* increases for both ground crack and study area locations (***Fig. 7.17b***). There are two spikes between 50-150 m where ground crack prevalence is greater than random, suggesting that it is more preferential at these locations closer to valley bottoms. This has been summarised using a single normal (gaussian) distribution due to the proximity of the two spikes (***Fig. 7.17c***) and transferred into an influence map which shows this spike in influence (yellow) just above the valley floor (***Fig. 7.17d***). Landslide KDE has been added to aid interpretation. The first peak coincides with peak landslide incidence, suggesting that cracks may be reflective of this. The second peak does not correlate with landslide incidence.

7.1.4.9. *Discontinued Parameters*

The study area is topographically diverse (***Fig. 7.18a***). The ground crack KDE curve is erratic with considerable peaks and troughs over scales as small as 100 m (***Fig. 7.18b***). Generally, it follows a similar pattern to the smoother background of the study area KDE, dipping below it at higher elevations. This is unrealistic and makes little mechanical sense. As such, no function has been fitted to explain the resulting influence curve (***Fig. 7.18c***).

Sub-Hillslope- (***Figs. 7.19a-c***) and Hillslope-scale (***Figs. 7.20a-c***) relief, *Sr* and *Hr*, and Roughness (***Figs. 7.21a-c***), *R*, display similar tendencies in that functions could easily be fitted to the resulting influence curves, however the lack of mechanical explanation means that they have not been. Ground cracking is more preferential at a *R* value of ~0.5 m. Given that the resolution of the data is 1 m, a *R* measurement of ~0.5 m is insignificant and does not link co-seismic ground cracking with the noticeable roughness that should be exhibited by co-seismic landslides.

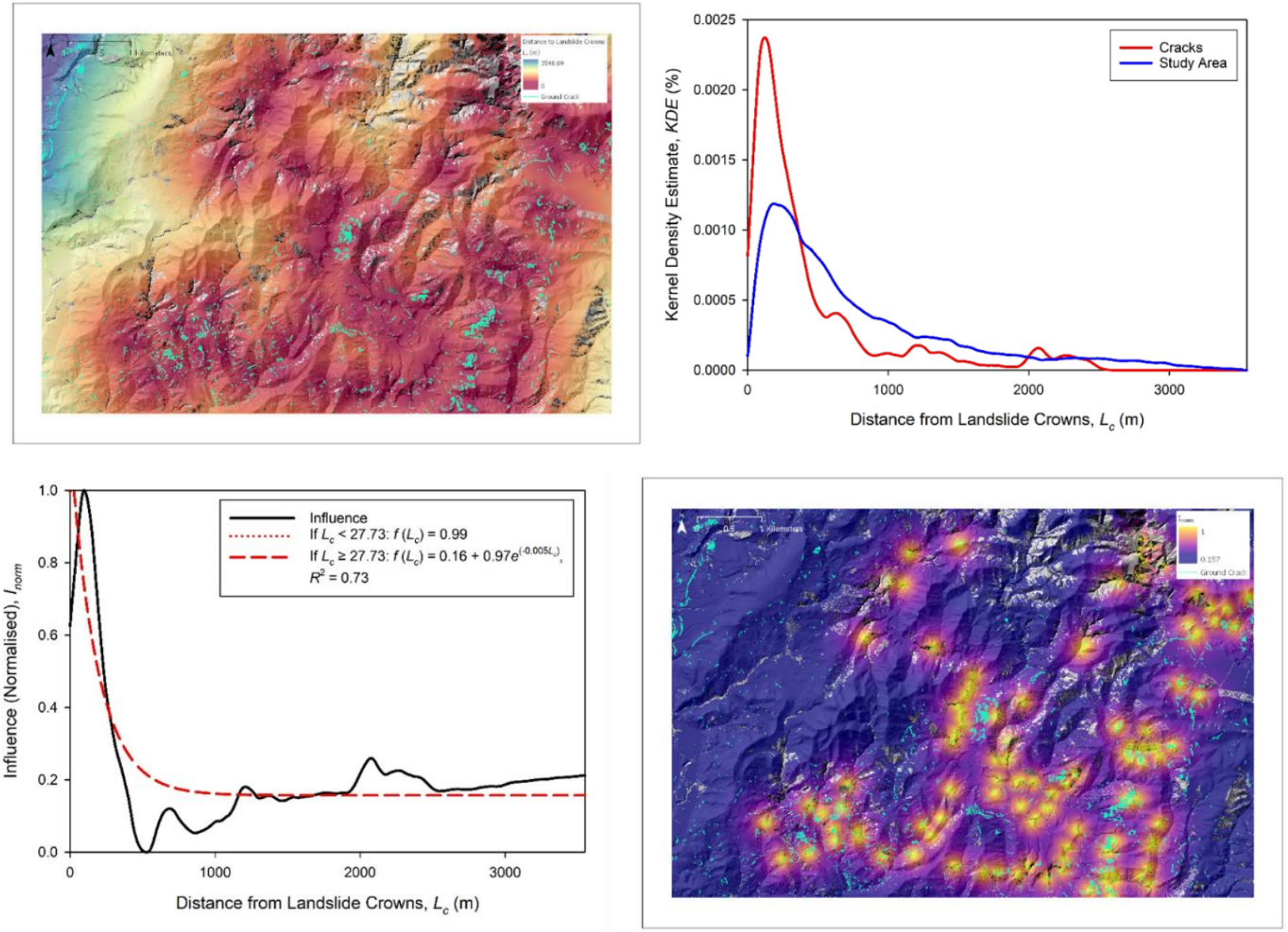

***Figs. 7.10a-d**: Distance to Landslide Crowns, Lc. **a**) Spatial Distribution map showing Lc values for all cells, overlaid by ground crack features; **b**) KDE curves for ground crack and study area; **c**) Influence curve and membership function; **d**) Influence map, created from the membership function.*

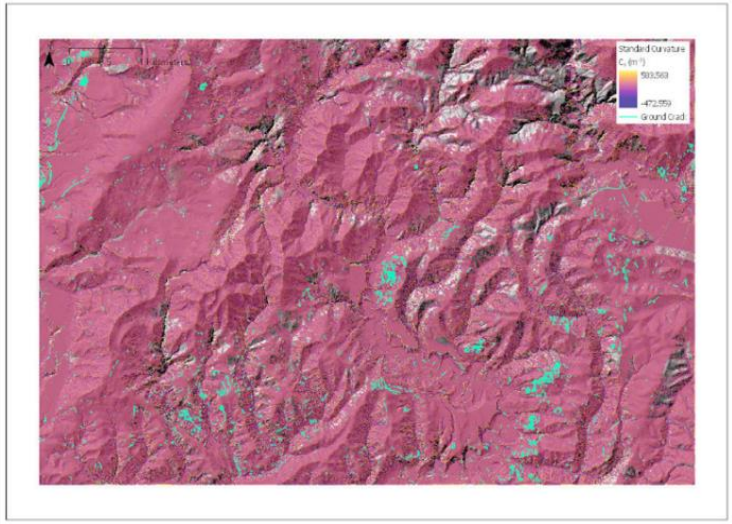

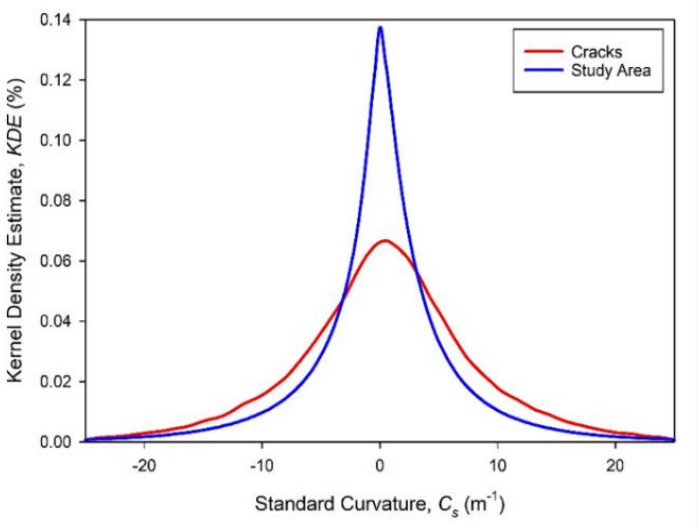

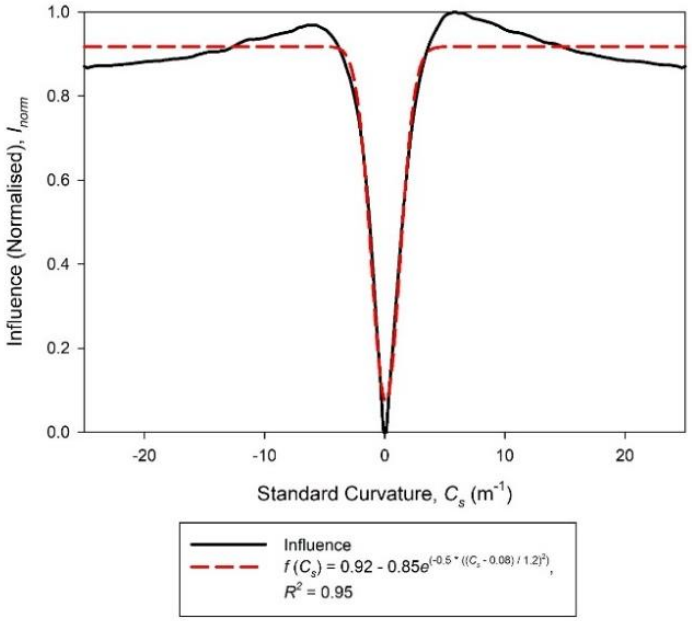

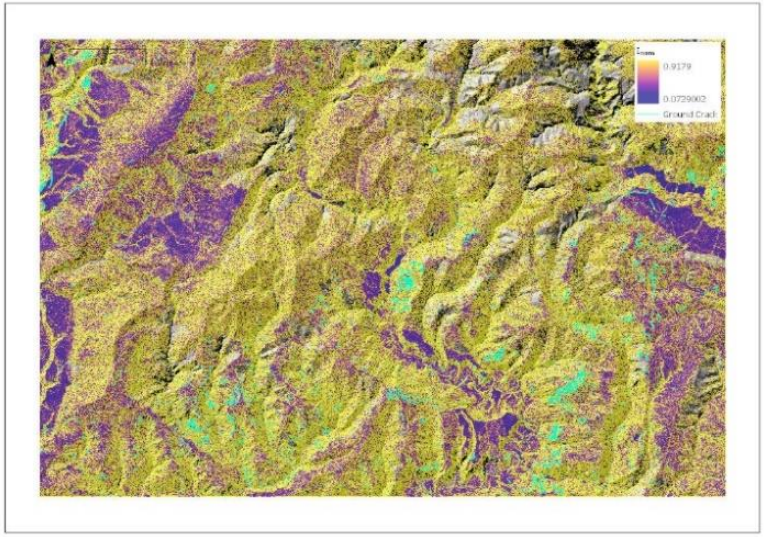

***Figs. 7.11a-d**: Standard Curvature, Cs: **a**) Spatial Distribution map showing Cs values of all cells, overlaid by ground crack features; **b**) KDE curves for ground crack and study area; **c**) Influence curve and membership function; **d**) Influence map, created from the membership function.*

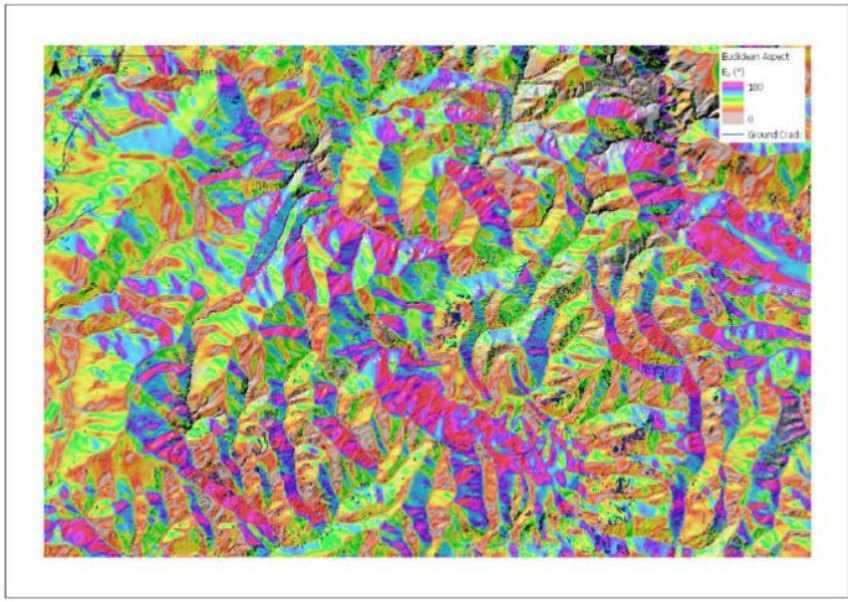

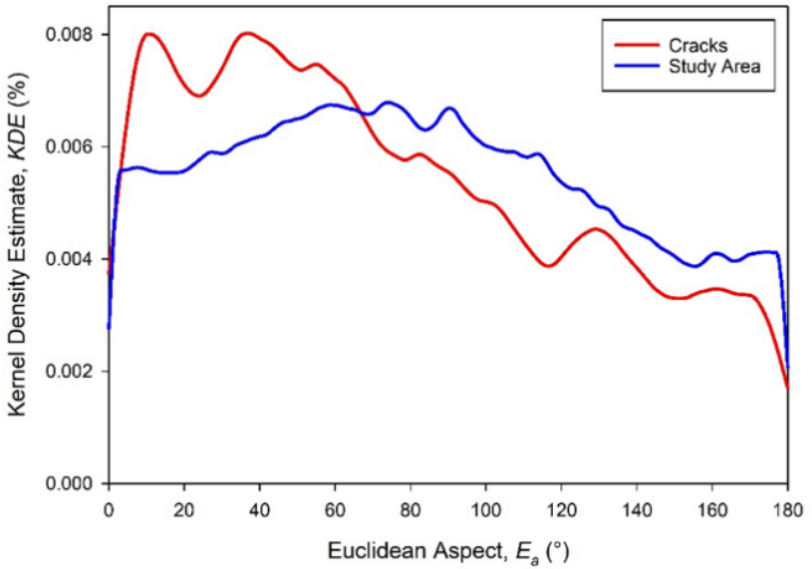

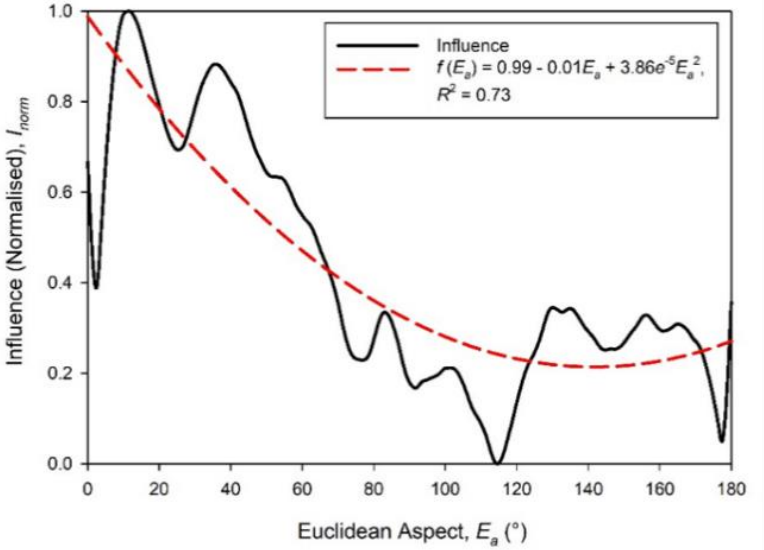

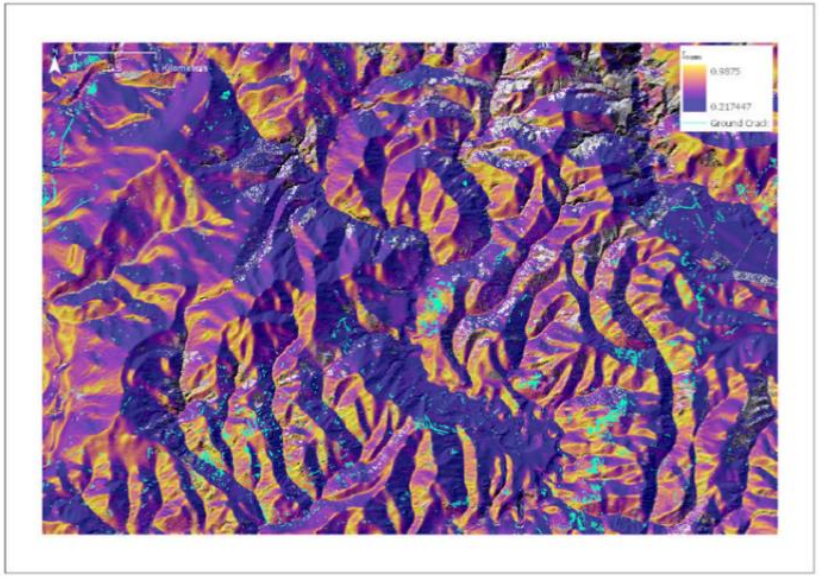

***Figs. 7.12a-d**: Euclidean Aspect, Ea: **a**) Spatial Distribution map showing Ea values of all cells, overlaid by ground crack features; **b**) KDE curves for ground crack and study area locations; **c**) Influence curve and membership function; **d**) Influence map, created from the membership function.*

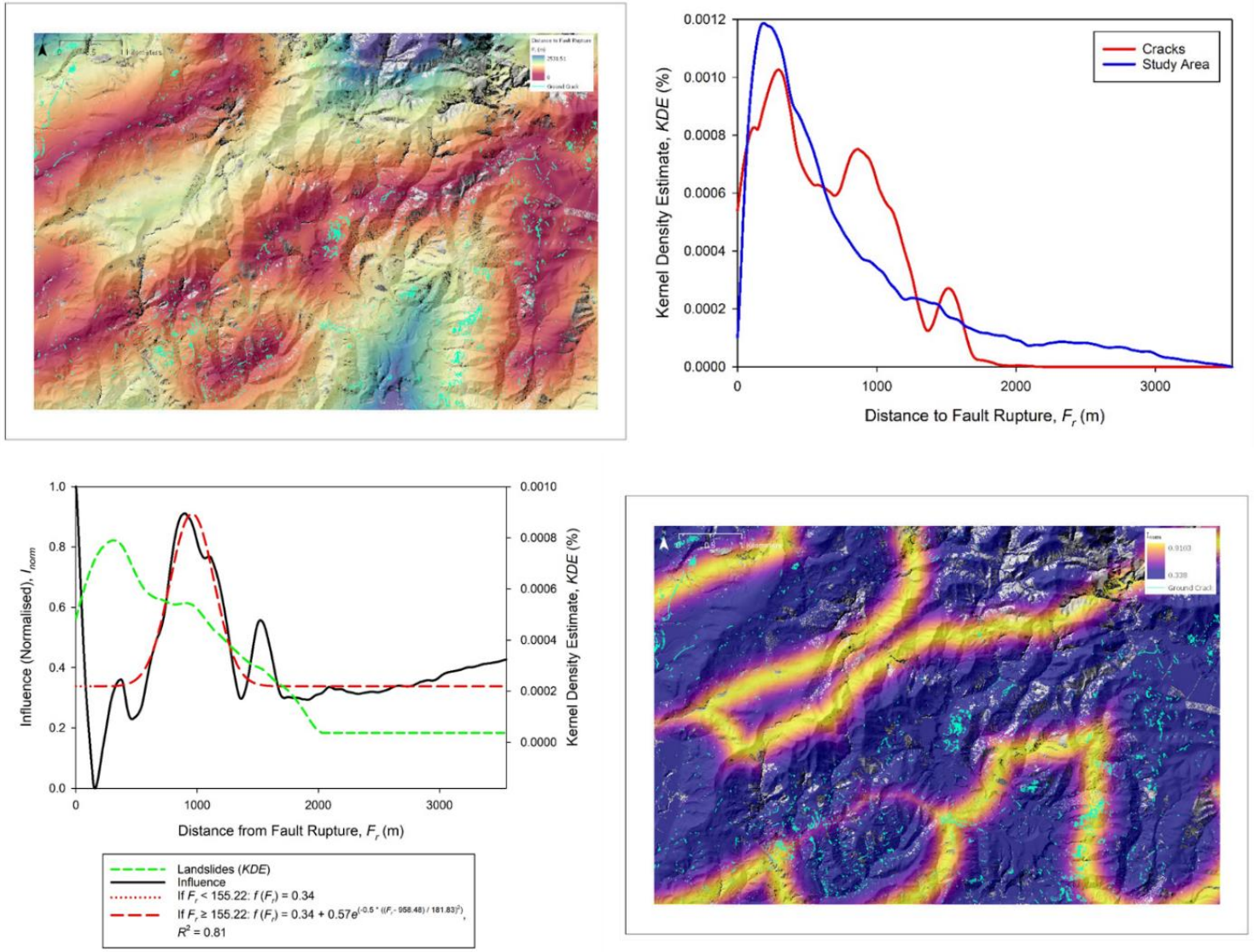

***Figs. 7.13a-d**: Distance to Fault Rupture, Fr: **a**) Spatial Distribution map Fr values of all cells, overlaid by ground crack features; **b**) KDE curves for ground crack and study area locations; **c**) Influence curve and membership function; **d**) Influence map, created from the membership function.*

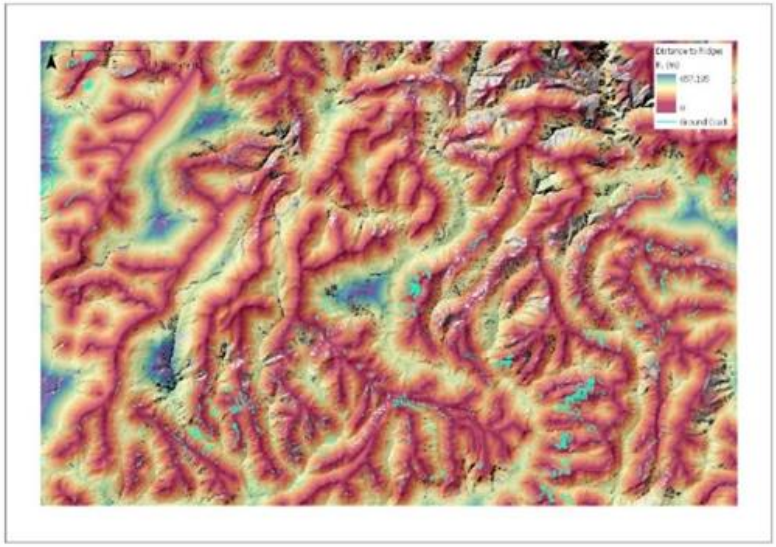

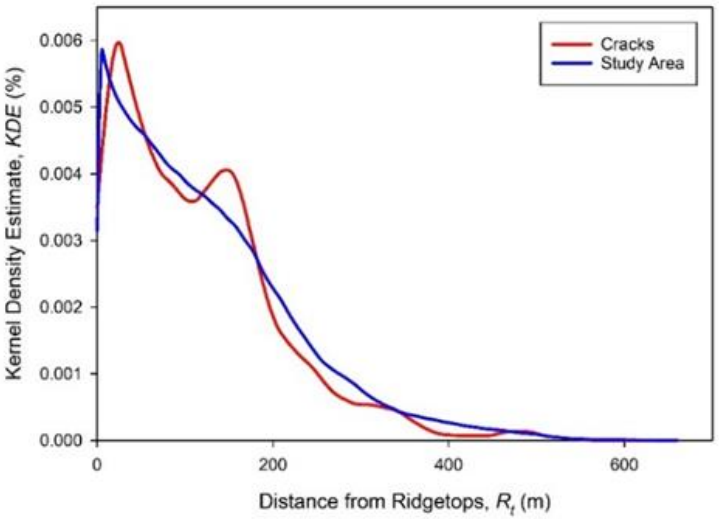

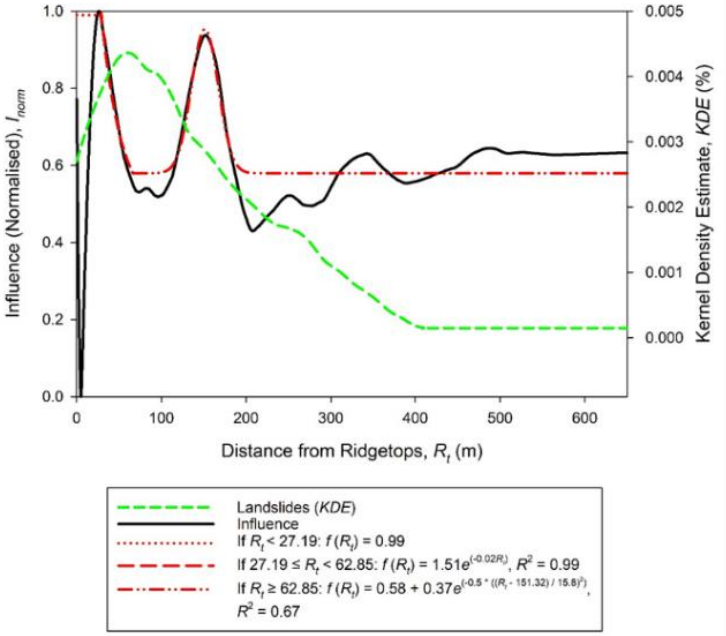

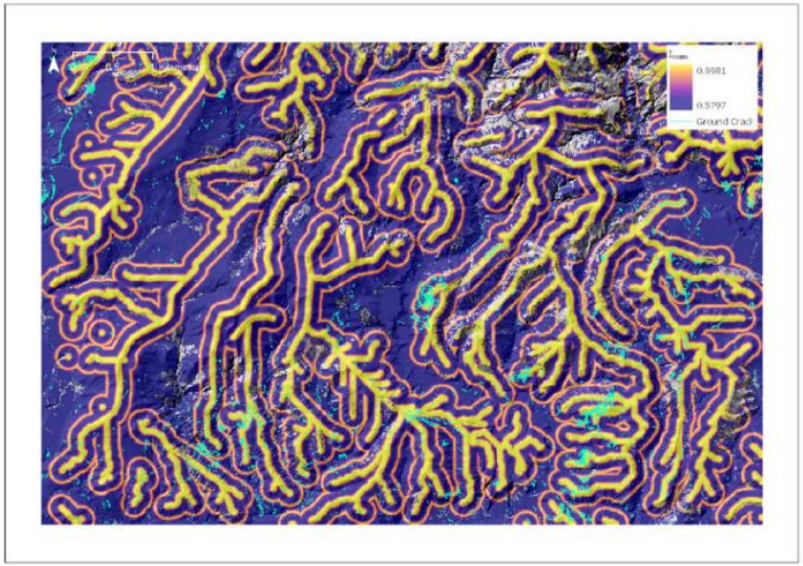

***Figs. 7.14a-d**: Distance to Ridgetops, Rt: **a**) Spatial Distribution map Sa values of all cells, overlaid by ground crack features; **b**) KDE curves for ground crack and study area locations; **c**) Influence curve and membership function; **d**) Influence map, created from the membership function.*

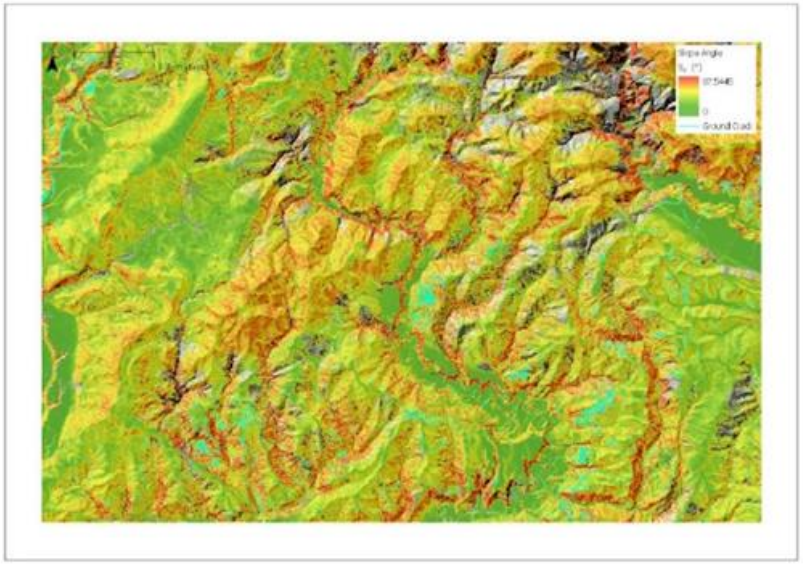

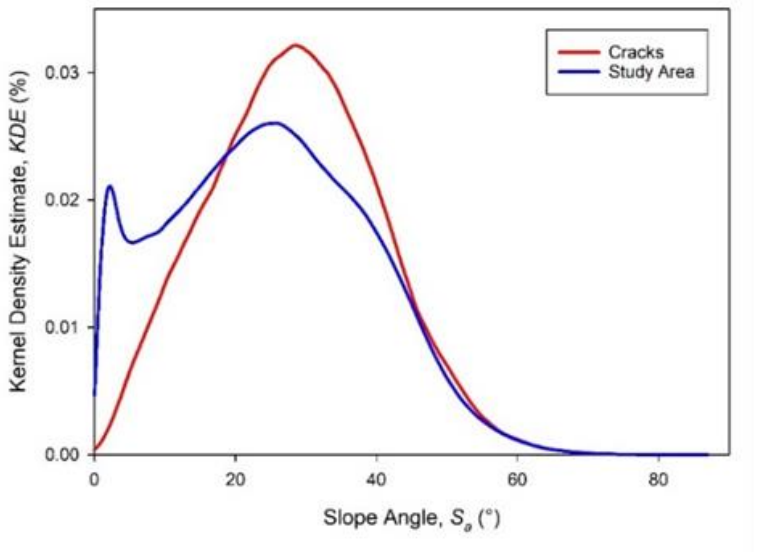

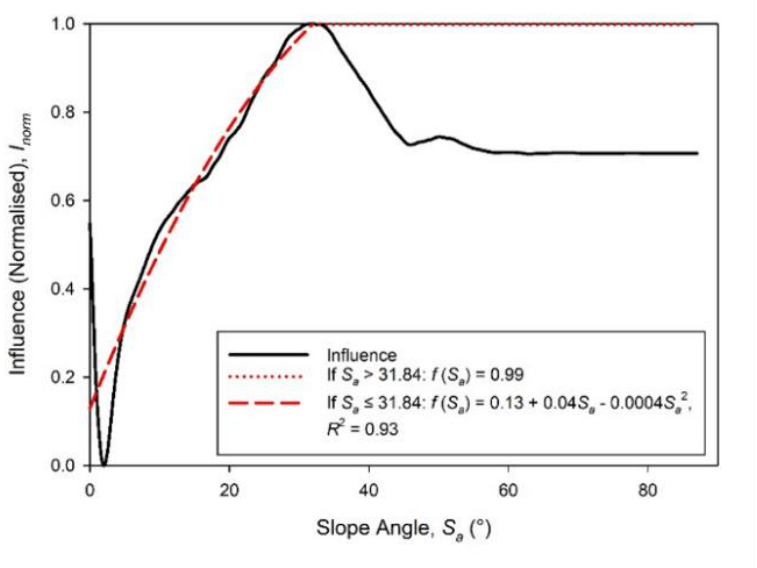

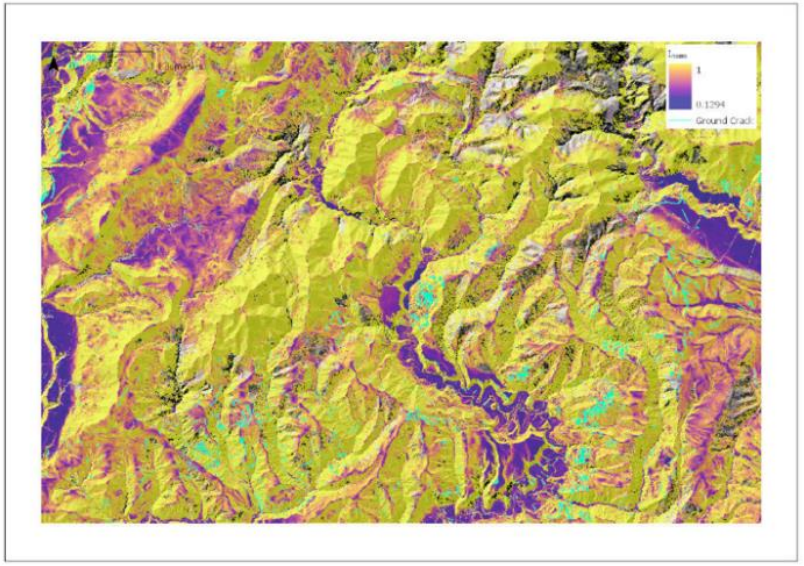

***Figs. 7.15a-d**: Slope Angle, Sa: **a**) Spatial Distribution map Sa values of all cells, overlaid by ground crack features; **b**) KDE curves for ground crack and study area locations; **c**) Influence curve and membership function; **d**) Influence map, created from the membership function.*

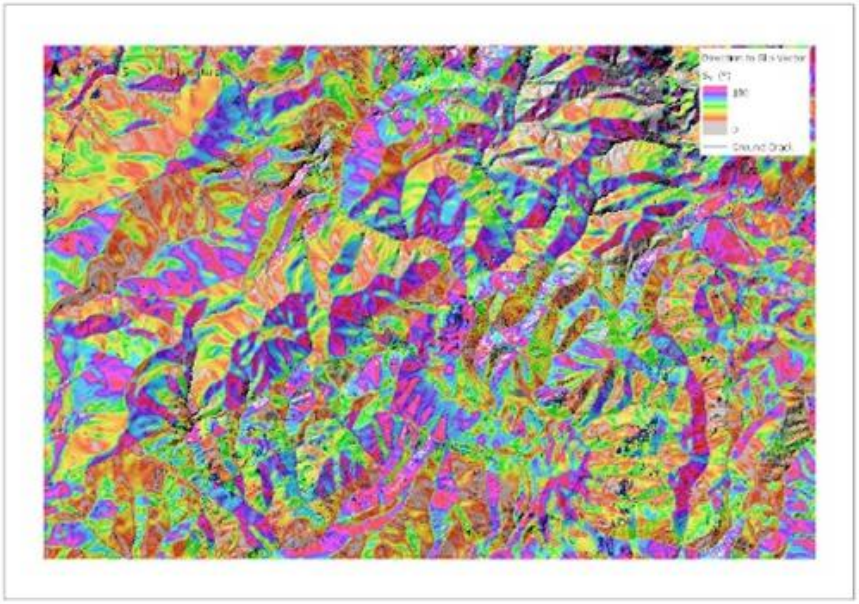

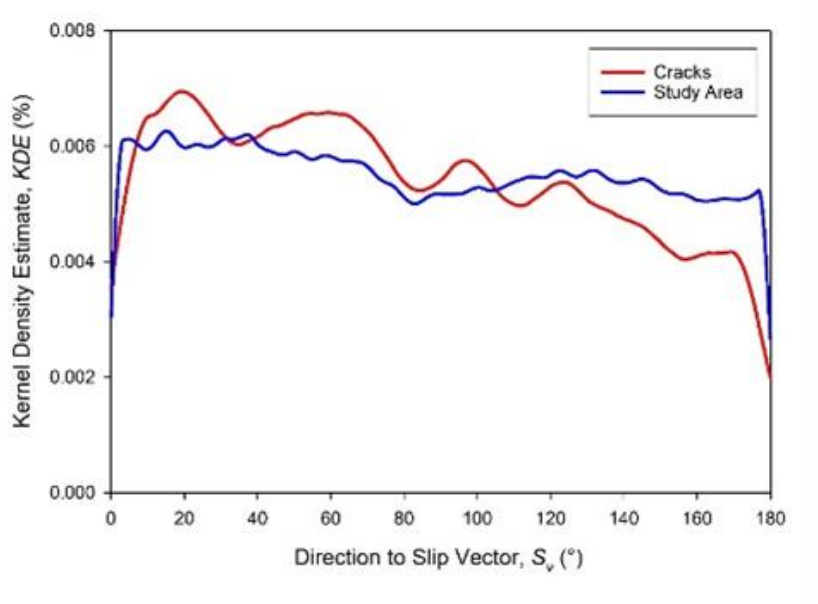

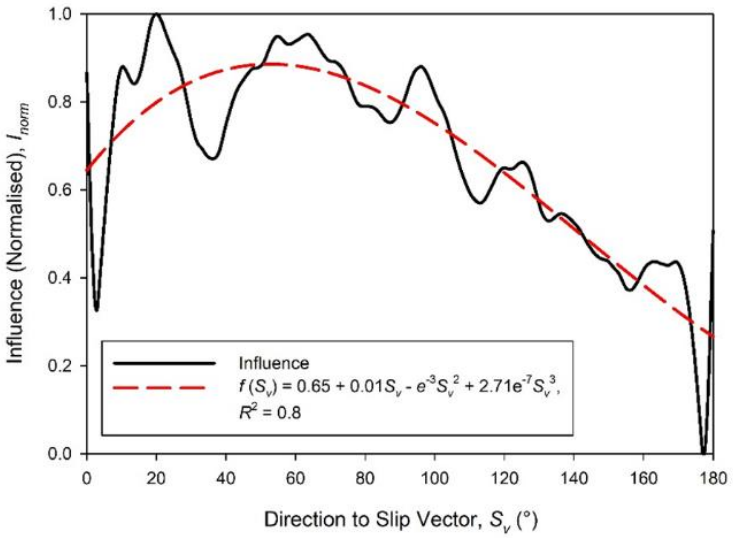

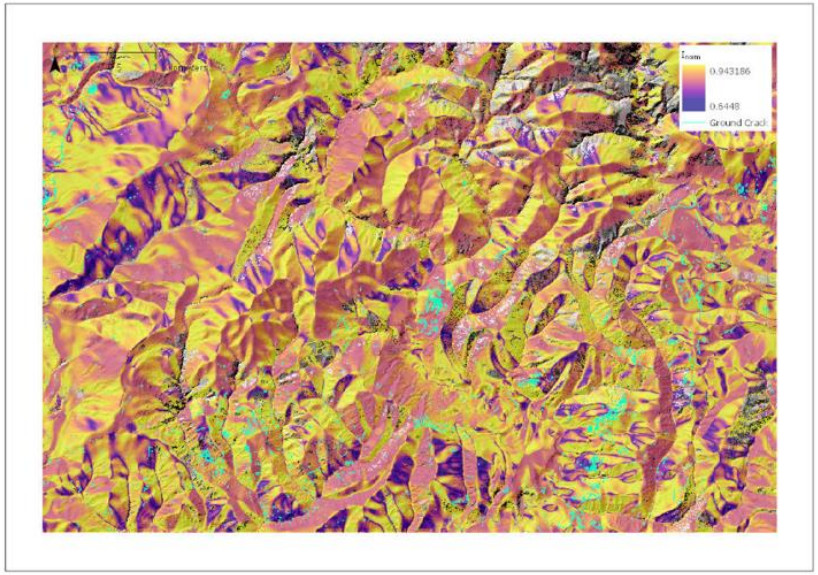

***Fig. 7.16a-d**: Direction to Slip Vector, Sv: **a**) Spatial Distribution map Sv values of all cells, overlaid by ground crack features; **b**) KDE curves for ground crack and study area locations; **c**) Influence curve and membership function; **d**) Influence map, created from the membership function.*

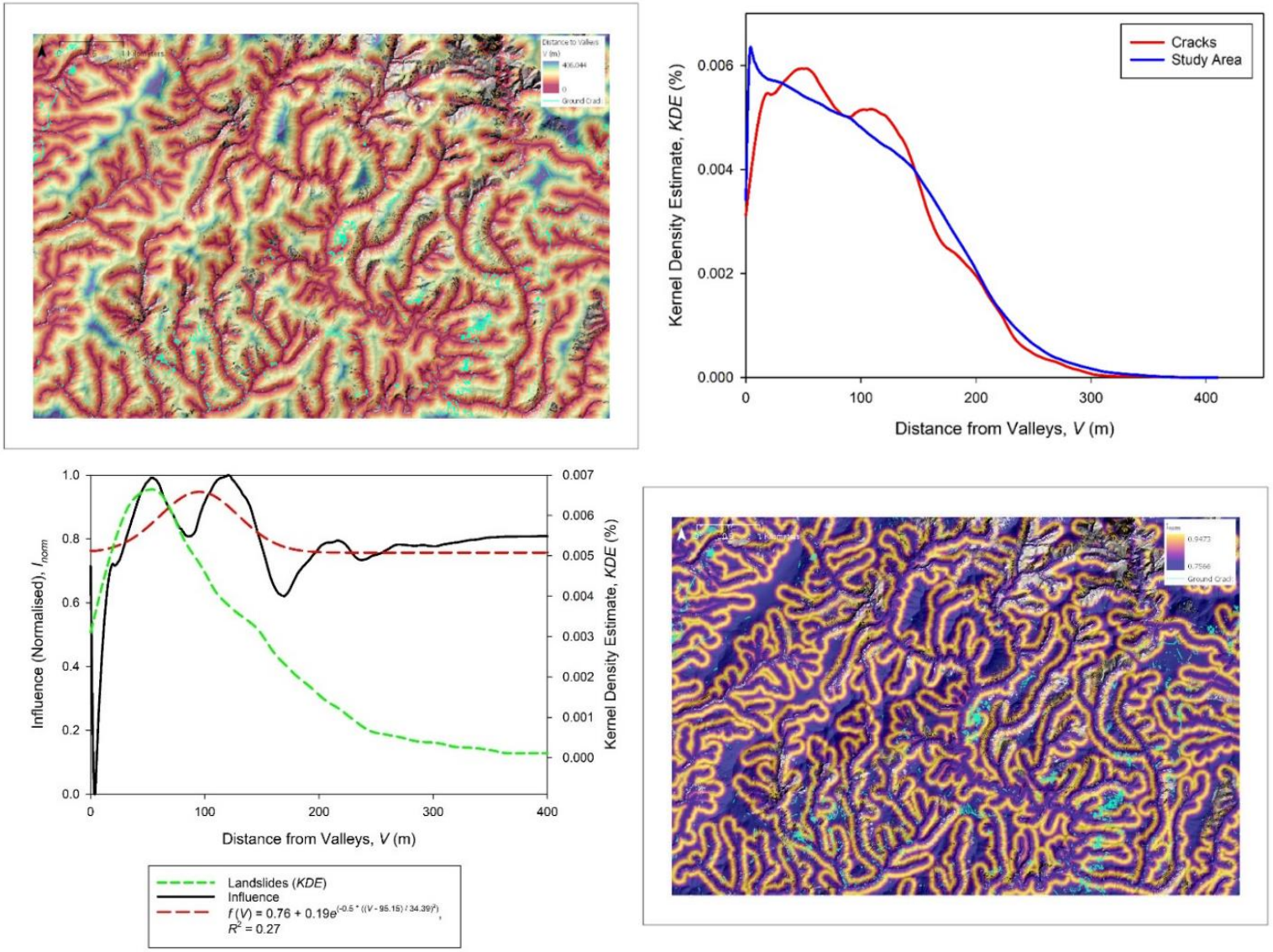

***Fig. 7.17a-d**: Direction to Valleys, V: **a**) Spatial Distribution map V values of all cells, overlaid by ground crack features; **b**) KDE curves for ground crack and study area locations; **c**) Influence curve and membership function; **d**) Influence map, created from the membership function.*

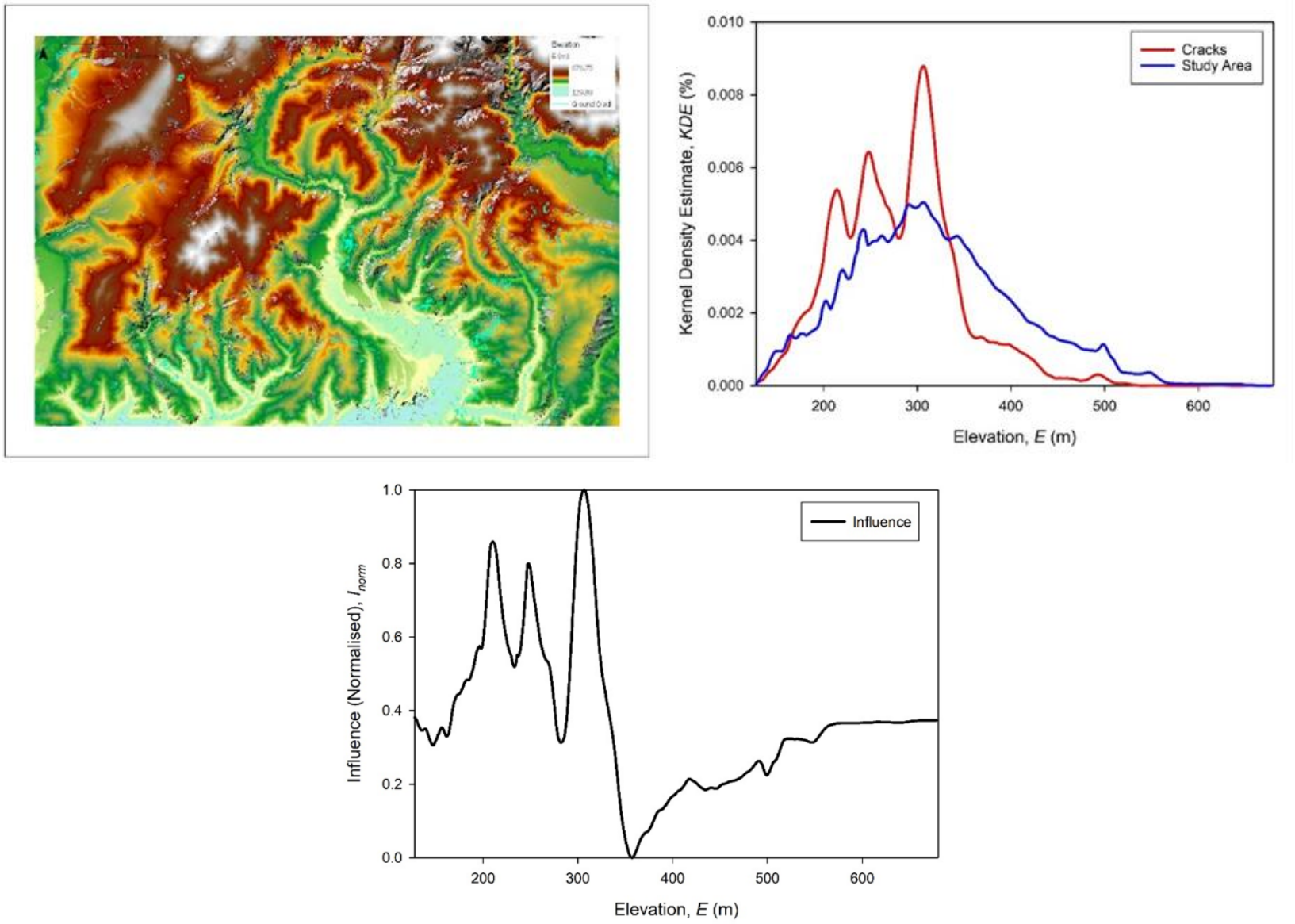

***Fig. 7.18a-d**: Elevation, E: **a**) Spatial Distribution map E values of all cells, overlaid by ground crack features; **b**) KDE curves for ground crack and study area locations; **c**) Influence curve and membership function.*

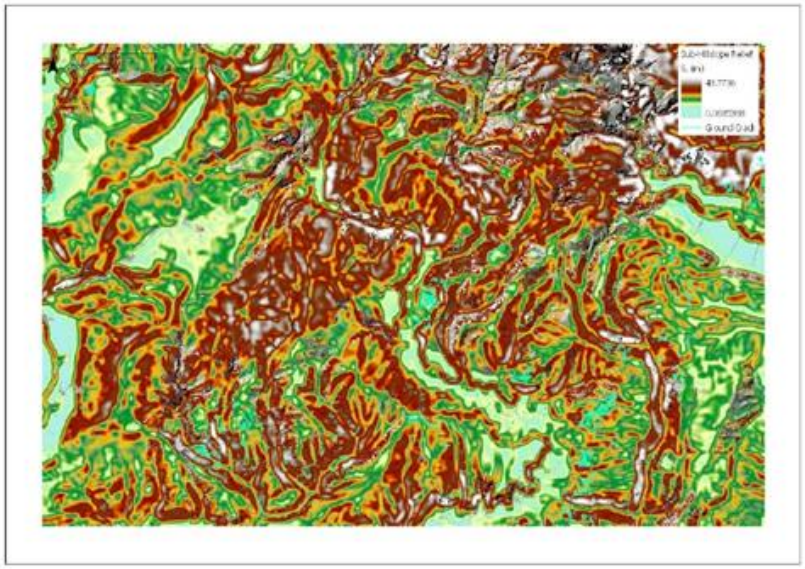

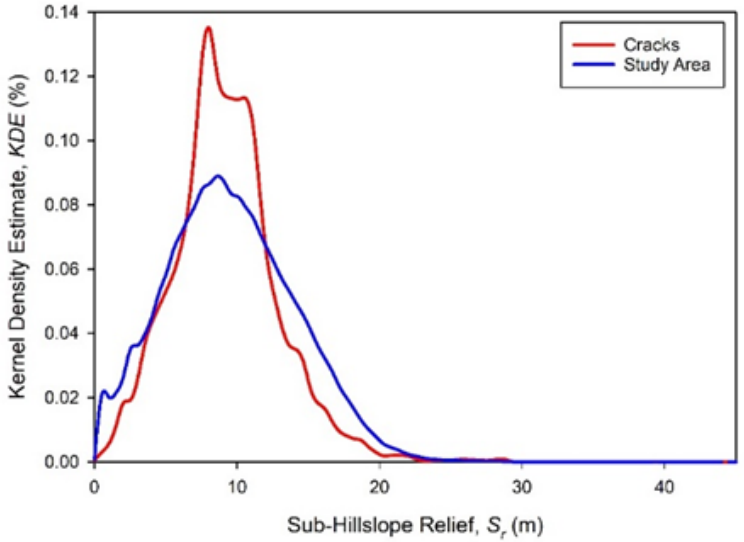

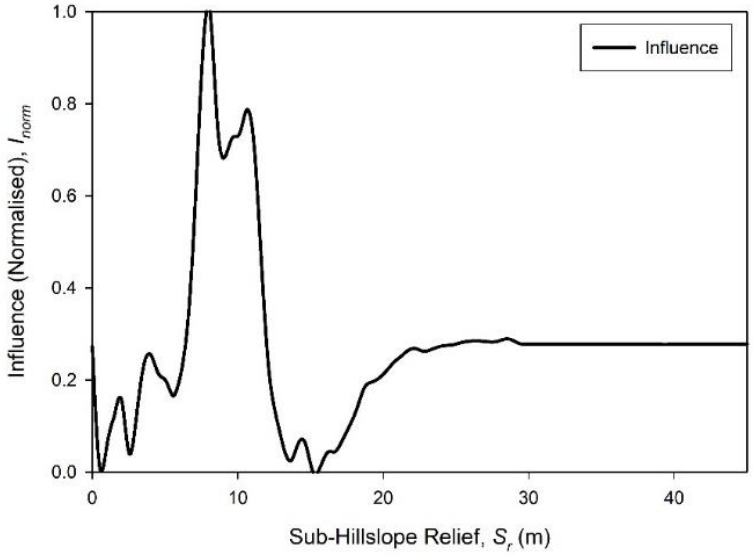

***Fig. 7.19a-c**: Sub-Hillslope Relief, Sr: **a**) Spatial Distribution map Sr values of all cells, overlaid by ground crack features; **b**) KDE curves for ground crack and study area locations; **c**) Influence curve and membership function.*

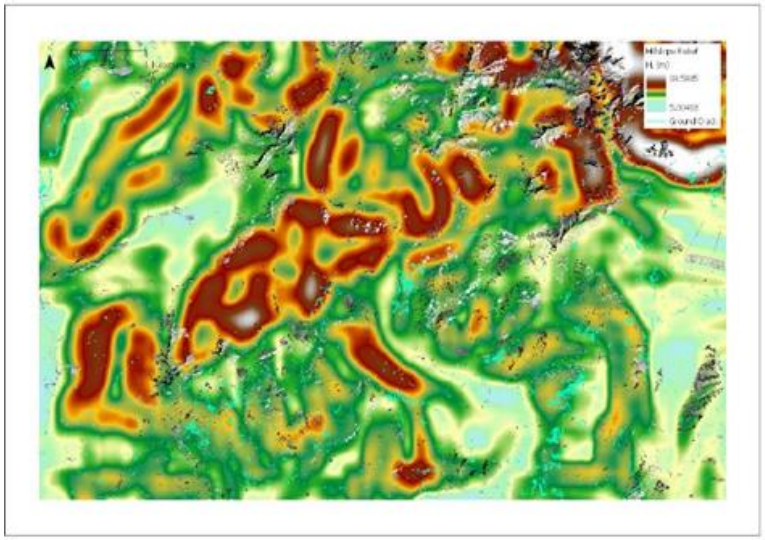

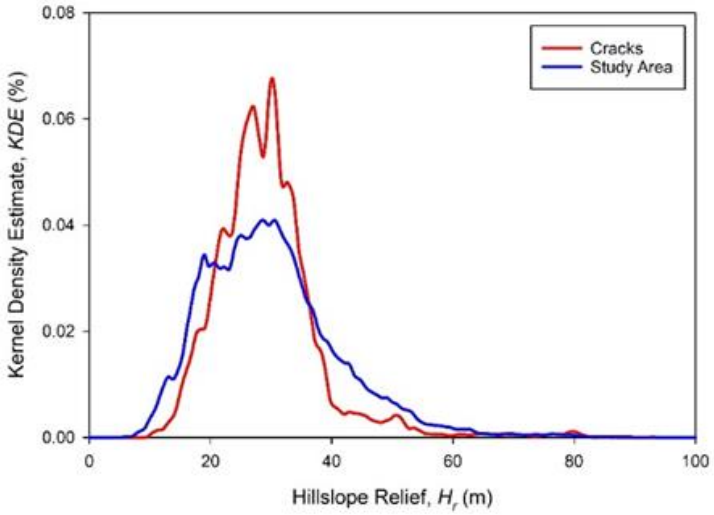

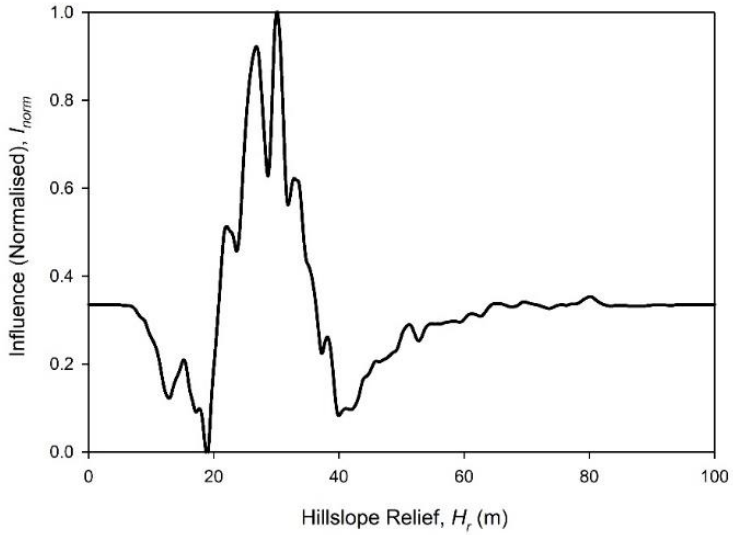

***Fig. 7.20a-c**: Hillslope Relief, Hr: **a**) Spatial Distribution map Hr values of all cells, overlaid by ground crack features; **b**) KDE curves for ground crack and study area locations; **c**) Influence curve and membership function.*

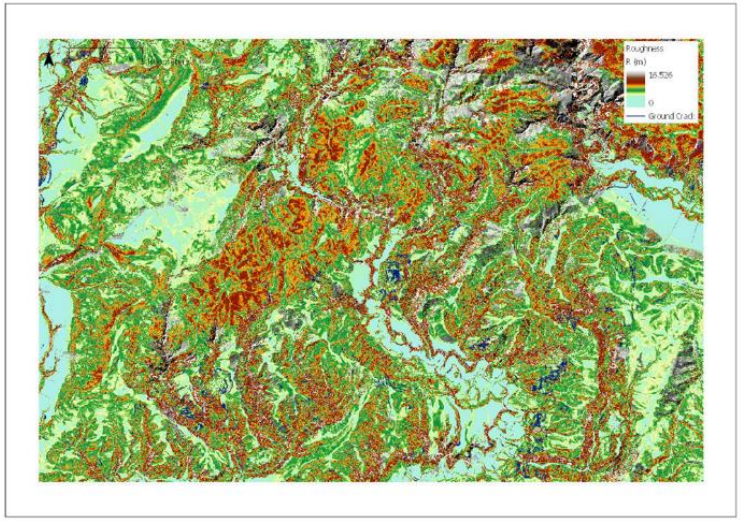

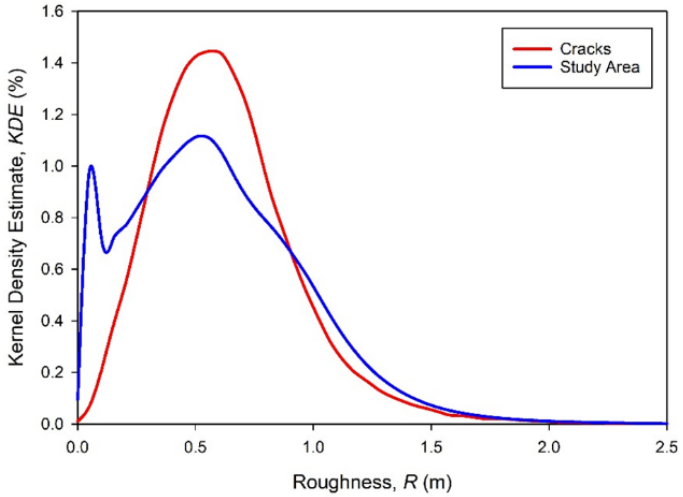

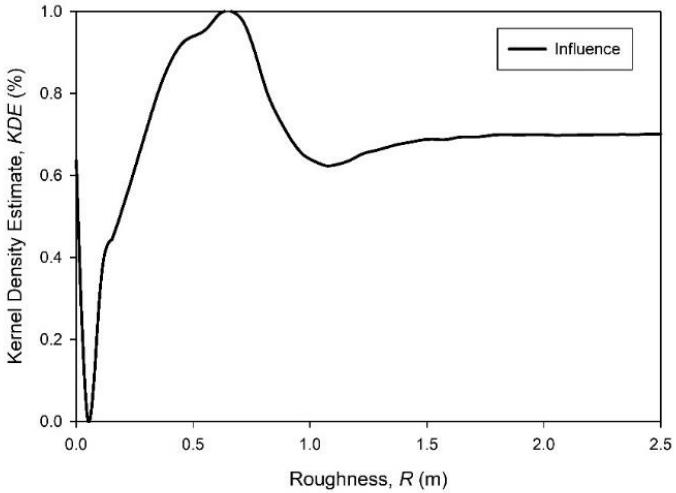

***Figs. 7.21a-c**: Roughness, R: **a**) Spatial Distribution map R values of all cells, overlaid by ground crack features; **b**) KDE curves for ground crack and study area locations; **c**) Influence curve and membership function.*

7.4.2. Aggregation and Accuracy Assessment

KDE/influence curves and resulting membership functions have highlighted which topographic parameters may control coseismic ground cracking (*Ch's. 7.4.1.1-8*). As such, these will be carried forward and aggregated in an attempt to detect areas where ground cracking may be preferentially located. To achieve the most accurate predictive outcome, models can be run using different parameter combinations and assessed against a control dataset, a binary raster produced from the ground crack inventory in this case. Doing this will also provide further insight into the relative importance of controlling parameters on ground cracking.

7.4.2.1. *Gamma Value*

The workflow of Kritikos & Davies (2014) was used for this purpose. Fuzzy Overlay using the membership functions of continued parameters (above – *Ch's. 7.4.1.1-8*) was iterated through increasing gamma values at 0.05 intervals between 0-1. 100 ground crack and study area pixels were randomly selected and overlay output values were extracted for each of these and plotted on a graph (***Fig. 7.22***). As per Kritikos & Davies (2014), the optimum gamma value must be estimated based off which one provides the greatest area between ground crack and study area curves. In this case, this was 0.7, however for a more conservative analysis, a value of 0.8 has been selected as the difference between 0.7 and 0.8 was marginal, and a value of 0.8 will assign more weight to ground crack controls as they are closer to the maximum threshold (ibid).

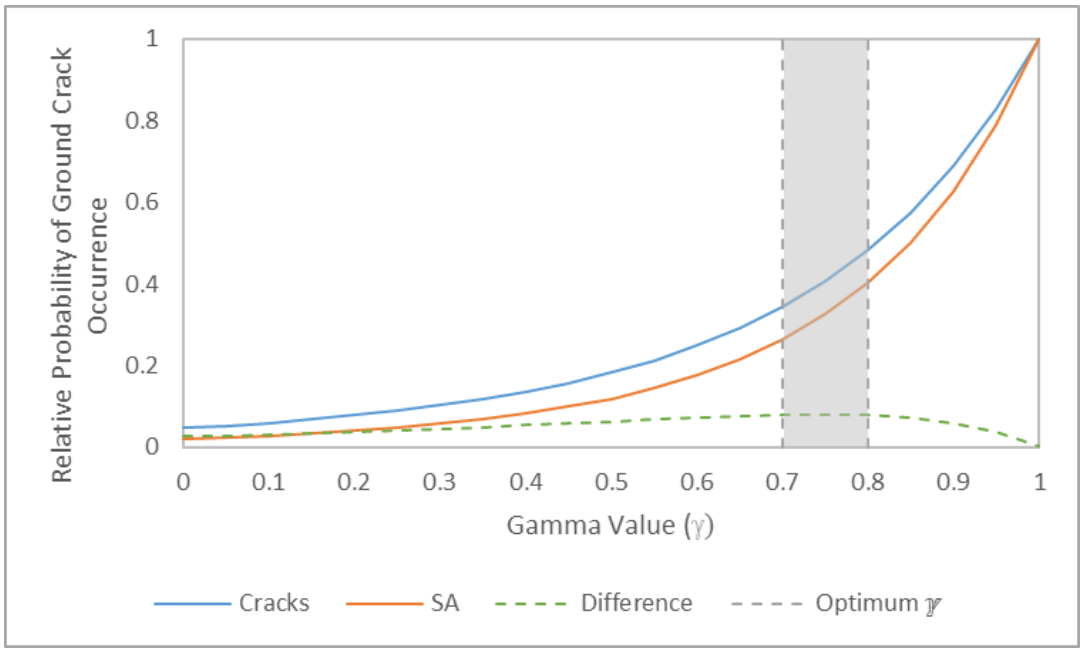

Fig. 7.22*: Graph comparing the relative probability of ground crack occurrence for ground crack and study area pixels. The difference between these two curves has also been plotted, and the optimum gamma range highlighted.*

7.4.2.2. Parameter Importance

Fig. 7.23 summarises the accuracy of all classification attempts. Classification using all eight parameters returned a benchmark AUC of 0.677 (yellow curve). AUC decreased by the greatest amount to 0.616 (red curve) following the omission of Lc. Given such, a classification attempt was run using only the membership function of Lc. This returned an AUC of 0.671, not too dissimilar from the benchmark classification using all eight parameters. Lc was then aggregated with Cs, Ea and Sa – as these also reduced the accuracy of model performance (albeit marginally) when omitted and returned three of the strongest membership functions. Model performance improved to 0.681.

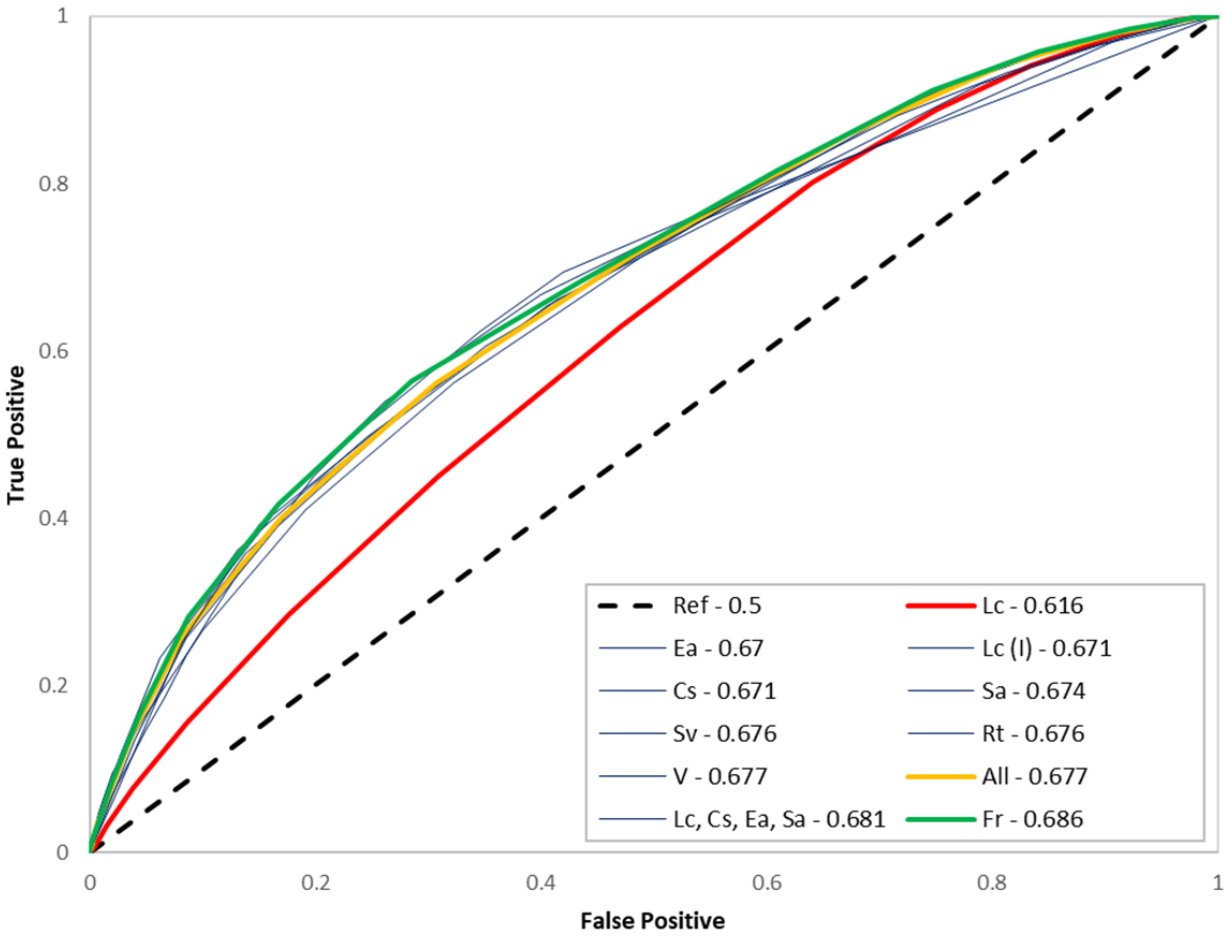

Fig. 7.23*: Receiver Operating Characteristic (ROC) curves, showing the ratio of true positive to false positive rates, for each model iteration run using Fuzzy Overlay. A reference curve has also been added for comparative purposes. Area Under Curve (AUC) values are listed for each model iteration in the key. Some curves have been coloured for visual purposes.*

The best performing model returned an AUC of 0.686 (***Fig. 7.23***) with the omission of Fr (green curve). Models with all other factors omitted either decreased or returned the same AUC, suggesting that they are important to the predictive model and significant controls on co-seismic ground cracking to some extent.

7.4.2.3. *Model Performance*

All models returned an AUC of > 0.5 (***Fig. 7.23***). This quantitatively/statistically confirms that coseismic ground cracking, and the influence of all eight continued factors on this, is not random (reference curve). However, as predictive tools none of the models can be considered statistically successful as no combination of factors produced an AUC > 0.7, which is required to deem a predictive model a success (Kritikos *et al.*, 2015). That said, this is a promising initial attempt and in reality, may only require some minor changes to membership functions or a more in-depth overall analysis than the scope of this study has allowed.

Therefore, the best-performing model (omission of Fr – green curve (***Fig. 7.23***)) was carried forward to produce a final predictive output (***Fig. 7.24***) and in turn, a binary predicting areas where ground cracks may, and may not, occur (described below). Qualitatively, the majority of ground cracks appear to be located in areas of higher hazard (***Fig. 7.24***). This suitably reflects the initial promise discussed in the previous paragraph. Areas of open field to the east of the study area are classified amongst the areas of lowest hazard, which is accurate. However, the model has not performed well in the NW region of the study area as it has classified the area as low hazard when in reality a number of ground cracks are present.

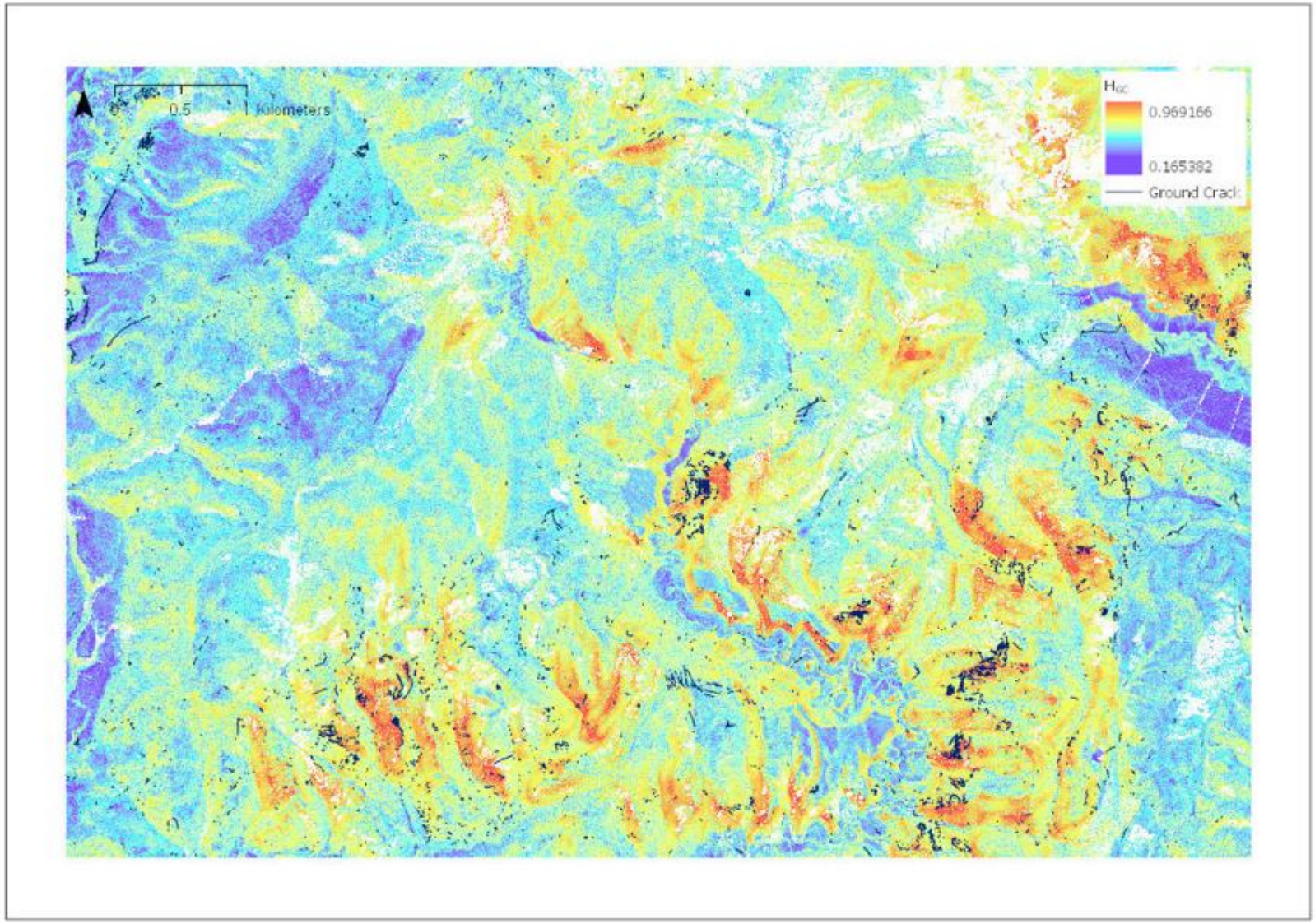

***Fig. 7.24**: Hazard of ground crack manifestation, HGC, according to a model run with the omission of distance to fault rupture, Fr. Areas of high (red/orange/yellow) and low (light/dark blue) hazard are evident throughout.*

A practical application of predictive models could be following an earthquake event to monitor hillslope which have been cracked but not developed to the point of full failure (e.g. Robinson *et al.*, 2018). To provide a suitable output, a hazard threshold must be ascertained using the extracted TP and FP rates. As an attempt at a best-performing model, sensitivity testing was undertaken on the best-performing classification output (***Fig. 7.24***). This was to determine which value provides the best threshold, in that values above it resonates with the occurrence of ground cracking (high hazard), and values below do not. This workflow follows that of Robinson *et al.* (2018). Extracted TP, FP, RTP and false negative (FN) rates were plotted against threshold value at 0.01 intervals. FN is the number of pixels predicting no ground crack presence, where this is actually the case in reality. The threshold with the largest area under the curve (AUC) value between the TP and FP curves was quantitatively deemed the best threshold value – 0.55 in this instance (***Fig. 7.25***). This is the point just before the FN rate increases beyond 50%, indicating that it is a suitable compromise. RTP rates remain miniscule throughout (<1%) until an unsuitable threshold of > 0.9 where the increase stems from the TP rate tending towards 1. This was then used to inform the final output, in that this was used to threshold the best-performing classification and produce a final binary raster highlighting areas where ground cracking is likely to have occurred, and areas where it is not.

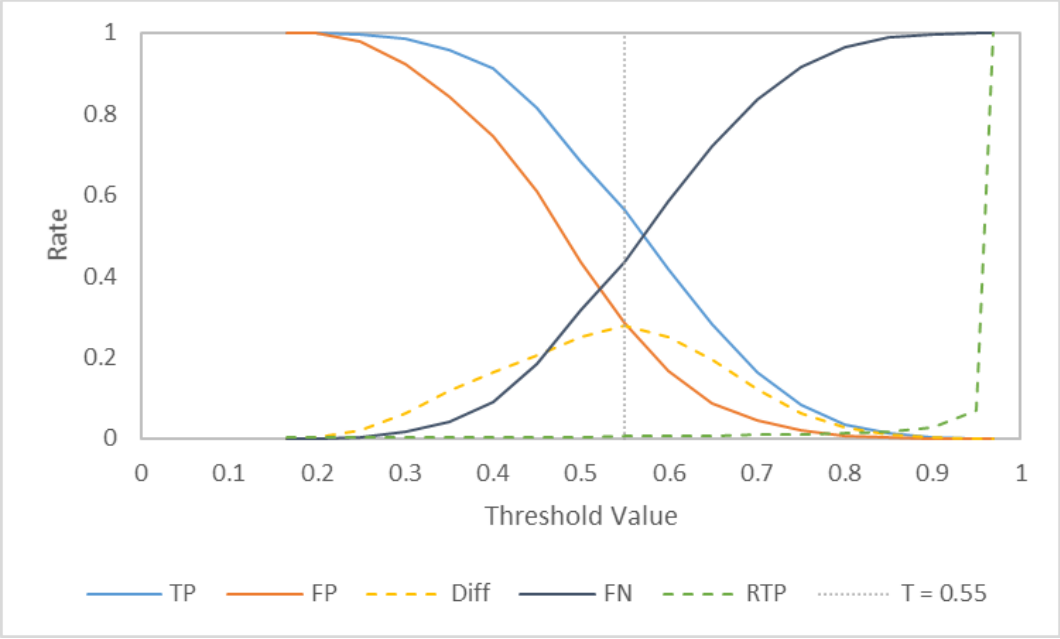

Fig. 7.25*: Graph of true positive, false positive, relative true positive and false negative rates for 0.01 threshold intervals of the Fuzzy Overlay model run with the omission of distance to fault rupture. The difference between true positive and false positive curves has been plotted (yellow) for visual clarity. The threshold of 0.55, the highest point of difference has also been highlighted (grey).*

Much like the final predictive output, the binary (***Fig. 7.26***) appears to semi-accurately (qualitatively) predict the location of ground crack clusters, most of which fall within areas returning a value of 1 (ground cracks present).

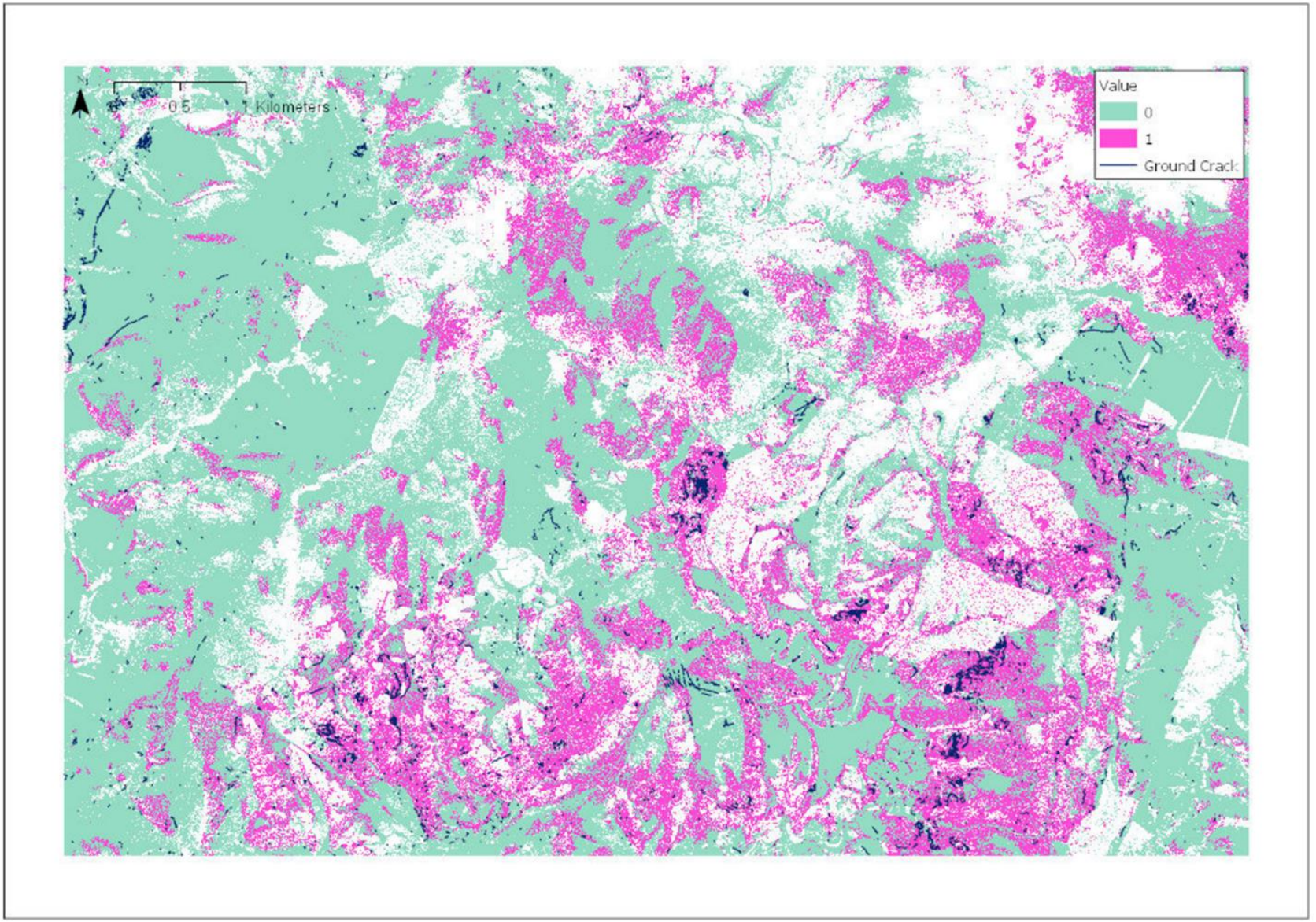

***Fig. 7.26**: Binary output of **Fig. 23**, thresholded according to the highest difference between true and false positive rates (Fig. 28). A value of 1 indicates areas where ground cracking will manifest, values of 0 indicate where it will not. The co-seismic ground crack inventory has been overlaid for interpretative purpose.*

7.5. SUMMARY

Results from this chapter will be further appraised in the forthcoming discussion (*Ch. 8*). The key points from *Ch. 7* are:

- The FL method has been used to quantitatively analyze the inventory, and the significance of a number of proximal and topographic controls on coseismic ground cracking. Whilst doing so, it has informed an attempt at automatically modelling the location of ground crack features.
- Based on KDE/influence curves and respective membership functions, eight of the twelve tested parameters (*Lc*, *Cs*, *Ea*, *Fr*, *Rt*, *Sa*, *Sv* and *V*) appear to control the occurrence of coseismic ground cracking to some extent.
- Aggregation and accuracy assessment indicate that the omission of *Lc* results in the largest reduction in model performance. The omission of *Cs*, *Ea*, *Rt*, *Sa* and *Sv* also decreased AUC. The omission of *V* did not affect AUC, and the omission of *Fr* improved model performance considerably.
- As predictive models, all were statistically unsuccessful however owing to their qualitative success, the relative merits of the predictive tools in reality will be discussed in the forthcoming discussion.

8. ANALYSIS AND DISCUSSION

Following the production of the coseismic ground crack inventory (*Ch. 4*), features were used to qualitatively assess an attempt to automatically extract ground cracks from a high-resolution digital terrain model (DTM) (*Ch. 5*). Features were also used to analyse the geomorphological characteristics of coseismic ground cracks, to see if any coherencies could be identified (*Ch. 6*). Finally, the inventory was used to statistically analyse the most influential spatial topographic controls on coseismic ground cracking; and consequently, to produce a susceptibility map which can potentially be used to inform decision making (*Ch. 7*). Results from *Ch's. 5*, *6* and *7* will now be analysed and discussed to address the initial Research Questions. The following chapter will be structured according to this remit. Some points of discussion have been visually summarised in ***Fig. 8.01*** which will be referred to throughout. Limitations will be discussed when appropriate and then summarised at the end of the chapter.

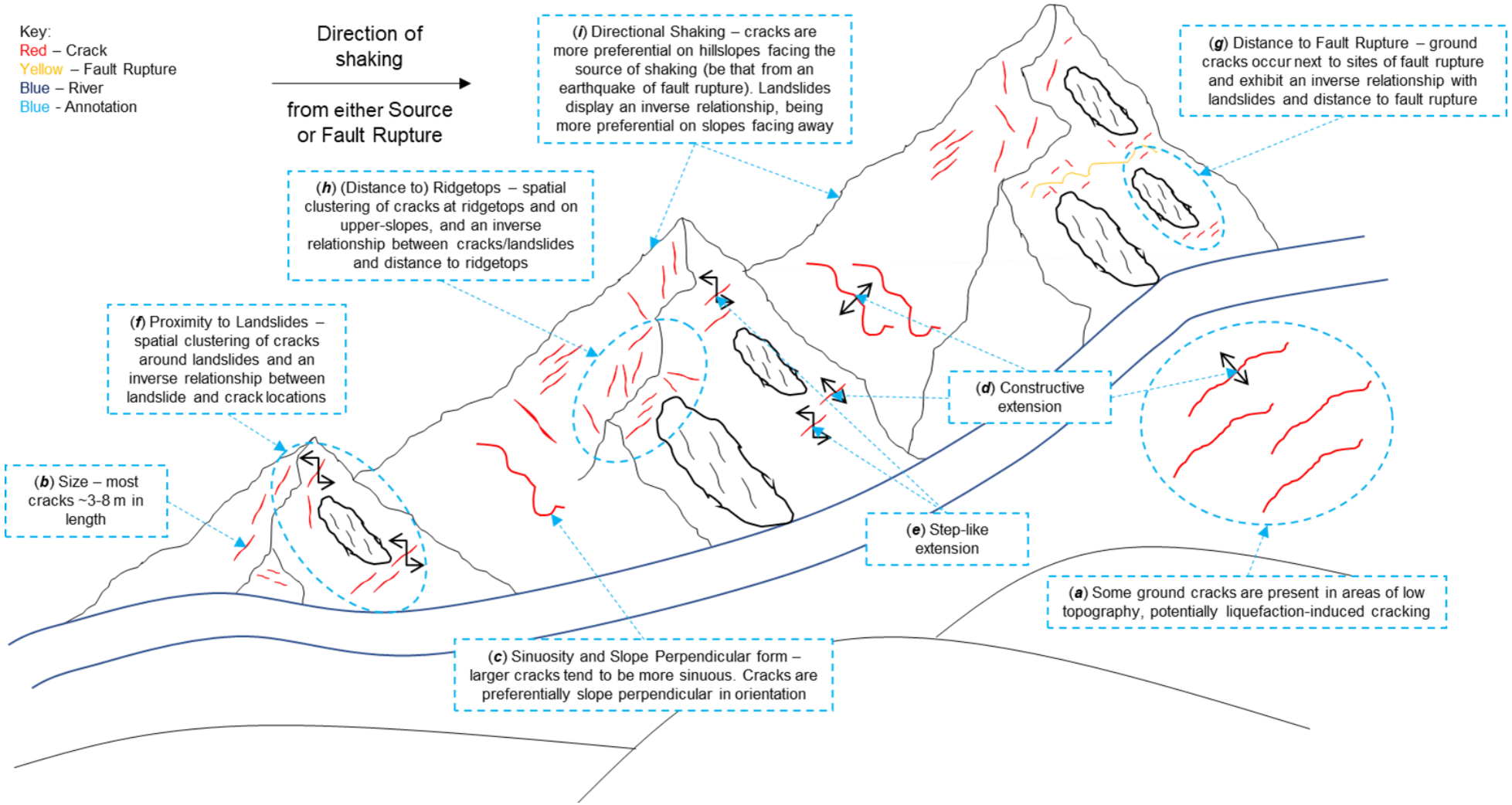

Fig 8.01*: Illustration depicting a summary of the results from Chs. 6 and 7, and therefore (based on these results) where in the landscape certain types of cracks might be likely to occur – the processes explaining potential reasons behind this will be outlined in the discussion, with references made to the diagram through the inset letters (**a**)-(**g**).*

8.1. SEMI-AUTOMATIC FEATURE DETECTION AND PREDICTION

8.1.1. Resolution and Ground Crack Form

Upon comparison of ***Figs. 5.07*** and ***5.09c***, there is a considerable difference in the success of detection attempts from North Yorkshire and New Zealand respectively. The North Yorkshire dataset (~10 cm resolution) is accurate enough to delineate between the geomorphological characteristics of crack walls and tips respectively. Characteristics shown are coherent enough to enable cracks to be semi-successfully delineated using threshold values (***Fig. 5.07***). However, in the lower resolution New Zealand dataset (~1 m resolution), crack wall and tip characteristics do not differ, and cracks do not show any coherent qualitative signatures that can be harnessed to aid automated extraction of these features. Hence, results from the analysis of the New Zealand dataset are relatively poor. This suggests that DTM resolution has a direct impact on success rates when attempting to extract small-scale features such as ground cracks. At ~1 m, the New Zealand dataset is still high-resolution however this may ultimately indicate that even this is unsuitable for detecting small scale features which are sub-metre in scale. Instead, a resolution more akin to the sub-metre scale of the North Yorkshire dataset is required.

Alternatively, ground crack form could contribute to the lack of success. Evans & Lindsay (2010) and Baruch & Filin (2011) semi-successfully detected gully networks from coarser DTM's than that are used here. That said, ground cracks are an order of magnitude narrower than most gully features (Sahoo *et al.*, 2007; Evans & Lindsay, 2010) and can therefore be of a scale below the resolution of the DTM. This would not be the case for gullies, which can therefore be easily extracted using metre-scale DTM data. Airborne Light Detection and Ranging (LiDAR) data with similar resolutions to the New Zealand dataset has also been successfully applied to detect small-scale archaeological features (e.g. Challis *et al.*, 2011; Bennett, 2012; Schneider, 2014). However, ground cracks appear to be much more random and less uniform in form than archaeological features. In most cases, these are anthropogenic or at least display an expected (geomorphological) signature which can pre-inform detection attempts and interpretation. ***Figs. 6.23a-b*** can be interpreted to highlight the erratic nature of crack shape and form through the lack of relationship between crack length and sinuosity (SDs). As such, ground cracks are probably more difficult to detect than other small-scale features. Both points combine to support the suggestion that data resolution must be case-specific. This qualitative inspection suggests that ~1 m data is not accurate enough to accurately document ground crack features.

8.1.2. Fuzzy Logic: Predictive Performance

All Fuzzy Logic (FL) models returned area under curve (AUC) measurements of > 0.5 but < 0.7 according to Receiver Operating Characteristic (ROC) curves (***Fig. 7.23***). AUC > 0.5 shows that the success of all model iterations as predictive mechanisms is greater than random. However, all models produced an AUC < 0.7, which is the threshold that needs to be reached to deem a model a quantitative success (Kritikos *et al.*, 2015). As such, all models were technically quantitatively unsuccessful. Some models came close – to within 0.014 of this success threshold (green curve – ***Fig. 7.23***), which suggests that only minimal changes to membership functions or a more detailed analysis (e.g. larger sample/study area) may well push some iterations over this threshold. This highlights a limitation of the semi-data-driven approach here in that the fitting of functions may be considered subjective as the user can ultimately prioritise a good statistical fit or model more generalised relationships according to the original influence curve (e.g. Robinson *et al.*, 2017). More generalised relationships were used in this instance to enhance the future applicability of results. In retrospect, using more complex, statistically fitting functions to model ground crack relationships may have been worthwhile due to the small-scale topographic change induced by cracks. Subjective decisions can hinder a model's (quantitative) predictive capacity but concurrently will not be all that difficult to rectify in the future.

As a critique to the accuracy assessment, using a pre-defined threshold (i.e. AUC = 0.7) could be considered arbitrary. Whilst being grounded in empirical theory (Kritikos *et al.*, 2015), the threshold has been directly transferred from studies focused on predicting coseismic landslides, and not ground cracks. Therefore, this may be unsuitable to adequately assess model outputs in this instance. Ground cracks are smaller than landslides and the inventory has been curated using polylines, meaning that all cracks are represented by a single line width. Ground truth data (GTD) will therefore be limited in comparison to landslides. A small sample of GTD as a ratio of pixels could explain high true positive (TP)/false positive (FP) rates and low relative true positive (RTP) rates (***Fig. 7.25***). Very small RTP rates signify considerable over-prediction at all thresholds. In real terms, the rapid increase in RTP rate represents the single pixel with the maximum hazard value, and thus can be ignored. RTP rates tend to be low and, in many cases, reflect the fact that features do actually occur in areas of high hazard, along with lots of FP's (Robinson *et al.*, 2018).

Results suggest that the method may not be a suitable means of pinpointing ground crack locations. However, given the scale of ground crack features, this may be an unrealistic expectation. As a method of hazard prediction in this instance it is safer to over-predict as opposed to under-predict as this reduces the chance of cracked areas being missed (see discussion on RTP rates above - ***Fig. 7.25***). With this in mind, the best performing model output (***Figs. 7.24*** and ***7.26***) could be considered a partial qualitative success. The majority of ground cracks appear to be located in areas of high hazard (***Fig. 7.24***) and areas where occurrence is likely (***Fig. 7.26***). Areas of flat, open field to the east of the study area are classified as low hazard, which is also accurate. Inaccuracies remain, for example in the north-west of the study region where a number of ground cracks are present, but the area has been classified as low hazard (***Figs. 7.24*** and ***7.26***). This may have played a major part in keeping all AUC values < 0.7. Cracks in this area may have been due to liquefaction-induced processes (see ***Fig. 8.01(a)***). The topography of the area is low, ruling out a lot of the spatial topographic controls that have been calculated in Ch.7 – as most are contingent on steep topography. Also, the proximity of these cracks to the nearest site of fault rupture seems to suggest that direct surface or extensional cracking is not the cause in this instance. This area of low topography is likely to have higher ground water levels than the surrounding hillslopes (e.g. Chen et al, 2009), encouraging liquefaction-induced ground cracking by increasing pore pressure and reducing shear strength of the surface (Ishihara, 1993). Even in this setting of relatively high relief, this may evidence the presence of liquefaction-induced cracking.

Whilst not perfect, if considered from a different perspective the model shows promise in predicting areas where coseismic ground cracking may be more likely to occur. This could be used within the context of susceptibility monitoring or emergency hazard response to focus and inform further investigation. In real terms, it will be invaluable for decision makers to have access to data indicating the location of incipient hillslope failure so that they can quickly and easily narrow down their search area for potentially unstable slopes. As a result, choosing which places to scrutinise/monitor/evacuate will be better informed. For example, despite major over-prediction, model outputs from Robinson *et al.* (2018) were most-notably used to inform aerial reconnaissance flight paths following the Kaikoura earthquake in 2016. Whilst results were not quantitatively perfect, they were still sufficient to provide near-real-time information that was otherwise not available.

As highlighted in *Ch. 7*, a major advantage of the FL method is the speed at which it can be applied (e.g. Pradhan, 2011). This is key in the context of coseismic ground cracking, as large aftershocks may trigger more landsliding as cracked slopes are carried

over failure thresholds by further seismic shaking (Petley *et al.*, 2005; Meunier *et al.*, 2008; Dunning *et al.*, 2008). As such, cracked slopes need to be identified quickly following a major shaking event and FL appears to be the most suitable method to accurately achieve this. Modelling based on Newmark's sliding block theory (Newmark, 1965) has been deemed far too inaccurate in the past (e.g. Parise & Jibson, 2000; Gallen *et al.*, 2016) and conventional inventory production is too slow for this purpose (e.g. Williams *et al.*, 2018). For example, following the Gorkha Earthquake in Nepal in 2015, Kargel *et al.* (2016) took 38 days to complete a preliminary landslide inventory. 12 days after the mainshock, there was a large aftershock (e.g. Avouac *et al.*, 2015) and 51 days after the event, the emergency response had officially transitioned into a recovery phase (Nepal Army, 2016). Therefore, the inventory did not serve much of a purpose in terms of immediate secondary hazard prediction or emergency humanitarian response. Timescales for inventory production would almost certainly be even longer for ground cracks.

For the method to be applied rapidly, data needs to be readily available and ideally pre-downloaded (Robinson *et al.*, 2017). Automation could go some way to ensuring that this is always the case, and must be explored further (e.g. Robinson *et al.*, 2018). In the case of ground cracking, another major issue is that data ideally needs to be of the required resolution (<~1 m, see *Ch. 8.4.1*). This is lacking in most locations, even in New Zealand, where only 8 m DTM data was available pre-earthquake. It would be interesting for a future study to investigate how the modelling of small-scale features is affected by coarser DTM resolutions. Whilst lower, they would also be lower in noise levels and may therefore perform well using the generalised membership functions fitted using this study.

. For coseismic ground cracking and ensuing incipient hillslope failure to be addressed (e.g. Petley *et al.*, 2005; Parker *et al.*, 2015) all seismically active areas at risk of coseismic landsliding ideally need to be covered with high-resolution LiDAR data. To make a hazard assessment site-specific, a sample post-earthquake inventory also needs to be created (Robinson *et al.*, 2017). Mapping coseismic ground cracking requires very high-resolution imagery, which is not yet available from commercial satellites (see *Ch. 4*). As such, this will have to be rapidly acquired manually following an event. Robinson *et al.* (2018) used global relationships and found these to result in major over-prediction. Furthermore, creating site-specific membership data also increases levels of contribution to global datasets (Kritikos *et al.*, 2015), enhancing the accuracy and future applicability of these. The most time-consuming data product is shaking data. Obviously, shaking data is needed to inform an area of interest, however incorporating it into the model is much more time consuming (Robinson *et al.*, 2017). Like post-event imagery, this is also something

that cannot be acquired pre-event. Based on other studies, and the pre-existing relationship between shaking and coseismic landsliding (e.g. Keefer, 1984; Parker *et al.*, 2015; Massey *et al.*, 2018) it is highly possible that the inclusion of shaking data may increase model accuracy (Robinson *et al.*, 2017; 2018). That said, the performance of the model without such data is promising. Future research should therefore address whether an increase in accuracy is worth the extra computational time. Finally, although quick to apply as a process, a limitation of the FL model is that it requires trained experts who are very familiar with the process if this rapidity is to be harnessed. Ultimately, this discussion highlights that if a post-earthquake modelling response is to be successful, a clear process needs to be in place to inform smooth execution. Ideally, data needs to be pre-processed and acquired rapidly by the correct personnel; and there needs to be a continued approach to (semi-) automation.

8.1.3. Summary

Ultimately, results suggest that the ~1 m DTM data used in this study is not suitable for detecting and analysing co-seismic ground cracks. This may be due to the potentially and at least partly random nature of ground crack features, however despite this the much higher resolution ~10 cm North Yorkshire dataset showed promising performance, indicating that this may ultimately be due to the relationship between data resolution and feature scale. Quantitatively, all models run using FL were marginally unsuccessful. However, a qualitative inspection and discussion has argued that the best performing model output (***Figs. 7.24*** and ***7.26***) shows promise if contextualised under the premise of informing decision making. It has also highlighted an area where liquefaction-induced ground cracking may be present. If the capabilities of the model are to be harnessed to their full potential there are several logistical considerations that need to be made regarding the acquisition and processing of data. If these can be overcome, FL may be a promising solution to post-earthquake ground crack hazard assessment. Therefore, high-resolution LiDAR data shows promise in detecting and predicting small-scale ground crack features, however improvements are ultimately needed to both data and methodological accuracy making this a key area for potential future research.

8.2. (GROUND CRACK) MECHANICAL INFERENCES

Feature Statistics (*Ch. 6*) have provided interesting insight into the geomorphological characteristics of coseismic ground cracks. In turn, this can be assessed to consider and make inferences regarding the occurrence and extension of coseismic ground cracks.

8.2.1. Ground Crack Propagation

Results from long profile analysis (***Table 6.1***, ***Figs. 6.15b*** & ***6.17b***) indicate that ground cracks rarely exceed ~10 m in length, and more commonly have a length of ~7 m. This is supported by probability density (***Fig. 6.13***) which suggests that crack length is most commonly ~3-8 m throughout the inventory. The probability density distribution also exhibits both a rollover (~6.3 m) and power-law scaling after this point. Ultimately, this all suggests that there are fewer small or very large features within the inventory (***Fig. 8.01(b)***). Potential reasons will be discussed through the power-law scaling and rollover exhibited by probability density (***Fig. 6.13***) and in turn visibility and/or the expression of seismic strain on the surface. Power-law scaling shows that crack frequency decreases as a function of crack length. Power-law scaling can also be harnessed to predict the frequency of cracks of a given length(s). If manipulated, this has potential to be converted into a relative measure to quantify earthquake damage, similar to the manner employed with coseismic landslides (e.g. Barlow *et al.*, 2012). However, to do this would ideally require further input from other crack-focused studies that encompass a wider parameter space (Malamud *et al.*, 2004). The rollover tends to be a function of data resolution (Hovius & Stark, 2001). The rollover (~6.3 m) may be higher than anticipated given the resolution of the data source (0.2 m aerial photography) and represents a lack of very small- (< ~3 m) and large- (> ~8 m) scale features. The apparent lack of small-scale features could be explained by visibility issues preferentially occluding small features. Despite the high-resolution of the aerial photography, small-scale features are still much more difficult to detect via visual interpretation. They are more likely to be entirely obscured by other objects and shadowing (Morgan *et al.*, 2010). Also, shorter cracks may be narrower, reducing their visibility even further. When putting this into context it is perhaps not surprising that the rollover threshold is considerably higher than data resolution.

The lack of small- and large-scale features can also offer insight into ductile or creeping hillslope deformation, and the relationship between this and seismic shaking. Hillslopes are likely deforming in a creeping or ductile manner, as they exhibit surface

cracking and are yet to fail. Strain is cumulative and non-reversible (Kilburn & Petley, 2003), which may increase the length of smaller cracks over time and result in longer average lengths. Strain can also fluctuate, often due to relative pore pressure changes within a hillslope (Petley & Allison, 1997). Positive fluctuations may increase crack length, negative fluctuations may cause cracks to close up. Crack growth also increases exponentially with length (Main *et al.*, 1993) and they can coalesce into larger features through the positive reinforcement of stress at crack tips (Costin, 1987). As such, strain accumulation may result in surface cracks increasing in length over time. Given that the inventory was created based on imagery taken one-two months after the earthquake, cracks may have increased in length slightly (to ~3-8 m) but not yet developed into long (>~10 m) features. Shaking may also not have been strong enough to induce widespread, large-scale cracking. Given the strength and complexity of shaking during the event (e.g. Hamling *et al.*, 2017; Bradley *et al.*, 2017) it is difficult to fathom the intensity of shaking required to form these. It could be assumed therefore that larger cracks may have developed into full hillslope failure.

Alternatively, a lack of small-scale features can be interpreted to suggest a link between seismic shaking and minimum feature length. Seismic shaking can apply huge stresses on hillslopes. This can induce instantaneous shallow and deeper-seated failure (Petley *et al.*, 2005). Alternatively, it can trigger ductile deformation within a hillslope (Petley *et al.*, 2002; Dunning *et al.*, 2007) which can be expressed through surface cracking. As such, a certain threshold of stress from seismic shaking must reach the surface in order to ‘crack’ the ground. This level of stress may be so large that it is unlikely to result in the expression of strain below a certain threshold (i.e. rollover in this case, ***Fig. 6.13***). A similar theory is noticed in co-seismic landsliding, whereby localised stresses across a small potential failing mass are never sufficiently high to generate failure. This may be due to positive feedbacks between shear stress, gravity and normal stress which compound each other and the resulting force imbalance (e.g. Barlow *et al.*, 2012). Therefore, through interpretation of crack length, co-seismic ground cracking could provide further evidence as to the relationship between seismic shaking and surface damage.

Path sinuosity may be a function of crack length (***Fig 6.22***). As such, longer cracks are less linear (***Fig. 8.01(c)***). This could infer a topographic control on ground cracking if interpreted through a stress relief narrative. Co-seismic ground cracking is inherently a form of stress relief triggered by seismic shaking. The most effective form of strain/stress relief must be perfectly linear cracking as this is the most effective way of a crack propagating from one place to another. If longer cracks are less likely to be linear, there

may be an external control on strain expression which forces a crack to deviate from a perfectly linear path. This could be a topographic control; whereby ground cracking is forced to follow or traverse the contour. Faulting on the other hand tends to propagate in a straight line (Anderson & Anderson, 2010; Li *et al.*, 2010) as it has the energy to overcome these topographic barriers. The fact that cracks appear to have a preferentially slope perpendicular orientation (***Figs. 6.14a-6.17d***,***6.21*** and ***8.01(c)***) compounds this further as it suggests that there may be a mechanism forcing cracks to propagate across-slope as opposed to downslope.

8.2.2. Ground Crack Extension

Cross Slope Profile analysis has provided some interesting insight which can be harnessed to discuss the extension mechanism of coseismic ground cracks (i.e. how cracks open-up laterally), and how this may differ depending on the position of these on a hillslope. As per the methodology (*Ch. 6.1.2.2*), extension mechanisms have been split into 'constructive-like' and 'step-like' (***Figs. 6.05a-b***). As will be discussed forthcoming, this can potentially be related to (incipient) landslide activity.

Firstly, the presence of small (< 2 m) step values across all slope angles and proximities to landslides (***Figs. 6.18a-b*** and ***6.19a-b***) suggests that coseismic ground cracks can extend in a constructive-like manner in all environments (***Fig. 8.01(d)***). The fact that there is no obvious control (in terms of slope angle or proximity to landslide crown) on this infers that it is common for the ground to crack and for that crack to extend laterally parallel to the topography contours. Obviously, this is slightly assumptive, however other results (e.g. ***Figs 6.17a*** and ***6.21***) prove that the majority of ground cracks occur in a hillslope perpendicular direction.

In contrast, results suggest that slope angle (and proximity to landslides) may exert a control on the step-like extension of ground cracks (***Fig. 8.01(e)***). The weak positive correlation between step size and slope angles <~10° (***Fig. 6.18a***) suggests that higher step values are limited to steeper slopes. This link is feasible when considered in the context of hillslope failure and suggests that step-like extension may be linked to internal hillslope stresses and stability and in turn incipient landsliding. As has already been discussed, seismic shaking can upset the usual steady state equilibrium of stresses within a hillslope (e.g. Selby, 2005), potentially causing damage (by cracking the landscape) or full hillslope failure (landsliding). Steeper slopes are known to have a considerable influence on hillslope failure as they increase gravitational, and therefore shear stress (e.g.

Keefer, 1984). Theoretically, this influence will increase as slope angle also increases. Therefore, if seismic shaking is to induce damage in the form of cracking, this positive correlation between slope angle and shear stress could be expressed through increasing step values. As such, we can infer that a larger step value could be indicative of a more hazardous incipient landslide, one which is more likely to fail as the hillslope is further from a steady state of equilibrium. This in theory may be consolidated through the weak negative correlation between step size and proximity to landslide crowns (***Fig. 6.19a***), as larger step sizes are much more commonplace close to existing sites of hillslope failure. Therefore, step size could potentially be assessed to indicate the stability of a hillslope.

Whilst interesting points of discussion, these must be grounded in the limitations surrounding the Cross Slope Profile analysis method employed here. Ultimately, as cracks were mapped using polylines, there is no measurement to quantify crack width. As such, elevation cross profiles had to be extracted using the resolution of the data source – the 1 m DTM. Some cracks may have been narrower than this, as was widely the case with ground cracks resulting from the Kashmir Earthquake in 2005 (Sahoo *et al.*, 2007), meaning that some smaller steps may have been missed. This may have skewed results slightly and exaggerated the influence of slope angle on step size.

8.2.3. Summary

The size distribution of ground crack features can be interpreted through deformation mechanics. The lack of small-scale features (***Fig. 8.01(b)***) may support the notion of a landscape having a minimum strain threshold, in that stress (from seismic shaking) needs to overcome this to induce damage to the landscape. It may also support the irreversible strain induced by ductile deformation, in that positive strain deviation may result in crack length increasing both over time and as cracks grow – as part of a cycle of positive feedback. The lack of large-scale features ***Fig. 8.01(b)*** may be due to the infancy of cracks as the landscape is in the early stages of deformation, or that the shaking was insufficient to develop cracks to their full potential. A lack of linearity in cracking (***Fig. 8.01(c)***) has provided a novel insight into the potential topographic control on ground crack occurrence, location and character across the landscape. This is further supported as constructive-like extension occurs on all types of hillslope (***Fig. 8.01(d)***), and by the preferentially slope perpendicular propagation of ground cracks (***Fig. 8.01(c)***). Larger step-like extension (***Fig. 8.01(e)***) is limited to steeper slopes, likely due to a link with gravitational and therefore shear stress.

8.3. SPATIAL TOPOGRAPHIC CONTROLS

Results indicate that a number of spatial topographic parameters appear to exert a control on coseismic ground cracking. The relative level of this control differs by parameter; however, it is suggested that these can be grouped into two groups which ultimately highlight the control of proximity to coseismic landsliding; and impact of topographic site effects on coseismic ground cracking respectively.

8.3.1. Proximity to Coseismic Landslides

A number of results suggest the presence of a spatial link between coseismic ground cracking and landsliding, which may indicate a (spatial) interdependency and therefore control (***Fig. 8.01(f)***). This may also indicate that cracking, to a greater or lesser degree, is driven by many of the same controls as coseismic slope failure, implying a gravitational control. AUC analysis (***Fig. 7.23***) highlights that the combined influence of all eight factors (yellow curve) on coseismic ground cracking is greater than random (dashed line). This suggests that a combination of these do exert a significant control on co-seismic ground cracking. However, further AUC analysis highlights that parameters do not have equal levels of influence. As ***Fig. 7.23*** shows, most of the predictive capacity can be attributed to proximity to landslides – distance to landslides alone makes up 99% of the model's predictive capacity, and the omission of distance to landslides from the model (red curve) results in a considerable reduction in performance. Further supporting this, Long Profile analysis (***Figs. 6.14a-6.15b***) highlights the concurrent peaks in the kernel density estimate (KDE) of ground crack and landslide elevations. This is therefore (statistically) the strongest spatial topographic control on coseismic ground cracking. However, the fact that this does not constitute the entire predictive capacity of the model suggests that other parameters do still exert a control, but to a lesser extent. These are Euclidean Aspect, Direction to Slip Vector, Slope Angle, and Distance to Ridgetops and Valley Bottoms. Interestingly, some of these controls may actually further emphasise the spatial control of coseismic landsliding.

Upon comparison with other similar studies which have focused on coseismic landsliding, slope angle (***Fig. 7.16a/c***) appears to exert a similar control on coseismic ground cracking (Robinson *et al.*, 2017). The link between slope angle and ground cracking indicative of incipient landsliding has been discussed in the previous chapter, however FL results quantitatively confirm this. Whilst initially thought to be more relevant to

topographic site effects, distance to ridgetops can also be used to further support the spatial control of coseismic landslides. Comparing the first peak of the influence curve to a KDE representing the distance of landslides from ridgetop locations (***Fig. 7.15c***) reveals a contradiction as when one is increasing/peaks, the other decreases/troughs. This highlights where ground cracks have and have not developed into full hillslope failure respectively and provides an interesting support to the concept of incipient landsliding. It also shows high levels of ground crack occurrence close to landslide locations, as both peaks in the influence curve surround the peak in landslide KDE (***Fig. 7.15c***). The proximity of both to ridgetop locations will be further discussed in the following sub-chapter. Finally, distance to valleys of both ground cracks and landslides (***Fig. 7.18c***) also highlights a clear spatial relationship between the two, with the first peak in the influence curve coinciding with the peak in landslide KDE. The second peak in influence could also be said to be proximal to this peak.

Despite not being a statistically significant control on coseismic ground cracking (***Fig. 7.23***), distance to fault rupture also provides an insight into the spatial correlation between coseismic landsliding and ground cracking. It is technically deemed statistically insignificant as the omission of it resulted in the best performing model (green curve), confirmed by the highest AUC value (***Fig. 7.23***). That said, this difference was negligible and the distance to fault rupture still provides an interesting point of discussion. Comparison of the influence curve for distance to fault rupture with a landslide KDE for the same measurement (***Fig. 7.14c***) could be harnessed to suggest that ground cracking is less prevalent closer to fault rupture locations because it has developed into full hillslope failure. As distance increases and seismic shaking consequently has a reduced impact (e.g. Trufinac, 1994; Hovius & Meunier, 2012), shaking may not have been strong enough to induce landsliding, instead resulting in ground cracking (potentially indicative of incipient landsliding – ***Fig. 8.01(g)***). This has already been discussed in *Ch. 8.2.1*. Due to the locality of this study, this is assumptive, however this does agree with conventional relationships between distance to fault rupture and coseismic landsliding as per other studies (e.g. Martha *et al.*, 2017; Massey *et al.*, 2018). Whilst potentially highlighting a spatial correlation between coseismic ground cracking and landsliding, results from distance to fault rupture also outline a key limitation of this research – the subjectivity of membership functions. Given the proximal relationship between co-seismic landslides and sites of fault rupture (e.g. Kargel *et al.*, 2016), it is unlikely that this will not exert a control on the location of coseismic ground cracking, especially given how useful parameter results have been in explaining ground crack locations. As such, the mechanical

complexities of the interrelationship between coseismic ground cracking, landsliding and fault rupture locations may not have been suitably reflected in the membership function and consequently in a predictive capacity. This is a limitation of the semi-data driven approach, however this and other studies (e.g. Kritikos *et al.*, 2015) would argue that this is necessary to make results more widely applicable. Despite being quantitatively unsuccessful, there is a case that distance to fault rupture has provided a vital, albeit semi-quantitative, insight into the spatial occurrence of coseismic ground cracks.

Ultimately, the relationship between, and therefore control of coseismic landsliding on ground cracking is evident through a number of different parameters, which may suggest that cracking is an expression of incipient landslide activity (***Fig. 8.01 (f)***). Due to this proximity, there must be some reason as to why certain parts of a hillslope have not developed into full failure. One hypothesis can be drawn from internal hillslope conditions. Damage expression on the surface means that areas of ground cracking and landsliding on a hillslope have likely entered into the advanced stage of failure, whereby cracks grow and coalesce into a shear surface through increasing positive feedback (Petley *et al.*, 2005). However, after this point of internal 'failure' has occurred, hillslope failure becomes partially dependent on other processes such as slope angle, downslope geometry (e.g. gravitational influences) and pore pressure (ibid). For example, groundwater levels have been known to affect pore water pressure and in turn microcracking (Atkinson, 1984; Kilburn & Petley, 2003). Seismic shaking can also affect internal conditions (Meunier *et al.*, 2008). As internal conditions can differ locally, deformation may not have advanced to a runaway brittle stage on some parts of a hillslope (Petley *et al.*, 2005) – instead, disturbance in these areas has been expressed through ground cracks, which may be indicative of incipient landsliding, but equally may not be indicative of future instability.

An alternative suggestion is that areas of cracking are a surface expression of shallower failure, as gravitational stress on these parts of the hillslope are not large enough to overcome internal hillslope strength (Kilburn & Petley, 2003). The only likely explanation for this is through topographic site effects, as seismic shaking interacts with gravitational stress to induce hillslope failure (Meunier *et al.*, 2008). This interaction may have differed between locations, resulting in the exertion of different levels of change in shear stress.

Initially, it was also a possibility that cracking was an expression of pre-existing landslide scars (e.g. McKean & Roering, 2003; Glenn *et al.*, 2006; Ventura *et al.*, 2011). However, the misalignment of ground crack influence and landslide KDE in distance to ridgetop and fault rupture (***Figs. 7.14c*** and ***7.15c***) suggest this not to be the case. That

said, ground cracking may be an expression of pre-existing *incipient* landslide scars. As has been acknowledged above, ground cracking can be a surface expression of internal damage whereby this has not yet developed into full hillslope failure (e.g. Dunning *et al.*, 2007). For reasons discussed above, an area of deformation may never transition from the brittle to the ductile phase if the conditions are not right for this to occur (e.g. Kilburn & Petley, 2003). In real terms, this will translate to an incipient landslide or area of ground cracking 'creeping' down a hillslope, being reactivated at certain points in time potentially (but not necessarily) by, seismic or pluvial events which accelerate the damage threshold considerably (although never to the point of brittle failure). The damage potential that areas like this hold is considerable – as they represent areas of incipient landsliding that have potentially developed over a number of seismic/pluvial cycles (Parker *et al.*, 2015). As such, the continued monitoring of these areas is extremely important to see how, when and if they develop into full failure – and to attempt to monitor what the controlling factors on this are. In real terms, this study could provide a credible workflow for identifying areas for future focused monitoring.

8.3.2. Topographic Site Effects

Results provide a new, novel insight which generally supports our understanding of topographic site effects (TSE). Most relevant to this is that coseismic ground cracking appears to be more preferential closer to ridgetop locations (***Fig. 8.01(h)***). This is shown in Long Profile analysis (***Fig. 6.14a***), and the ridgetop- (***Fig. 7.15c***) and curvature-specific (***Fig. 7.12c***) influence curves. The largest peaks in the KDE of elevation values is concurrent between ground cracks and both ridgetops and landslides (***Fig. 6.14a***). Initially, the larger peak in the KDE of ground crack elevation appears to suggest a stronger spatial correlation with ridgetops than landslide locations. However, Long Profile analysis considers all values independently of spatial proximity. FL analysis on the other hand builds on this to quantify spatial proximity to features. Therefore, what has been discussed in the previous sub-chapter in that the strongest proximal relationship is between ground cracks and landslides still holds. According to the ridgetop influence curve (***Fig. 7.15c***), damage in general, whether that be cracking or landsliding, is much more preferential closer to ridgetop locations. Both ground crack influence and landslide KDE then decrease as distance from ridgetops increases. Cracking is more preferential at non-zero curvature values (***Fig. 7.12c***) and less preferential at values tending to towards 0. This concurs with

the relationship between landslides and curvature (e.g. Kritikos *et al.*, 2015; Robinson *et al.*, 2017), suggesting that discontinuities may be necessary to induce full hillslope failure.

Ultimately, all results mentioned indicate that damage is more preferential closer to ridgetop locations (***Fig. 8.01(h)***). This could be explained by TSE, in that shaking intensity is greatest at ridgetop locations as it is focused up through the topography via diffraction (Meunier *et al.*, 2008). Stronger shaking is likely to induce more damage, whether that be in the form of full or incipient hillslope failure (Hovius & Meunier, 2012). The relationship between full and incipient hillslope failure has been discussed in the previous sub-chapter, however in reference to ridgetop locations, the slight difference in ground crack and landslide locations could be explained by the fact that landsliding at ridgetop locations can be constrained by a lack of regolith (e.g. Keefer, 2000). Alternatively, cracks may form directly upslope of landslide locations as the removal of mass has caused the slumping of scarp material and consequently surface cracking (e.g. Ventura *et al.*, 2011). There may be a number of different mechanisms explaining cracking close to ridgetop locations and it is important to stress that all instances of cracking should not be assigned to a single explanation.

Once again, limitations must be considered when making assumptions regarding proximity to ridgetops. The subjectivity of membership functions has already been discussed, but this is particularly pertinent for ridgetops due to the complex double peak of the influence curve. This was the most difficult curve to fit as it was deemed important to consider both peaks in line with both existing TSE and landslide theory. The more manipulation required, the more error this may induce. Preceding this, the ridgetop dataset was difficult to produce. Results must be considered with these limitations in mind but that said, they are what was expected when grounded in TSE theory.

Results from directional shaking also provided some interesting relationships which conform to both TSE and hillslope deformation. Directional shaking appears to be a considerable control on ground cracking, with cracking being more preferential on slopes facing both the epicentre (Euclidean Aspect - ***Figs. 7.13a-c***) and fault rupture locations (Direction to Slip Vector - ***Figs. 7.17a-d***). This is depicted in ***Fig. 8.01(i)***. The relationship is stronger for Euclidean Aspect, likely due to the proximity of the study area to the epicentre. If done on a regional scale, it is expected that the opposite would be the case, as the majority of the damage regionally was induced by fault rupture (e.g. Hamling *et al.*, 2017; Kaiser *et al.*, 2017). That said, in this case both can be discussed in tandem as the spatial confinement of the project means that it is likely that shaking from both sources affected hillslope stability in a similar manner. Cracking being more preferential on

hillslopes facing the sources of shaking is the inverse of the behaviour exhibited by coseismic landsliding, which is more preferential on slopes facing away from the epicentre (Robinson *et al.*, 2017) as shown in ***Fig. 8.01***. This and other studies (e.g. Kritikos *et al.*, 2015) may indicate that seismic shaking may force material into/outwards from a hillslope depending on its orientation in relation to a source of shaking. Hillslopes that are facing a seismic source are more likely to have material forced into them by shaking, as this will increase normal stress (e.g. Newmark, 1965). As a result, the interaction between local slope aspect and directional shaking may strengthen a hillslope through sediment compaction (Brain *et al.*, 2017). Whilst source-facing hillslopes are unlikely to have been 'strengthened' literally in this instance, they may have been strengthened in the sense of being made less prone to full hillslope failure. As a result, damage may be in the form of incipient hillslope failure or cracking, as a hillslope has been unable to develop into full failure. This may mean that damage is more likely to 'remain' (or at least appear to 'remain') on hillslopes facing the seismic source of shaking. On the other hand, on hillslopes facing away from the seismic source shaking is likely to force material out from a hillslope. Through increasing shear stress (e.g. Selby, 2005), this may make a hillslope more prone to full failure. Directional shaking results provide a novel perspective to existing TSE theory, which states that shaking is more amplified on slopes facing away from a seismic source (e.g. Geli *et al.*, 1988; Meunier *et al.*, 2008). By grounding the results from this study in the context of hillslope processes, they provide further evidence that damage is more likely to occur on slopes facing away from a source of seismic shaking, and that such shaking is therefore more amplified on these slopes than it is on hillslopes facing the source.

Ultimately, the relationships shown by co-seismic ground cracking in relation to both proximity to ridgetops and directional shaking adds further (novel) insight and evidence to the suggestive impact of TSE on hillslope damage. Analysis here and elsewhere (e.g. Robinson *et al.*, 2017) suggests that it is necessary to consider this in the context of coseismic ground cracking.

8.3.3. Summary

Proximity to landsliding appears to be the most influential control on coseismic ground cracking (***Fig. 8.01(f)***). Reasons for this could be explained by differences in internal hillslope conditions, which govern whether or not a part of a hillslope cracks or fails completely. Other parameters also exert a control on cracking however many also

intrinsically link back to landsliding (e.g. Slope Angle). Distance to Fault Rupture offers an interesting insight into the impact of seismic shaking on the landscape through the inverse nature of the relationship between the prevalence of ground cracking and landsliding respectively as distance increases. This inverse relationship was also prevalent in other parameters, most notably distance to ridgetops. Coseismic ground cracking appears to further validate conventional TSE theory as landscape damage was greater nearer ridgetop locations (***Fig. 8.01(h)***) and on hillslopes facing the seismic source (***Fig. 8.01(i)***). The latter is the inverse of behaviour exhibited by co-seismic landsliding, offering insight into the interrelationship between shaking propagation and local slope aspect. This may in turn be linked to material compaction, as seismic waves force material into hillslopes facing the shaking source which may limit the damage to cracking as opposed to full hillslope failure.

8.4. SUMMARY OF LIMITATIONS

Limitations have been acknowledged and discussed throughout the course of this thesis. Whilst these do not need to be revisited in detail, it is useful to provide a summary which in turn will then be used to directly inform future research suggestions in Ch. 9.

Firstly, the lack of pre-existing research available on co-seismic ground cracking presented a challenge in terms of a lack of initial scholarly guidance. Whilst highlighted through a number of publications (e.g. Petley *et al.*, 2006; Owen *et al.*, 2008), ground cracking has not to my knowledge been the focus of research efforts and remained very much secondary. As a result, there were no documented approaches regarding how to go about exploring this.

Secondly, the size of the study area and the locality of this to the epicentre may have skewed results through a combination of under-sampling and the fact that this was focused on an area that was affected by very strong seismic shaking. No data could be obtained from areas of weaker shaking for comparison due to resource (material and temporal) constraints. It also ruled out the study of peak ground acceleration (PGA) and geology, owing to a lack in variation of these variables within the study area extent.

Thirdly, there were a number of methodological limitations regarding inventory production. These revolved around imagery (shadow etc.) and methodology (subjectivity) used, and the fact that the inventory was not validated using fieldwork. These have all been addressed in *Ch. 4*, which justifies such actions.

Finally, the Fuzzy Logic workflow (*Ch. 7*) provided a number of challenges. The ridgetop dataset was difficult to produce, with no widely recognised method able to inform this. As such, there may be inaccuracies within the dataset, and any ensuing analysis. PGA and geology were excluded from analysis (see above), and as such the impact of these is unknown. The fitting of membership curves was semi-data-driven – as discussed (*Ch. 7.3.3* and throughout *Ch. 8*), this was necessary in an attempt to make results as widely applicable as possible. However, this inevitably introduced some subjectivity into the methodology, which is always open to contestation. No chapter summary will be provided here, as key points will be outlined in the Conclusions in *Ch. 9*.

9. CONCLUSIONS

9.1. OVERVIEW AND MAIN RESEARCH FINDINGS

Few studies have explored in detail the ground cracks that appear during earthquakes. These could be a potential indicator of incipient landsliding, i.e. partial hillslope failure, and thus have the potential to develop into landslide hazards. Ground cracks may be a surface expression of the retention of damage by hillslopes, damage which may make them more prone to full failure or reactivation in the future, potentially as a result of future seismic or pluvial events. The overall aim of this study has therefore been to improve our understanding of coseismic ground cracking – namely its geomorphological characteristics and the most influential controlling factors on its occurrence, with a view to using this knowledge to inform an attempt at predicting where in the landscape ground cracks are most likely to occur.

The aim and associated research questions have been addressed by the creation of a coseismic ground crack inventory using high resolution aerial photography captured following the 2016 Kaikoura earthquake in New Zealand. The earthquake resulted in considerable geomorphological damage in the form of landsliding and ground cracking. To begin with, the inventory was used to validate an attempt at automatically detecting ground crack features, which was pre-informed using a higher-resolution (Digital Terrain Model) DTM from North Yorkshire, UK. This enabled the comparison of various resolutions of source data which provided insight into the suitability of these for detecting small-scale features such as ground cracks. Ultimately, ~1 m DTM data was not sufficient for this purpose highlighting that feature size and data resolution always need to be critically assessed prior to undertaking analysis. The inventory was then used to extract feature statistics of ground cracks from a 1 m DTM, which were then manipulated to provide information on crack dimensions, shape and position on the landscape. Cracks were 7 m on average with fewer small- and large-scale features, and preferentially propagated in a slope perpendicular direction implying a topographic control as cracking tended to follow the contour. Fuzzy Logic was used to statistically analyse a number of topographic and proximal derivatives from the DTM to determine the most influential spatial topographic controls on coseismic ground cracking. Results conformed to and therefore validated some pre-existing concepts. Proximity to landsliding appears to be the most influential spatial topographic control, potentially linking ground cracking to incipient landsliding. Cracking was more preferential at ridgetop locations and on source-facing hillslopes,

conforming to topographic site effects (TSE). Statistical relationships between ground cracks and parameters were then used to inform a spatial prediction attempt for ground crack locations, which was found to have great potential and will provide direction to drive future research and decision making. This research has accomplished the aim of improving our understanding of coseismic ground cracking through the answers gained to the following research questions.

9.1.1. Research Question 1

Can high-resolution LiDAR data be used to semi-automatically and accurately detect and predict small-scale ground crack features?

Results are promising – however sub-meter scale DTM data is required to do this successfully. Ultimately, despite showing great promise more research is needed to unlock the potential to detect cracks semi-automatically. The following conclusions helped to answer this question:

Sub-meter scale DTM data is required to semi-automatically detect and extract ground crack features

Despite being high resolution, the 1 m DTM from New Zealand is not of the required resolution to automatically detect and extract ground crack features from the landscape. This is likely due to the relationship between crack size and data resolution, as cracks may be narrower than the 1 m DTM cell size. This is supported by the fact that semi-automatic extraction of ground crack features performed well on ~10 cm DTM data from North Yorkshire. Cracks displayed coherent topographic signatures, and the data was resolute enough to detect the slightly different characteristics expressed by cracks walls and crack tips. Ultimately the suggestion is that, in the case of coseismic ground cracks, sub-meter scale DTM data is required to successfully detect and extract features.

Predicting ground crack locations has great potential, and may be a valuable contribution to decision making

An attempt at predicting ground crack locations was quantitatively unsuccessful as all model outputs did not achieve the required threshold value. That said, all came very close despite the omission of shaking data, and some minor alterations to membership functions may have pushed model outputs over this threshold. All models achieved very high relative true positive rates, suggesting substantial over-prediction. This could partially be explained by the scale of ground cracks and therefore the ratio of crack to study area pixel

numbers. Qualitatively, the best performing model output was very promising, as the majority of ground cracks appear to lie in areas predicted to be high hazard. This has practical potential for susceptibility monitoring as it can provide decision makers with an initial indication of where ground cracks, and therefore unstable slopes, are likely to be located. This can inform more focused investigation, ongoing monitoring and even evacuation. As Fuzzy Logic can be applied quickly, it can be applied following an earthquake to indicate which hillslopes may be vulnerable to failure in the event of an aftershock, heavy rainfall or even unprovoked reactivation in the future. However, this would be contingent on data being readily available and rapidly acquired.

Coseismic ground cracks appear to exhibit a similar probability density distribution to landslides, whereby feature frequency is a function of crack length after the rollover ~6.3 m. As such, crack frequency has the potential to be predicted in the future.

9.1.2. Research Question 2

What are the geomorphological characteristics of coseismic ground cracking?

Coseismic ground cracks are commonly ~7 m and predominantly between ~3-8 m in size and do not have a random orientation, propagating in a preferentially slope perpendicular direction. Longer cracks tend to be more sinuous. Results suggest a topographic influence may force ground cracks to propagate along the contour. To provide some more detail:

Coseismic ground cracks are commonly ~7 m and most are between ~3-8 m in size.
Lack of very small-scale features may be due to data resolution and methodological constraints (e.g. occlusion, subjectivity etc.). Alternatively, lack of very small- and large-scale features may offer an insight into the relationship between seismic shaking and hillslope deformation. Strain accumulation and positive pore pressure fluctuations (and positive feedback mechanisms as a result of this) may cause a lack of very small-scale features. This also may be an indication that a certain strain threshold is required in order to crack the ground – this may be large enough to ensure that very small cracks rarely ensue. Large-scale cracks have likely developed into full hillslope failure or the timescale between the earthquake and acquisition of aerial photography was not long enough to enable cracks to lengthen into longer features.

Topography may exert a control on ground crack propagation

The sinuosity of ground cracks, and preferentially slope perpendicular nature of their form on the landscape suggests that cracking may follow the topographic contour as it propagates through the landscape.

9.1.3. Research Question 3

What are the spatial topographic controls on coseismic landsliding?

Proximity to landslides is the most influential spatial topographic control. Cracks also exhibit an inverse spatial relationship with landsliding through distance to ridgetops and fault rupture, suggesting a link between ground cracking and both incipient and full hillslope failure. Cracks preferentially occur closer to ridgetop locations and on source-facing slopes, pointing to the influence of topographic sites effects (TSE). To expand on these points:

Coseismic ground cracking may be a surface expression of incipient landsliding

Proximity to coseismic landsliding was the strongest spatial topographic control on coseismic ground cracking, accounting for the majority of model predictive performance. Other parameters which have a strong link with landsliding (e.g. slope angle) also exert a control on coseismic ground cracking. Distance to ridgetops, valley bottoms and sites of fault rupture highlighted the coincidence between increases in ground crack occurrence and decreases in landslide occurrence, and vice versa. According to results from Cross Slope Profile analysis, there was a positive correlation between increasing step size and slope angle. Cracks on steeper slopes had larger step values, suggesting a gravitational influence. Ultimately, this all suggests that cracking may be a surface expression of incipient landsliding. Other processes may control which parts of a slope fail completely and which do not, including internal conditions such as pore pressure, and gravitational influences as there must be a reason as to why cracked areas have not reached the stage of brittle deformation and failure.

Coseismic ground cracking supports conventional topographic site effects (TSE) theory

Coseismic ground cracking is more preferential at and near to ridgetop locations, likely due to stronger shaking experienced here and potentially due to the lack of regolith for full failure, or cracking upslope of slumping mass. It is also more preferential on slopes facing the source of shaking. This is the opposite of the relationship between directional shaking and coseismic landsliding, suggesting that hillslope failure may be impacted by the

interaction between seismic shaking and local slope aspect, and the resulting impact that this has on normal and shear stress. Directional shaking may force material into/outwards from a hillslope, encouraging cracking/landsliding respectively – cracking may ensue as a hillslope is unable to develop into full failure due to material being compacted into a hillslope. This notion further supports the previous point, and likely indicates that cracking is an expression of incipient landsliding.

Answers to research questions have both improved our understanding of coseismic ground cracking and provided clear potential direction for future research.

9.2. FUTURE RESEARCH

Limitations of this study can be capitalised on to inform a number of useful research directions, which will only increase our knowledge of coseismic ground cracking. Considering limitations in the context of the experiences gained from writing this thesis provides the opportunity to transform them into a suggestion for a coherent and comprehensive template for a future research project. There are two key pillars to this.

Firstly, future research into coseismic ground cracking using a similar approach must be upscaled and build upon the data sources and methodologies used in this instance. Upscaling will help to determine whether or not local findings from this study are still relevant on a regional scale. This would ideally involve a much bigger study area (akin to coseismic landslide studies) to produce a larger sample of ground crack features. A larger study area and sample size would address any ambiguity surrounding the local scope of this study, and any impact that this may have had on results. It would also enable the inclusion of peak ground acceleration/velocity and geology in the study remit, which have been deemed a key control on coseismic landsliding in past studies (e.g. Jibson *et al.*, 2000). Furthermore, a larger sample size, and a larger study area available for cross examination will only improve the significance of the statistical relationships calculated from Fuzzy Logic. It would be interesting to see whether or not this further validated results from this study and/or informed a more successful prediction attempt. If prediction attempts can be continuously improved, this will have positive implications for geomorphological study and as has been outlined throughout this thesis, humanitarian purposes – for example with the potential to result in more accurately informed monitoring decisions.

Upscaling could be used in tandem with higher-resolution Light Detection and Ranging (LiDAR) data, which will inevitably increase the accuracy geomorphological analysis and the statistical relationships extracted as the slight topographic differences caused by ground cracks will be detected with greater proficiency. Using field validation to ground-truth a digitized ground crack inventory is paramount and will increase the accuracy and robustness of such (Guzzetti *et al.*, 2012) and therefore any results that stem from the use of it.

The second pillar focuses on further validation of data on coseismic ground cracking. To achieve this, further insight is needed into how cracking evolves following an earthquake to determine whether or not it actually poses a future hazard (e.g. in the form of developing into post-seismic landsliding). This is important as ground cracking therefore has great potential to contribute to the ongoing discussion on post-earthquake legacy (e.g. Dadson *et al.*, 2004), and in turn may provide crucial insight into landscape evolution following an earthquake, and consequently post-earthquake hazard and risk. Hypothetically, this study has shown that this could be achieved using a number of LiDAR surveys at regular intervals after an earthquake, perhaps coupled with the in-situ monitoring of crack movements. Surveys could then be compared to see (potentially quantitatively) how cracks and the landscape in general evolve.

This thesis has made sensible and realistic considerations of resource constraints to provide some focused initial findings regarding original subject matter. Most importantly, it may provide a solid foundation which can be built upon going forward by using both the findings and lessons learned to inform any future research.

APPENDICES

Aerial Photography, Point Cloud data (New Zealand) and vector shapefiles courtesy of GNS Science:

https://www.gns.cri.nz/Home/Products/Databases

Point Cloud data (North Yorkshire) courtesy of COBRA (Durham University & Cleveland Potash Ltd):

http://community.dur.ac.uk/cobra/

PlanetLabs Imagery courtesy of Planet Labs Ltd:

https://www.planet.com/

REFERENCES

AAM NZ Limited, 2017. *Volume 27413A14NOK*. 141116 EQ Wide Area Response. Napier, NZ: AAM NZ Limited.

Abrahamson, N.A. and Somerville, P.G., 1996. Effects of the hanging wall and footwall on ground motions recorded during the Northridge earthquake. *Bulletin of the Seismological Society of America*, *86*(1B), pp.S93-S99.

Abrahamson, N., Atkinson, G., Boore, D., Bozorgnia, Y., Campbell, K., Chiou, B., Idriss, I.M., Silva, W. and Youngs, R., 2008. Comparisons of the NGA ground-motion relations. *Earthquake Spectra*, *24*(1), pp.45-66.

Aki, K., 1984. Asperities, barriers, characteristic earthquakes and strong motion prediction. *Journal of Geophysical Research: Solid Earth*, *89*(B7), pp.5867-5872.

Anderson, H., Beanland, S., Buck, G., Darby, D., Downes, G., Haines, J., Jackson, J., Robinson, R. and Webb, T., 1994. The 1968 May 23 Inangahua, New Zealand, earthquake: an integrated geological, geodetic, and seismological source model. *New Zealand Journal of Geology and Geophysics*, *37*(1), pp.59-86.

Anderson, J.G., Brune, J.N., Anooshehpoor, R. and Ni, S.D., 2000. New ground motion data and concepts in seismic hazard analysis. *Current Science*, pp.1278-1290.

Anderson, R.S. and Anderson, S.P., 2010. *Geomorphology: the mechanics and chemistry of landscapes*. Cambridge University Press.

ArcGIS Pro. (v. 2.3.3). Redlands, CA, USA: Environmental Systems Research Institute (ESRI).

Ardizzone, F., Cardinali, M., Galli, M., Guzzetti, F. and Reichenbach, P., 2007. Identification and mapping of recent rainfall-induced landslides using elevation data collected by airborne Lidar. *Natural Hazards and Earth System Science*, *7*(6), pp.637-650.

Aydan, Ö., Ohta, Y. and Hamada, M., 2009. Geotechnical evaluation of slope and ground failures during the 8 October 2005 Muzaffarabad earthquake, Pakistan. *Journal of Seismology*, *13*(3), pp.399-413.

Baltsavias, E.P., 1999. Airborne laser scanning: basic relations and formulas. *ISPRS Journal of Photogrammetry and Remote Sensing*, *54*(2-3), pp.199-214.

Barredo, J., Benavides, A., Hervás, J. and van Westen, C.J., 2000. Comparing heuristic landslide hazard assessment techniques using GIS in the Tirajana basin, Gran Canaria Island, Spain. *International Journal of Applied Earth Observation and Geoinformation*, *2*(1), pp.9-23.

Baruch, A. and Filin, S., 2011. Detection of gullies in roughly textured terrain using airborne laser scanning data. *ISPRS Journal of Photogrammetry and Remote Sensing*, *66*(5), pp.564-578.

Beavan, J., Fielding, E., Motagh, M., Samsonov, S. and Donnelly, N., 2011. Fault location and slip distribution of the 22 February 2011 Mw 6.2 Christchurch, New Zealand, earthquake from geodetic data. *Seismological Research Letters*, *82*(6), pp.789-799.

Beavan, J., 2016. New Zealand GPS velocity field: 1995 – 2013. *New Zealand Journal of Geology and Geophysics*. 59,5–14. doi:10.1080/00288306.2015.11128

Bennett, R., Welham, K., Hill, R.A. and Ford, A., 2012. A comparison of visualization techniques for models created from airborne laser scanned data. *Archaeological Prospection*, *19*(1), pp.41-48.

Bindi, D., Luzi, L., Massa, M. and Pacor, F., 2010. Horizontal and vertical ground motion prediction equations derived from the Italian Accelerometric Archive (ITACA). *Bulletin of Earthquake Engineering*, *8*(5), pp.1209-1230.

Bollinger, L., Sapkota, S.N., Tapponnier, P., Klinger, Y., Rizza, M., Van Der Woerd, J., Tiwari, D.R., Pandey, R., Bitri, A. and Bes de Berc, S., 2014. Estimating the return times of great Himalayan earthquakes in eastern Nepal: Evidence from the Patu and Bardibas strands of the Main Frontal Thrust. *Journal of Geophysical Research: Solid Earth*, *119*(9), pp.7123-7163.

Bouchon, M. and Barker, J.S., 1996. Seismic response of a hill: the example of Tarzana, California. *Bulletin of the Seismological Society of America*, *86*(1A), pp.66-72.

Bradley, B.A., Razafindrakoto, H.N. and Polak, V., 2017. Ground-Motion Observations from the 14 November 2016 M w 7.8 Kaikoura, New Zealand, Earthquake and Insights from Broadband Simulations. *Seismological Research Letters*, *88*(3), pp.740-756.

Brain, M.J., Rosser, N.J. and Tunstall, N., 2017. The control of earthquake sequences on hillslope stability. *Geophysical Research Letters*, *44*(2), pp.865-872.

Brenstrum, E., 1998. *The New Zealand Weather Book*. Nelson: Craig Potton Pub.

Brunsden, D. and Prior, D.B., 1984. *Slope Instability*. Chichester: John Wiley & Sons.

Bui, D.T., Pradhan, B., Lofman, O., Revhaug, I. and Dick, O.B., 2012. Landslide susceptibility mapping at Hoa Binh province (Vietnam) using an adaptive neuro-fuzzy inference system and GIS. *Computers & Geosciences*, *45*, pp.199-211.

Bull, W.B., 2011. *Tectonically Active Landscapes*. Chichester: John Wiley & Sons.

Burbank, D.W., Leland, J., Fielding, E., Anderson, R.S., Brozovic, N., Reid, M.R. and Duncan, C., 1996. Bedrock incision, rock uplift and threshold hillslopes in the northwestern Himalayas. *Nature*, *379*(6565), p.505.

Burbank, D.W. and Anderson, R.S., 2009. *Tectonic Geomorphology*. Chichester: John Wiley & Sons.

Carrara, A., 1983. Multivariate models for landslide hazard evaluation. *Journal of the International Association for Mathematical Geology*, *15*(3), pp.403-426.

Challis, K., Forlin, P. and Kincey, M., 2011. A generic toolkit for the visualization of archaeological features on airborne LiDAR elevation data. *Archaeological Prospection*, *18*(4), pp.279-289.

Chen, L., Yuan, X., Cao, Z., Hou, L., Sun, R., Dong, L., Wang, W., Meng, F. and Chen, H., 2009. Liquefaction macrophenomena in the great Wenchuan earthquake. *Earthquake Engineering and Engineering Vibration*, *8*(2), pp.219-229.

Chen, X.Q., Li, Y., Gao, Q. and Jia, S.T., 2012). Distribution characteristics of Geo-hazards in Ganxi Valley after the Wenchuan earthquake. *Environmental Earth Sciences*, 65(4), pp.965-973.

Chiswell, S.M., Bostock, H.C., Sutton, P.J. and Williams, M.J., 2015. Physical oceanography of the deep seas around New Zealand: a review. *New Zealand Journal of Marine and Freshwater Research*, *49*(2), pp.286-317.

Collins, B.D., Jibson, R.W., 2015. Assessment of Existing and Potential Landslide Hazards Resulting from the April 25, 2015 Gorkha, Nepal Earthquake Sequence. *USGS OpenFile Report 2015-1142*.

Cowan, H.A. and McGlone, M.S., 1991. Late Holocene displacements and characteristic earthquakes on the Hope River segment of the Hope Fault, New Zealand. *Journal of the Royal Society of New Zealand*, *21*(4), pp.373-384.

Cowan, H., Nicol, A. and Tonkin, P., 1996. A comparison of historical and paleoseismicity in a newly formed fault zone and a mature fault zone, North Canterbury, New Zealand. *Journal of Geophysical Research: Solid Earth*, *101*(B3), pp.6021-6036.

Cox, N.J., 2007. Kernel estimation as a basic tool for geomorphological data analysis. *Earth Surface Processes and Landforms: The Journal of the British Geomorphological Research Group*, *32*(12), pp.1902-1912.

Cubrinovski, M., Bray, J.D., Taylor, M., Giorgini, S., Bradley, B., Wotherspoon, L. and Zupan, J., 2011. Soil liquefaction effects in the central business district during the February 2011 Christchurch earthquake. *Seismological Research Letters*, *82*(6), pp.893-904.

Cubrinovski, M., Bray, J., de la Torre, C., Olsen, 4.M., Bradley, B., Chiaro, G., Stock, E. and Wotherspoon, L., 2017. Liquefaction effects and associated damages observed at the Wellington CentrePort from the 2016 Kaikoura earthquake. *Bulletin of the New Zealand Society for Earthquake Engineering*, 50(2), pp. 152-173.

Cui, P., Chen, X.Q., Zhu, Y.Y., Su, F.H., Wei, F.Q., Han, Y.S., Liu, H.J. and Zhuang, J.Q., 2011. The Wenchuan earthquake (May 12, 2008), Sichuan province, China, and resulting geohazards. *Natural Hazards*, *56*(1), pp.19-36.

Dadson, S.J., Hovius, N., Chen, H., Dade, W.B., Lin, J.C., Hsu, M.L., Lin, C.W., Horng, M.J., Chen, T.C., Milliman, J. and Stark, C.P., 2004. Earthquake-triggered increase in sediment delivery from an active mountain belt. *Geology*, 32(8), pp.733-736.

Dai, F.C., Lee, C.F. and Ngai, Y.Y., 2002. Landslide risk assessment and management: an overview. *Engineering Geology*, *64*(1), pp.65-87.

Dai, F.C., Xu, C., Yao, X., Xu, L., Tu, X.B. and Gong, Q.M., 2011. Spatial distribution of landslides triggered by the 2008 Ms 8.0 Wenchuan earthquake, China. *Journal of Asian Earth Sciences*, 40(4), pp.883-895.

Davies, A. J. (2017). Transport infrastructures performance and management in the South Island of New Zealand during the first 100 days following the 2016 M_w 7.8 Kaikōura earthquake. *Bulletin of the New Zealand Society for Earthquake Engineering*. 50, pp. 271-298.

Delloite, 2017. The Forgotten impact – Kaikoura Earthquake: Wellington still paying the price.

Dellow, G., Yetton, M., Massey, C., Archibald, G., Barrell, D.J.A., Bell, D., Bruce, Z., Campbell, A., Davies, T., De Pascale, G. and Easton, M., 2011. Landslides caused by the 22 February 2011 Christchurch earthquake and management of landslide risk in the immediate aftermath. *Bulletin of the New Zealand Society for Earthquake Engineering*, *44*(4), pp.227-238.

Dellow, S., Massey, C., Cox, S., Archibald, G., Begg, J., Bruce, Z., Carey, J., Davidson, J., Della Pasqua, F., Glassey, P. and Hill, M., 2017. Landslides caused by the M_w 7. 8 Kaikōura earthquake and the immediate response. *Bulletin of the New Zealand Society for Earthquake Engineering, 50(2),* pp 106-116.

Densmore, A. and Hovius, N. (2000) 'Topographic fingerprints of bedrock landslides' Geology 28(4): 371-374.

Dunning, S.A., Mitchell, W.A., Rosser, N.J. and Petley, D.N., 2007. The Hattian Bala rock avalanche and associated landslides triggered by the Kashmir Earthquake of 8 October 2005. *Engineering Geology*, *93*(3-4), pp.130-144.

Duff, D., 1994. *Holmes' Principles of Physical Geology. New York:* Chapman & Hall, 791 p.

Environmental Systems Research Institute, 2019. ArcGIS Pro Help. *How Flow Accumulation Works*. [online] Available at: https://pro.arcgis.com/en/pro-app/tool-reference/spatial-analyst/how-flow-accumulation-works.htm (last accessed 19 November 2019).

Evans, B., Fredrich, J.T. and Wong, T.F., 1990. The brittle-ductile transition in rocks: Recent experimental and theoretical progress. *The Brittle-Ductile Transition in Rocks, Geophys. Monogr. Ser*, *56*, pp.1-20.

Evans, M. and Lindsay, J.B., 2010. Quantifying gully erosion in upland peatlands at the landscape scale: gully mapping from a high resolution LiDAR DEM. *Earth Surface Processes and Landforms*, *35*, pp.876-886.

Evans, D., 2016. Airborne laser scanning as a method for exploring long-term socio-ecological dynamics in Cambodia. *Journal of Archaeological Science*, *74*, pp.164-175.

Excel 2016. (2016). Redmond, WA, USA: Microsoft.

Fensham, R.J. and Fairfax, R.J., 2002. Aerial photography for assessing vegetation change: a review of applications and the relevance of findings for Australian vegetation history. *Australian Journal of Botany*, *50*(4), pp.415-429.

Fowler, A., 1999. Potential climate change impacts on water resources in the Auckland Region (New Zealand). *Climate Research*, *11*(3), pp.221-245.

Froude, M.J. and Petley, D., 2018. Global fatal landslide occurrence from 2004 to 2016. *Natural Hazards and Earth System Sciences*, *18*, pp.2161-2181.

Gallant, J.C. and Wilson, J.P. eds., 2000. *Terrain analysis: principles and applications*. Chichester: John Wiley & Sons.

Galli, M., Ardizzone, F., Cardinali, M., Guzzetti, F. and Reichenbach, P., 2008. Comparing landslide inventory maps. *Geomorphology*, *94*(3-4), pp.268-289.

García-Rodríguez, M.J., Malpica, J.A., Benito, B. and Díaz, M., 2008. Susceptibility assessment of earthquake-triggered landslides in El Salvador using logistic regression. *Geomorphology*, *95*(3-4), pp.172-191.

Gerrard, J., 1994. The landslide hazard in the Himalayas: geological control and human action. *Geomorphology and Natural Hazards*, pp. 221-230.

Gledhill, K., Ristau, J., Reyners, M., Fry, B. and Holden, C., 2011. The Darfield (Canterbury, New Zealand) Mw 7.1 earthquake of September 2010: A preliminary seismological report. *Seismological Research Letters*, *82*(3), pp.378-3

Glenn, N.F., Streutker, D.R., Chadwick, D.J., Thackray, G.D. and Dorsch, S.J., 2006. Analysis of LiDAR-derived topographic information for characterizing and differentiating landslide morphology and activity. *Geomorphology*, *73*(1-2), pp.131-148.

Godt, J.W., Baum, R.L. and Lu, N., 2009. Landsliding in partially saturated materials. *Geophysical research letters*, *36*(2).

Green, R.A., Olson, S.M., Cox, B.R., Rix, G.J., Rathje, E., Bachhuber, J., French, J., Lasley, S. and Martin, N., 2011. Geotechnical aspects of failures at Port-au-Prince seaport during the 12 January 2010 Haiti earthquake. *Earthquake Spectra*, *27*(S1), pp.S43-S65.

Grapes, R., Little, T. and Downes, G., 1998. Rupturing of the Awatere Fault during the 1848 October 16 Marlborough earthquake, New Zealand: historical and present day evidence. *New Zealand Journal of Geology and Geophysics*, *41*(4), pp.387-399.

Guzzetti, F., Galli, M., Reichenbach, P., Ardizzone, F. and Cardinali, M.J.N.H., 2006. Landslide hazard assessment in the Collazzone area, Umbria, Central Italy. *Natural Hazards and Earth System Science*, *6*(1), pp.115-131.

Guzzetti, F., Cardinali, M., Reichenbach, P. and Carrara, A., 2000. Comparing landslide maps: A case study in the upper Tiber River Basin, central Italy. *Environmental Management*, *25*(3), pp.247-263.

Guzzetti, F., Mondini, A.C., Cardinali, M., Fiorucci, F., Santangelo, M. and Chang, K.T., 2012. Landslide inventory maps: New tools for an old problem. *Earth-Science Reviews*, *112*(1-2), pp.42-66.

Hamling, I.J., Hreinsdóttir, S., Clark, K., Elliott, J., Liang, C., Fielding, E., Litchfield, N., Villamor, P., Wallace, L., Wright, T.J. and D'Anastasio, E., 2017. Complex multifault rupture during the 2016 M_w 7.8 Kaikōura earthquake, New Zealand. *Science*, *356*(6334), p.eaam7194.

Hancox, G.T., Perrin, N.D. and Dellow, G.D., 2002. Recent studies of historical earthquake-induced landsliding, ground damage, and MM intensity in New Zealand. *Bulletin of the New Zealand Society of Earthquake Engineering*, *35*(2), pp.59-95.

Harp, E.L. and Jibson,.R.W., 1995. Inventory of landslides triggered by the 1994 Northridge, California earthquake. *An Open Repository of Earthquake-triggered Ground Failure Inventories, U.S. Geological Survey data release collection. Available at* at https://doi.org/10.5066/F7H70DB4

Harp, E.L. and Jibson, R.W., 1996. Landslides triggered by the 1994 Northridge, California, earthquake. *Bulletin of the Seismological Society of America*, *86*(1B), pp.S319-S332.

Harris, R.A., Simpson, R.W. and Reasenberg, P.A., 1995. Influence of static stress changes on earthquake locations in southern California. *Nature*, *375*(6528), p.221.

Harvey, K.R. and Hill, G.J.E., 2001. Vegetation mapping of a tropical freshwater swamp in the Northern Territory, Australia: a comparison of aerial photography, Landsat TM and SPOT satellite imagery. *International journal of Remote Sensing*, *22*(15), pp.2911-2925.

Hervás, J. and Bobrowsky, P., 2009. Mapping: inventories, susceptibility, hazard and risk. In *Landslides–Disaster Risk Reduction* (pp. 321-349). Berlin: Springer.

Hesse, R., 2010. LiDAR-derived Local Relief Models–a new tool for archaeological prospection. *Archaeological Prospection*, *17*(2), pp.67-72.

Hovius, N., Stark, C.P. and Allen, P.A., 1997. Sediment flux from a mountain belt derived by landslide mapping. *Geology*, *25*(3), pp.231-234.

Hovius, N., Meunier, P., Lin, C.W., Chen, H., Chen, Y.G., Dadson, S., Horng, M.J. and Lines, M., 2011. Prolonged seismically induced erosion and the mass balance of a large earthquake. *Earth and Planetary Science Letters, 304(3-4)*, pp.347-355.

Hovius, N. and Meunier, P (2012) 'Earthquake ground motion and patterns of seismically induced landsliding', pp. 24-36 in Clague, J. J. and Stead, D. (eds) *Landslides: Types, Mechanisms and Modelling*. Cambridge: Cambridge University Press.

Huang, Y. and Jiang, X., 2010. Field-observed phenomena of seismic liquefaction and subsidence during the 2008 Wenchuan earthquake in China. *Natural Hazards*, *54*(3), pp.839-850.

Hungr, O., Leroueil, S. and Picarelli, L., 2014. The Varnes classification of landslide types, an update. *Landslides*, *11*(2), pp.167-194.

Hussain, A. and Yeats, R.S., 2009. Geological setting of the 8 October 2005 Kashmir earthquake. *Journal of Seismology*, *13*(3), pp.315-325.

Ishihara, K., 1993. Liquefaction and flow failure during earthquakes. *Geotechnique*, *43*(3), pp.351-451.

Jayangondaperumal, R. and Thakur, V.C., 2008. Co-seismic secondary surface fractures on southeastward extension of the rupture zone of the 2005 Kashmir earthquake. *Tectonophysics*, *446*(1-4), pp.61-76.

Jenness, J., 2006. Topographic Position Index (tpi_jen.avx) extension for ArcView 3.x, v. 1.3a. Jenness Enterprises. Available at: http://www.jennessent.com/arcview/tpi.htm.

Jibson, R.W., Harp, E.L. and Michael, J.A., 2000. A method for producing digital probabilistic seismic landslide hazard maps. *Engineering Geology*, *58*(3-4), pp.271-289.

Jibson, R.W., Allstadt, K.E., Rengers, F.K. and Godt, J.W., 2018. *Overview of the geologic effects of the November 14, 2016, Mw 7.8 Kaikoura, New Zealand, earthquake* (No. 2017-5146). US Geological Survey.

Jiang, N., Hay, J.E. and Fisher, G.W., 2004. Classification of New Zealand synoptic weather types and relation to the Southern Oscillation Index. *Weather and Climate*, *23*, pp.3-23.

Kaiser, A., Holden, C., Beavan, J., Beetham, D., Benites, R., Celentano, A., Collett, D., Cousins, J., Cubrinovski, M., Dellow, G. and Denys, P., 2012. The M_w 6.2 Christchurch

earthquake of February 2011: preliminary report. *New Zealand journal of Geology and Geophysics*, *55*(1), pp.67-90.

Kaiser, A., Balfour, N., Fry, B., Holden, C., Litchfield, N., Gerstenberger, M., D'Anastasio, E., Horspool, N., McVerry, G., Ristau, J. and Bannister, S., 2017. The 2016 Kaikōura, New Zealand, earthquake: preliminary seismological report. *Seismological Research Letters*, *88*(3), pp.727-739.

Kamp, U., Growley, B.J., Khattak, G.A. and Owen, L.A., 2008. GIS-based landslide susceptibility mapping for the 2005 Kashmir earthquake region. *Geomorphology, 101(4)*, pp.631-642.

Kao, M.H., 2002. Thermo-tectonic implications of zircon and apatite FT data of the Marlborough Region, South Island, New Zealand. *Terrestrial, Atmospheric and Oceanic Sciences*, *13*(2), pp.109-124.

Keefer, D.K., 1984. Landslides caused by earthquakes. *Geological Society of America Bulletin, 95(4)*, pp.406-421.

Keefer, D.K., 2000. Statistical analysis of an earthquake-induced landslide distribution—the 1989 Loma Prieta, California event. *Engineering Geology, 58(3-4)*, pp.231-249.

Keefer, D.K., 2002. Investigating landslides caused by earthquakes–a historical review. *Surveys in Geophysics, 23(6)*, pp.473-510

Kellogg, K.S., 2001. Tectonic controls on a large landslide complex: Williams Fork Mountains near Dillon, Colorado. *Geomorphology*, *41*(4), pp.355-368.

Khan, S.F., Kamp, U. and Owen, L.A., 2013. Documenting five years of landsliding after the 2005 Kashmir earthquake, using repeat photography. *Geomorphology*, *197*, pp.45-55.

Khattak, G.A., Owen, L.A., Kamp, U. and Harp, E.L., 2010. Evolution of earthquake-triggered landslides in the Kashmir Himalaya, northern Pakistan. *Geomorphology*, *115*(1-2), pp.102-108.

Khazai, B. and Sitar, N., 2004. Evaluation of factors controlling earthquake-induced landslides caused by Chi-Chi earthquake and comparison with the Northridge and Loma Prieta events. *Engineering Geology*, *71*(1-2), pp.79-95.

Kilburn, C.R. and Petley, D.N., 2003. Forecasting giant, catastrophic slope collapse: lessons from Vajont, Northern Italy. *Geomorphology*, *54*(1-2), pp.21-32.

Korup, O., 2005. Geomorphic imprint of landslides on alpine river systems, southwest New Zealand. *Earth Surface Processes and Landforms*, *30*(7), pp.783-800.

Kritikos, T., Robinson, T.R. and Davies, T.R., 2015. Regional coseismic landslide hazard assessment without historical landslide inventories: A new approach. *Journal of Geophysical Research: Earth Surface*, *120*(4), pp.711-729.

Langridge, R.M. and Berryman, K.R., 2005. Morphology and slip rate of the Hurunui section of the Hope Fault, South Island, New Zealand. *New Zealand Journal of Geology and Geophysics*, *48*(1), pp.43-57.

Larsen, I.J., Montgomery, D.R. and Korup, O., 2010. Landslide erosion controlled by hillslope material. *Nature Geoscience*, *3*(4), p.247.

Leroueil, S., Locat, A., Eberhardt, E. and Kovacevic, N., 2012. Progressive failure in natural and engineered slopes, in *Landslides and Engineered Slopes,* edited by: Eberhardt, E., Froese, C., Turner, AK, and Leroueil, S., London: Taylor & Francis Group, 3146.

Li, C.Y., Wei, Z.Y., Ye, J.Q., Han, Y.B. and Zheng, W.J., 2010. Amounts and styles of coseismic deformation along the northern segment of surface rupture, of the 2008 Wenchuan Mw 7.9 earthquake, China. *Tectonophysics*, *491*(1-4), pp.35-58.

Lin, J. and Stein, R.S., 2004. Stress triggering in thrust and subduction earthquakes and stress interaction between the southern San Andreas and nearby thrust and strike-slip faults. *Journal of Geophysical Research: Solid Earth*, *109*(B2).

Lin, G.W., Chen, H., Chen, Y.H. and Horng, M.J., 2008. Influence of typhoons and earthquakes on rainfall-induced landslides and suspended sediments discharge. *Engineering Geology*, *97*(1-2), pp.32-41.

Litchfield, N. J., P. Villamor, R. J. Van Dissen, A. Nicol, P. M. Barnes, D. J. A. Barrell, J. Pettinga, R. M. Langridge, T. A. Little, J. Mountjoy, *et al.*, 2018. Surface fault rupture from the M_w 7.8 2016 Kaikōura earthquake, New Zealand, and insights into factors controlling multi-fault ruptures. *Bulletin of the. Seismological Society of America, 50(2)*, pp.73-84

Lorrey, A.M. and Bostock, H., 2017. The climate of New Zealand through the Quaternary. In *Landscape and Quaternary Environmental Change in New Zealand*. Paris: Atlantis Press. pp. 67-139.

Main, I.G., Sammonds, P.R. and Meredith, P.G., 1993. Application of a modified Griffith criterion to the evolution of fractal damage during compressional rock failure. *Geophysical Journal International*, *115*(2), pp.367-380.

Mahmood, I., Qureshi, S.N., Tariq, S., Atique, L. and Iqbal, M.F., 2015. Analysis of landslides triggered by October 2005, Kashmir Earthquake. *PLoS currents*, *7*.

Malamud, B.D., Turcotte, D.L., Guzzetti, F. and Reichenbach, P., 2004. Landslide inventories and their statistical properties. *Earth Surface Processes and Landforms*, *29*(6), pp.687-711.

Marc, O., Hovius, N., Meunier, P., Uchida, T. and Hayashi, S., 2015. Transient changes of landslide rates after earthquakes. *Geology*, *43*(10), pp.883-886.

Marc, O., Hovius, N. and Meunier, P., 2016. The mass balance of earthquakes and earthquake sequences. *Geophysical Research Letters*, *43*(8), pp.3708-3716.

Martha, T.R., Kerle, N., Jetten, V., van Westen, C.J. and Kumar, K.V., 2010. Characterising spectral, spatial and morphometric properties of landslides for semi-automatic detection using object-oriented methods. *Geomorphology*, *116*(1-2), pp.24-36.

Martha, T.R., Roy, P., Mazumdar, R., Govindharaj, K.B. and Kumar, K.V., 2017. Spatial characteristics of landslides triggered by the 2015 M w 7.8 (Gorkha) and M w 7.3 (Dolakha) earthquakes in Nepal. *Landslides*, *14*(2), pp.697-704.

Massey, C. I.; Della Pasqua, F.; Taig, T.; Lukovic, B.; Ries, W.; Heron, D., Archibald, G., 2014. Canterbury Earthquakes 2010/11 Port Hills Slope Stability: Risk assessment for Redcliffs. *GNS Science Consultancy Report* 2014/78. 123 p. + Appendices.

Massey, C., Townsend, D., Rathje, E., Allstadt, K.E., Lukovic, B., Kaneko, Y., Bradley, B., Wartman, J., Jibson, R.W., Petley, D.N. and Horspool, N., 2018. Landslides triggered by the 14 November 2016 M w 7.8 Kaikōura earthquake, New Zealand. *Bulletin of the Seismological Society of America*, *108*(3B), pp.1630-1648.

McGown, A., Radwan, A.M. and Gabr, A.W.A., 1977. Laboratory testing of fissured and laminated soils. In *Proc. IX int. Conf Soil Mech. and Found. Eng* (Vol. 1, pp. 205-210).

McKean, J. and Roering, J., 2004. Objective landslide detection and surface morphology mapping using high-resolution airborne laser altimetry. *Geomorphology*, *57*(3-4), pp.331-351.

Metternicht, G., Hurni, L. and Gogu, R., 2005. Remote sensing of landslides: An analysis of the potential contribution to geo-spatial systems for hazard assessment in mountainous environments. *Remote Sensing of Environment*, *98*(2-3), pp.284-303.

Meunier, P., Hovius, N. and Haines, A., 2007. Regional patterns of earthquake-triggered landslides and their relation to ground motion. *Geophysical Research Letters 34*: L20408

Meunier, P., Hovius, N. and Haines, J.A., 2008. Topographic site effects and the location of earthquake induced landslides. *Earth and Planetary Science Letters, 275(3)*, pp.221-232.

Molnar, P., Anderson, R.S. and Anderson, S.P., 2007. Tectonics, fracturing of rock, and erosion. *Journal of Geophysical Research: Earth Surface*, *112*(F3).

Morgan, J.L., Gergel, S.E. and Coops, N.C., 2010. Aerial photography: a rapidly evolving tool for ecological management. *BioScience*, *60*(1), pp.47-59.

Moss, R.E., Thompson, E.M., Scott Kieffer, D., Tiwari, B., Hashash, Y.M., Acharya, I., Adhikari, B.R., Asimaki, D., Clahan, K.B., Collins, B.D. and Dahal, S., 2015. Geotechnical effects of the 2015 magnitude 7.8 Gorkha, Nepal, earthquake and aftershocks. *Seismological Research Letters*, *86*(6), pp.1514-1523.

NZ Parliament, 2019 - https://www.parliament.nz/en/pb/research-papers/document/00PLEcoRP2016031/major-new-zealand-earthquakes-since-1855 (last accessed December 2018)

New Zealand Transport Agency (NZTA), 2016. Kaikoura Earthquake Update — 20 December http://www.nzta.govt.nz/assets/traffic/Kaikoura-Earthquake-newsletter-update-20161220.pdf. (last accessed December 2018)

Nicol, A., 1992. Tectonic structures developed in Oligocene limestones: implications for New Zealand plate boundary deformation in North Canterbury. *New Zealand Journal of Geology and Geophysics*, *35*(3), pp.353-362.

Nicol, A. and Van Dissen, R., 2002. Up-dip partitioning of displacement components on the oblique-slip Clarence Fault, New Zealand. *Journal of Structural Geology*, *24*(9), pp.1521-1535.

Nicol, A. and Beavan, J., 2003. Shortening of an overriding plate and its implications for slip on a subduction thrust, central Hikurangi Margin, New Zealand. *Tectonics*, *22*(6).

Nicol, A., Seebeck, H. and Wallace, L., 2017. Quaternary tectonics of New Zealand. In *Landscape and Quaternary environmental change in New Zealand* (pp. 1-34). Paris: Atlantis Press.

Norris, R.J. and Cooper, A.F., 2001. Late Quaternary slip rates and slip partitioning on the Alpine Fault, New Zealand. *Journal of Structural Geology*, *23*(2-3), pp.507-520.

Oglesby, D.D., Archuleta, R.J. and Nielsen, S.B., 2000. The three-dimensional dynamics of dipping faults. *Bulletin of the Seismological Society of America*, *90*(3), pp.616-628.

Owen, L.A., Kamp, U., Khattak, G.A., Harp, E.L., Keefer, D.K. and Bauer, M.A., 2008. Landslides triggered by the 8 October 2005 Kashmir earthquake. *Geomorphology*, *94*(1-2), pp.1-9.

Parise, M. and Jibson, R.W., 2000. A seismic landslide susceptibility rating of geologic units based on analysis of characteristics of landslides triggered by the 17 January, 1994 Northridge, California earthquake. *Engineering Geology*, *58*(3-4), pp.251-270.

Parker, R., 2010. Controls on the distribution of landslides triggered by the 2008 Wenchuan earthquake, Sichuan Province, China (Doctoral dissertation, Durham University).

Parker, R., 2013. Hillslope memory and spatial and temporal distributions of earthquake-induced landslides (Doctoral dissertation, Durham University).

Parker, R.N., Densmore, A.L., Rosser, N.J., De Michele, M., Li, Y., Huang, R., Whadcoat, S. and Petley, D.N., 2011. Mass wasting triggered by the 2008 Wenchuan earthquake is greater than orogenic growth. *Nature Geoscience*, *4*(7), p.449.

Parker, R.N., Hancox, G.T., Petley, D.N., Massey, C.I., Densmore, A.L. and Rosser, N.J., 2015. Spatial distributions of earthquake-induced landslides and hillslope preconditioning in northwest South Island, New Zealand. *Earth Surface Dynamics.*, *3*(4), pp.501-525.

Pearce, A.J. and O'Loughlin, C.L., 1985. Landsliding during a M 7.7 earthquake: influence of geology and topography. *Geology*, *13*(12), pp.855-858.

Petley, D.N. and Allison, R.J., 1997. The mechanics of deep-seated landslides. *Earth Surface Processes and Landforms: The Journal of the British Geomorphological Group*, *22*(8), pp.747-758.

Petley, D.N., Bulmer, M.H. and Murphy, W., 2002. Patterns of movement in rotational and translational landslides. *Geology*, *30*(8), pp.719-722.

Petley, D.N., 2004. The evolution of slope failures: mechanisms of rupture propagation. *Natural hazards and earth system sciences.*, *4*(1), pp.147-152.

Petley, D.N., Dunning, S.A., Rosser, N.J. and Hungr, O., 2005a. The analysis of global landslide risk through the creation of a database of worldwide landslide fatalities. *Landslide Risk Management. Balkema, Amsterdam*, pp.367-374.

Petley, D.N., Higuchi, T., Petley, D.J., Bulmer, M.H. and Carey, J., 2005b. Development of progressive landslide failure in cohesive materials. *Geology*, *33*(3), pp.201-204.

Petley, D.N., Mantovani, F., Bulmer, M.H. and Zannoni, A., 2005c. The use of surface monitoring data for the interpretation of landslide movement patterns. *Geomorphology*, *66*(1-4), pp.133-147.

Petley, D.N., Dunning, S.A., Rosser, N.J. & Kausar, AB., 2006. Incipient landslides in the Jhelum Valley, Pakistan following the 8th October 2005 earthquake. In: Marui, H. Disaster mitigation of debris flows, slope failures and landslides. *Frontiers in Science Series*. Tokyo, Japan: Universal Academy Press; 2006:47 – 56.

Petley, D.N., Hearn, G.J., Hart, A., Rosser, N.J., Dunning, S.A., Oven, K. and Mitchell, W.A., 2007. Trends in landslide occurrence in Nepal. *Natural Hazards*, *43*(1), pp.23-44.

Petley, D. (2018). *The research legacy of the Wenchuan Earthquake: a new review*. [online] The Landslide Blog. Available at: https://blogs.agu.org/landslideblog/2018/05/15/research-legacy-1/ [Accessed 15 Feb. 2019].

Philip, H. and Meghraoui, M., 1983. Structural analysis and interpretation of the surface deformations of the El Asnam earthquake of October 10, 1980. *Tectonics*, *2*(1), pp.17-49.

Pike, R.J., 1988. The geometric signature: quantifying landslide-terrain types from digital elevation models. *Mathematical Geology*, *20*(5), pp.491-511.

Pollitz, F.F. and Sacks, I.S., 2002. Stress triggering of the 1999 Hector Mine earthquake by transient deformation following the 1992 Landers earthquake. *Bulletin of the Seismological Society of America*, *92*(4), pp.1487-1496.

Popescu, M.E., 2002, July. Landslide causal factors and landslide remediatial options. In *3rd International Conference on Landslides, Slope Stability and Safety of Infra-Structures* (pp. 61-81).

Rajendran, K., Rajendran, C.P., Thakkar, M. and Tuttle, M.P., 2001. The 2001 Kutch (Bhuj) earthquake: Coseismic surface features and their significance. *Current Science*, pp.1397-1405.

Rattenbury, M.S., Townsend, D.B. and Johnston, M.R., 2006. *Geology of the Kaikoura area* (Vol. 1, No. 250,000). Institute of Geological & Nuclear Sciences.

Rattenbury, M.S. and Isaac, M.J., 2012. The QMAP 1: 250 000 geological map of New Zealand project. *New Zealand Journal of Geology and Geophysics*, *55*(4), pp.393-405.

Razak, K.A., Straatsma, M.W., Van Westen, C.J., Malet, J.P. and De Jong, S.M., 2011. Airborne laser scanning of forested landslides characterization: Terrain model quality and visualization. *Geomorphology*, *126*(1-2), pp.186-200.

Remondo, J., González-Díez, A., De Terán, J.R.D. and Cendrero, A., 2003. Landslide susceptibility models utilising spatial data analysis techniques. A case study from the lower Deba Valley, Guipúzcoa (Spain). *Natural Hazards*, *30*(3), pp.267-279.

Reyners, M., Robinson, R., Pancha, A. and McGinty, P., 2002. Stresses and strains in a twisted subduction zone—Fiordland, New Zealand. *Geophysical Journal International*, *148*(3), pp.637-648.

Rib, H.T. and Liang, T., 1978. Recognition and identification. *Transportation Research Board Special Report*, (176).

Roback, K., Clark, M.K., West, A.J., Zekkos, D., Li, G., Gallen, S.F., Chamlagain, D. and Godt, J.W., 2018. The size, distribution, and mobility of landslides caused by the 2015 Mw7. 8 Gorkha earthquake, Nepal. *Geomorphology*, *301*, pp.121-138.

Robinson, T.R., Davies, T.R., Wilson, T.M., Orchiston, C. and Barth, N., 2016. Evaluation of coseismic landslide hazard on the proposed Haast-Hollyford Highway, South Island, New Zealand. *Georisk: Assessment and Management of Risk for Engineered Systems and Geohazards, 10(2)*, pp.146-163.

Robinson, T.R., Rosser, N.J., Densmore, A.L., Williams, J.G., Kincey, M.E., Benjamin, J. and Bell, H.J., 2017. Rapid post-earthquake modelling of coseismic landsliding intensity and distribution for emergency response decision support. *Natural Hazards and Earth System Sciences.*, *17*(9), pp.1521-1540.

Robinson, T.R., Rosser, N.J., Davies, T.R., Wilson, T.M. and Orchiston, C., 2018. Near-Real-Time Modeling of Landslide Impacts to Inform Rapid Response: An Example from

the 2016 Kaikōura, New Zealand, EarthquakeNear-Real-Time Modeling of Landslide Impacts to Inform Rapid Response. *Bulletin of the Seismological Society of America*, *108*(3B), pp.1665-1682.

Ross, T.J., 2004. *Fuzzy Eogic with engineering Applications* (Vol. 2). New York: Wiley.

Rosser, N.J., Petley, D.N., Lim, M., Dunning, S.A. and Allison, R.J., 2005. Terrestrial laser scanning for monitoring the process of hard rock coastal cliff erosion. *Quarterly Journal of Engineering Geology and Hydrogeology*, *38*(4), pp.363-375.

Rossetto, T. and Peiris, N., 2009. Observations of damage due to the Kashmir earthquake of October 8, 2005 and study of current seismic provisions for buildings in Pakistan. *Bulletin of Earthquake Engineering*, *7*(3), pp.681-699.

Saba, S.B., van der Meijde, M. and van der Werff, H., 2010. Spatiotemporal landslide detection for the 2005 Kashmir earthquake region. *Geomorphology*, *124*(1-2), pp.17-25.

Sader, S.A. and Vermillion, S., 2000. Remote sensing education: An updated survey. *Journal of Forestry*, *98*(4), pp.31-37.

Sahoo, R.N., Reddy, D.V. and Sukhija, B.S., 2007. Evidence of liquefaction near Baramulla (Jammu and Kashmir, India) due to the 2005 Kashmir earthquake. *Current Science*, *92*(3), pp.293-295.

Samia, J., Temme, A., Bregt, A., Wallinga, J., Guzzetti, F., Ardizzone, F. and Rossi, M., 2017. Do landslides follow landslides? Insights in path dependency from a multi-temporal landslide inventory. *Landslides*, *14*(2), pp.547-558.

Salinger, M.J., 1980. New Zealand climate: I. precipitation patterns. *Monthly Weather Review*, *108*(11), pp.1892-1904.

Sato, H.P., Hasegawa, H., Fujiwara, S., Tobita, M., Koarai, M., Une, H. and Iwahashi, J., 2007. Interpretation of landslide distribution triggered by the 2005 Northern Pakistan earthquake using SPOT 5 imagery. *Landslides*, *4*(2), pp.113-122.

Schijve, J., 2001. *Fatigue of Structures and Materials*. London: Springer.

Schneider, J.F., 2009. Seismically reactivated Hattian slide in Kashmir, Northern Pakistan. *Journal of Seismology*, *13*(3), pp.387-398.

Schneider, A., Takla, M., Nicolay, A., Raab, A. and Raab, T., 2015. A template-matching approach combining morphometric variables for automated mapping of charcoal kiln sites. *Archaeological Prospection*, *22*(1), pp.45-62.

Shulmeister, J. ed., 2016. *Landscape and Quaternary Environmental Change in New Zealand* (Vol. 3). London: Springer.

Selby, M.J., 2005. *Hillslope Materials and Processes.* Oxford: Oxford University Press.

SigmaPlot. (v. 14). San Jose, CA, USA: Systat Software Inc.

Snow, R.S., 1989. Fractal sinuosity of stream channels. *Pure and Applied Geophysics*, *131*(1-2), pp.99-109.

Somerville, P., Irikura, K., Graves, R., Sawada, S., Wald, D., Abrahamson, N., Iwasaki, Y., Kagawa, T., Smith, N. and Kowada, A., 1999. Characterizing crustal earthquake slip models for the prediction of strong ground motion. *Seismological Research Letters*, *70*(1), pp.59-80.

Smith, K., 2004. *Environmental Hazards: Assessing Risk and Reducing Disaster*. 4th ed. Oxford: Routledge.

Smith, R.O., Vennell, R., Bostock, H.C. and Williams, M.J., 2013. Interaction of the subtropical front with topography around southern New Zealand. *Deep Sea Research Part I: Oceanographic Research Papers*, *76*, pp.13-26.

Sornette, A. and Sornette, D., 1990. Earthquake rupture as a critical point: Consequences for telluric precursors. *Tectonophysics*, *179*(3-4), pp.327-334.

Stark, C.P. and Hovius, N., 2001. The characterization of landslide size distributions. *Geophysical Research Letters*, *28*(6), pp.1091-1094.

Stata. (v. 15). College Station, TX, USA: StataCorp LLC.

StataCorp. 2017. *Stata 15 Base Reference Manual*. College Station, TX: Stata Press.

Stein, R.S., 2003. Earthquake conversations. *Scientific American*, *288*(1), pp.72-79.

Stevenson, J. R. (2017). Economic and social reconnaissance: Kaikōura earthquake 2016, *Kaikōura Earthquake Special Issue, Bulletin of the New Zealand Society of Earthquake* Engineering, 50, pp.343-351.

Štular, B., Kokalj, Ž., Oštir, K. and Nuninger, L., 2012. Visualization of lidar-derived relief models for detection of archaeological features. *Journal of Archaeological Science*, *39*(11), pp.3354-3360.

Suggate, R.P., Stevens, G.R., Te Punga, M.T., 1978. *The Geology of New Zealand* (Vol. 2). EC Keating, Government Printer.

Sutton, P.J., 2003. The Southland Current: a subantarctic current. *New Zealand Journal of Marine and Freshwater Research*, *37*(3), pp.645-652.

Tanyaş, H., Van Westen, C.J., Allstadt, K.E., Jessee, M.A.N., Görüm, T., Jibson, R.W., Godt, J.W., Sato, H.P., Schmitt, R.G., Marc, O. and Hovius, N., 2017. Presentation and analysis of a worldwide database of earthquake-induced landslide inventories. *Journal of Geophysical Research: Earth Surface*, *122*(10), pp.1991-2015.

Tanyaş, H., Allstadt, K.E. and van Westen, C.J., 2018. An updated method for estimating landslide-event magnitude. *Earth Surface Processes and Landforms*, *43*(9), pp.1836-1847.

Taylor, S.R., Bonner, B.P. and Zandt, G., 1986. Attenuation and scattering of broadband P and S waves across North America. *Journal of Geophysical Research: Solid Earth*, *91*(B7), pp.7309-7325.

Tralli, D.M., Blom, R.G., Zlotnicki, V., Donnellan, A. and Evans, D.L., 2005. Satellite remote sensing of earthquake, volcano, flood, landslide and coastal inundation hazards. *ISPRS Journal of Photogrammetry and Remote Sensing*, *59*(4), pp.185-198.

Trifunac, M.D., 1994. Q and high-frequency strong motion spectra. *Soil Dynamics and Earthquake Engineering*, *13*(3), pp.149-161.

Trigila, A., Iadanza, C. and Spizzichino, D., 2010. Quality assessment of the Italian Landslide Inventory using GIS processing. *Landslides*, *7*(4), pp.455-470.

Uchida, T., Marc, O., Sens-Schönfelder, C., Sawazaki, K., Meunier, P. and Hovius, N., 2014, May. Constraints on post-earthquake elevated landslide rate: towards forecasting of a general mechanism?. In *EGU General Assembly Conference Abstracts* (Vol. 16).

U.S. Geological Survey (USGS) (2016). Magnitude 7.8 Earthquake in New Zealand , https://www.usgs.gov/news/magnitude-78-earthquake-newzealand. (last accessed December 2016.

Van Dissen, R. and Nicol, A., 2009. Mid-late Holocene paleoseismicity of the eastern Clarence Fault, Marlborough, New Zealand. *New Zealand Journal of Geology and Geophysics*, *52*(3), pp.195-208.

Van Westen, C.J., Van Asch, T.W. and Soeters, R., 2006. Landslide hazard and risk zonation—why is it still so difficult?. *Bulletin of Engineering Geology and the Environment*, *65*(2), pp.167-184.

Varnes, D.J., 1978. Slope movement types and processes. *Special Report*, 176, pp.11-33.

Ventura, G., Vilardo, G., Terranova, C. and Sessa, E.B., 2011. Tracking and evolution of complex active landslides by multi-temporal airborne LiDAR data: The Montaguto landslide (Southern Italy). *Remote Sensing of Environment*, *115*(12), pp.3237-3248.

Walcott, R.I., 1978. Geodetic strains and large earthquakes in the axial tectonic belt of North Island, New Zealand. *Journal of Geophysical Research: Solid Earth*, *83*(B9), pp.4419-4429.

Wallace, L.M., Barnes, P., Beavan, J., Van Dissen, R., Litchfield, N., Mountjoy, J., Langridge, R., Lamarche, G. and Pondard, N., 2012. The kinematics of a transition from subduction to strike-slip: An example from the central New Zealand plate boundary. *Journal of Geophysical Research: Solid Earth*, *117*(B2).

Wang, C.Y., Wang, C.H. and Manga, M., 2004. Coseismic release of water from mountains: Evidence from the 1999 (Mw= 7.5) Chi-Chi, Taiwan, earthquake. *Geology*, *32*(9), pp.769-772.

Wells, D.L. and Coppersmith, K.J., 1994. New empirical relationships among magnitude, rupture length, rupture width, rupture area, and surface displacement. *Bulletin of the seismological Society of America*, *84*(4), pp.974-1002.

Williams, J.G., Rosser, N.J., Kincey, M.E., Benjamin, J., Oven, K.J., Densmore, A.L., Milledge, D.G., Robinson, T.R., Jordan, C.A. and Dijkstra, T.A., 2018. Satellite-based emergency mapping using optical imagery: experience and reflections from the 2015 Nepal earthquakes. *Natural Hazards and Earth System Sciences.*, *18*, pp.185-205.

Wolf, P.R. and Dewitt, B.A., 2000. *Elements of photogrammetry: with applications in GIS* (Vol. 3). New York: McGraw-Hill.

Xu, C., Xu, X. and Shyu, J.B.H., 2015. Database and spatial distribution of landslides triggered by the Lushan, China Mw 6.6 earthquake of 20 April 2013. *Geomorphology*, *248*, pp.77-92.

Yee, C.S. and Harr, R.D., 1977. *Effect of wetting mode on shear strength of two aggregated soils* (Vol. 303). Department of Agriculture, Forest Service, Pacific Northwest Forest and Range Experiment Station.

Yin, Y., Wang, F. and Sun, P., 2009. Landslide hazards triggered by the 2008 Wenchuan earthquake, Sichuan, China. *Landslides*, *6*(2), pp.139-152.

Zadeh, L.A., 1965. Fuzzy sets. *Information and control*, *8*(3), pp.338-353.

Zakšek, K., Oštir, K. and Kokalj, Ž., 2011. Sky-view factor as a relief visualization technique. *Remote Sensing*, *3*(2), pp.398-415.

Zielke, O. and Arrowsmith, J.R., 2008. Depth variation of coseismic stress drop explains bimodal earthquake magnitude-frequency distribution. *Geophysical Research Letters*, *35*(24).

Zhu, X.X., Tuia, D., Mou, L., Xia, G.S., Zhang, L., Xu, F. and Fraundorfer, F., 2017. Deep learning in remote sensing: A comprehensive review and list of resources. *IEEE Geoscience and Remote Sensing Magazine*, *5*(4), pp.8-36.